

https://dspace.org/

Synthesis, characterization and photocalytic activity of TiO2 and TiO2 based quaternary mixed metal oxides supported on carbon and fly ash based materials

Hlekelele, Lerato

2018

https://hdl.handle.net/10539/26989

Downloaded from a DSpace repository. https://dspace.org/

SYNTHESIS, CHARACTERIZATION AND PHOTOCATALYTIC ACTIVITY OF TiO_2 AND TiO_2 BASED QUATERNARY MIXED METAL OXIDES SUPPORTED ON CARBON AND FLY ASH BASED MATERIALS.

---

by

LERATO HLEKELELE

Student Number: 776827

Dissertation in fulfillment of the requirement for the degree

PHILOSOPHIAE DOCTOR

in

SCHOOL OF CHEMISTRY

in the

FACULTY OF SCIENCE

of the

UNIVERSITY OF THE WITWATERSRAND

Supervisor : Assoc. Prof. S H Durbach

: Dr. P J Franklyn

DECLARATION

I hereby declare that this dissertation, which I herewith submit for the research qualification

PHILOSOPHIAE DOCTORAL IN CHEMISTRY

to the University of the Witwatersrand, school of chemistry, is, apart from the recognized assistance of my supervisors, my own work and has not previously been submitted by me to another institution to obtain a research diploma or degree.

_____ on this ____ day of _____

(Candidate)

_____ on this ____ day of _____

(Supervisor)

_____ on this ____ day of _____

(Supervisor)

DEDICATION

This thesis is dedicated first of all to the author and giver of my life, my Lord and personal savior Jesus Christ. The grace and mercy of Jesus have ensured that I have the necessary skills to complete this work. My parents, Moroa Gertrude Hlekelele and Thabo Michael Mahlangu, who were used by God to bring up an incredibly difficult person that I am. I have also dedicated this thesis to my sisters, nephews, and nieces: Dimakatso Patience Hlekelele, Temoso Petunia Hlekelele Richards Zitha, Mathapelo Hlekelele Mogorosi, Mapaseka Hlekelele, Naledi Zitha, Kabelo Hlekelele, Amohelang Hlekelele, and Kamohelo Hlekelele.

"Therefore I tell you, do not be anxious about your life, what you will eat or what you will drink, nor about your body, what you will put on. Is not life more than food, and the body more than clothing. Look at the birds of the air: they neither sow nor reap nor gather into barns, and yet your Heavenly Father feeds them. Are you not of more value than they? And which of you by being anxious can add a single hour to his span of life."

Matthew 6:25-27

ACKNOWLEDGMENT

I would like to express my genuine appreciation to the following people and institutions for the backing and support they gave me throughout my Ph.D.:

- My supervisors, Assoc. Prof Shane Hilton Durbach and Dr. Paul John Franklyn for their guidance, support, motivation and for the sincere care they showed in my work. Assoc. Prof Durbach has been more than an advisor. He has been a friend, a father, and a spiritual advisor. The role that he played in my life since the day I met him in 2008 has been significant and I will never forget it.
- Dr. Derek Tantoh Ndinteh, Prof Rui Krause and the late Dr. Sarah Manki Maoela for the training they afforded me during my masters at the University of Johannesburg. Dr. Ndinteh, just like Assoc. Prof Durbach has been instrumental in my growth as a man, Christian, and scientist; the memory of his efforts will remain with me until I die.
- It has been a real pleasure being at the University of the Witwatersrand, where I met friends and a possible lifetime partner. These include Dr. Farai Dziike, Tumelo Phaahlamohlaka, Dr. David Kumi, Manthako Lethobane, Dr. Zikhona Tetana, Dr. Manoko Maubane, Ofentse Makgae, Alice Magubane, Tiisetso Moimane, and Karabo Mashiloane. It has been real.
- My non-Witsie friends: Solomon Mothwa, Thabo Matshaya, Olga Sekhaolelo, Nkosinathi Hadebe, Nomvuyo, Nomadolo, Lebogang Meje, and Dr. Vongani Chauke. Dr. Vongani Chauke has been instrumental in my postgraduate studies, giving me guidance with my dissertation and thesis.

- Dr. Rudolph Erasmus, Prof Dave Billing, Prof Alexander Ziegler, Dr. Moira Bode, Ms. Memory Zimwandeyi and Mr. Peter JUma, all Witsies, were very instrumental in my finishing my Ph.D.

ABSTRACT

The fast industrialization that has been the key to the increased quality of the lives of humans and other animals has not been without its disadvantages. The epitome to this is the continued generation of coal fly ash (CFA) which is the by-product of burning coal for the production of electricity. Millions of tons of this material are produced all over the world and it is both dangerous and expensive to dispose of. Furthermore, industrialization has also come with the production of various useful chemicals, some of which end up contaminating water systems. An example of these problematic chemicals is classed as endocrine disrupting chemicals (EDCs) because they affect the hormonal system of animals. Bisphenol-A (BPA) is an example of an EDC and it interferes with male reproductive organs and has been detected in the environment, including water systems. This, therefore, necessitates that methods of cleaning water be improved.

Semiconductor photocatalysis, especially TiO_2, has been shown to be a potentially effective method of removing organic contaminants from water because of its high mineralization efficiency and simplicity. However, efforts to use TiO_2 for photocatalysis in the visible region has remained inefficient because of its large band gap and high recombination rate of the photoinduced electrons (e^-) and holes (h^+). It is for these reasons that the focus of this research was to synthesize highly active photocatalysts for the photodegradation of BPA. This was achieved by immobilizing TiO_2 on nitrogen-doped carbon nanotubes (NCNTs), carbon nanofibers (CNFs) and zeolites. Furthermore, this research involved modifying TiO_2 with Ag nanoparticles and also by incorporating W^{6+} and Zn^{2+} into the crystal lattice of TiO_2 to form quaternary mixed metal oxides (QMMOs).

NCNTs were synthesized using a 2-stage chemical vapor deposition technique by decomposing melamine on the surface of CFA in a nitrogen atmosphere at various

temperatures (800, 850 and 900 °C). The morphology, nitrogen content, crystallinity and thermal stability of the NCNTs were found to vary with synthesis temperature.

The NCNTs synthesized at 850 °C and the CNFs were purified and functionalized by stirring them in 5 % HF for 24 h followed by heating to 60 °C in HNO_3 and H_2SO_4 (1:3) for 12 h. The confirmation of the removal of CFA from the NCNTs as well as CNFs and their functionalization was confirmed by various analytical techniques. TiO_2 nanoparticles were loaded onto these materials at different loadings (1, 5 and 20 % m/m of shaped carbon nanomaterials (SCNMS)) by a surfactant wrapping sol-gel/hydrothermal method. The formation of these composites was confirmed by various analytical techniques. It was observed from photoluminescence (PL) measurements that the emission intensity of these composites was lower than that of TiO_2 indicating reduced recombination of e^- and h^+. The efficiency at which TiO_2 and these composites photodegraded BPA was measured, where it was found that the composites showed higher efficiencies relative to that of TiO_2 except for those that consisted of 20 % CNFs/NCNTs (m/m).

In a separate study, zeolites (CFA_Zeo) were synthesized by fusing CFA with NaOH followed by hydrothermally treating the mixture. Zeolitization of CFA yielded rod-like materials which were found to be zeolite-X. Thereafter TiO_2 was loaded onto various masses of CFA_Zeo (15 and 30 % m/m of CFA_Zeo) by the resin gel technique and then these composites were decorated with 1 % Ag nanoparticles by the NaOH-urea deposition-precipitation technique. Here it was observed by TEM that the CFA_Zeo rods were completely coated with TiO_2 nanoparticles and that the Ag nanoparticles were on top of these. The photocatalytic efficiencies of TiO_2 and these composites were tested under UV and visible light. The composites were shown to have superior photocatalytic activities to that of TiO_2 by itself under both UV and visible light ($\lambda > 400$ nm).

The incorporation of W^{6+} and Zn^{2+} at various concentrations (up to 30 % m/m) into the crystal lattice of TiO_2 (anatase phase) was achieved by the resin gel technique to form QMMOs. This was confirmed by PXRD where it was shown that the diffraction patterns of the QMMOs were similar to that of TiO_2 except for the observation that the (101) reflection of the QMMOs was slightly shifted relative to that of TiO_2. The optical absorption signature of the QMMOs and TiO_2 were studied using UV-diffuse reflectance spectroscopy (DRS). It was found that they were similar except for the observation that QMMOs had an absorption peak in the visible range whereas the absorption spectrum of TiO_2 was flat in this region. TiO_2 and the QMMOs were composited with 10 % (m/m) NCNTs using a hydrothermally modified resin gel technique. The formation of the composites was confirmed by TGA, TEM, and PL. The photocatalytic efficiencies of TiO_2, QMMOs and TiO_2/QMMOs loaded on NCNTs were evaluated under UV-light ($\lambda > 400$ nm). The QMMOs loaded on NCNTs showed the highest efficiencies whereas TiO_2 showed the least activity.

TABLE OF CONTENTS

Section ***Page***

Declaration....i

Dedication....ii

Acknowledgments....iii

Abstract....iv-vii

Table of contents....viii-xii

List of Figures....xiii-xviii

List of Tables....xix-xx

List of Abbreviations....xxi-xxiii

CHAPTER 1 : INTRODUCTION....1

1.1 Background....1
1.2 Problem statement....2
1.3 Justification....4
1.4 Aims and objectives....8
1.4.1 Aims....8
1.4.2 Objectives....8
1.5 Thesis outline....10
1.6 References....12

CHAPTER 2 : LITERATURE REVIEW....20

2.1 Introduction....20

2.1.1 Water scarcity and pollution 20
2.1.2 Endocrine disruptive chemicals 23
2.1.2.1 Bisphenol A 27
2.2 Nanotechnology 30
2.2.1 Titanium dioxide 31
2.2.1.1 Titanium dioxide polymorphs 31
2.2.1.2 Synthesis of TiO_2 nanoparticles 33
2.2.1.2.1 The precipitation method 33
2.2.1.2.2 The solvothermal (hydrothermal) method. 33
2.2.1.2.3 The sol-gel method. 34
2.2.1.2.4 The Pechini method. 35
2.2.1.2.5 The resin gel method. 35
2.2.2 Heterogeneous TiO_2 photocatalysis 36
2.2.3 Limitations of TiO_2 as a photocatalyst 41
2.2.4 Strategies for improving photocatalytic performance of TiO_2. 42
2.2.4.1 Morphological modifications 42
2.2.4.2 Chemical modifications 43
2.2.4.2.1 Anion doping 43
2.2.4.2.2 Cation doping 44
2.2.4.2.3 Coupled semiconductors 46
2.2.4.2.4 Mixed metal oxides 47
2.2.4.3 Supported TiO_2 nanoparticles 48
2.3 Fly ash 50
2.3.1 Application of fly ash 51
2.3.1.1 TiO_2/fly ash photocatalyst 54
2.3.1.2 Zeolites derived from fly ash 55
2.3.1.3 Zeolites in photocatalysis 58
2.4 Carbon nanomaterials 58
2.4.1 Carbon nanomaterials synthesized from fly ash 60
2.4.2 Nitrogen doped carbon nanomaterials 62
2.4.3 Enhancing the photocatalytic efficiency of TiO_2 with SCNMs 65
2.5 References 69

CHAPTER 3 : EXPERIMENTAL 99

3.1 Introduction 99
3.2 Characterization of materials 99
3.2.1 Transmission electron microscopy (TEM) 100
3.2.2 Scanning electron microscopy (SEM) 102
3.2.3 Energy dispersive X-ray spectroscopy (EDS) 103
3.2.4 Powder X-ray diffraction (PXRD) crystallography 103
3.2.5 Laser Raman spectroscopy 105
3.2.6 Fourier transform infrared (FTIR) spectroscopy 107
3.2.7 Thermogravimetric analysis (TGA) 108
3.2.8 Brunauer Emmett and Teller (BET) surface area measurement 109
3.2.9 Elemental analysis 110
3.2.10 Ultra-violet diffuse reflectance spectroscopy (UV-DRS) 111
3.3 Photocatalytic degradation 114
3.4 References 116

CHAPTER 4 : Morphological and crystallinity differences in NCNTs synthesized by CVD of melamine over coal fly ash† 118

4.1 Introduction 118
4.2 Experimental 120
4.2.1 Preparation of materials 120
4.2.2 Material characterization 121
4.3 Results and discussion 121
4.3.1 Fly ash characterization 121
4.3.2 Characterization of the products formed over CFA in the two-stage CVD reactor 129
4.3.3 Characterization of NCNTs synthesized from 5 % Fe/$CaCO_3$. 146
4.4 Conclusions 149
4.5 References 151

CHAPTER 5 : Photodegradation of BPA on purified fly ash synthesized CNFs and NCNTs composited with TiO_2 prepared by the surfactant wrapping sol-gel/hydrothermal method 158

5.1 Introduction 158
5.2 Experimental 161
5.2.1 Chemicals 161
5.2.2 Synthesis and purification of NCNTs and CNFs 161
5.2.3 Synthesis of CNF/NCNTs-TiO_2 composites by the surfactant wrapping sol-gel/hydrothermal method. 162
5.2.4 Materials characterization 164
5.2.5 Photocatalytic testing 164
5.3 Results and discussion 164
5.3.1 Materials characterization 164
5.4 Photodegradation studies 180
5.4.1.1 Effect of the mass of catalyst in solution. 181
5.4.1.2 Effect of solution pH 183
5.4.1.3 Effect of initial BPA concentration 184
5.4.1.4 Effect of reaction temperature 186
5.4.2 Evaluation of the photoactivity of the various materials 186
5.5 Conclusions 190
5.6 References 192

CHAPTER 6 : Titania anchored on CFA derived zeolites by resin gel technique decorated with Ag nanoparticles for UV and visible light photodegradation of BPA. 201

6.1 Introduction 201
6.2 Experimental 204
6.2.1 Zeolite formation 204
6.2.2 Catalyst preparation 204
6.2.3 Catalyst characterization 206
6.2.4 Photocatalytic measurements 206

6.3 Results and discussion 206
6.3.1 Materials characterization 206
6.3.2 Photocatalytic measurements 217
6.4 Conclusions 224
6.5 References 226

CHAPTER 7 : Synthesis of TiO_2 based quaternary mixed metal oxides by incorporating W^{6+} and Zn^{2+} into its anatase lattice structure loaded on coal fly ash synthesized NCNTs for photodegradation of BPA. 237

7.1 Introduction 237
7.2 Experimental 240
7.2.1 Synthesis of QMMOs. 240
7.2.2 Synthesis of QMMOs and NCNTs composites 241
7.2.3 Materials characterization 242
7.2.4 Photocatalytic measurements 242
7.3 Results and discussion 242
7.3.1 Characterization of pure metal oxides 242
7.3.1.1 PXRD characterization of pure metal oxides 242
7.3.1.2 Raman analyses of pure metal oxides 244
7.3.1.3 TEM and EDX analyses of pure metal oxides 246
7.3.2 Characterization of QMMOs 250
7.3.2.1 PXRD analyses of QMMOs 250
7.3.2.2 Laser Raman analyses of QMMOs 253
7.3.3 Characterization of TiO_2 and QMMOs loaded on 10 % NCNTs 257
7.3.4 Photocatalytic testing 262
7.4 Conclusion 265
7.5 References 266

CONCLUSIONS AND FUTURE PERSPECTIVES 271

Conclusion 271
Future perspective 274

References: 284

APPENDIX 1 .....

LIST OF FIGURES

Figure ***Description*** ***Page***

Figure 2.1. Line drawings representing the molecular structures of: (a) Bisphenol A, and (b) The repeating unit of a polycarbonate plastic.[55] 28

Figure 2.2. Representations of the unit cells of: (a) Anatase, where the octahedra have Ti^{4+} at the centres and oxygen species at the apexes. The adjacent octahedra are edge face sharing, (b) Rutile, where the octahedra have Ti^{4+} at their centres and oxygen ions at each of the corners. The adjacent octahedra are interchangeably corner and edge sharing and (c) Brookite. The octahedra have Ti^{4+} at their centres and oxygen ions at each of the apexes. The in-line octahedra are alternately corner and edge sharing.[78] 32

Figure 2.3. A representation of the photocatalytic process.[87] 39

Figure 2.4. A schematic representation of the separation of photogenerated electron-hole pairs by means of binary semiconductor systems.[80] 46

Figure 2.5. A pie-chart representation of the current utilization of CFA.[148] 51

Figure 2.6. A line drawing showing the basic structure of zeolites.[201] 56

Figure 2.7. Zeolite network showing voids.[187] 56

Figure 2.8. Structure of a buckyball.[217] 59

Figure 2.9. Structure of carbon nanotube.[218] 59

Figure 2.10. Model of CNTs showing nitrogen incorporated on (1) the wall and (2) direct substitution.[202] 63

Figure 2.11. Bonding configurations for nitrogen atoms when doped into a graphitic carbon lattice.[235] 64

Figure 2.12. A representation of a TiO_2-CNT couple where the CNT inhibits electron-hole recombination by acting as a sink that scavenges electrons.[254,259,261] 66

Figure 2.13. A representation of the photosensitization mechanism suggested by Wang *et al.*[262] 67

Figure 2.14. A representation of CNTs acting as impurities through the presence of the Ti-O-C bond.[259] 68

Figure 3.1. A photograph of the FEI TECNAI T12 TEM that was used in these studies. 101

Figure 3.2. A photograph of the FEI Nova Nanolab FEG-SEM that was used in these studies. 103

Figure 3.3. A photograph of the Bruker D2-Phaser PXRD that was used in these studies. 105

Figure 3.4. A photograph of the Bruker Senterra laser Raman spectrometer that was used in these studies. 106

Figure 3.5. A photograph of the Bruker Tensor 27 FTIR spectrometer that was used in these studies. 107

Figure 3.6. A photograph of the Perkin Elmer Pyris 1 TGA that was used in these studies. 108

Figure 3.7 A photograph of the Micromeritics RS232 BET surface area analyzer that was used in these studies. 109

Figure 3.8. A photograph of a Carlo Erba EA 1108 Organic Elemental Analyzer like the one that was used in these studies. 111

Figure 3.9. A photograph of the Praying Mantis Cary 500 UV-DRS that was used in these studies. 113

Figure 3.10. A photograph of the Newport model 69911 solar simulator that was used in these studies. 114

Figure 4.1 PXRD pattern of unreacted CFA. 123

Figure 4.2 (a)-(b) SEM micrographs of CFA and (c)-(d) TEM micrographs of unreacted CFA and soot aggregates therein. 124

Figure 4.3. Laser Raman spectroscopy spectrum showing inorganic constituents of unreacted CFA. 125

Figure 4.4. A laser Raman spectrum showing the D and G peaks of carbonaceous materials in unreacted CFA. 126

Figure 4.5 A FTIR spectrum of unreacted CFA. 127

Figure 4.6. A thermogram of unreacted CFA 128

Figure 4.7 Weight derivative plot of unreacted CFA 129

Figure 4.8. PXRD pattern of CFA together with the black products which had been synthesized at 800, 850 and 900 °C. 131

Figure 4.9. FTIR spectra of unreacted CFA, melamine and the C_xN_y materials that were synthesized at different temperatures. 132

Figure 4.10. SEM micrographs and tube diameter ranges of the NCNTs that were synthesized at: 800 °C (a) & (d), 850 °C (b) & (e), 900 °C (c) & (f). .. 134

Figure 4.11. TEM micrographs of NCNTs that were synthesized at: 800 °C (a)-(b), 850 °C (c)-(d) and 900 °C (e)-(f)..... 135

Figure 4.12. Schematic of reactions conducted at: (i) 800 °C where multiwalled NCNTs were formed, (ii) 850 °C where NCNTs with circular compartments were formed and (iii) 900 °C where NCNTs with typical bamboo morphology were formed. 137

Figure 4.13. TEM micrographs of NCNTs synthesized at 850 °C..... 138

Figure 4.14. Laser Raman spectra of the NCNTs that were synthesized at (a) 800, (b) 850 and (c) 900 °C. 140

Figure 4.15. I_G/I_D values of the NCNTs that were synthesized at various temperatures.. 141

Figure 4.16. TGA derivatives of NCNTs synthesized at (a) 800, (b) 850 and (c) 900 °C. 143

Figure 4.17. TGA thermograms of NCNTs that were synthesized at various temperatures. 144

Figure 4.18. TEM micrographs of the morphological variations of NCNTs that were synthesized at (a) 800 °C, (b) 850 °C and (c) 900 °C. 145

Figure 4.19. TEM micrographs of the NCNTs that were synthesized from the reaction of melamine over 5% Fe/$CaCO_3$ at: (a) 800 °C, (b) 850 °C and (c) 900 °C. 146

Figure 4.20. Laser Raman spectra of the NCNTs synthesized from the reaction of melamine over 5% Fe/$CaCO_3$ at various synthesis temperatures. 148

Figure 4.21. TGA weight derivative plots of NCNTs synthesized using 5 % Fe/$CaCO_3$ at (a) 800 °C, (b) 850 °C and (c) 900 °C. 149

Figure 5.1. SEM micrographs of: (a) Raw NCNTs, (b) Purified NCNTs, (c) Raw CNFs and (d) Purified CNFs. 165

Figure 5.2. TEM micrographs of: (a) CNFs, (b) NCNTs, (c) TiO_2, (e,e1) TiO_2/20_%_CNFs, (f,f1) TiO_2/_20_%_NCNTs and (d) is an SEM micrograph of TiO_2. 167

Figure 5.3. TGA thermograms of: (a) Raw CNFs, purified CNFs, TiO_2/CNFs based composites and (b) Raw NCNTs, purified NCNTs, TiO_2/NCNTs based composites. 170

Figure 5.4. Laser Raman spectra of: (a) raw NCNTs, (b) purified NCNTs, (c) raw CNFs and (d) purified CNFs. 172

Figure 5.5. Laser Raman spectra of: (a) TiO_2 and CNFs based composites, (b) Expansion of the TiO_2 $E_{g(1)}$ peak of TiO_2 and CNFs based composites, (c) TiO_2 and NCNTs based composites and (d) Expansion of the TiO_2 $E_{g(1)}$ peak of TiO_2 and NCNTs based composites. 173

Figure 5.6. PXRD patterns of CFA as well as raw and purified CNMs. 175

Figure 5.7. PXRD patterns of TiO_2 and TiO_2_CNFs/NCNTs composites. 176

Figure 5.8. Photoluminescence spectra of unbound TiO_2 and various composites. 178

Figure 5.9. UV-DRS Tauc's plots of TiO_2 and various potential photocatalysts. 180

Figure 5.10. The effect of the mass of photocatalyst (i.e. unbound TiO_2) on the photodegradation of 50 ml of 120 ppm solution (pH 7) of BPA in water at 22 °C. 182

Figure 5.11. The effect of solution pH on the % BPA of 50 ml of 120 ppm that was photodegraded in water using 60 mg TiO_2 as a photocatalyst, at 22 °C. 183

Figure 5.12. The effect of the initial concentration of BPA on the % BPA photodegraded in a 50 ml solution at pH 13 using 60 mg TiO_2 at 22 °C. 185

Figure 5.13. Photodegradation of BPA using the various TiO_2_CNFs/NCNTs photocatalysts at conditions given in **Table 5.5**..... 187

Figure 6.1. PXRD patterns of CFA and CFA_Zeo..... 208

Figure 6.2 FTIR spectra of CFA and CFA_Zeo 209

Figure 6.3. SEM images of (a) CFA and (b) CFA_Zeo 210

Figure 6.4. TEM micrographs of (a) CFA_Zeo, (b) TiO_2, (c) TiO_2/CFA_Zeo(30%), (d) TiO_2/CFA_Zeo(15%), (e) Ag/TiO_2/CFA_Zeo(30%) and (f) Ag/TiO_2/CFA_Zeo(15%). 211

Figure 6.5. (a) PXRD pattern of TiO_2 and the composites and (b) insert showing the (101) reflection. 215

Figure 6.6. UV-vis DRS absorption spectra of TiO_2 and composites 216

Figure 6.7. Photoluminescence spectrum of TiO_2 and composites 217

Figure 6.8. Photodegradation of BPA under full solar simulator spectrum. 220

Figure 6.9. Photodegradation of BPA under visible light. 222

Figure 6.10.Schematic diagram of charge separation by Ag and CFA_Zeo under UV-light. 223

Figure 6.11. Schematic representation of visible light excitation of Ag nanoparticles.... 224

Figure 7.1. PXRD patterns of TiO_2, WO_3 and ZnO. 243

Figure. 7.2. Laser Raman spectrum of (a) ZnO and (b) expansion of the laser Raman spectrum of ZnO to show the low intensity peaks. 244

Figure. 7.3. Laser Raman spectrum of WO_3..... 245

Figure. 7.4. Laser Raman spectrum of TiO_2. 246

Figure 7.5. (a) TEM image of WO_3, (b) WO_3 particle size distribution, (c) EDS spectra of WO_3 nanoparticles and (d) TEM image of particle which the EDS spectra was recorded on. 247

Figure 7.6. (a) TEM image of ZnO, (b) ZnO particle size distribution, (c) EDS spectra of ZnO nanoparticles and (d) TEM image of particle which the EDS spectra was recorded on. 248

Figure 7.7. (a) TEM image of TiO_2, (b) TiO_2 particle size distribution, (c) EDS spectra of TiO_2 nanoparticles and (d) TEM image of particle which the EDS spectra was recorded on. 249

Figure 7.8. (a) PXRD patterns of TiO_2 and various QMMOs and (b) insert showing the (101) and (004) reflections of TiO_2 and various QMMOs. 250

Figure 7.9. Graph showing the variation of the a lattice parameters of TiO_2 and QMMOs 252

Figure 7.10. (a) Laser Raman spectra of TiO_2 and QMMOs and (b) insert showing the Eg peak 253

Figure 7.11. TEM images of (a) TWZ703, (b) TWZ712, (c) TWZ721 and (d) TWZ730. EDS spectra of (e) TWZ703, (f) TWZ712, (g) TWZ721 and TWZ730. 255

Figure 7.12. UV-DRS spectra of TiO_2 and QMMOs 257

Figure 7.13. (a) PXRD patterns of TiO_2/QMMOs and 10 % NCNTs composites and (b) insert showing the (101) reflection. 258

Figure 7.14. TEM images of (a) TiO_2/10%NCNTs, (b) TWZ730/10%NCNTs, (c) TWZ721/10%NCNTs, (d) TWZ712/10%NCNTs and (e) TWZ703/10%NCNTs 259

Figure 7.15. Thermograms of TiO_2 and QMMOs loaded onto 10 % NCNTs. 260

Figure 7.16. Photoluminescence emission spectra of TiO_2, QMMO and composites. 261

A.3.1. Two-stage chemical vapor deposition set-up. 277

A.3.2. One-stage chemical vapor deposition setup 277

A5.1. Effect of temperature on the photodegradation of 50 ml of 120 ppm neutral solution of BPA in water at 22 °C 278

A.7.1. PXRD pattern of ZnO °C calcined at 400 and ZnO calcined at 800 °C. 279

A.7.3. PXRD patterns of TiO_2 before (calcined at 400 °C) and after calcining at 800 °C. 281

A.7.4. PXRD patterns of TiO_2 and the various QMMOs calcined at 800 °C. 282

A.7.5. PXRD patterns of ZnO and the various QMMOs calcined at 800 °C. 283

LIST OF TABLES

Table ***Description*** ***Page***

Table 2.1. Some human nuclear receptors and their related functions.[37] 25

Table 2.2. The toxicity of BPA towards aquatic life.[36] 29

Table 2.3. Crystalline parameters of TiO_2 polymorphs.[78] 32

Table 4.1. Composition of unreacted CFA as determined by XRF spectroscopy. . 122

Table 4.2. Masses and percentage yields of black products that were formed. 130

Table 4.3. Percentage nitrogen present in the carbonaceous materials as determined by the CHNS analysis. 132

Table 4.4. Percentage N incorporated into tubes and their diameter range 147

Table 5.1. CNM ratios in composites and sample labelling. 163

Table 5.2. Surface areas of the various samples and the CNMs weight percentages along with their I_D/I_G values 171

Table 5.3. PL emission intensities and band gap energies (Tauc's plot) of the various potential photocatalysts 179

Table 5.4. Optimum conditions for evaluating the photocatalytic efficiencies of the various potential TiO_2_CNFs/NCNTs catalysts. 186

Table 5.5. Summary of the photodegradation efficiencies of the various TiO_2_CNFs/NCNTs photocatalysts after 4 h (X_{4h}, %). 187

Table 6.1. The composition of CFA as determined by XRF. 207

Table 6.2. EDS Elemental composition of CFA and CFA_Zeo 208

Table 6.3. BET surface areas and TiO_2 crystallite sizes. 213

Table 6.4. Adsorption equilibrium and photocatalytic activities of the various photocatalysts 219

Table 7.1. Sample names and calcination temperatures applied for the concentration study of the various QMMOs. 241

Table 7.2. Summary of the particle sizes, (101) reflection positions and lattice parameters of TiO_2 and the various QMMOs. 251

Table 7.3. Adsorption equilibria concentrations of BPA on various photocatalysts. 263

LIST OF ABBREVIATIONS

BET - Brunauer-Emmett-Teller

BPA - Bisphenol-A

CB – Conduction band

CCVD – Catalytic chemical vapor deposition

CFA - Coal fly ash

CNFs – Carbon nanofibers

CNTs – Carbon nanotubes

DOC – Dissolved organic matter

DOS - Density of states

DWCNTS – Double-walled carbon nanotubes

e^- - Electron

EBSD – Electron back-scattered diffraction detector

EDC - Endocrine disrupting chemicals

EDS – Energy dispersive X-ray spectroscopy

eV – electron volt

FeBAD - The foetal bases of adult diseases

FTIR – Fourier transform infrared spectroscopy

h^+ - hole

hGO – Reduced graphene oxide

HPLC – High-performance liquid chromatography

LVRPA – Local volumetric rate of photon absorption

MWCNTs – Multi-walled carbon nanotubes

NCNTs – Nitrogen-doped carbon nanotubes

nm – Nanometre

NOM – Natural organic matter

OVRPA – Overall volumetric rate of photon absorption

PL – Photoluminescence

ppm – Parts per million

PXRD – Powder X-ray diffraction

SCCM – Standard centimeter per minute

SEM – Scanning electron microscopy

SPR - Surface plasmon resonance

SUVA – Specific ultraviolet absorbance

SWCNTs – Single-walled carbon nanotubes

TEM – Transmission electron microscopy

TGA- Thermogravimetric analysis

TNT – Titanium nanotubes

UV- Ultraviolet

UV-DRS – Ultraviolet- diffusion reflectance spectroscopy

VB – Valence band

VRPA – Volumetric rate of photon absorption

WHO – World health organization

CONFERENCE PRESENTATIONS

The work discussed in this thesis has been presented at international and national conferences.

- Hlekelele, L, Franklyn, P.J. and S.H. Durbach. *Synthesis of nitrogen-doped carbon nanotubes from coal fly ash as a catalyst by 2-stage CVD setup*. **Poster presentation**. Department of Science and Technology/Centre of Excellence in Strong Materials (DST/CoE-SM), Student Presentation Workshop 2014. University of the Witwatersrand, South Africa, May 2014.

- Hlekelele, L, Franklyn, P.J. and S.H. Durbach. *Rise of renewable energy from the ashes*. **Oral presentation**. The 5th IUPAC International Conference on Green Chemistry 2014. Durban, South Africa, 17-21 August 2014.

- Hlekelele, L, Franklyn, P.J. and S.H. Durbach. *Let the SUN fall onto TiO_2: incorporation of Zn^{2+} and W^{6+} into TiO_2 crystal lattice.* **Poster presentation**. Catalysis Society of South Africa 25th Annual Conference 2014. Pretoria, South Africa, 9-12 November 2014.

- Hlekelele, L, Franklyn, P.J. and S.H. Durbach. *Clean water from Coal Fly Ash*. **Poster presentation**. Department of Science and Technology/Centre of Excellence in Strong Materials (DST/CoE-SM), Student Presentation Workshop 2015. University of the Witwatersrand, South Africa, May 2015.

- Hlekelele, L, Franklyn, P.J. and S.H. Durbach. *Clean water from Coal Fly Ash*. **Poster presentation**. Cross-Faculty Student Presentation 2015. University of the Witwatersrand, South Africa, October 2015.

- Hlekelele, L, Franklyn, P.J. and S.H. Durbach. *NCNTs and CNFs grown from coal fly ash, decorated by TiO_2, for the photodegradation of BPA.* **Oral presentation**. Catalysis Society of South Africa 26th Annual Conference 2015. Hermanus, South Africa, 15-18 November 2015.

- Hlekelele, L, Franklyn, P.J. and S.H. Durbach. *Decomposition of melamine on the surface of fly ash to grow nitrogen-doped carbon nanotubes (NCNTs).* **Poster presentation**. The 52nd Annual Conference of the Microscopy Society of Southern Africa (MSSA) 2015. Pretoria, South Africa, 29 November-5 December 2015.

- Hlekelele, L, Franklyn, P.J. and S.H. Durbach. *Ag/TiO_2 loaded on fly ash derived zeolites for photodegradation of bisphenol-A.* **Poster presentation**. Department of Science and Technology/Centre of Excellence in Strong Materials (DST/CoE-SM), Student Presentation Workshop 2016. University of the Witwatersrand, South Africa, May 2016.

- Hlekelele, L, Franklyn, P.J. and S.H. Durbach. *Ag/TiO_2 loaded on fly ash derived zeolites for photodegradation of bisphenol-A.* **Poster presentation**. DST-NRF Nanotechnology symposium 2016. CSIR, South Africa, 27-28 June 2016.

- Hlekelele, L, Franklyn, P.J. and S.H. Durbach. *Ag/TiO_2 loaded on fly ash derived zeolites for photodegradation of bisphenol-A.* **Poster presentation**. Catalysis Society of South Africa 27th Annual Conference 2016. Drankensberg, South Africa, 15-18 November 2015.

PEER-REVIEWED PUBLICATIONS

- Results coming out of this work have either been published or a manuscript has been prepared for publication.

- Hlekelele Lerato, Paul J. Franklyn, Pranav K. Tripathi, and Shane H. Durbach. "Morphological and crystallinity differences in nitrogen-doped carbon nanotubes grown by chemical vapor deposition decomposition of melamine over coal fly ash." *RSC Advances* **6** (80), 76773-76779 (2016).

- Hlekelele Lerato, Paul J. Franklyn and Shane H. Durbach. "Novel synthesis of Ag decorated TiO_2 anchored on zeolites derived from coal fly ash for photodegradation of bisphenol-A". ***prepared manuscript for submission in New Journal of Chemistry.***

- Hlekelele Lerato, Paul J. Franklyn and Shane H. Durbach. "Photocatalytic degradation of bisphenol-A over purified fly ash grown carbon nanofiber/ nitrogen-doped carbon nanotube/titania composites". ***Prepared manuscript for submission in Environmental Science and Technology.***

CHAPTER 1:

INTRODUCTION

1.1 Background

Rapid industrialization which is a reality in modern day, beneficial as it is, results in processes that threaten the environment. For instance, since the 1920s the combustion of coal has been used widely to provide energy for electric power stations, which has resulted in the production of millions of tons of solid waste coal fly ash (CFA). It is estimated that the current annual production of CFA in the world is 600 million tons.[1] Disposal of large amounts of this CFA into landfills and lagoons has become a global problem as it is toxic.[1] This has necessitated that regulations be implemented with regards to its disposal.[1]

Another problem that has resulted from rapid industrialization, along with population growth and climate complications is the rapid decrease in the availability of fresh water. Whilst it is said that 2.6 billion people have limited sanitation, it is estimated that 1.2 billion people in the world lack access to safe drinking water which results in the death of millions of people, more especially children.[2] This situation is expected to become worse with time as the discharge of contaminants into the water systems keeps increasing, thus putting more stress onto this already threatened and important commodity. An increase in the number of these contaminants ranging from: distillates, heavy metals, evolving micro-pollutants (e.g. endocrine disrupting chemicals (EDCs) and nitrosamines), etc. are ending up in water bodies.[3,4]

Some of the important consequences of this dire water supply situation relate to food production and environmental conservation, which affect the economies of all societies (i.e. 3rd world, developing and developed). For instance, the problems associated with water scarcity may result in a situation where the quality of human life might be hugely compromised resulting in significantly increased fatalities unless new ways of cleaning water are found.[1]

As mentioned previously, EDCs are among the numerous contaminants discharged into water systems. EDCs are typically synthetic and useful chemicals "gone wrong", in a sense that their originally intended applications were: plasticizers, pesticides, and solvents, amongst others.[2–4] Unfortunately, some of these useful products have been found to be endocrine disruptors. EDCs affect the normal functioning of the endocrine system where they block or mimic and upset some of the important bodily functions. For example, bisphenol-A (BPA), which is readily found in the environment (including water systems), is a type of EDC that is amongst other negative effects suspected of interfering with male reproductive organs.[5–8] Thus the discharging of such products into water systems has enormous effects on the quality of water resources.

1.2 Problem statement

The disposal of CFA in landfills and lagoons is currently the foremost option in many countries.[9–11] Nevertheless, more severe regulations for waste disposal in landfills, along with a developing recycling philosophy, have fortified that it be recycled and reused.[12] The 'beauty' and the 'beast' of CFA is its chemical composition richness, which makes it both toxic and potential raw material for

various applications. Any potential use of CFA is viewed as important and has advantages such as: (i) It provides a beneficial use of free raw material, (ii) It leads to the preservation of natural resources, as well as (iii) The abolition of waste. Even so, it is said that the current utilization of CFA in the world is only 16 %, meaning that more than 500 million tons of the 600 million tons still has to be disposed of, indicating that a lot still has to be done.[12,13]

The issues associated with water pollution are as bad as that of CFA and there is obviously still a long way to go considering the large number of fatalities that arise as a result of water-borne diseases.[14,15] Orthodox water purification techniques address a lot of the water treatment challenges, nonetheless, they are frequently expensive as they require intense chemical treatment, sophisticated infrastructure and use a lot of energy. This impedes their use in less economically developed societies where they are needed the most. Additionally, the use of certain chemicals in these techniques might also result in the salinization and pollution of water.[2] An example of this is chlorination, one of the most widely used methods for disinfection, which unfortunately yields by-products that are suspected to be carcinogenic and mutagenic.[16,17] Also chemically treating water contaminants can result in the formation of toxic by-products; for instance, the reduction of some dyes can result in toxic aromatic amines.[18] It is clear that there is a lot of work that still needs to be done to make water cleaning treatment procedures less expensive and safer, which necessitates the development of robust and novel technologies.

Indeed, not all is lost as scientific research keeps getting more sophisticated with time. A fairly new area of activity in water research referred to as environmental nanotechnology, has begun to offer some optimism in the alleviation of the effects

of such contamination.[18] Here researching the properties of materials on the nanoscale has enthused the expansion as well as the use of novel and relatively cheap techniques, which have comprised contaminant detection and treatment for environmental conservation.[18] Indeed, there is an expectation that with the advancement of nanotechnology in this area of research, a cleaner, healthier and improved environment will come about as a result.

1.3 Justification

The past two decades have seen numerous researchers focusing their attention on the reclamation of CFA, such that Ahmaruzzman wrote a detailed review on the subject.[12] This is mainly because of the physical and chemical properties of CFA. The numerous different applications of CFA vary significantly amid themselves. For instance, using CFA as a structural filler depends chiefly on its ability to be compacted to a strong layer of low unit weight. This is mainly a function of particle size distribution as well as spherical particle content. For this purpose, the chemical properties of CFA do not matter much, even though there is some benefit in using CFA with high CaO content with regards to post-compaction.[12] In the case of using CFA for cement purposes, the chemical property requirements are stricter. Here the CFA used has to be uniform and chemically consistent.

Nevertheless, numerous applications for CFA have been researched. CFA applications that are relevant for the purposes of this thesis include its use as catalyst support, a catalyst for the synthesis of carbon nanomaterials (CNMs) and deriving zeolitic materials from it. For heterogeneous catalysis, catalyst nanoparticles are usually supported on catalyst supports where the activity is largely based on the

interactions that exist between the support and catalyst. Some of the most commonly used support materials are metal oxides such as alumina, silica, and titania amongst others. CFA is chemically composed predominantly of SiO_2 and Al_2O_3, which are thermally stable and are thus good candidates for the role of the catalyst support. One possible area of application of CFA is as a support in photocatalysis because CFA already contains TiO_2 (photocatalytic material) and both silica and alumina have been used as catalyst support materials for TiO_2 in photocatalysis.[1] Another well-researched application of CFA is for the synthesis of zeolitic material; this is possible as CFA contains both the primary constituents of zeolites, silica, and alumina. Zeolitic materials can be used in various fields, including as supports for photocatalyst materials.[19–21] Furthermore CFA can be used as a catalyst for the synthesis of CNMs.[22–25] CNMs have also been used for a variety of applications, which have included as supports for photocatalysts.[26–29]

Since the initial report by Fujishima and Honda on the subject of using photocatalysis for cleaning water, a substantial amount of research has been performed in this field.[30] Titanium dioxide (TiO_2) in the anatase phase is one of the most favored semiconductors for this application. This is because of its properties which include its: high photo-reactivity, non-toxicity, cheapness, photo-stability, chemical, and biological inertness.[31] Despite these positive attributes of TiO_2 as a photocatalyst, there are unfortunately several shortcomings associated with its use in this regard: (i) its large band gap (which means that sunlight, which is primarily composed of visible light, cannot be used as an effective source of energy), (ii) the high recombination rate of photogenerated holes and electrons. In order to circumvent these issues, several strategies have been investigated which have shown

that the photocatalytic properties of TiO_2 can be modified by changing its: crystal structure, particle size, surface area, surface hydroxyl groups, and band gap.[32] Currently, there are no viable cost-effective, environmentally safe alternatives to TiO_2 as a photocatalyst, necessitating extensive research on improving its photocatalytic properties.[33]

One method of improving the photoactivity of TiO_2 is to combine it with CNMs and/or zeolitic materials to synthesize composites or hybrids.[19,26,34–36] In the case of CNMs, this is aimed at exploiting their intrinsic properties which includes: high surface area, high electrical conductivity, high mechanical strength, chemical inertness, and 1-D geometric structures. The role of CNMs in these materials includes: (i) reducing the agglomeration of TiO_2 nanoparticles, (ii) increasing the surface area of the photocatalyst, (iii) making it easier to collect the photocatalyst from an aqueous suspension, (iv) increasing the lifetime of the photocatalyst, (v) decreasing the electron/hole recombination rate, as well as (vi) increasing the adsorption capacity of the photocatalyst.[36] The possibilities of benefiting from these type of materials are endless as the CNMs may also act as co-catalysts, thus increasing the photoactivity of TiO_2.[37] Similarly composites of TiO_2 with zeolitic materials have resulted in decreased electron/hole recombination rates.[19,38]

With regards to making affordable materials for photocatalysis, as it was alluded to earlier, CFA is a solid waste material that is generated in large quantities and is essentially free. Fortunately, CFA has inherent properties that can be exploited for the synthesis of CNMs and zeolitic materials which have been shown to be useful materials for increasing the photoactivity of titanium dioxide.[23–25,39–44]

Likewise, another way of making the process even cheaper is to decrease titania's large band gap (3.2 eV) so that sunlight can be used as a source of free energy. One method to achieve this has been through doping TiO_2 with various types of materials such as anions, platinum group metals (PGMs), other metal oxides and cations.[44-49] In order for this to be effective, it has been important that the right combination of materials were used. For instance, PGMs, and silver (Ag) in particular have been shown to shift the absorption of photocatalysts into the visible region through the formation of the surface plasmon resonance (SPR) phenomena.[45–47] Also, because PGMs have higher 4d and 5d energy orbitals this results in them having higher work functions relative to TiO_2.[45-47] Consequently a Schottky barrier forms, which reduces the recombination of photogenerated charge carriers and extends their lifetime as well as improves the photoactivity of TiO_2.[48]

Doping is an important aspect of improving the photoactivity of TiO_2. For example, doping the crystal lattice of TiO_2 with cations such as W^{6+} (74 pm) and Zn^{2+} (74 pm), which have similar ionic radii to Ti^{4+} (74.5 pm), may result in the modification of the bulk of TiO_2. This is possible since TiO_2, in the anatase phase, is able to accommodate oxidation state changes.[49]

The search for inexpensive, greener and sustainable sunlight harvesters provides a good motivation to develop such materials in order to translate solar radiation into useful chemical energy for the photodegradation of organic pollutants in water. In this regard, there is a great deal of research in the use of CFA for the synthesis of zeolitic materials,[50] but no reports on the use CFA derived zeolitic materials (especially not from CFA) as support materials for photocatalysts. Likewise the SPR phenomenon, as a result of making composites of TiO_2 with Ag nanoparticles,

has never been investigated on TiO_2 anchored on zeolites or zeolite-derived materials. Similarly, CFA, a toxic waste material, has never before been studied as a catalyst to synthesize two different types of CNMs i.e. carbon nanofibers (CNFs) and nitrogen-doped carbon nanotubes (NCNTs) to be used as photocatalyst supports. Equally, novel quaternary mixed metal oxides (QMMOs) composed of TiO_2 doped with W^{6+} and Zn^{2+}, have never before been anchored onto these CNMs and assessed for their ability to photodegrade a known EDC i.e. BPA.

1.4 Aims and objectives

1.4.1 Aims

The main purpose of this work was to investigate how CFA derived materials could be used to modify the photocatalytic properties of TiO_2 and doped TiO_2 based materials.

1.4.2 Objectives

This research is primarily driven by using a toxic waste material (CFA) for the purpose of modifying the surface, morphological, optical and chemical properties of TiO_2 for the photodegradation of bisphenol-A. The difficulties experienced in achieving this fully, necessitated the use of other materials in conjunction with CFA derived zeolites, CNFs, and NCNTs in order to design an optimum photocatalyst. Hence the objectives in this research were to:

- Investigate if CFA could be used as a catalyst for the growth of NCNTs using a 2-stage chemical vapor deposition (CVD) setup at various temperatures.

- Determine if there was a correlation between the morphology, the amount of nitrogen incorporated and the graphicity of NCNTs as a function of the temperature at which they were synthesized.
- Examine if acetylene could be decomposed on the surface of CFA to synthesize CNFs by CVD.
- Investigate if CNFs and NCNTs could be coated with TiO_2 nanoparticles at various loadings by a hydrothermally modified surfactant wrapping sol-gel technique.
- Study if the presence of NCNTs or CNFs had any influence on the photocatalytic efficiency of TiO_2 by monitoring their BPA photodegradation efficiencies.
- Explore if zeolitic materials could be derived from CFA by a 2-step alkali fusion hydrothermal technique.
- Determine if composites consisting of zeolitic materials and TiO_2 at various zeolitic material loading could be synthesized by resin gel technique.
- Assess if making composites of TiO_2 with CFA derived zeolites had any influence on the photocatalytic efficiency of TiO_2 by monitoring their efficiencies at photodegrading BPA.
- Evaluate if the deposition of Ag nanoparticles on TiO_2 as well as composites of TiO_2 and zeolites, made by the DPU-NaOH technique, had any influence on the efficiency at which they would photodegrade BPA.
- Investigate if it was possible to incorporate W^{6+} and Zn^{2+} into the crystal lattice of TiO_2 to synthesize QMMOS with various loadings by the resin gel technique.
- Study the effects of incorporating W^{6+} and Zn^{2+} into the crystal lattice of TiO_2 on the chemical properties of TiO_2.
- Compare the photocatalytic efficiency at which selected QMMOs photodegraded BPA relative to TiO_2.

- Investigate if selected QMMOs could be hydrothermally coated onto NCNTs and determine the efficiency at which these composite materials could photodegrade BPA.

1.5 Thesis outline

The following is an outline of how this thesis is structured, in terms of highlighting the key elements of each chapter.

Chapter 2: Here a literature review of the related areas of this study is presented. The initial part of this chapter is a discussion of water scarcity and water pollution, with emphasis on organic contaminants and in particular EDCs. Thereafter the uses of nanotechnology and photocatalysis in environmental applications are discussed. Since TiO_2 was used as a photocatalyst in the studies presented in this thesis, a review of its crystal structure, properties, and drawbacks is also covered. Similarly, the various methods that have been used to modify the properties of TiO_2 including CFA, CNMs and synthetic procedures, are also comprehensively reviewed in this chapter.

Chapter 3: This chapter provides a comprehensive discussion of the experimental and analytical processes that were used in this research. Different physical and chemical characterization methods are also discussed in this chapter including the details of their experimental setups. In addition, some of the key equations relevant to this work are discussed.

Chapter 4: In this chapter, the synthesis of NCNTs using CFA as a catalyst in a 2-stage CVD setup is presented. Likewise, the various methods of characterization of

these NCNTs are discussed in detail. Here special attention is paid to the morphological properties, graphicity and % nitrogen incorporated in the various NCNTs that were synthesized.

Chapter 5: The synthesis of CNFs and their purification along with NCNTs is highlighted in this chapter. Thereafter special attention is paid to the synthesis of composites with these purified materials and TiO_2 by a modified surfactant wrapping sol-gel/hydrothermal method. Finally, the chapter ends with an evaluation of the photocatalytic efficiencies of these composites by monitoring the rate at which they were able to photodegrade BPA.

Chapter 6: In this chapter, the synthesis of a zeolitic material formed from CFA by a 2-step alkali fusion technique is reported. Furthermore, the resin gel synthesis of TiO_2 and CFA derived zeolite composites is reported along with the NaOH-DPU decoration of these composites with Ag nanoparticles. As before the chapter ends with an emphasis on evaluating the photocatalytic efficiencies of these materials.

Chapter 7: The focus in this chapter is on the synthesis of QMMOs using the resin gel technique as well as their full structural characterization. Also in this chapter, selected QMMOs were supported on CFA grown NCNTs and then evaluated for their photocatalytic efficiencies with respect to the photodegradation of BPA.

Chapter 8: This final chapter summarizes the main findings of this research, presents conclusions along with the recommendations and future prospects that have arisen from this work.

References: At the end of each chapter, there is a list of the references used in that chapter.

1.6 References

1. Ashbolt, N. J. Risk analysis of drinking water microbial contamination versus disinfection by-products (DBPs). *Toxicology* **198,** 255–262 (2004).

2. Schug, T. T., Janesick, A., Blumberg, B. & Heindel, J. J. Endocrine disrupting chemicals and disease susceptibility. *J. Steroid Biochem. Mol. Biol.* **127,** 204–15 (2011).

3. Borch, J., Axelstad, M., Vinggaard, A. M. & Dalgaard, M. Diisobutyl phthalate has comparable anti-androgenic effects to di-n-butyl phthalate in fetal rat testis. *Toxicol. Lett.* **163,** 183–90 (2006).

4. Fromme, H., Küchler, T., Otto, T., Pilz, K., Müller, J. & Wenzel, A. Occurrence of phthalates and bisphenol A and F in the environment. *Water Res.* **36,** 1429–1438 (2002).

5. Steinmetz, R., Mitchner, N. A., Grant, A., Allen, D. L., Bigsby, R. M. & Ben-jonathan, N. The Xenoestrogen Bisphenol A Induces Growth , Differentiation , and c-fos Gene Expression in the Female Reproductive Tract. *J. Endocrinol*. **139,** 2741–2747 (2016).

6. Cederroth, C. R., Zimmermann, C. & Nef, S. Soy, phytoestrogens and their impact on reproductive health. *Mol. Cell. Endocrinol.* **355,** 192–200 (2012).

7. Niederberger, C. Re: Urine bisphenol-A (BPA) level in relation to semen quality. *J. Urol.* **186,** 1415 (2011).

8. Maffini, M. V., Rubin, B. S., Sonnenschein, C. & Soto, A. M. Endocrine disruptors and reproductive health: The case of bisphenol-A. *Mol. Cell. Endocrinol.* **254–255,** 179–186 (2006).

9. Gitari, W. M., Fatoba, O. O., Petrik, L. F. & Vadapalli, V. R. K. Leaching characteristics of selected South African fly ashes: effect of pH on the release of major and trace species. *J. Environ. Sci. Health. A. Tox. Hazard. Subst. Environ. Eng.* **44,** 206–20 (2009).

10. Qian, G., Cao, Y., Chui, P. & Tay, J. Utilization of MSWI fly ash for stabilization/solidification of industrial waste sludge. *J. Hazard. Mater.* **129,** 274–81 (2006).

11. Bryan, A. L., Hopkins, W. A., Parikh, J. H., Jackson, B. P. & Unrine, J. M. Coal fly ash basins as an attractive nuisance to birds: parental provisioning exposes nestlings to harmful trace elements. *Environ. Pollut.* **161,** 170–7 (2012).

12. Ahmaruzzaman, M. A review on the utilization of fly ash. *Prog. Energy Combust. Sci.* **36,** 327–363 (2010).

13. Ahmaruzzaman, M. Industrial wastes as low-cost potential adsorbents for the treatment of wastewater laden with heavy metals. *Adv. Colloid Interface Sci.* **166,** 36–59 (2011).

14. Barker, R., Van Koppen, B. & Shah, T. *A global perspective on water scarcity and poverty: Achievements and challenges for water resources management.* (International Water Management Institute, 2000).

15. Rockström, J. & Barron, J. Water productivity in rainfed systems: Overview of challenges and analysis of opportunities in water scarcity prone savannahs. *Irrig. Sci.* **25,** 299–311 (2007).

16. Takagi, H., Mitsumori, K., Onodera, H. & Nasu, M. Improvement of a two-stage carcinogenesis model to detect modifying effects of endocrine disrupting chemicals on thyroid carcinogenesis in rats. *Cancer Lett*. **178,** 1–9 (2002).

17. Muncke, J. Endocrine disrupting chemicals and other substances of concern in food contact materials: An updated review of exposure, effect and risk assessment. *J. Steroid Biochem. Mol. Biol.* **127,** 118–127 (2011).

18. Kuvarega, A. T. Photocatalytic performance of nitrogen-platinum group metal co-doped TiO_2 supported on carbon nanotubes for visible-light degradation of organic pollutants in water. (University of Johannesburg, 2012).

19. Tayade, R. J., Kulkarni, R. G. & Jasra, R. V. Enhanced Photocatalytic Activity of TiO_2-Coated NaY and HY Zeolites for the Degradation of Methylene Blue in Water. *Ind. Eng. Chem. Res*. **46,** 369–376 (2007).

20. Bossmann, S. H., Turro, C., Schnabel, C., Pokhrel, M. R., Payawan,, L. M., Baumeister, B. & Wörner, M. $Ru(bpy)_3^{2+}$ /TiO_2-Codoped Zeolites: Synthesis, Characterization, and the Role of TiO_2 in Electron Transfer Photocatalysis. *J. Phys.*

Chem. B **105,** 5374–5382 (2001).

21. Xu, Y. & Langford, C. H. Photoactivity of titanium dioxide supported on MCM41, zeolite X, and zeolite Y. *J. Phys. Chem. B* **101,** 3115–3121 (1997).

22. Hintsho, N., Shaikjee, A., Franklyn, P. & Durbach, S. The effect of CO_2 on the CVD synthesis of carbon nanomaterials using fly ash as a catalyst. *RSC Adv.* **5,** 53776–53781 (2015).

23. Hintsho, N. Shaikjee, A., Masenda, H., Naidoo, D., Billing, D., Franklyn, P. & Durbach, S. Direct synthesis of carbon nanofibers from South African coal fly ash. *Nanoscale Res. Lett.* **9,** 387 (2014).

24. Salah, N., Al-ghamdi, A. A., Memic, A., Habib, S. S. & Khan, Z. H. Formation of Carbon Nanotubes from Carbon-Rich Fly Ash: Growth Parameters and Mechanism. *Mater. Manuf. Process.* **31,** 146–156 (2016).

25. Hlekelele, L., Tripathi, P., Franklyn, P. J. & Durbach, S. H. Morphological and crystallinity differences in Nitrogen- Doped Carbon Nanotubes grown by Chemical Vapor Deposition Decomposition of Melamine over Coal Fly Ash. *RSC Adv.* **6,** 76773–76779 (2016).

26. Gao, B., Chen, G. Z. & Li Puma, G. Carbon nanotubes/titanium dioxide ($CNTs/TiO_2$) nanocomposites prepared by conventional and novel surfactant wrapping sol-gel methods exhibiting enhanced photocatalytic activity. *Appl. Catal. B Environ.* **89,** 503–509 (2009).

27. Perera, S. D., Sanjaya D. Mariano, R. G., Vu, K., Nour, N., Seitz, O., Chabal, Y. & Balkus, K. J. Hydrothermal synthesis of graphene-TiO_2 nanotube composites with enhanced photocatalytic activity. *ACS Catal.* **2,** 949–956 (2012).

28. Hintsho, N., Petrik, L., Nechaev, A., Titinchi, S. & Ndungu, P. Photo-catalytic activity of titanium dioxide carbon nanotube nano-composites modified with silver and palladium nanoparticles. *Appl. Catal. B Environ.* **156–157,** 273–283 (2014).

29. Dahl, M., Liu, Y. & Yin, Y. Composite titanium dioxide nanomaterials. *Chem. Rev.* **114,** 9853–9889 (2014).

30. Fujishima, A. & Honda, K. Photolysis-decomposition of water at the surface of an irradiated semiconductor. *Nature* **238,** 37–38 (1972).

31. Hoffmann, M. R., Martin, S. T., Choi, W. & Bahnemannt, D. W. Environmental Applications of Semiconductor Photocatalysis. *Chem. Rev.* **95,** 69–96 (1995).

32. Chen, X. & Mao, S. S. Titanium Dioxide Nanomaterials : Synthesis , Properties , Modifications, and Applications. *Chem. Rev.***1**, 2891-2959 (2007).

33. Woan, k., Pyrgiotakis, G. & Sigmund, G. Photocatalytic Carbon-Nanotube-TiO_2 Composites. *Adv. Mat.* **21,** 2233–2239 (2009).

34. Anpo, M., Yamashita, H., Ichihashi, Y., Fujii, Y. & Honda, M. Photocatalytic Reduction of CO_2 with H_2O on Titanium Oxides Anchored within Micropores of Zeolites: Effects of the Structure of the Active Sites and the Addition of Pt. *J. Phys. Chem. B* **101,** 2632–2636 (1997).

35. Yu, Y., Jia, R., Zheng, J., Zhao, J., Li, L., Song, J. & Zhu, Z. Enhancement of adsorption and photocatalytic activity of TiO_2 by using carbon nanotubes for the treatment of azo dye. *Appl. Catal. B Environ.* **61,** 1–11 (2005).

36. Eder, D. & Windle, A. H. Carbon-inorganic hybrid materials: The carbon-nanotube/TiO_2 interface. *Adv. Mater.* **20,** 1787–1793 (2008).

37. Leary, R. & Westwood, A. Carbonaceous nanomaterials for the enhancement of TiO_2 photocatalysis. *Carbon* **49,** 741–772 (2011).

38. Takeda, N., Torimoto, T., Sampath, S., Kuwabata, S. & Yoneyama, H. Effect of inert supports for titanium dioxide loading on enhancement of photodecomposition rate of gaseous propionaldehyde. *J. Phys. Chem.* **99,** 9986–9991 (1995).

39. Musyoka, N. M., Petrik, L. F., Balfour, G., Gitari, W. M. & Hums, E. Synthesis of hydroxy sodalite from coal fly ash using waste industrial brine solution. *J. Environ. Sci. Health. A. Tox. Hazard. Subst. Environ. Eng.* **46,** 1699–707 (2011).

40. Shigemoto, N., Sugiyama, S., Hayashi, H. & Miyaura, K. Characterization of Na-X, Na-A, and coal fly ash zeolites and their amorphous precursors by IR, MAS NMR and XPS. *J. Mater. Sci.* **30,** 5777–5783 (1995).

41. Koukouzas, N., Vasilatos, C., Itskos, G., Mitsis, I. & Moutsatsou, A. Removal of heavy metals from wastewater using CFB-coal fly ash zeolitic materials. *J. Hazard. Mater.* **173,** 581–8 (2010).

42. Molina, A. & Poole, C. A comparative study using two methods to produce zeolites

from fly ash. *Miner. Eng.* **17,** 167–173 (2004).

43. Dunens, O. M., MacKenzie, K. J. & Harris, A. T. Synthesis of multiwalled carbon nanotubes on fly ash derived catalysts. *Environ. Sci. Technol.* **43,** 7889–94 (2009).

44. Yasui, A., Kamiya, Y., Sugiyama, S., Ono, S., Noda, H. & Ichikawa, Y. Synthesis of Carbon Nanotubes on Fly Ashes by Chemical Vapor Deposition Processing. *Ieej Trans. Electr. Electron. Eng.* **4,** 787–789 (2009).

45. Wu, F., Hu, X., Fan, J., Liu, E., Sun, T., Kang, L., Hou, W., Zhu, C. & Liu, H. Photocatalytic Activity of Ag/TiO_2 Nanotube Arrays Enhanced by Surface Plasmon Resonance and Application in Hydrogen Evolution by Water Splitting. *Plasmonics* **8,** 501–508 (2013).

46. Zhou, X., Liu, G., Yu, J. & Fan, W. Surface plasmon resonance-mediated photocatalysis by noble metal-based composites under visible light. *J. Mater. Chem.* **22,** 21337 (2012).

47. Wang, P., Huang, B., Dai, Y. & Whangbo, M.-H. Plasmonic photocatalysts: harvesting visible light with noble metal nanoparticles. *Phys. Chem. Chem. Phys.* **14,** 9813–9825 (2012).

48. Fu, X., Long, J., Wang, X., Leung, D., Ding, Z., Wu, L., Zhang, Z., Li, Z. & Fu, X. Photocatalytic reforming of biomass: A systematic study of hydrogen evolution from glucose solution. *Int. J. Hydrogen Energy* **33,** 6484–6491 (2008).

49. Franklyn, P. Synthesis, Characterization and Structural Investigations of Nanoparticulate forms of selected (W,Ti,Al,Ba) Mixed Metal Oxides. (University of

Cambridge, 2011).

50. Anpo, M., Yamashita, H., Ichihashi, Y., Fujii, Y. & Honda, M. Photocatalytic Reduction of CO_2 with H_2O on Titanium Oxides Anchored within Micropores of Zeolites: Effects of the Structure of the Active Sites and the Addition of Pt. *J. Phys. Chem. B* **101,** 2632–2636 (1997).

CHAPTER 2:

LITERATURE REVIEW

2.1 Introduction

The emphasis of this literature review is three-fold: i) Water pollution, ii) The problems associated with the large quantities of toxic coal fly ash (CFA) that are produced annually and iii) Nanotechnology. The focus in this research was on whether CFA could be repurposed for the removal of a model organic water pollutant i.e. BPA. The key method used to achieve this was nanotechnology, through a process called photocatalysis. Consequently an in-depth review on the use of TiO_2 as a photocatalyst, its advantages, drawbacks, etc. was the focus of a great deal of this review. Furthermore, the various techniques that have been used to modify the properties of TiO_2 and thus improve its photocatalytic efficiency, as well as the relevant synthetic procedures associated with these, have been discussed.

2.1.1 Water scarcity and pollution

The earth's surface is covered mostly by water, which accounts for 70 % of its total surface area.[1] Even so, one of the main problems that arise is that only 3 % of the total earth's surface water is drinkable, and safe water is imperative for everyday life.[1,2] Research has shown that water scarcity affects mostly underdeveloped countries.[3] For instance, in 2009 the human population in Africa surpassed the 1 billion mark and has continued to grow at an annual rate of 2.5 %.[2] However, almost a third of these 1 billion Africans are without safe drinking water and about 60 % are without adequate sanitation.[1,2] Research has shown that a correlation exists between diseases such as malaria, cholera, typhoid fever, etc. and the poor supply as

well as the quality of water.[4–6] This lack of potable water threatens the longevity of human life and is estimated to have resulted in more than 2 million human fatalities a year (75 % of whom were children under the age of 5 years).[1,2] It has been approximated that 50 % of the bedridden hospital patients in Africa have been affected by water-borne diseases because of a lack of potable water and inadequate sanitation.[3] In the year 1995, 10 African states experienced severe water scarcity and it is projected that by 2025 this number would have increased to 14.[3]

A clear correlation between malnutrition, poverty and the availability of safe water has been shown.[7] For example, malnourishment affects almost 1 billion people in the world and is a direct indication of food scarcity.[8] In this regard, it has been approximated that by the year 2050, an additional 5600 km^3 of clean water would be required for use in irrigation to feed the growing population in the fight against malnutrition.[9] Farming is pivotal in the fight against poverty and malnutrition, but is threatened by increasing water scarcity. The International Water Management Institute (IWMI) has reported that a third of the world's population will experience grave water scarcity in the first 25 years of the 21st century with sub-Saharan Africans and semi-arid Asians being the most affected.[2] The implications of these findings to the poor are gruesome. Some of the effects of water scarcity might become evident by the insolvency of farmers who lose their land due to the lack of irrigation and consequently the loss of their workforce; equally, wetlands could be lost as a result of upstream water paucity.

The pursuit of good quality water has been an endeavor for human beings since the beginning of time. R.L. Calderon reported that in the days of old, humans settled in locations where clean water was accessed at ease; when the quality of this water was

believed to be compromised or the supply was threatened they would then abandon these locations in pursuit of clean water.[10] It makes sense that at some point these people figured out that there were other ways to circumvent abandoning areas that had poor quality water and thus began to seek methods to improve these supplies. R.L. Calderon has also pointed out that the first documentation on the treatment of drinking water was found in Egyptian hieroglyphics with methods employed that are similar in principle to those being used today.[10] These included: distillation, filtration, and chemical reactions.[10]

As previously stated, water contamination poses a threat to the survival of mankind as well as to different types of organisms. Apart from naturally occurring chemicals, anthropological process such as agriculture and increased industrialization, have resulted in manmade chemicals finding their way into water systems.[11–15] For instance, having industrialization and agriculture alongside mining has produced effluents which have grown in volume and complexity due to new processes that have been developed and implemented.[10,16] Similarly, the integrity of most inland raw water assets has continued to depreciate as a result of the release of the effluents therein.[17] Effluents that are not treated generally contain contaminants that compromise the quality of fresh water sources and sewage water systems. These contaminants range from organics, heavy metals, biologicals to other inorganic compounds, some of which have been shown to have deleterious health consequences even at trace levels.[12,15,18–20] Likewise amongst other devastating health effects some of these contaminants have been reported to be: mutagens,[17,21–24] carcinogens[25–29] and endocrine disruptors.[27,30–36] Consequently, the challenges that are faced by the world today with regards to the supply of clean water, are severe

due to: population growth, climate conditions (droughts), contaminated industrial and domestic effluents and stricter health regulations.

Preserving human life and that of other living organisms is hence a desirable endeavor, which necessitates the advancement of water treatment processes for the removal of these harmful chemicals, to reduce them to levels where they are considered to be safe.

2.1.2 Endocrine disruptive chemicals

In the past 20 years, studies have been aimed at understanding the risks associated with a variety of foreign chemicals in the body. Some of these chemicals have been shown to mimic how hormones act in the endocrine system of human beings and animals; these types of chemicals have been classified as endocrine disruptive chemicals (EDCs).[34,35,37–39] Researchers were first made aware of EDCs through the observation of changes that occurred in the reproductive systems of different types of fish and molluscs which were sampled downstream of sewage treatment plants.[40]

EDCs are usually synthetic chemicals which are specifically designed as plasticizers, pesticides or solvents, but unfortunately, have been shown to have adverse health effects.[33,41–43] EDCs have been found to have: i) Caused changes in normal hormone levels, ii) Hindered or encouraged the fabrication and metabolism of hormones or iii) Altered the movement of hormones, thereby having adversely influenced bodily functions that were controlled by their disruption.[38,44]

Furthermore, EDCs have been found to have similar structural features to those of numerous hormones and have been capable of behaving the same way as hormones, by adopting their modes of action, transport as well as storage within cells.[40] Given the extent

of the shared properties and similarities between EDCs and hormones, research has shown there is almost no endocrine system that is immune to their effects.[45]

The disruptions caused by EDCs have been reported to occur predominantly through nuclear hormone receptors (e.g. progesterone, androgen, estrogenic and retinoid, among others).[33,40,41] Some of the human nuclear receptors, their functions, and examples of EDCs that affect specific receptors are shown in **Table 2.1**.[37]

Table 2.1. Some human nuclear receptors and their related functions.[37]

Receptor	Physiological function	Endogenous ligand	Example of EDCs
Oestrogen	Female sexual development	Estradiol	Alkyl phenols
			Phthalates
			BPA
			Dioxins
			Furans
			Halogenated
Androgen	Male sexual development	Testosterone	Polyhalogenated hydrocarbons
			Pesticides
			Phthalates
			Plasticizers
Progesterone	Female sexual development	Progesterone	BPA
			Fungicides
			Insecticides
			Herbicides
Peroxisome proliferator-	Lipid homeostasis	Lipids and fatty acids	BPA
			Pesticides
			Organotins
Glucocorticoid	Development metabolism stress	Cortisol	BPA
			Phthalates

It is important that the characteristics of the endocrine system are understood in order to more fully comprehend the mechanisms by which EDCs affect it. In certain cases, the health consequences of exposure to certain EDCs vary with age. For instance, it has been found that adults would have to be continuously exposed to certain EDCs at high

concentrations for their toxicity to be observed.[46] On the other hand during the developmental stages of fetuses, low concentrations of certain EDCs have been found to be poisonous; equally low doses of exposure have shown disruptions that have lasted longer than their exposure time.[47] So much so that "The foetal bases of adult diseases (FeBAD)" is a phrase that has been derived from the persistent effects that EDCs have been shown to have on developing human bodies into adulthood.[37] FeBAD has also been used to track the interactions between a developing human body and its environment in order to ascertain whether this may have influenced its susceptibility to develop diseases at later stages.[47,48] In this regard several animal studies have suggested that the effects of EDCs could be extended to offspring and subsequent generations.[37] For example, studies of children who had been exposed to dioxins and polychlorinated biphenyls in their prenatal stages, have shown that their exposures to these EDCs were linked with long-term to permanent negative neurological effects specific to psychomotor and cognitive development, as well as to signs of behavioral abnormalities.[37,49] Similarly, evidence has linked occupational exposure to some pesticides (organochlorine in particular) during pregnancy to stillbirth.[40,44–48] Likewise, exposure to organochlorine pesticides along with dioxins has also been linked to endometriosis.[49]

As dire as this may seem, the human epidemiological data that exists on the adverse effects of EDCs on human beings is inadequate to capture the havoc wrecked by these chemicals as it is only limited to pharmaceutical dosing, occupational and accidental exposure.[39] Hence the adverse effects of EDCs are undoubtedly more pronounced than has been documented.

Evidence of similar effects has also been noted in the animal kingdom. For example, a certain type of female fish has been observed to develop male features when they were

exposed to phytoandrogens that were present in effluents from paper mills.[45] In contrast to the anthropogenic chemicals mentioned previously, naturally occurring plant compounds (such as phytoestrogens and androgens), which are chemically similar to steroid hormones, can also behave as EDCs in mammals.[50] A clear example of this was when it was demonstrated that female sheep became infertile and male sheep began to lactate after having grazed on plants that were rich in phytoestrogen compounds.[51]

In the research presented in this thesis a synthetic EDC, i.e. [2,2-Bis(4-hydroxyphenyl)propane] known as bisphenol A or BPA, was studied as a model pollutant with specific emphasis on its removal from standard solutions by photodegradation through novel photocatalysts.

2.1.2.1 Bisphenol A

In the last two to three decades, there has been a notable interest by policymakers and scientists concerning the detrimental effects of synthetic EDCs on human health.[50-51] This interest has been brought about as numerous therapeutic and industrial chemicals (e.g. phthalates and BPA) have been classified as EDCs. Although BPA (**Figure 2.1(a)**) was first synthesized in 1905 through the reaction of phenol and acetone in the presence of a catalyst, its estrogenic properties were only first reported in 1936.[52]

Approximately 2.7 billion kilograms of BPA is produced annually, making it one of the highest quantities of chemicals that is synthesized in the world.[53] BPA is mainly used in the manufacturing of: polycarbonate (**Figure 2.1(b)**) plastics, plastic products (such as: toys, water pipes, eyeglass lenses, medical equipment, and tubing) and well as epoxy-resins in the lining of metal cans.[54–58] Other minor applications of BPA include the manufacturing of tetrabromobisphenol A (which is used as a flame retardant),

polysulfones, polyarylate resins, antioxidants and aromatic polyesters with phthalic acid.[53,59–62]

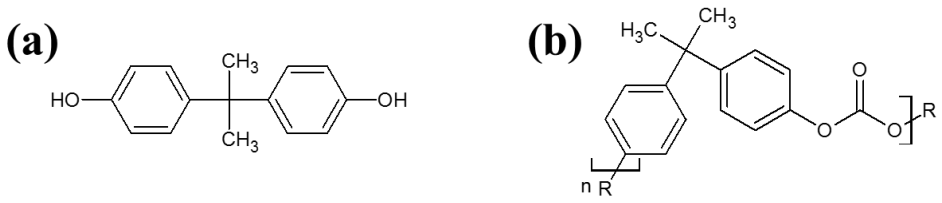

Figure 2.1. Line drawings representing the molecular structures of: (a) Bisphenol A, and (b) The repeating unit of a polycarbonate plastic.[55]

Numerous studies have been aimed at quantifying the levels of BPA in the environment, as well as identifying their potential sources. Since BPA is not a naturally occurring compound, its presence in the environment has to have been as a result of human activity. Consequently, traces of BPA would, therefore, be expected to be found in the water systems and atmosphere. For this reason, potential sources of BPA, such as foods, drinking water, air, dust and leaching from landfills have been studied vigorously.[53] For example, modest concentrations of BPA have been measured in river sediments as they have acted as sinks that released this EDC into the water systems.[63–66] However, it has been found that sewage sludge contained higher concentrations of BPA as compared to the river and sea sediments; this is likely attributed to the variety of household products that contain BPA.[37] Numerous reports have been published on the negative effects of BPA towards living organisms. For example, BPA has been found to be toxic to both freshwater and sea water-living species.[36] **Table 2.2** provides a list of some of the sea and freshwater species that have been negatively affected by BPA.[36]

Table 2.2. The toxicity of BPA towards aquatic life.[36]

Seawater species	Toxicity
Skeletonema costatum	96 hour EC_{50} based on cell count 1 mg/L and based on chlorophyll-A content 1.8 mg/L
Menidia	96 hour LC_{50}, 9.4 mg/L
Mysidopsis bahia	96 hour LC_{50}, 1.1mg/L
Freshwater species	Toxicity
Pimephales promelas	96 hour LC_{50} in static test 4.7 mg/L and in flow-through test 4.6 mg/L
Daphnia magna	48 hour EC_{50}, 10 mg/L
Pimephales promelas	96 hour LC_{50} in static test 4.7 mg/L and in

Studies that have focused upon the toxicity of BPA towards human beings have suggested that children were more susceptible to BPA than adults, citing reasons such as their rapid physical development as well as their higher metabolic and respiratory rates.[40] In regard to the mode of transmission to young children, since BPA has octanol to water partitioning coefficient of 3.32 this has suggested to researchers that BPA would be likely to partition into breast milk. Indeed a study in healthy breast milk has shown that BPA concentrations of up to 0.8 ng/mL were present.[40,67,68]

In related studies on human beings and laboratory animals, the data acquired has suggested that the intake of BPA resulted in multiple negative health effects which included: estrogenic potency, pancreatic β-cell function disruption, obesity, diabetes, cardiovascular diseases, liver damage, and thyroid hormone disruptions.[69–74] Significantly, some of these adverse effects of BPA have been observed in human beings at exposure concentrations as low as 1 ng/L.[40] Exposure of BPA has also been reported to cause prostate cancer in

men.[54,73,75–78]Similarly studies have also indicated that exposure of BPA to female rats affected their uteruses and vaginal openings by having increased the heights of their luminal epithelial cells.[74]

Alarmingly, although the technology used in wastewater treatment plants has evolved over the years, BPA has still been detected in the effluents of several industrial and municipal waste treatment plants.[36]

2.2 Nanotechnology

Nanotechnology is an area of modern science that is rapidly developing in various areas including physics, chemistry, medicine, material science, biology, and engineering.[1,2] Materials in which at least one dimension is in the nanoscale range (i.e. less than 100 nm) are referred to as nanomaterials; these nanomaterials are the basis of nanotechnology.[1,2] The field of nanotechnology is growing immensely because of the unique properties that elements and compounds possess on the nanoscale as opposed to their bulk states. An example of this phenomenon includes the highly catalytic properties of nano-gold particles, which contradict the notion that gold is always inert. Hence it is extremely desirable that methods for developing nanomaterials for use in highly functional novel technologies are investigated since these have the potential of bettering lives and addressing numerous problems (including environmental pollution).

One of the most researched subfields of nanotechnology is nano-catalysis. Nano-catalysis has been researched with the aim of exploiting the unique properties of nanomaterials. The primary objective of researchers in the nano-catalysis field has been to promote as well as drive catalytic chemical reactions through the manipulation of the size and morphology of various nanomaterials. Research in the field of nano-catalysis has included the characterization and understanding of chemical and physical properties of nano-catalysts.

These studies have been aimed at acquiring further understanding of nanomaterials and thus the development of novel ones as well as an understanding of how they work. Hence this area of research has the potential to address issues surrounding the ever-increasing environmental pollution problems that face the world. Consequently, scientists in this field will need to seek to provide answers that will address these problems with the view of developing greener chemical materials and processes.

2.2.1 Titanium dioxide

Titanium dioxide or titania (TiO_2) is a very common inorganic mineral that is naturally sourced from rutile and ilmenite ores. TiO_2 exists in several polymorphic forms of which the most stable phases include: anatase, rutile, and brookite.[79,80] Since numerous studies have focused on these phases, the sections which follow are in-depth discussions of these.

2.2.1.1 Titanium dioxide polymorphs

The anatase polymorph of TiO_2 (crystal structure in **Figure 2.2(a)**) is the kinetic product of the oxidation of Ti^{4+} and is less thermodynamically stable than the rutile phase (crystal structure in **Figure 2.2(b)**).[81] Also, the anatase phase is known to transform into the rutile phase when exposed to high pressure and/or temperature.[80], On the other hand, the brookite phase of TiO_2 is the least stable polymorph and is known to convert relatively easily into the more stable rutile and anatase phases.[82] The crystal structure of brookite is given in **Figure 2.2(c)**, while a summary of the crystal information of the three TiO_2 polymorphs is found in **Table 2.3**. [78]

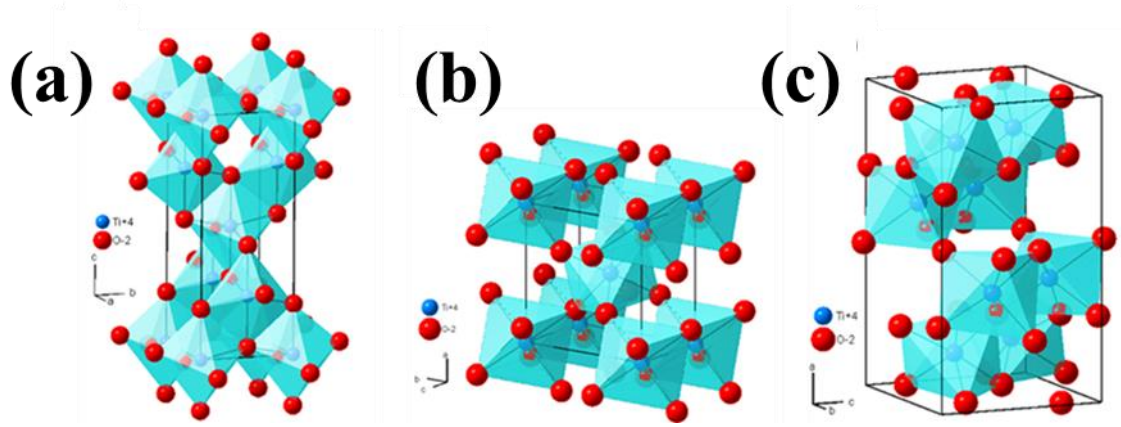

Figure 2.2. Representations of the unit cells of: (a) Anatase, where the octahedra have Ti^{4+} at the centers and oxygen species at the apexes. The adjacent octahedra are edge face sharing, (b) Rutile, where the octahedra have Ti^{4+} at their centers and oxygen ions at each of the corners. The adjacent octahedra are interchangeably corner and edge-sharing and (c) Brookite. The octahedra have Ti^{4+} at their centers and oxygen ions at each of the apexes. The in-line octahedra are alternately corner and edge sharing.[78]

Table 2.3. Crystalline parameters of TiO_2 polymorphs.[78]

	Anatase	Rutile	Brookite
Crystal system	Tetragonal	Tetragonal	Orthorhombic
Point group	4/mmm	4/mmm	Mmm
Space group	$I4_1/amd$	P42/mmm	Pbca
Z	4	2	8
Unit cell: a (Å)	3.7845	4.5937	9.184
b (Å)	3.7845	4.5937	5.447
c (Å)	9.5143	2.9587	5.145
Unit cell vol ($Å^3$)	136.3	62.4	257.4

2.2.1.2 Synthesis of TiO_2 nanoparticles

Several methods have been reported in the literature which has described the synthesis of phase and size-controlled TiO_2 nanoparticles.[81] Similarly, a variety of Ti^{4+} sources have been used where the choice of metal salt has often been dictated to by the method of synthesis.[79] Some of the most common methods of synthesis of TiO_2 are discussed below, leading up to the introduction and discussion of the resin gel technique which was predominantly used in this research.

2.2.1.2.1 The precipitation method

A homogeneous solution can form a precipitate when the physical conditions of the solution have been altered. For example, when conditions such as solution pH, temperature, solvent, and reactant concentration, etc. have been altered, this has been known to induce the formation of a precipitate.[2,83] Precipitate formation in a solution has frequently occurred via a two-step process: i) Nucleation and ii) Agglomeration. Metal oxides nanoparticles (e.g. TiO_2) have been synthesized using precipitation methods.[2,81,83] This method involves the precipitation of metals ions as metal hydroxides (in alkaline chemicals such as NaOH, NH_4OH and CH_4N_2O), followed by calcination in air or oxygen.[79]

2.2.1.2.2 The solvothermal (hydrothermal) method.

The solvothermal method has loosely been described as one that has required elevated pressures, moderate temperatures, and a solvent.[81,84] Consequently solvothermal synthesis has often been performed in high-pressure reactors called autoclaves, which have been able to easily achieve these conditions.[78-80] The term hydrothermal has been used to describe a solvothermal method in which water was

used as the solvent. The principles of the hydrothermal technique have followed those of other wet synthesis methods i.e. a metal precursor when added to a solvent was able to induce hydrolysis and which led to the formation of a precipitate that was subsequently collected. The heat or pressure that has usually been associated with the hydrothermal method has often been sufficient for the production of crystalline materials.[2,81,83] This has been advantageous over other synthetic procedures, where post-treatments such as calcination have often been required to convert their amorphous products to crystalline ones.[2,81,83] In those cases the post-treatments have often led to the formation of larger particles and particle agglomeration.[2,81,83] In an attempt to control the size and shape of nanoparticles synthesized by the solvothermal process, surfactants have often been used to create micelles which have then acted as capping agents or templates for their synthesis.[83]

2.2.1.2.3 The sol-gel method.

Typically, the sol-gel procedure has involved the hydrolysis and polymerization of a metal precursor which was either an inorganic salt or a metal alkoxide.[2] Metal alkoxides have been preferred over inorganic metal precursors because of the ease at which they have been known to hydrolyze .[2] Here organic solvents and/or acids, (e.g. citric acid, isopropanol and methanol) that were capable of complexing the metal atoms to create a gel have been commonly used.[83] Alternatively water has also been used as the solvent. In such cases, the gel was created when the attractive dispersion forces in solution were sufficient during nucleation.[83] Reports to have indicated that when this method was used the morphology, phase and size of the nanoparticles could be controlled by manipulating the aging time, solution pH and the metal source.[83]

2.2.1.2.4 The Pechini method.

The Pechini method was developed in 1967 as a modified sol-gel technique and was intended for metals that were unable to be used in the orthodox sol-gel procedure, because of their unfavorable hydrolysis equilibria.[78] The technique has functioned on the principle that complexes have been known to form between metal ions and polydentate ligands (e.g. citric acid).[85] Here compounds with two or more alcohol functional groups (e.g. glycerol or ethylene glycol) have been added to introduce linkages between the chelates by the poly-esterification reaction.[85,86] These formed gels which were subsequently dried to remove all the solvent. Thereafter they were heated to induce pyrolysis of the carbonaceous materials and ultimately to form agglomerates of metal oxide nanoparticles.[85]

2.2.1.2.5 The resin gel method.

The resin gel technique was developed as an extension of the Pechini method, where a carbon-based polymer chain (e.g. polyethylene glycol) was added in excess amounts to the solutions of metal ions, in order to stabilize them through complex formation.[81-82] As with the Pechini method that was described previously, the polymer coordinated metal ions were allowed to be steadily desolvated into hard waxes.[86] Then upon heating, these hard waxes were found to spontaneously ignite because of the large amounts of polymer. Unfortunately, the processes that occur during the desolvation and pyrolysis stage are still not fully understood.[86] However, in a previous study, it was observed that the solvent had to be completely evaporated to form a hard wax in order for reproducible homogeneous phase distributions and sizes to be achieved.[82] Again, the influence of the solvent during combustion is still not known, but it has been reported to be undesirable.[86] Similarly, it is also unclear

which is the best way to combust the polymer, as it has been reported that rapid heating of the hard waxes has yielded uniform nanoparticles with small particle size distributions.[86] However, it has also been shown that gradual heating allowed for more control over the phase and polymorphs of these nanoparticles. In particular, when TiO_2 was synthesized in our laboratories by the resin gel method, it was found that the gradual heating method consistently yielded the anatase polymorph, whereas rapid heating yielded nanoparticles with some degree of the rutile polymorph.[86] This was believed to have occurred due to the high temperatures that were required in order to achieve rapid ignition.[86]

2.2.2 Heterogeneous TiO_2 photocatalysis

The semiconductor industry has been one of the most influential scientific sectors for the advancement of technology. In the late 1940s, the first semiconductor material, called a transistor, was recognized at Bell laboratories.[87] The transistor went on to be used widely for radio electronics.[87] In the present day, it is hard to find an electronic component without transistors; they are widely used in microelectronics found in gadgets such as cell phones, DVD/CD players, computers, etc.[88] In the year 2006, Intel® released dual-core chips which contained more than 1.7 billion transistors on a surface that had dimensions smaller than 20 mm x 25 mm.[89]

Semiconductors (e.g. TiO_2) possess an electrical conductivity that is intermediate between insulators (e.g. plastics) and conductors (e.g. metals). The band structure of metals/conductors does not have a gap between the filled valence band and the empty conduction energy level, hence minimal energy is required for the material to conduct electricity. Consequently, conductors are able to transport electrons through their lattice even at absolute zero. A material which has a band gap that is so large that electron

transportation is not feasible is termed an insulator. In the case of semiconductors, a band gap is observed between the filled valence band and the empty conduction band. Here energy quanta are required to facilitate the promotion of electrons from the valence band to the conduction band.[90] The band gap of semiconductors is in known to be in the range of 1-4 eV.

Since the band gap of TiO_2 (in the anatase phase) is 3.2 eV, only radiations with a frequency greater than 774 THz (violet light) can promote valence electrons into its conduction band.

There are two different types of semiconductors, intrinsic and extrinsic. Intrinsic semiconductors possess the same number of free bonding electrons and positively charged vacancies (holes) that are created upon the excitation of electrons into the conduction band from the valence band. The number of electrons that are able to go through the band gap is dictated by the Fermi function which indicates the probability of an electron occupying an available energy level. Another important factor that governs the promotion of electrons to the conduction level is the density of states (DOS).[91] In the case of conductors the Fermi level coincides with the conduction band because of the absence of the band gap. A different case is observed in semiconductors where the DOS of conduction electrons do not lie within the Fermi level but at the top of the band gap. For this reason, the position of the Fermi level indicates the ability of an electron to go from the valence band, through the band gap into the conduction band.[91]

On the other hand for extrinsic semiconductors, the Fermi level is situated at a level that is somewhat above or below either the valence or conduction band.[91] The position depends on the materials doped into the lattice, which could either be electron rich or electron deficient. Generally, if additional electrons are added into the lattice, the semiconductor is

said to be n-type, whereas if the dopant is electron deficient the semiconductor is said to be a p-type .[83]

Nevertheless, in both types of semiconductors, positively charged vacancies (which are called holes) are left in the valence band when electrons are promoted from that band to the conduction band. Since the electrons that have been excited and promoted to the conduction band possess higher energy than those that remain in the valence band, they tend to lose their excess energy (in the form of photons or heat) when they return to the conduction band.[90] The process in which electrons spontaneously return to their valence bands is called the electron/hole recombination.[90]

Semiconductors have a void region where there is no energy available to encourage the recombination of the electron and the holes produced through photo-excitation. Hence upon photo-excitation, there is enough time in the nanosecond region for the ionization products to interact with the gaseous or liquid species adsorbed on the semiconductor surface.[86] If the integrity of the semiconductor is not compromised and the charge carriers that are photo-induced interact through charge transfer with species that are adsorbed on their surface continuously and exothermically, the process is called heterogeneous photocatalysis.[80]

The process of heterogeneous photocatalysis is initiated through the photo-ionization of an organic or inorganic semiconductor which generates positively charged holes (h^+) and electrons (e^-) (**Figure 2.3**).[87]

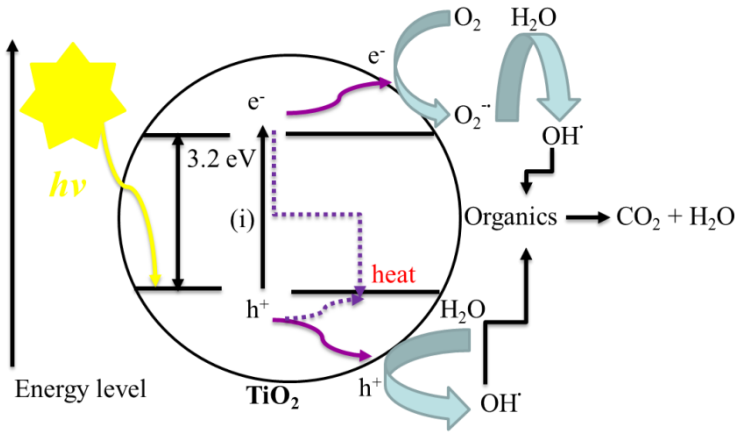

Figure 2.3. A representation of the photocatalytic process.[87]

As previously stated, the ionization process occurs through the excitation of electrons from the valence band into the conduction band. This occurs as a consequence of the semiconductor absorbing electromagnetic radiation with a wavelength equal to or greater than that of the semiconductor band gap. The fate of the photo-induced charge carriers can then follow different routes: (i) The electrons can travel to the semiconductor surface where they interact with adsorbed species, (ii) The semiconductor can donate these electrons for the reduction of electron accepting species such as oxygen which is present in aerated solutions, (iii) The holes can also travel to the semiconductor surface and oxidize electron rich species.[86-87]

The likelihood and the speed at which charge transfer between photo-ionization products and adsorbed species occurs depends on the energy band positions of the conduction and valence bands as well as the redox levels of the adsorbed species.[92] The charge transfer processes described above compete with the electron and hole recombination process.[87] For instance, the recombination of the charge carriers can happen either on the surface of the semiconductor or in its volume. As described previously, this process is accompanied

by the release of heat energy. Another competing process for the fate of these photo-generated species is back-donation, where electrons recombine with donors.[87]

Quantum yield, which is defined as the number of events per photon absorbed, is used as an indication of the efficiency of photocatalysis.[87] In a heterogeneous system light gets scattered on the semiconductor surface and renders the process of measuring absorbed light difficult.[83] Measuring the quantum yield of a heterogeneous photocatalysis system requires that it is assumed that no radiation is scattered and so this is referred to as the apparent quantum yield.[93] In a case where the photocatalytic reaction yields products, the yield of a particular product can be used to measure the quantum efficiency of the system.[87]

Calculations that are used to determine the quantum yield of a photocatalytic system have to include all the possible pathways that can be undertaken by the electrons and holes.[87] The efficiency (ø) of an ideal photocatalytic system is given by the relationship: [87]

$$ø \propto \frac{k_{CT}}{k_{CT}+k_r} \qquad (\mathbf{2.2.2.1})$$

Here the quantum yield is found to be directly proportional to the charge transfer process (k_{CT}) and inversely proportional to the sum of the charge transfer process and the electron-hole recombination rate (k_r) that occurs in the volume of the semiconductor as well as on its surface.[87] Implicit in this equation is the assumption that the products of the photocatalytic reaction diffuse into solution quick enough to avoid back-donation.[80] In the absence of back-donation and electron-hole recombination then ø = 1, meaning that the rate of charge transfer relies on the diffusion of the electrons and holes.[87]

2.2.3 Limitations of TiO_2 as a photocatalyst

The anatase and rutile polymorphs of TiO_2 are the only two with known photocatalytic properties.[87] Although TiO_2 has been shown to be a more potent photocatalyst than other semiconductors, it has several limitations, which include: i) A large band gap that falls in the UV region of the spectrum and ii) A low rate of charge transfer to the surface.[94,95]

There is an incongruity between the energy band gap of TiO_2 and the sunlight spectra, where the only overlaps are found in the UVA and UVB (290 to 400 nm) portions of the spectrum. This means that only high energy light sources can be used to excite TiO_2; consequently, only 5 % of the solar energy that reaches the earth's surface can be harvested by TiO_2 photocatalysis.[96] This has limited the potential of TiO_2 photocatalysis as an environmentally sustainable technology.[2,80,83,97,98]

Apart from the wide band gap of TiO_2, another serious limitation to its use in photocatalysis is its low efficiency.[97,98] This comes as a result of the recombination rate of its photogenerated electrons and holes being significantly higher than its charge transfer rate.[88] Equally, the reaction rates of TiO_2 in photocatalysis are modest and thus insufficient for intense processes such as the cleansing of highly polluted industrial discharges.[88] One obvious approach to increase the reaction rate of TiO_2 would be to increase the light flux.[80] However, since this is affected by saturation, which occurs at relatively low irradiance, this again limits efficiency.[80] Another would be to increase mass transport, typically by using TiO_2 in suspension. However, this has required that the TiO_2 be separated from the water after decontamination and has proved particularly difficult (especially for nanoparticles) as well as more costly.[92,99] Increasing the amount of TiO_2 used is yet another alternative to increase the number of charge carriers. However, this is disadvantageous because in addition to increasing the costs it results in enlarged turbidity that decreases the depth at

which radiation can penetrate, and even further decreases the quantum yield.[90] The potential of environmentally sustainable TiO_2 photocatalysis and the problems associated with its low efficiency have led to numerous scientists researching methods to alter TiO_2 to attain proficient photoactivity in the visible spectrum with improved quantum efficiency. A brief description of some of the strategies that have been used to improve the photocatalytic performance of TiO_2 is given in the section which follows.

2.2.4 Strategies for improving the photocatalytic performance of TiO_2.

Numerous methods, classified as either morphological or chemical modifications, have been used to refine the photocatalytic efficiency of TiO_2.[80,100–102] Chemical modifications have included the incorporation of foreign materials into the structure of TiO_2, whereas morphological ones have influenced its physical properties such as porosity, surface area, particle size, and structure.

2.2.4.1 Morphological modifications

Some of the most researched areas in the study of the photocatalytic efficiency of TiO_2 have been in their morphological modification.[80,97,98,103] For instance, monodispersed TiO_2 nanoparticles are the most common type used.[88] This is not only because the diameter of monodispersed TiO_2 nanoparticles can easily be controlled, but also because altering it can lead to increased surface area and reduced bulk recombination.[92] Here the aim is to exploit these advantages without compromising other important features such as crystallinity. Various one-dimensional morphologies of TiO_2 have been investigated such as nanorods, nanotubes, nanoneedles, and nanobelts amongst others.[80,100,104,105] All of these have had: tailored morphologies, controlled porosities, vectorial charge transfers and low

electron-hole recombinations at their grain boundaries.[95-97] However, even more, pivotal to improving the photocatalytic properties of TiO_2 has been its chemical modification. An in-depth review of some of the strategies for the chemical modification of TiO_2 will now follow.

2.2.4.2 Chemical modifications

2.2.4.2.1 Anion doping

In recent times, a significant portion of research into the chemical modification of TiO_2 has been focused on reducing its band gap by introducing anion dopants into its structure.[2,83] Significantly, there are numerous disagreements and debates about the manner in which anion doping of TiO_2 enhances its photocatalytic efficiency.[83] These disagreements have generally stemmed from the different techniques that have been employed to incorporate various anions into TiO_2.[83] This suggests that it is very likely that different methods of synthesis yield materials with different properties.[95] Hence queries associated with the chemical identity of the anion, its position in the solid and how it is involved in photocatalysis still need to be investigated and answered. Doping TiO_2 with anions can either occur interstitially or substitutionally, with each of these affecting the properties of the resultant products differently.[96] Likewise, since the surface reactivity and photocatalytic properties of the resultant materials can be impacted, it is also essential to investigate if the doped species are segregated at the surface of TiO_2 or are incorporated into the bulk sites.[96] Similarly, there is also a lack of clarity about how the doping anions interact with titanium and oxygen as well as how this affects the stability of the resultant material.[96]

Nevertheless, recent studies have shown that the band gap of TiO_2 was narrowed upon doping with anions such as chloride, iodide, sulphur, phosphorus, nitrogen, carbon and boron, amongst others.[95,101] Consequently it was found that the resultant materials absorbed in the visible portion of the spectrum, which increased their photocatalytic activity under such irradiation.[95]

It has been shown that the band gap of TiO_2 was decreased by the replacement of some of the oxygen atoms in the TiO_2 lattice by nitrogen.[96] Nitrogen can easily be substituted into TiO_2 structure because of its comparable atomic size with oxygen as well as its high stabilization and small ionization energies.[106] Doping TiO_2 with carbon has also been shown to end in intra-band gap states just above the valence band of TiO_2, from which visible light photoionization becomes achievable.[106] Other anions such as sulphur and phosphorus have also been shown to narrow the band gap of TiO_2.[96] It was reported that the insertion of sulphur into the lattice of TiO_2 was considerably harder than for other anions because of its large ionic radius.[107,108] Doping TiO_2 with fluoride anions has not been shown to reduce the band gap energy of TiO_2, however, it was shown to have increased the surface acidity and assisted the formation of Ti^{3+} ions due to charge reparation between F^- and Ti^{4+}.[109–111] Co-doping with nitrogen and fluoride has also been investigated and shown to offer some synergistic advantages, with nitrogen having narrowed the band gap and fluoride having enhanced charge separation.[106,111]

2.2.4.2.2 Cation doping

Unlike with anion doping, the photocatalytic efficiencies of TiO_2 doped with various metals have shown plenty of inconsistent results.[80] This was believed to be because TiO_2 doped with metals was found to depend on the: i) Nature of the dopant

and its contents, ii) Concentration of metal used, iii) Synthesis method, iv) Type of TiO_2 used and sometimes v) Identity of the target contaminant along with the conditions used.[112] Modifying TiO_2 with transition metals such as Co, V, and Fe has been shown to successfully narrow the band gap of TiO_2.[80] Conversely transition metals have also been known to either block reaction sites or act as sites for electron-hole recombination (thus decreasing the photocatalytic activity of TiO_2).[113]

Doping with noble metals such as silver, gold, platinum, and palladium has been shown to improve the visible light photocatalytic quantum efficiency of TiO_2 through the formation of surface plasmon resonance.[114–117] Noble metals have also been shown to act as electron trap sites when deposited on the surface of TiO_2, which promoted interfacial charge transfer via the formation of Schottky barriers and thus decreased electron-hole recombination.[118]

Rare earth metals such as lanthanum, neodymium, samarium, europium, gadolinium, and ytterbium, amongst others have been used as dopants in TiO_2 due to their unique chemical, physical and electronic properties.[79,96,109,110] Among these properties are that they: i) Possess f-orbitals which has resulted in increased adsorption of organic contaminants onto the surfaces of TiO_2 through complex formation, ii) Behave as good electron trappers, iii) Have unique electronic structures that have enhanced the optical properties of the photocatalyst.[119–122] As an example, it has been shown that the photocatalytic activity of TiO_2 was improved by doping rare earth metal ions on TiO_2.[120,123]

Alkaline-earth metals have also been shown to be good dopants for increasing the quantum efficiency of TiO_2 by decreasing electron-hole recombination.[123–129] For

example, Be^{2+} doped TiO_2 was shown to have greater photocatalytic activity when compared to unbound TiO_2.[112] This observation was attributed to Be^{2+} having filled interstitial sites in the TiO_2 which increased its electron density and hence improved its photocatalytic activity.[112]

2.2.4.2.3 Coupled semiconductors

One of the approaches that have been well researched in order to obtain improved charge separation has involved the coupling of two semiconductors (metal oxides), each with different energy levels.[80,130,131] Several semiconductors such as cadmium sulphide, tin dioxide, bismuth sulphide, tungsten oxide, and zirconium dioxide have been coupled with TiO_2 in order to narrow its band gap.[132,133] Similarly, semiconductors with wide band gaps and conduction bands of low energy (e.g. TiO_2 or ZnO) have been combined with semiconductors with narrower band gaps and conduction bands with higher energy (e.g. WO_3 or CdS).[131] Then upon photo-excitation, photo-generated electrons have amassed at the lower lying conduction band of one of the two semiconductors, while holes gathered at the valence band of the other semiconductor particle, as exemplified in **Figure 2.4**.[80]

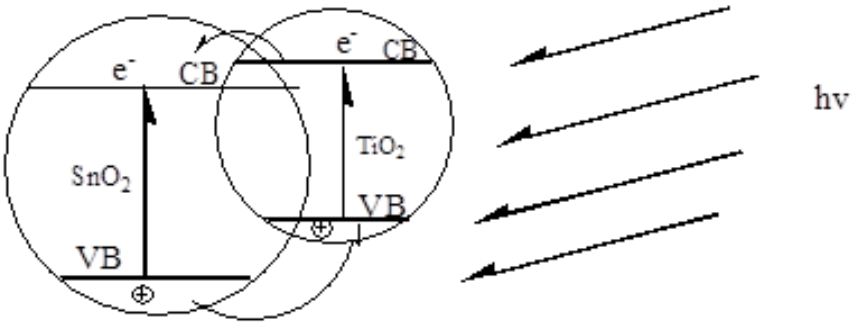

Figure 2.4. A schematic representation of the separation of photogenerated electron-hole pairs by means of binary semiconductor systems.[80]

Li *et al*. analyzed the microstructure and phase composition of a binary semiconductor system consisting of TiO_2 and $BiFeO_3$ and showed that a core-shell morphology was formed.[134] This binary system resulted in photo-absorption being stretched into the visible range as a function of the concentration of $BiFeO_3$.[125] This binary system was shown to have higher photocatalytic efficiencies as compared to the unbound TiO_2 and $BiFeO_3$ when by themselves.[134] In another instance, TiO_2 nanotubes were coupled with $ZnFe_2O_4$ to once again form core-shell structures which were found to reduce their electron-hole recombination and to extend their photo-response into the visible part of the spectrum.[135] It is believed that one of the reasons why this kind of morphology was effective was that there was lattice correspondence between the core and shell which helped attain improved passivation and minimized structural defects.[79] Similarly, the improved photocatalytic efficiency of binary semiconductors is also believed to be connected to the: i) Geometry of the particles, ii) Particle size and iii) Interaction surface between the particles. This has prompted many scientists to focus upon procedures that form core-shell structures between two semiconductors, as the above-mentioned parameters have generally been able to be controlled through their method of synthesis.

2.2.4.2.4 Mixed metal oxides

Unlike with coupled oxides, mixed metal oxides can be described as compounds which are composed of more than one type of metal ion or the same metal ion but in different oxidation states present in a single crystal. Mixed metal oxides are classified with respect to the number of atoms in a single crystal. For instance, a ternary mixed metal oxide consists of 3 atoms whereas a quaternary mixed metal oxide has 4 atoms.

As previously stated, TiO_2 is a well-known semiconductor which has been extensively investigated for photocatalytic applications because of its optical properties. TiO_2 exists in three polymorphs: anatase, rutile, and brookite, with the last being the least stable .[81] The packing of the lattice of anatase and rutile differ; anatase is relatively loosely packed with large vacancies as compared to rutile (see **Figure 2.2** and **Table 2.3**).[82] Consequently, other metal ions have been incorporated into the crystal lattice of TiO_2 through various methods, which have included: i) Titanium replacement, ii) Vacancy occupation and iii) Point defects.[82] These methods have been possible because TiO_2, especially the anatase polymorph, was able to easily accommodate oxidation state changes.[82]

Tungsten oxide and zinc oxide are both examples of materials which have been studied as possible photocatalysts.[136–139] The ionic radius of Ti^{4+} is 61 pm, whereas the radii of Zn^{2+} and W^{4+} are 55 and 60 pm respectively. Since anatase can assume different oxidation states and the radii of Zn^{2+}, as well as W^{4+}, are similar to that of Ti^{4+}, this has made it possible for these ions to be incorporated into its crystal lattice.[82] Hence any technique (like the resin gel method discussed in **section 2.2.1.2.5**) which can be used to synthesize mixed metal oxides like this, allows for the systematic manipulation of the electronic structure of TiO_2 and hence its optical properties.

2.2.4.3 Supported TiO_2 nanoparticles

Supporting or immobilizing TiO_2 is commonly done for at least two reasons: i) In order to simplify the task of separating TiO_2 nanoparticles from decontaminated water after photocatalysis and ii) To avoid coagulation of TiO_2 nanoparticles during the photodegradation process.[80,97,98] From surveying literature that is available, it can be established that the criteria for ideal support for a TiO_2 photocatalyst are as follows:

- The supporting material should be translucent as well as chemically inert to the contaminant molecules, their intermediates and the surrounding aqueous system.[140–143]

- The supporting material should adequately bond either physically or chemically to the TiO_2 without compromising its reactivity.[130]

- The supporting material should have a high surface area and a strong adsorption affinity towards the pollutants.[133,144–146]

- The supporting material should allow for the fast and easy recovery of the photocatalyst, as well as its reuse with little or no regeneration.[141,145]

Several materials have been investigated as photocatalyst supports, especially for the photodegradation of pollutants in water, in order to satisfy the above criteria. These materials have included: glass (glassy mesh, fabric, wool, beads, and reactors), microporous cellulosic membranes, monoliths, fly ash, activated carbon, carbon nanotubes, zeolites, alumina, clay, polymers, and stainless steel.[143,147] Many times an important criterion of such supports have been minimized or excluded i.e. do they improve the photocatalytic efficiency of TiO_2 by either reducing the recombination of electron-hole pairs or by extending its photo-absorption into the visible region? A great deal of research has to be focused in this area, particularly with an emphasis on using cheap materials for this purpose. These latter points have been the focus of a great deal of the research presented in this thesis. One such material used in this regard i.e. fly ash will now be discussed.

2.3 Fly ash

The use of coal for firing power generating stations became prevalent in the 1920s.[148] This has resulted in the production of millions of tons of coal fly ash (CFA) and related by-products.[149] The quantity of CFA effluents from factories and thermal power plants has been cumulative throughout the world, and its disposal has developed into a solemn environmental problem.[150–152] It is approximated that only 16 % of the CFA generated is reused.[148] Hence a considerable quantity of CFA is still disposed of in landfills and/or lagoons, which in addition to the loss of land incurs extra charges.[149] CFA is extremely toxic because it contains numerous trace metals which are poisonous (e.g. As, Pb and Hg).[148,153–155]

Interest in finding cost-effective and safe ways of reusing CFA is of environmental and industrial importance.[148] For instance, the practice of disposing of CFA as landfill has come under scrutiny because of its potential toxicity .[148] This has resulted in the disposal of CFA becoming expensive and heavily regulated.

In order to research various applications of CFA, it is crucial that its properties be understood. This has resulted in the widespread characterization of CFA with the primary aim of understanding its: composition, mineralogy, surface chemistry and reactivity.[148] The afore-mentioned research has shown that four primary classes of coal exist i.e. bituminous, sub-bituminous, anthracite, and lignite, with each differing in terms of their: heating value, chemical composition, texture and geological source.[148,155]

CFA mainly consists of fine glassy powdery particles that are principally spherical and which are either compact or hollow.[148] In addition to the trace quantities of the metals discussed previously, CFA is predominantly composed of a variety of metal oxides which usually are present in the following order: $SiO_2 > Al_2O_3 > Fe_2O_3 > CaO > MgO > K_2O >$

$Na_2O > TiO_2$.[156] The chemical compositions of CFA are determined mostly by two factors: i) The geological properties of the coal sources from which they are combusted, ii) The methods which are used for their treatment and packing.[148] As will be discussed shortly, the interesting and complex chemical and physical properties of CFA have led to research on their usage.

2.3.1 Application of fly ash

Research and understanding of the properties of CFA have led to several applications of CFA, the major of which has been as an auxiliary component for materials used in the construction industry.[148,155] A summary of the industries that currently use CFA is found in **Figure 2.5**.[148]

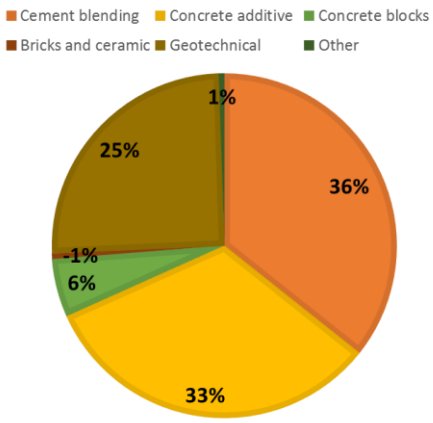

Figure 2.5. A pie-chart representation of the current utilization of CFA.[148]

For example, since CFA has pozzolanic properties (i.e. they assist in the consumption of calcium hydroxide to make cementitious materials) one of its main applications has been as a fractional auxiliary material for clinker in Ordinary Portland Cement (OPC).[141] A second major set of applications of CFA is in the geotechnical industry where it is used in various areas for grouting, asphalt filling, sub-grade stabilization, pavement base coursing, general engineering filling, structural filling, soil amendments and infilling.[156–158] CFA is

also used as a stabilizer because of the advantageous effects it imparts. For instance, it has been reported that CFA decreases the tendency of soil swelling when water is absorbed.[159–162] Soil swelling is a problem because the soil tends to expand when wet and shrink when dry.[162] This, in turn, can then lead to pressure being exerted that can result in cracks in pavements, basement floors, driveways, pipelines, and foundations.[156] In these cases it is believed that the presence of CFA alters the mineralogy of the soil, due to its pozzolanic properties, converting it into a more granular state which retains less water and hence reduces its swelling.[156]

CFA has important physicochemical alterable features such as bulk density, particle size, porosity and water holding volume that allow it to be used as an adsorbent.[155] Hence initial reports on the use of CFA as an adsorbent for environmental purposes were published as early as the 1970s, where it was used for the removal Cu^{2+} from industrial water effluents.[163] Since then CFA has been widely used as a cheap adsorbent for the removal of heavy metals such as Ni, Pb, Cd, Hg, As, and Cr, etc.[148,154–156,164–174] However, in some of the above-mentioned studies CFA was modified before use as an adsorbent. This was done in a variety of ways, including impregnating it with Al and Fe, transforming it into zeolites, acid treating or washing it and/or performing other physical and chemical modifications to it.[154,156,172]

CFA has also been used to adsorb other contaminants apart from inorganic ions; several organic compounds have also been adsorbed using CFA. For example, CFA has been shown to have a high adsorption capacity towards phenol.[175,176] It has also been successfully used for the adsorption of chlorinated phenols.[161] Although the adsorption capacity of CFA was found to be inferior to that of activated carbon for the removal of polychlorinated biphenyls (PCBs), its low cost still makes it an economically viable alternative for the decontamination of organics from waste-water.[177] CFA has also been

actively used as an adsorbent for flue gas desulphurization processes, where it was reported that its efficiency was enhanced (ostensibly due to increased surface area) when it was mixed with calcium hydroxide.[178]

Since CFA is rich in mineral content, numerous researchers have also endeavored to recover useful elements from CFA. Aluminum is one of these elements which has been recovered from CFA by various techniques, including by use of sulphuric acid.[152,179] For instance, a study that involved the direct leaching of aluminum using sulphuric acid yielded an 18 % Al recovery, whereas an 85 % Al recovery was achieved when pellets formed from CFA, CaO and fine coal were thermally treated.[156,179] Titanium (IV), iron (III) along with aluminum have also been recovered from CFA where three extraction techniques were paralleled: i) Selective pH precipitation, ii) Crystallization and iii) Solvent extraction.

Yet another field in which CFA has been shown to play a significant environmental conservation role is in heterogeneous catalysis.[148,155,156] In heterogeneous catalysis, the active catalyst/s can be supported on various materials.[80,97,98,143,180] Here the overall catalyst activity is governed by both the active catalyst/s and its/their interaction with the support material. The most commonly used materials as catalyst supports include metal oxides such as alumina, silica, magnesium dioxide and titanium dioxide.[181–184] Given that CFA is primarily composed of alumina and silica, this provides some of the desirable properties that are required of catalyst support, including good thermal stability.[184]

In this regard, catalysts prepared by treating CFA with lime and then supporting Ni on them were used to demonstrate that carbon dioxide-methane reforming could be achieved.[185] Furthermore, these stable catalysts were shown to be capable of high conversions and had activities that rivaled more orthodox catalysts like Ni/Al_2O_3 and Ni/SiO_2.[185] In a related manner, various metals such as iron, vanadium, nickel, and copper

have also been supported on CFA to produce catalyst systems that were capable of reducing nitrous oxide.[148,185–188] Alternatively, sulphated zirconia has been loaded onto CFA using the sol-gel method, in order to yield thermally stable nano-crystalline catalysts which were used for the liquid phase benzylation of benzene and toluene with benzyl chloride.[189] These catalysts yielded satisfactory conversions of 87% and 93 % for benzene and toluene (93%) respectively.[189] In addition, studies have also shown that CFA could itself be used as an active catalyst.[148,187,189], For example, it has been established that hydrogen peroxide could be triggered by CFA with iron(III) to oxidize a dye (reactive black 5) by an advanced oxidation process (AOP).[190]

Finally, other applications of CFA have included its use in agriculture, ceramic and glass production, geopolymer formation,[191] the recovery of germanium[192] and gallium,[193] as well as in the production of zeolites (which will be discussed later).[156]

2.3.1.1 TiO_2/fly ash photocatalyst

As has been discussed in **section 2.3**, CFA is primarily composed of metal oxides like alumina and silicon dioxide. This means, at least in theory, if TiO_2 were to be coupled with CFA that the resultant composites may have the same benefits (as described previously) as those derived when TiO_2 is coupled with other metal oxides. Another potential benefit that could be obtained from coupling TiO_2 with CFA could be the increased surface acidity due to hydroxyl groups.[130,194,195] If this were to occur the hydroxyl groups, which have the capability of accepting the photo-generated hydroxyl radicals would prevent the recombination of the electron-hole pairs and in turn increase the quantum efficiency of the procedure.[130]

Several models have been proposed to account for the increased surface acidity in multi-metal oxides composites.[196] One of these has been proposed by Tanabe *et al*., where it was

suggested that the cation (of the dopant metal oxide) is inserted into the lattice of the host metal without compromising its coordination number.[196] In other words, the dopant cation remains bonded to the same number of oxygen atoms, although these are now coordinated differently and hence create a charge inequity.[196]

In order for the charge imbalance to be satisfied, it was further suggested that Brönsted sites would form when the charge inequity is negative or Lewis sites would form when the charge is positive.[130,196]

Research, dating back to 1983, has been performed on the photocatalytic efficiency of different CFAs.[197] Indeed other semiconductors, apart from TiO_2, have also been used alongside CFA for photocatalysis. For instance, Zhang *et al*., have reported on the visible light photodegradation of methylene blue where $BiVO_4$ was supported on CFA.[198] However, fewer studies have been reported on photocatalysts composed of CFA and TiO_2. For example, Wang *et al*. have reported on the visible light photodegradation of methylene blue and phenol over TiO_2/CFA which was photosensitized with polypyrrole.[199] Similarly, Pengwei *et al*., have reported on the enhanced photocatalytic photodegradation of rhodamine blue over AgCl/TiO_2 films supported on CFA cenospheres.[200]

2.3.1.2 Zeolites derived from fly ash

In **section 2.3.1** it was mentioned that zeolites could be derived from CFA. In this section, the synthesis of zeolites from CFA will be discussed in depth. Zeolites are crystalline networks consisting of aluminum–silicates, with alkali and alkaline metals as counter-ions.[201–203] A typical zeolite structure mainly consists of a tetrahedral skeleton composed of $[SiO_4]^{4-}$ and $[AlO_4]^{5-}$, where the constituents of this framework are connected at the vertex through the sharing of oxygen atoms (**Figure 2.6**).[201]

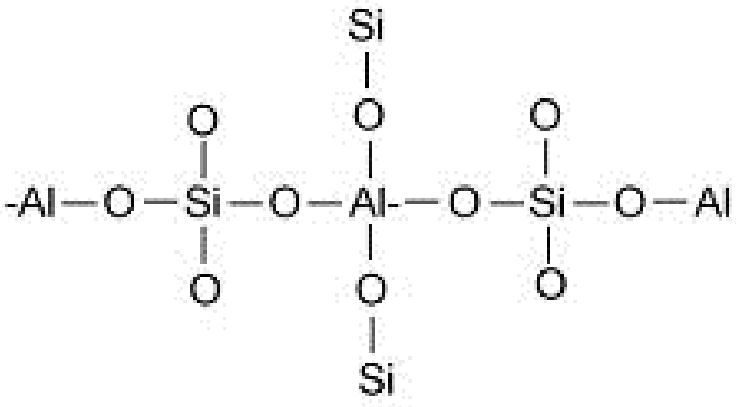

Figure 2.6. A line drawing showing the basic structure of zeolites.[201]

These tetrahedra make-up a 3D system (**Figure 2.7)**[187] which has lots of voids and open spaces that are responsible for most of their attractive properties (especially for adsorption and size exclusion).[204] The properties of zeolites that make it a suitable material for applications in photocatalysis, include: i) photochemical stability, chemically unreactive and thermally stable, ii) high surface area, and iii) the capability of zeolites to contribute in electron-transfer progressions either as an electron acceptor.[19]

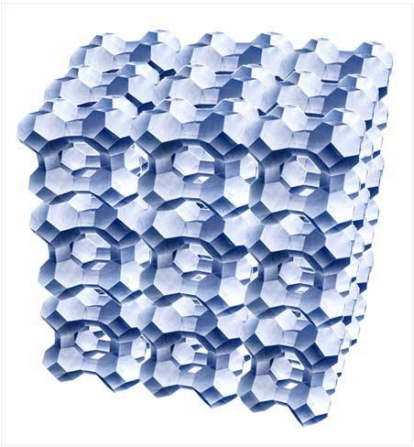

Figure 2.7. Zeolite network showing voids.[187]

The replacement of Si^{4+} by Al^{3+} in these tetrahedra explains the presence of the negative charge in the structure shown in **Figure 2.6**. These, in turn, give rise to high cation exchange capacity, reaching up to 5 meq/g provided that the voids are big enough to allow for the admission of these cations.[201]

Since CFA is high in alumina and silica, as was discussed in **section 2.3**, it is an ideal candidate material for the synthesis of zeolites.[201–203] The seminal report on the synthesis of zeolites from fly ash by a hydrothermal technique was published in 1985.[205] Since then a great deal of research has yielded multiple patents and technical articles on the subject.[201] Most of the synthetic techniques that have been reported on this subject have been based on the dissolution of CFA in basic solutions (KOH and NaOH), followed by the precipitation of zeolitic material.[206–208] Although these techniques were based on the same principles, variations therein have yielded zeolites with different properties. For instance, the classical alkaline conversion of CFA has focused on mixtures of dissimilar activation solution to CFA ratios under varied synthetic conditions (i.e. temperature, pressure, and reaction time) to attain diverse kinds of zeolites.[201,209,210] The yields in this conversion process have been found to be enhanced by the fusion of CFA with alkaline materials.[206,211] The two-stage synthesis procedure has also been used as an alternative alkaline based hydrothermal synthesis of high purity zeolites from CFA.[211] However, a major drawback to obtaining decent yields from these synthetic methods has been the high temperatures required for the dissolution of CFA in alkaline solutions.[201] Nevertheless, zeolitic materials of high quality have been derived from CFA and used for various applications as will be discussed shortly.

2.3.1.3 Zeolites in photocatalysis

The benefits of coupling TiO_2 with other metal oxides (e.g. SiO_2 and Al_2O_3) have been discussed extensively in the previous **sections (2.3.1 and 2.3.1.1)**. Hence the same benefits would be expected by coupling TiO_2 with zeolites (which are themselves aluminosilicates). Moreover, since zeolites have high adsorption capacities (including for organic contaminants) it would also be expected that when coupled with TiO_2 the quantum efficiency of such photocatalysts would be enhanced.[212] Indeed there are several reports where the photocatalytic efficiency of TiO_2 coupled with zeolites have been reported. For instance, Ichiura *et al*., described the removal of acetaldehyde from water by photocatalysis using TiO_2-zeolite sheets that were prepared via the papermaking method.[213] Here they showed that zeolites adsorbed modest amounts of acetaldehyde in the dark but when illuminated with UV light, a significant improvement in the disappearance of acetaldehyde was observed.[213] Ichiura also published several other reports on the subject.[212–214] In addition, Masakazu *et al*., have reported on the photocatalytic reduction of carbon dioxide with water using TiO_2 anchored in the micropores of zeolites.[215]

2.4 Carbon nanomaterials

In 1985 Smalley *et al*. were the first to report on the synthesis and chemistry of the C_{60} molecule, which was then named after the famous American architect: Richard Buckminster Fuller (i.e. Buckminster fullerenes or fullerenes for short).[216] The structure of the C_{60} fullerenes is composed of 5 and 6 membered carbon rings and is arranged in a geometry that is likened to that of a cage (**Figure 2.8**).[216]

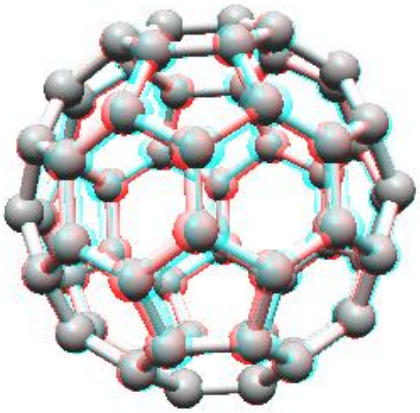

Figure 2.8. Structure of a buckyball.[217]

Research in this area then led to the rediscovery of the long, thin and graphitic tubular structures (also composed of 5 and 6 membered carbon rings), which were then named carbon nanotubes (CNTs) by Iijima (**Figure 2.9**).[217]

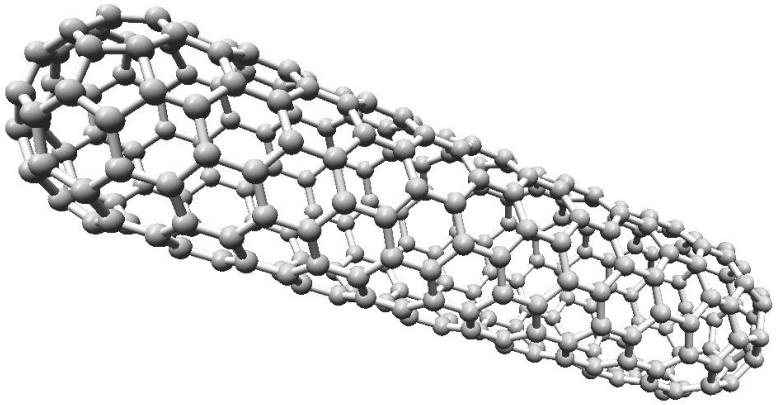

Figure 2.9. Structure of carbon nanotube.[218]

A CNT is best imagined as a sheet of graphite that has been rolled into a tube.[218] CNTs are dissimilar to diamond (which has a three-dimensional structure with carbon atoms organized tetrahedrally) in that the carbon atoms are organized hexagonally to form two dimensional sheets.[219]. The properties of CNTs depend

upon on how the carbon atoms are arranged, i.e. the geometry in which the sheets are rolled along a plane.[220] There are three known geometries i.e. armchair, zig-zag and chiral.[2,83] Other factors that influence the properties of CNTs include their diameter, length, and their morphology.[2,83] CNTs can also exist as single-walled (SWCNTs), double-walled (DWCNTs) or multi-walled (MWCNTs) structures. DWCNTs consist of two walls, whereas MWCNTs are made of concentric SWCNTs.[83] On the other hand, carbon nanofibers are less graphitic than CNTs and their main variation is that they do not consist of a hollow cavity.[221]

Fullerene-based carbonaceous materials have been shown to possess unique, yet excellent physical properties which result because of their highly symmetric geometry.[83,216,222] For example, theoretical and experimental data have revealed that CNTs have tremendously high elastic moduli (comparable to that of a diamond) i.e. greater than 1 TPa.[2,83,223] Equally CNTs have been reported to have strengths that are between 10–100 times greater than that of the strongest steel at a fraction of its mass.[2,83,223] Similarly CNTs have been determined to be able to resist decomposition in vacuum to temperatures as high as 2800 °C.[2,83] It has also been established that CNTs conduct heat approximately double that of diamonds and that they conduct electricity at a capacity that is three orders of magnitude higher than copper wires.[2,83]

2.4.1 Carbon nanomaterials synthesized from fly ash

Since CNTs were rediscovered almost two decades ago an assortment of methods that have been established for their synthesis.[217,224] The most common of these methods include arc-discharge, laser ablation, gas-phase catalytic growth from

carbon monoxide (CO) and chemical vapor deposition (CVD) from hydrocarbons.[2,83,225] The CVD method is most commonly used for CNT synthesis mainly because high yields of CNTs can be obtained.[223] However, one drawback of the technique is that the purity of the CNTs formed is not usually as good as with some of the other techniques (e.g. laser ablation).[226,227]

Individual transition metals like nickel, cobalt, and iron have often been used for the synthesis of CNTs.[225] Numerous studies have suggested that using iron as a catalyst for the CVD synthesis of CNTs has yielded MWCNTs; by contrast several other groups have obtained SWCNTs.[225,228,229] Similar trends have been observed with cobalt and nickel where MWCNTs were predominantly formed, except for when certain conditions such as reaction temperature and duration were controlled which led to the formation of SWCNTs.[225] On the other hand mixtures of transition metals have been shown to be more potent at catalyzing the formation of CNTs. For instance, an iron-cobalt catalyst has been shown to produce SWCNTs, while an iron-nickel catalyst produced MWCNTs.[225,230] In the case of anchored catalysts, the connections between the support and the catalyst nanoparticles have played an important part in the growth procedure.[223,225,231] The supports usually used in the CVD synthesis of CNTs are: silica, alumina and other metal oxides.[231]

Since silica and alumina have been used as supports for Fe, Co and Ni in the synthesis of CNTs, it seems fitting that CFA (composed mostly of SiO_2 and Al_2O_3 and modest amounts of iron) be trialed as both a catalyst and catalyst support in such reactions. Indeed there are a few studies where CFA has been used as a catalyst for the decomposition of various hydrocarbons in the production of shaped carbon nanomaterials (SCNMs). For example, Oscar *et al*. have used a fixed bed catalytic

CVD method to demonstrate that CNTs could be synthesized on CFA that was impregnated with Fe.[7], On the other hand, Nath and Sahajwalla have shown that when polyvinyl alcohol was pyrolyzed at 500 °C over CFA it yielded a range of SCNMs that included: ropes, branches, whiskers, and graphene sheets.[232] In research performed by our own group CNFs have been synthesized by the CVD of acetylene over waste CFA in a reducing gas atmosphere.[233] Similarly a study of the effect of carbon dioxide on the morphology of CNFs synthesized has also been conducted under similar conditions.[234] These exciting results have shown that there is a cheap and effective way of reproducibly synthesizing useful SCNMs from waste CFA. Nevertheless, the usefulness of such SCNMs is limited by their apparent inertness and inability to dissolve in most solvents.[223,235] This has necessitated that they are modified to render them more useful for further applications. This is the subject that will now be discussed.

2.4.2 Nitrogen-doped carbon nanomaterials

As it was alluded to earlier, the surface characteristics of pristine CNTs typically render them inert for chemical applications. For this reason surface modifications of these CNTs have been required. One way of achieving this has been through functionalization by treating pristine CNTs with strong mineral acids, which has also helped control their properties.[2,83,223,236] However, a much more controlled way of modifying CNTs has been through the systematic introduction of heteroatoms (e.g. N, B, P, and S) into their crystalline structure.[235,237–241]

It has been found that the integration of nitrogen into the carbon network did not necessarily have to be substitutional in order to effect changes in the properties of CNTs.[223,242,243] For instance, since nitrogen contains an extra electron by comparison with

carbon, its incorporation into the carbon network could result in an n-type semiconducting material.[223,235] Alternatively, its inclusion into these networks could generate defects due to its atomic size (see arrow 1 in **Figure 2.10**) or even the rearrangement of surface carbon atoms if situated on the walls of CNTs (see arrow 2 in **Figure 2.10**).[235,244–246] As the electronic properties of such materials depend solely on the new geometries produced, including a diverse variety of wall morphologies, here even p-type materials could form.[235]

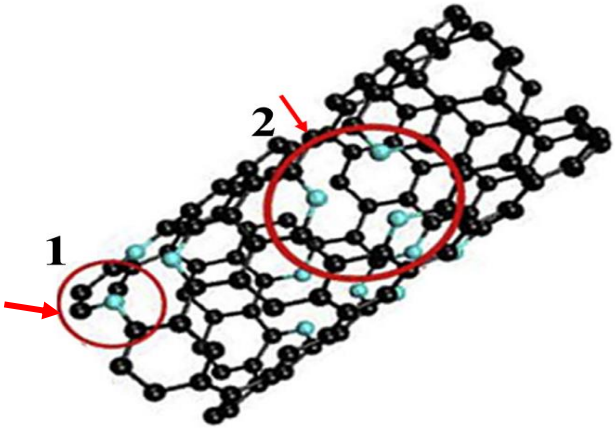

Figure 2.10. Model of CNTs showing nitrogen incorporated on (1) the wall and (2) direct substitution.[202]

The incorporation of nitrogen atoms into a graphitic carbon lattice has been found to occur predominantly in three bonding configurations, namely: 1) Pyridinic, 2) Pyrrolic, and 3) Quaternary (**Figure 2.11**).[244,245,247–249]

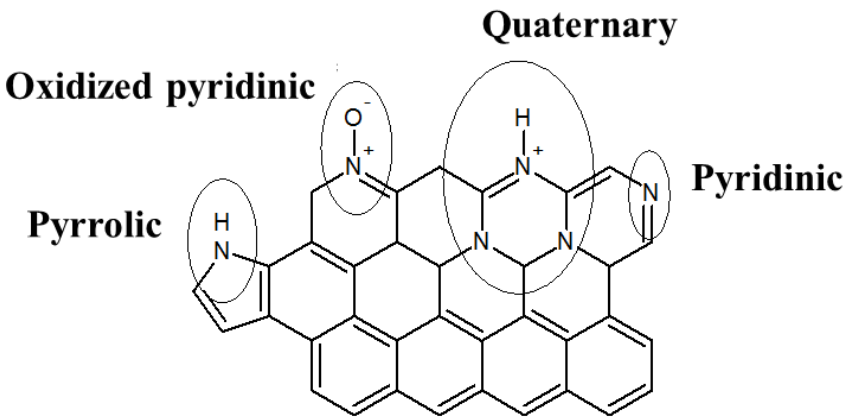

Figure 2.11. Bonding configurations for nitrogen atoms when doped into a graphitic carbon lattice.[235]

Pyridinic nitrogen atoms bond at the ends of two carbon atoms and thus cause defects in the graphene structure as well as the donation of p-orbital electrons to the π-system (**Figure 2.11**).[249] On the other hand pyrrolic nitrogen atoms donate two p-orbital electrons to the π-system and form pentagons, along with four other carbon atoms (**Figure 2.11**).[249] Finally quaternary nitrogen atoms are those that replace carbon atoms in the six-membered ring (**Figure 2.11**).[249] Also of note is that the hybridization state of nitrogen atoms in graphitic materials has been found to differ i.e. sp^3 for pyrrolic nitrogen and sp^2 for pyridinic and quaternary nitrogen.[245] A variant of the pyridinic nitrogen has also been observed i.e. oxidized pyridinic nitrogen (**Figure 2.11**), where the nitrogen atom was found to carry a positive charge as it was bonded to two carbon atoms and one oxygen atom.[223,245]

With regard to the properties of these CNTs, Ghosh *et al*., have shown that when nitrogen atoms were incorporated into such graphitic networks in the quaternary configuration, this introduced extra sub-levels in the unoccupied states near the Fermi level.[250] Conversely they showed that pyridinic nitrogen atom substituents

were detrimental to the existing sub-levels.[250] These results have suggested that the electrical properties of CNTs could be adapted through the systematic integration and regulation of the concentration of diverse types of nitrogen. Likewise, it has been found that the spin density and charge distribution of carbon atoms in a graphitic structure could be predisposed by the presence of nitrogen dopants, which were found to activate the surface of the material and thus make it more reactive.[251,252] Indeed this sort of modification has been known to enhance the catalytic performance of N-doped graphene as well as N-doped CNTs (NCNTs) in various reactions, e.g. the oxygen reduction reaction (ORR).[244,253] Similarly, Van Dommele *et al*. have reported superior catalytic activities for the Knoeve-Nagel condensation reaction for NCNTs which had greater concentrations of pyridinic nitrogen.[251]

2.4.3 Enhancing the photocatalytic efficiency of TiO_2 with SCNMs

SCNMs have received a considerable amount of interest in catalysis, especially in heterogeneous photocatalysis.[98,220,222,254–256] Indeed, CNTs have shown potential to aid in all three of the ways in which the photocatalytic activity of TiO_2 can be improved including through their: i) High surface area and good quality active sites, ii) Hindrance of electron-hole pair recombination and iii) Shift in the absorption of the photocatalyst to the visible part of the spectrum (by either modifying the band-gap and/or through sensitization).[219,254–257] Consequently, this has resulted in thousands of research outputs in the field over the past decade or so, with most scientists reporting attempts to develop composites or mixtures of TiO_2 and SCNMs with superior photocatalytic activities.[98,222,258] SCNMs have been extensively reported to have synergistically improved the photocatalytic quantum efficiency of TiO_2, through the hindrance of electron-hole pair

recombination.[254,256,259] This is believed to have occurred in a manner similar to that when TiO_2 was coupled with metals for the same purpose.[98] The reason for this is that CNTs have been shown to have electronic properties which were: metallic, semiconducting or insulating.[223,235,244,245,260] Hence when CNTs have been coupled with TiO_2 in an above-mentioned manner, then Schottky barriers with space charge regions at their boundaries formed.[98] Although TiO_2 is an n-type semiconductor, when it has been coupled to CNTs with lower Fermi levels, then the photo-induced electrons were able to easily move in the direction of these tubes.[98] Here the CNTs were believed to have acted as electron sinks/scavengers due to their high electrical conductivities and great electron storage capacities (**Figure 2.12**).[214,219,98,221] Consequently this was believed to have left an excess of positively charged holes in the valence band of TiO_2 that then migrated to its surface and partook in REDOX reactions with the adsorbed species.[98] In this way, the n-type TiO_2 semiconductor is thought to have essentially behaved as a p-type semiconductor.[98]

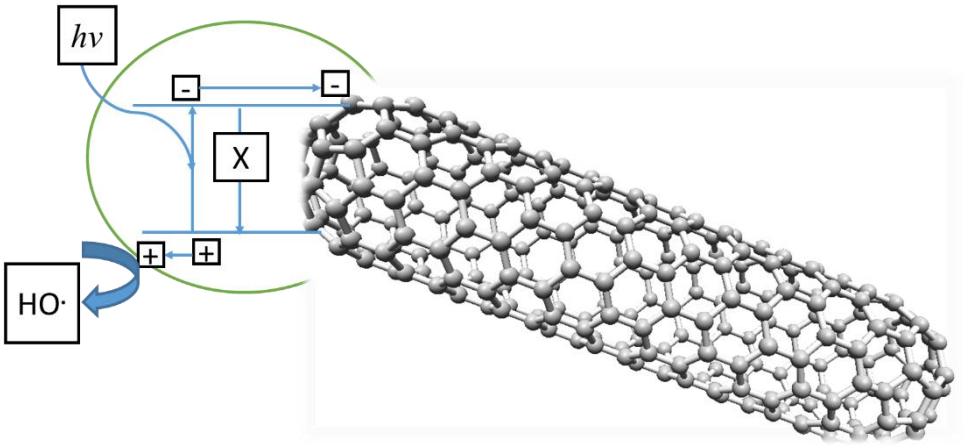

Figure 2.12. A representation of a TiO_2-CNT couple where the CNT inhibits electron-hole recombination by acting as a sink that scavenges electrons.[254,259,261]

Conversely, Wang and co-workers have proposed an alternative mechanism, where they have suggested that CNTs improved the photocatalytic efficiency of TiO_2, pushing its absorption into the visible part of the spectrum, by acting as photosensitizers (**Figure 2.13**).[262]

In this proposed mechanism, it has been suggested that the photo-induced electrons in the CNTs were transferred into the conduction band of the TiO_2, which allowed the adsorbed oxygen molecules on their surfaces to be reduced to superoxide radicals.[262] In this way it was suggested that the "cationic" CNTs then extracted electrons from the valence band of the TiO_2, leaving positively charged holes, which resulted in the formation of hydroxyl radicals.[259,262]

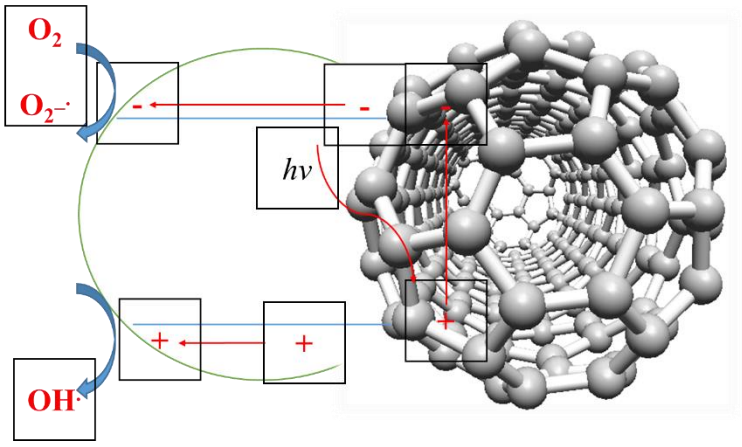

Figure 2.13. A representation of the photosensitization mechanism suggested by Wang *et al.*[262]

The two mechanisms outlined in **Figure 2.12** and **Figure 2.13** have been extensively cited, despite their contradictory views as to whether a physical mixture or an intimate chemical contact was required to affect the desired outcomes.[98] An alternative mechanism to the above-mentioned ones has been proposed in which it

has been suggested that the heightened photocatalytic activity for CNT–TiO_2 composites (indicated in **Figure 2.14**) may have been due to two separate effects: i) The formation of Ti-O-C bonds and ii) Increased numbers of mid-band-gap states.[259]

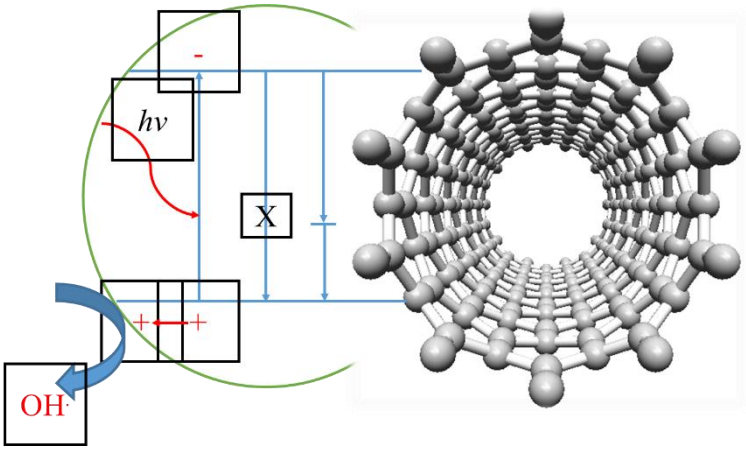

Figure 2.14. A representation of CNTs acting as impurities through the presence of the Ti-O-C bond.[259]

It has been proposed that the first effect i.e. the formation of Ti-O-C bonds was akin to the formation of TiO_2 doped with carbon, which has been known to result in a red-shift in the absorption of the resultant composite, making it possible to excite them with visible light.[263] Furthermore it was speculated that the second effect may have resulted from increased numbers of mid-band-gap states in CNTs, which arose due to defects in the formation of the CNT-TiO_2 composite.[259] Although it is believed that both of these effects gave rise to the higher photocatalytic activity, it has been proposed that the electronic-band structure of the CNTs played a more significant role.[259] However, the authors of this alternative mechanism have also

shown that the CNTs in such CNT-TiO_2 composites were able to be oxidized during photocatalysis.[259] Hence it has also been suggested that the oxidation of these CNTs may have generated even more mid-band-gap states due to these defects and thus may have further improved the photo-generation of electron-hole pairs.[259]

2.5 References

1. Kuvarega, A. T. Photocatalytic performance of nitrogen-platinum group metal co-doped TiO_2 supported on carbon nanotubes for visible-light degradation of organic pollutants in water. (University of Johannesburg, 2012).
2. Dlamini, N. L. Doped nanotitanium dioxide for photocatalytic applications. (University of Johannesburg, 2012).
3. Pan africa chemistry network. Africa's Water Quality- A Chemical Science perspective. *Royal Society of Chemistry* (2010).
4. Crump, J. A. & Mintz, E. D. Global trends in typhoid and paratyphoid fever. *Chinese J. Infect. Chemother.* **11,** 241-246 (2011).
5. Braune, E. & Xu, Y. The role of ground water in sub-Saharan Africa. *Ground Water* **48,** 229–238 (2010).
6. Nkem, J. N., Munang, R. & Jallow, B. Decentralizing Solutions For Rural Water Supply Under Climate Impacts In Sub-Saharan Africa. *Environ. Sci. Policy Sustain. Dev.* **53,** 14–17 (2011).
7. Barker, R., Van Koppen, B. & Shah, T. *A global perspective on water scarcity and poverty: Achievements and challenges for water resources management*. International Water Management Institute (2000).

8. Rockström, J. & Barron, J. Water productivity in rainfed systems: Overview of challenges and analysis of opportunities in water scarcity prone savannahs. *Irrig. Sci.* **25,** 299–311 (2007).

9. Prüss, A., Kay, D., Fewtrell, L. & Bartram, J. Estimating the burden of desease from water, sanitation and hygiene at a global level. *Environ. Health Perspect.* **110,** 537–542 (2002).

10. Calderon, R. L. The epidemiology of chemical contaminants of drinking water. *Food Chem. Toxicol.* **38,** 13–20 (2000).

11. Pye, V. I. & Patrick, R. Ground water contamination in the United States. *Science* **221,** 713–718 (1983).

12. Bove, F. J., Fulcomer, M. C., Klotz, J. B., Esmart, J., Dufficy, E. M. & Savrin, J. E. Public Drinking Water Contamination and Birth Outcomes. *Am. J. Epidemiol.* **141,** 850–862 (1995).

13. Kilvington, S., Gray, T., Dart, J.,Morlet, N., Beeching, J. R., Frazer, D. G. & Matheson, M. Acanthamoeba Keratitis: The Role of Domestic Tap Water Contamination in the United Kingdom. *Investig. Ophthalmol. Vis. Sci.* **45,** 165–169 (2004).

14. Wright, J., Gundry, S. & Conroy, R. Household drinking water in developing countries: A systematic review of microbiological contamination between source and point-of-use. *Trop. Med. Int. Heal.* **9,** 106–117 (2004).

15. Rozemeijer, J. C. & Broers, H. P. The groundwater contribution to surface water contamination in a region with intensive agricultural land use (Noord-Brabant, The Netherlands). *Environ. Pollut.* **148,** 695–706 (2007).

16. Ross, G. The public health implications of polychlorinated biphenyls (PCBs) in the environment. *Ecotoxicol. Environ. Saf.* **59,** 275–291 (2004).

17. Ohe, T., Watanabe, T. & Wakabayashi, K. Mutagens in surface waters: A review. *Mutat. Res. Rev. Mutat. Res.* **567,** 109–149 (2004).

18. Daughton, C. G. Non-regulated water contaminants: emerging research. *Environ. Impact Assess. Rev.* **24,** 711–732 (2004).

19. Richardson, S. Disinfection by-products and other emerging contaminants in drinking water. *TrAC Trends Anal. Chem.* **22,** 666–684 (2003).

20. Savelski, M. J. & Bagajewicz, M. J. On the optimality conditions of water utilization systems in process plants with single contaminants. *Chem. Eng. Sci.* **55,** 5035–5048 (2000).

21. Grant, W. F., Lee, H. G., Logan, D. M. & Salamone, M. F. The use of Tradescantia and Vicia faba bioassays for the in situ detection of mutagens in an aquatic environment. *Mutat. Res. Mol. Mech. Mutagen.* **270,** 53–64 (1992).

22. Meier, J. R., Knohl, R. B., ,Coleman, W.E., Ringhand, H. P., Munch, J. W., William H., Kaylor Robert P. & Streicher Frederick C., Kopfler. Studies on the potent bacterial mutagen, 3-chloro-4-(dichloromethyl)-5-hydroxy-2(5H)-furanone: aqueous stability, XAD recovery and analytical determination in drinking water and in chlorinated humic acid solutions. *Mutat. Res.* **189,** 363–373 (1987).

23. Carneiro, P. A., Umbuzeiro, G. A., Oliveira, D. P. & Zanoni, M. V. B. Assessment of water contamination caused by a mutagenic textile effluent/dyehouse effluent bearing disperse dyes. *J. Hazard. Mater.* **174,** 694–699 (2010).

24. Matsumoto, S., Mantovani, T., Malaguttii, M. I. A., Dias, A. L., Fonseca, I. C. & Marin-Morales, A. M. Genotoxicity and mutagenicity of water contaminated with tannery effluents as evaluated by the micronucleus test and comet assay using the fish Oreochromis niloticus and chromosome aberrations in onion root-tips. *Genet. Mol. Biol.* **29,** 148–158 (2006).

25. Krupadam, R. J., Khan, M. S. & Wate, S. R. Removal of probable human carcinogenic polycyclic aromatic hydrocarbons from contaminated water using molecularly imprinted polymer. *Water Res.* **44,** 681–688 (2010).

26. Ashbolt, N. J. Risk analysis of drinking water microbial contamination versus disinfection by-products (DBPs). *Toxicology* **198,** 255–262 (2004).

27. Theiss, J. C., Stoner, G. D., Shimkin, M. B. & Weisburger, E. K. Test for carcinogenicity of organic contaminants of United States drinking waters by pulmonary tumor response in strain A mice. *Cancer Res.* **37,** 2717–20 (1977).

28. Richardson, S., Plewa, M., Wagner, E., Schoeny, R. & Demarini, D. Occurrence, genotoxicity, and carcinogenicity of regulated and emerging disinfection by-products in drinking water: A review and roadmap for research. *Mutat. Res. Mutat. Res.* **636,** 178–242 (2007).

29. Wilkins, J. R., Reiches, N. A. & Kruse, C. W. Organic chemical contaminants in drinking water and cancer. *Am. J. Epidemiol.* **110,** 420–448 (1979).

30. Klavarioti, M., Mantzavinos, D. & Kassinos, D. Removal of residual pharmaceuticals from aqueous systems by advanced oxidation processes. *Environ. Int.* **35,** 402–417 (2009).

31. Nakada, N., Shinohara, H., Murata, A., Kentaro, K., Managaki, S., Nobuyuki, S. & Hideshige, T. Removal of selected pharmaceuticals and personal care products (PPCPs) and endocrine-disrupting chemicals (EDCs) during sand filtration and ozonation at a municipal sewage treatment plant. *Water Res.* **41,** 4373–4382 (2007).

32. Belgiorno, V., Rizzo, L., Fatta, D., Rocca, D. C., Giusy, L., Nikolaou, A., Naddeo, V. & Meric, S. Review on endocrine disrupting-emerging compounds in urban wastewater: occurrence and removal by photocatalysis and ultrasonic irradiation for wastewater reuse. *Desalination* **215,** 166–176 (2007).

33. Rogers, J. A., Metz, L. & Yong, V. W. Review: Endocrine disrupting chemicals and immune responses: A focus on bisphenol-A and its potential mechanisms. *Mol. Immunol.* **53,** 421–430 (2013).

34. Esplugas, S., Bila, D. M., Krause, L. G. T. & Dezotti, M. Ozonation and advanced oxidation technologies to remove endocrine disrupting chemicals (EDCs) and pharmaceuticals and personal care products (PPCPs) in water effluents. *J. Hazard. Mater.* **149,** 631–642 (2007).

35. Kim, S. D., Cho, J., Kim, I. S., Vanderford, B. J. & Snyder, S. A. Occurrence and removal of pharmaceuticals and endocrine disruptors in South Korean surface, drinking, and waste waters. *Water Res.* **41,** 1013–1021 (2007).

36. Petrovic, M., Solé, M., López de Alda, M. J. & Barceló, D. Endocrine disruptors in sewage treatment plants, receiving river waters, and sediments: integration of chemical analysis and biological effects on feral carp. *Environ. Toxicol. Chem.* **21,** 2146–2156 (2002).

37. Schug, T. T., Janesick, A., Blumberg, B. & Heindel, J. J. Endocrine disrupting chemicals and disease susceptibility. *J. Steroid Biochem. Mol. Biol.* **127,** 204–215 (2011).

38. Guillette, J. L. J., Crain, D. A, Rooney, A. A & Pickford, D. B. Organization verses activation: The role of endocrine disrupting contaminants (EDCs) during embryonic development in wildlife. *Environ. Health Perspect.* **103,** 1164–1457 (1995).

39. Cevasco, A., Urbatzka, R., Bottero, S., Massari, A., Pedemonte, F., Kloas, W. & Mandich, A. Endocrine disrupting chemicals (EDC) with (anti)estrogenic and (anti)androgenic modes of action affecting reproductive biology of Xenopus laevis: II. Effects on gonad histomorphology. *Comp. Biochem. Physiol. Part C Toxicol. Pharmacol.* **147,** 241–251 (2008).

40. Olujimi, O. O., Fatoki, O. S., Odendaal, J. P. & Okonkwo, J.O., S. Endocrine disrupting chemicals (phenol and phthalates) in the South African environment : a need for more monitoring. *Water Sa*. **36,** 671–682 (2010).

41. Muncke, J. Endocrine disrupting chemicals and other substances of concern in food contact materials: An updated review of exposure, effect and risk assessment. *J. Steroid Biochem. Mol. Biol.* **127,** 118–127 (2011).

42. Mezcua, M., Martínez-Uroz, M. A., Gómez-Ramos, M. M., Gómez, M. J., Navas, J. M. & Fernández-Alba, A.R. Analysis of synthetic endocrine-disrupting chemicals in food: A review. *Talanta* **100,** 90–106 (2012).

43. Kamikawa, Y. Kato, T., Onouchi, H., Kashiwagi, D., Maeda, K. & Yashima, E. Helicity induction on a poly(phenylacetylene) bearing a phosphonate residue by chiral dendrons. *J. Polym. Sci. Part A Polym. Chem.* **42,** 4580–4586 (2004).

44. Schug, T. T., Janesick, A., Blumberg, B. & Heindel, J. J. Endocrine disrupting chemicals and disease susceptibility. *J. Steroid Biochem. Mol. Biol.* **127,** 204–15 (2011).

45. Wang, L. S., Wang, L., Wang, L., Wang, G., Li, Z. H. & Wang, J. J. Effect of 1-butyl-3-methylimidazolium tetrafluoroborate on the wheat (Triticum aestivum L.) seedlings. *Environ. Toxicol.* **24,** 296–303 (2009).

46. Schug, T. T., Janesick, A., Blumberg, B. & Heindel, J. J. Journal of Steroid Biochemistry and Molecular Biology Endocrine disrupting chemicals and disease susceptibility. *J. Steroid Biochem. Mol. Biol.* **127,** 204–215 (2011).

47. Gore, A. C., Walker, D. M., Zama, A. M., Armenti, A. E. & Uzumcu, M. Early life exposure to endocrine-disrupting chemicals causes lifelong molecular reprogramming of the hypothalamus and premature reproductive aging. *Mol. Endocrinol.* **25,** 2157–68 (2011).

48. Adewale, H. B., Todd, K. L., Mickens, J. A. & Patisaul, H. B. The impact of neonatal bisphenol-A exposure on sexually dimorphic hypothalamic nuclei in the female rat. *Neurotoxicology* **32,** 38–49 (2011).

49. Vreugdenhil, H. J. I., Lanting, C. I., Mulder, P. G. H., Boersma, E. R. & Weisglas-Kuperus, N. Effects of prenatal PCB and dioxin background exposure on cognitive and motor abilities in Dutch children at school age. *J. Pediatr.* **140,** 48–56 (2002).

50. Cederroth, C. R., Zimmermann, C. & Nef, S. Soy, phytoestrogens and their impact on reproductive health. *Mol. Cell. Endocrinol.* **355,** 192–200 (2012).

51. Sweeney, T. Is exposure to endocrine disrupting compounds during fetal/post-natal development affecting the reproductive potential of farm animals? *Domest. Anim. Endocrinol.* **23,** 203–209 (2002).

52. Mendiratta, A. K. Method for making bisphenol. 303 (1986).

53. He, Y., Miao, M., Herrinton, L. J., Wu, C., Yuan, W., Zhou, Z. & Li, D. Bisphenol A levels in blood and urine in a Chinese population and the personal factors affecting the levels. *Environ. Res.* **109,** 629–33 (2009).

54. Vandenberg, L. N. Colborn, T., Hayes, T. B., Heindel, J. J., Jacobs, D. R., Lee, D. H., Shioda, T., Soto, A. M., vom Saal, F. S., Welshons, W. V., Zoeller, R. T. & Myers, J. P. Hormones and endocrine-disrupting chemicals: Low-dose effects and nonmonotonic dose responses. *Endocr. Rev.* **33,** 378–455 (2012).

55. Howdeshell, K. Peterman, P. H., Judy, B. M., Taylor, J. A., Orazio, C. E., Ruhlen, R. L., vom Saal, F. S. & Welshons, W. V. Bisphenol A is released from used polycarbonate animal cages into water at room temperature. *Environ. Health Perspect.* **111,** 1180–1187 (2003).

56. Carwile, J. L. Luu, H. T., Bassett, L. S., Driscoll, D. A., Yuan, C., Chang, J. Y., Ye, X., Calafat, A. M. & Michels, K. B. Polycarbonate Bottle Use and Urinary

Bisphenol A Concentrations. *Environ. Health Perspect.* **117,** 1368–1372 (2009).

57. Staples, C. A., Dom, P. B., Klecka, G. M., Sandra, T. O. & Harris, L. R. A review of the environmental fate, effects and exposures of bisphenol-A. *Chemosphere* **36,** 2149–2173 (1998).

58. Kang, J., Kondo, F. & Katayama, Y. Human exposure to bisphenol A. *Toxicology* **226,** 79–89 (2006).

59. Mezohegyi, G., Erjavec, B., Kaplan, R. & Pintar, A. Removal of bisphenol A and its oxidation products from aqueous solutions by sequential catalytic wet air oxidation and biodegradation. *Ind. Eng. Chem. Res.* **52,** 9301–9307 (2013).

60. Gould, J. C., Leonard, L. S., Maness, S. C., Wagner, B. L., Conner, K., Zacharewski, T., Safe, S., McDonnell, D. P. & Gaido, K. W. Bisphenol A interacts with the estrogen receptor α in a distinct manner from estradiol. *Mol. Cell. Endocrinol.* **142,** 203–214 (1998).

61. Sidhu, S., Gullett, B., Striebich, R., Klosterman, J., Contreras, J. & DeVito, Michael Endocrine disrupting chemical emissions from combustion sources: Diesel particulate emissions and domestic waste open burn emissions. *Atmos. Environ.* **39,** 801–811 (2005).

62. Niederberger, C. Re: Urine bisphenol-A (BPA) level in relation to semen quality. *J. Urol.* **186,** 1415 (2011).

63. Fromme, H., Thomas, K. & Wenzel, A. Occurrence of phthalates and bisphenol A and F in the environment. *Water Res.* **36,** 1429–1438 (2002).

64. Yamamoto, T., Yasuhara, A., Shiraishi, H. & Nakasugi, O. Bisphenol A in hazardous waste landfill leachates. *Chemosphere* **42,** 415–418 (2001).

65. Oehlmann, J., Oetken, M. & Schulte-Oehlmann, U. A critical evaluation of the environmental risk assessment for plasticizers in the freshwater environment in

Europe, with special emphasis on bisphenol A and endocrine disruption. *Environ. Res.* **108,** 140–149 (2008).

66. Staples, C. A, Dom, P. B., Klecka, G. M., Sandra, T. O. & Harris, L. R. A review of the environmental fate, effects, and exposures of Bisphenol A. *Chemosphere* **36,** 2149–2173 (1998).

67. Ying, G. G., Kookana, R. S. & Dillon, P. Sorption and degradation of selected five endocrine disrupting chemicals in aquifer material. *Water Res.* **37,** 3785–3791 (2003).

68. Kang, J.-H., Kondo, F. & Katayama, Y. Human exposure to bisphenol A. *Toxicology* **226,** 79–89 (2006).

69. Nadal, A., Alonso-Magdalena, P., Soriano, S., Quesada, I. & Ropero, A. B. The pancreatic beta-cell as a target of estrogens and xenoestrogens: Implications for blood glucose homeostasis and diabetes. *Mol. Cell. Endocrinol.* **304,** 63–8 (2009).

70. Alonso-Magdalena, P., Morimoto, S., Ripoll, C., Fuentes, E. & Nadal, A. The estrogenic effect of bisphenol a disrupts pancreatic ß-cell function in vivo and induces insulin resistance. *Environ. Health Perspect.* **114,** 106–112 (2006).

71. Alonso-Magdalena, P., Quesada, I. & Nadal, A. Endocrine disruptors in the etiology of type 2 diabetes mellitus. *Nat. Rev. Endocrinol.* **7,** 346–353 (2011).

72. Rubin, B. S. Bisphenol A: An endocrine disruptor with widespread exposure and multiple effects. *J. Steroid Biochem. Mol. Biol.* **127,** 27–34 (2011).

73. Rubin, B. S. & Soto, A. M. Bisphenol A: Perinatal exposure and body weight. *Mol. Cell. Endocrinol.* **304,** 55–62 (2009).

74. Boas, M., Feldt-Rasmussen, U. & Main, K. M. Thyroid effects of endocrine disrupting chemicals. *Mol. Cell. Endocrinol.* **355,** 240–248 (2012).

75. Paulose, T., Speroni, L., Sonnenschein, C. & Soto, A. M. Estrogens in the wrong

place at the wrong time: Fetal BPA exposure and mammary cancer. *Reprod. Toxicol.* **54**, 27–29 (2014).

76. Maffini, M. V., Rubin, B. S., Sonnenschein, C. & Soto, A. M. Endocrine disruptors and reproductive health: The case of bisphenol-A. *Mol. Cell. Endocrinol.* **254–255,** 179–186 (2006).

77. Murray, T. J., Maffini, M. V, Ucci, A. A., Sonnenschein, C. & Soto, A. M. Induction of mammary gland ductal hyperplasias and carcinoma in situ following fetal bisphenol A exposure. *Reprod. Toxicol.* **23,** 383–90 (2007).

78. Markey, C. M. Long-Term Effects of Fetal Exposure to Low Doses of the Xenoestrogen Bisphenol-A in the Female Mouse Genital Tract. *Biol. Reprod.* **72,** 1344–1351 (2005).

79. Fujishima, A. & Honda, K. Photolysis-decomposition of water at the surface of an irradiated semiconductor. *Nature* **238,** 37–38 (1972).

80. Chen, X. & Mao, S. S. Titanium Dioxide Nanomaterials: Synthesis, Properties, Modifications, and Applications. *Chem. Rev.* **107,** 2891–2959 (2007).

81. Franklyn, P. J. Hydrothermal synthesis and characterisation of titania nanoparticles. (University of the Witwatersrand, 2004).

82. Franklyn, P. Synthesis, Characterization and Structureal Investigations of Nanoparticulate forms of selected (W,Ti,Al,Ba) Mixed Metal Oxides. (University of Cambridge, 2011).

83. Kuvarega, A. T., Krause, R. W. M. & Mamba, B. B. Comparison between Base Metals and Platinum Group Metals in Nitrogen , M Codoped TiO_2 (M = Fe , Cu , Pd , Os) for Photocatalytic Removal of an Organic Dye in Water. *Journal of Nanomaterials*. **2014,** 1-12 (2014).

84. Wang, G., Wang, Q., Lu, W. & Li, J. Photoelectrochemical study on charge transfer

properties of TiO_2-B nanowires with an application as humidity sensors. *J Phys Chem B* **110,** 22029–22034 (2006).

85. Pechini, M. P. Method of preparing lead and alkaline earth titanates and niobates and coating method using the same to form a capacitor. (1967).

86. Franklyn, P. J. & Narrandes, A. Unlocking the Secrets Behind the Resin-Gel Synthesis for the Controlled Formation of Anatase and Rutile. *Proc. Int. Conf. Nanomater. Appl. Prop.* **1,** 1–17 (2012).

87. Riordan, M. & Hoddeson, L. The origins of the pn junction." *IEEE* Spectrum **34,** 46–51 (1997).

88. Sturm, J., Leifhelm, M., Schatzmayr, H., GroisB, S. & Zimmermann, H. Optical receiver IC for CD/DVD/blue-laser application. *IEEE J. Solid state circuits* **40,** 215–218 (2005).

89. Cameron, M. & Bhatia, R. Montecito: A Dual-Core, Dual-Thread Itanium Processor. *IEEE Micro* **25,** 10–20 (2005).

90. Chen, X. & Mao, S. S. Titanium Dioxide Nanomaterials : Synthesis, Properties, Modifications and Applications. *Chem. Rev.* **1,** 2891–2959 (2007).

91. Hoffmann, M. R., Martin, S. T., Choi, W. & Bahnemannt, D. W. Environmental Applications of Semiconductor Photocatalysis. *Chem. Rev.* **95,** 69–96 (1995).

92. Fujishima, A., Rao, T. N. & Tryk, D. A. Titanium dioxide photocatalysis. *J. Photochem. Photobiol. C Photochem. Rev.* **1,** 1–21 (2000).

93. Pozzo, R. L., Giombi, J. L., Baltanás, M. a & Cassano, A. E. The performance in a fluidized bed reactor of photocatalysts immobilized onto inert supports. *Catal. Today* **62,** 175–187 (2000).

94. Wold, A. Photocatalytic properties of titanium dioxide (TiO_2). *Chem. Mater.* **5,** 280–283 (1993).

95. Linsebigler, Amy L., Guangquan, L. & Yates, J. J. T. Photocatalysis on TiO_2 surfaces: principles, mechanisms, and selected results. *Chem. Rev.* **95,** 735–758 (1995).

96. Hurum, D. C., Agrios, A. G., Gray, K. A., Rajh, T. & Thurnauer, M. C. Explaining the enhanced photocatalytic activity of Degussa P25 mixed-phase TiO_2 using EPR. *J. Phys. Chem. B* **15,** 4545–4549 (2003).

97. Shan, A. Y., Ghazi, T. I. M. & Rashid, S. A. Immobilisation of titanium dioxide onto supporting materials in heterogeneous photocatalysis: A review. *Appl. Catal. A Gen.* **389,** 1–8 (2010).

98. Dahl, M., Liu, Y. & Yin, Y. Composite titanium dioxide nanomaterials. *Chemical Reviews* **114,** 9853–9889 (2014).

99. Ohko, Y. & Fujishima, A. Kinetic Analysis of the Photocatalytic Degradation of Gas-Phase 2-Propanol under Mass Transport-Limited Conditions with a TiO_2 Film Photocatalyst. *J. Phys. Chem. B* **102,** 1724–1729 (1998).

100. Leary, R. & Westwood, A. Carbonaceous nanomaterials for the enhancement of TiO_2 photocatalysis. *Carbon* **49,** 741–772 (2010).

101. Zheng, Z., Huang, B., Lu, J., Wang, Z., Qin, X., Zhang, X., Dai, Y. & Whangbo, M. H. Hydrogenated titania: synergy of surface modification and morphology improvement for enhanced photocatalytic activity. *Chem. Commun.* **48,** 5733-5735 (2012).

102. Testino, A., Bellobono, I. R., Buscaglia, V., Canevali, C., Arienzo, M. D., Polizzi, Stefano., Scotti, R. & Franca, M. Optimizing the Photocatalytic Properties of Hydrothermal TiO_2 by the Control of Phase Composition and Particle Morphology. A Systematic Approach. *JACS*. **129**, 3564–3575 (2007).

103. Shan, A. Y., Ghazi, T. I. M. & Rashid, S. A. Immobilisation of titanium dioxide

onto supporting materials in heterogeneous photocatalysis: A review. *Appl. Catal. A Gen.* **389,** 1–8 (2010).

104. Liu, J., Li, J., Sedhain, A., Lin, J. & Jiang, H. Structure and Photoluminescence Study of TiO_2 Nanoneedle Texture along Vertically Aligned Carbon Nanofiber Arrays. *J. Phys. Chem. C* **112,** 17127–17132 (2008).

105. Wang, Y. Q., Hu, G. Q., Duan, X. F., Sun, H. L. & Xue, Q. K. Microstructure and formation mechanism of titanium dioxide nanotubes. *Chem. Phys. Lett.* **365,** 427–431 (2002).

106. Chen, D., Jiang, Z., Geng, J., Wang, Q. & Yang, D. Carbon and Nitrogen Co-doped TiO_2 with Enhanced Visible-Light Photocatalytic Activity. *Ind. Eng. Chem. Res.* **46,** 2741–2746 (2007).

107. Tang, X., Li, D. & Tg, A. Sulfur-Doped Highly Ordered TiO_2 Nanotubular Arrays with Visible Light Response. *J. Phys. Chem. C* **112,** 5405–5409 (2008).

108. Sun, H., Bai, Y., Cheng, Y., Jin, W. & Xu, N. Preparation and Characterization of Visible-Light-Driven Carbon−Sulfur-Codoped TiO_2 Photocatalysts. *Ind. Eng. Chem. Res.* **45,** 4971–4976 (2006).

109. Czoska, A. M. Livraghi, S., Chiesa, M., Giamello, E., Agnoli, S., Granozzi, G., Finazzi, E., Di Valentiny, C. & Pacchioni, G. The nature of defects in fluorine-doped TiO_2. *J. Phys. Chem. C* **112,** 8951–8956 (2008).

110. Li, D., Haneda, H., Hishita, S. & Ohashi, N. Visible-Light-Driven N-F-Codoped TiO_2 Photocatalysts. 2. Optical Characterization, Photocatalysis, and Potential Application to Air Purification. *Chem. Mater.* **17,** 2596–2602 (2005).

111. Li, D., Haneda, H., Hishita, S. & Ohashi, N. Visible-Light-Driven N - F - Codoped TiO_2 Photocatalysts . 1 . Synthesis by Spray Pyrolysis and Surface Characterization. *Chem. Mater.* **17,** 2588–2595 (2005).

112. Li, Y., Peng, S., Jiang, F., Lu, G. & Li, S. Effect of doping TiO_2 with alkaline-earth metal ions on its photocatalytic activity. *J. Serbian Chem. Soc.* **72,** 393–402 (2007).

113. Klosek, S. & Raftery, D. Visible light driven V-doped TiO_2 photocatalyst and its photooxidation of ethanol. *J. Phys. Chem. B* **105,** 2815–2819 (2002).

114. Link, S. & El-sayed, M. A. Spectral Properties and Relaxation Dynamics of Surface Plasmon Electronic Oscillations in Gold and Silver Nanodots and Nanorods. *J. Phys. Chem. B* **103,** 8410–8426 (1999).

115. Zhou, X., Liu, G., Yu, J. & Fan, W. Surface plasmon resonance-mediated photocatalysis by noble metal-based composites under visible light. *J. Mater. Chem.* **22,** 21337 (2012).

116. Hirakawa, T. Charge separation and catalytic activity of Ag/ TiO_2 core-shell composite clusters under UV-irradiation. *J. Am. Chem. Soc.* **127,** 3928–3934 (2005).

117. Silva, C. G., Juárez, R., Marino, T., Molinari, R. & García, H. Influence of excitation wavelength (UV or visible light) on the photocatalytic activity of titania containing gold nanoparticles for the generation of hydrogen or oxygen from water. *J. Am. Chem. Soc.* **133,** 595–602 (2011).

118. Iliev, V., Tomova, D., Bilyarska, L., Eliyas, A. & Petrov, L. Photocatalytic properties of TiO_2 modified with platinum and silver nanoparticles in the degradation of oxalic acid in aqueous solution. *Appl. Catal. B Environ.* **63,** 266–271 (2006).

119. Ma, Y., Zhang, J., Tian, B., Chen, F. & Wang, L. Synthesis and characterization of thermally stable Sm,N co-doped TiO_2 with highly visible light activity. *J. Hazard. Mater.* **182,** 386–393 (2010).

120. El-Bahy, Z. M., Ismail, A. A. & Mohamed, R. M. Enhancement of titania by doping rare earth for photodegradation of organic dye (Direct Blue). *J. Hazard. Mater.* **166,**

138–143 (2009).

121. Li, F., Li, X., & Hou, M. Photocatalytic degradation of 2-mercaptobenzothiazole in aqueous La^{3+}–TiO_2 suspension for odor control. *Appl. Catal. B Environ.* **48,** 185–194 (2004).

122. Ji, P., Zhang, J., Chen, F. & Anpo, M. Study of adsorption and degradation of acid orange 7 on the surface of CeO_2 under visible light irradiation. *Appl. Catal. B Environ.* **85,** 148–154 (2009).

123. Parida, K. M. & Sahu, N. Visible light induced photocatalytic activity of rare earth titania nanocomposites. *J. Mol. Catal. A Chem.* **287,** 151–158 (2008).

124. Liang, C.-H., Li, F.-B., Liu, C.-S., Lü, J.-L. & Wang, X.-G. The enhancement of adsorption and photocatalytic activity of rare earth ions doped TiO_2 for the degradation of Orange I. *Dye. Pigment.* **76,** 477–484 (2008).

125. Xu, A.-W., Gao, Y. & Liu, H.-Q. The Preparation, Characterization, and their Photocatalytic Activities of Rare-Earth-Doped TiO_2 Nanoparticles. *J. Catal.* **207,** 151–157 (2002).

126. Štengl, V., Bakardjieva, S. & Murafa, N. Preparation and photocatalytic activity of rare earth doped TiO_2 nanoparticles. *Mater. Chem. Phys.* **114,** 217–226 (2009).

127. Li, J., Yang, X., Yu, X., Xu, L., Kang, W., Yan, W., Gao, H., Liu, Z. & Guo, Y. Rare earth oxide-doped titania nanocomposites with enhanced photocatalytic activity towards the degradation of partially hydrolysis polyacrylamide. *Appl. Surf. Sci.* **255,** 3731–3738 (2009).

128. Zou, Z., Ye, J. & Arakawa, H. Role of R in Bi_2RNbO_7 (R = Y, Rare Earth): Effect on Band Structure and Photocatalytic Properties. *J. Phys. Chem. B* **106,** 517–520 (2002).

129. Xu, H., Wu, C., Li, H., Chu, J., Sun, G., Xu, Y. & Yan, Yongsheng Synthesis,

characterization and photocatalytic activities of rare earth-loaded $BiVO_4$ catalysts. *Appl. Surf. Sci.* **256,** 597–602 (2009).

130. Fu, X., Clark, L. A., Yang, Q. & Anderson, M. A. Enhanced Photocatalytic Performance of Titania-Based Binary Metal Oxides: TiO_2/SiO_2 and TiO_2/ZrO_2. *Environ. Sci. Technol.* **30,** 647–653 (1996).

131. Kim, H., Kim, J., Kim, W. & Choi, W. Enhanced Photocatalytic and Photoelectrochemical Activity in the Ternary Hybrid of CdS/TiO_2 /WO_3 through the Cascadal Electron Transfer. *J. Phys. Chem. C* **115,** 9797–9805 (2011).

132. Zhao, Z.-G., Zhao, Z.-G., Miyauchi, M. & Miyauchi, M. Nanoporous-Walled Tungsten Oxide Nanotubes as Highly Active Visible-Light-Driven Photocatalysts13. *Angew. Chemie Int. Ed.* **47,** 7051–7055 (2008).

133. Tian, G., Fu, H., Jing, L., Xin, B. & Pan, Kai Preparation and Characterization of Stable Biphase TiO_2 Photocatalyst with High Crystallinity , Large Surface Area , and Enhanced Photoactivity Preparation and Characterization of Stable Biphase TiO_2 Photocatalyst with High. *J. Phys. Chem. C* **112**, 3083–3089 (2008).

134. Li, S., Lin, Y. H., Zhang, B. P., Li, J. F. & Nan, C. W. $BiFeO_3$ / TiO_2 core-shell structured nanocomposites as visible-active photocatalysts and their optical response mechanism. *J. Appl. Phys.* **105,** 1–6 (2009).

135. Xuan, S., Jiang, W., Gong, X., Hu, Y. & Chen, Z. Magnetically Separable Fe_3O_4 /TiO_2 Hollow Spheres: Fabrication and Photocatalytic Activity. *J. Phys. Chem. C* **113,** 553–558 (2009).

136. Chai, S. Y., Kim, Y. J. & Lee, W. I. Photocatalytic WO_3/TiO_2 nanoparticles working under visible light. *J. Electroceram.* **17,** 909–912 (2006).

137. Iliev, V., Tomova, D., Rakovsky, S., Eliyas, A. & Puma, G. L. Enhancement of photocatalytic oxidation of oxalic acid by gold modified WO_3/TiO_2 photocatalysts

under UV and visible light irradiation. *J. Mol. Catal. A Chem.* **327,** 51–57 (2010).

138. Anandan, S., Sivasankar, T. & Lana-Villarreal, T. Synthesis of TiO_2/WO_3 nanoparticles via sonochemical approach for the photocatalytic degradation of methylene blue under visible light illumination. *Ultrason. Sonochem.* **21,** 1964–1968 (2014).

139. Rajbongshi, B. M., Samdarshi, S. K. & Boro, B. Multiphasic bi-component TiO_2 – ZnO nanocomposite: synthesis, characterization and investigation of photocatalytic activity under different wavelengths of light irradiation. *J Mater Sci Mater Electron* **26,** 377–384 (2015).

140. Song, K. Y., Park, M. K., Kwon, Y. T., Lee, H. W., Chung, W. J. & Lee, W. I. Preparation of Transparent Particulate MoO_3/TiO_2 and WO_3/TiO_2 Films and Their Photocatalytic Properties. *Chem. Mater*. **13**, 2349–2355 (2001).

141. Portela, R., Sánchez, B., Coronado, J. M., Candal, R. & Suárez, S. Selection of TiO_2-support: UV-transparent alternatives and long-term use limitations for H_2S removal. *Catal. Today* **129,** 223–230 (2007).

142. Takeda, N., Torimoto, T., Sampath, S., Kuwabata, S. & Yoneyama, H. Effect of inert supports for titanium dioxide loading on enhancement of photodecomposition rate of gaseous propionaldehyde. *J. Phys. Chem.* **99,** 9986–9991 (1995).

143. Li Puma, G., Bono, A. & Collin, J. G. Preparation of titanium dioxide photocatalyst loaded onto activated carbon support using chemical vapor deposition: A review paper. *J. Hazard. Mater.* **157,** 209–219 (2008).

144. Machado, L. C. R., Torchia, C. B. & Lago, R. M. Floating photocatalysts based on TiO_2 supported on high surface area exfoliated vermiculite for water decontamination. *Catal. Commun.* **7,** 538–541 (2006).

145. Bosc, F., Ayral, A., Keller, N. & Keller, V. Room temperature visible light

oxidation of CO by high surface area rutile TiO_2-supported metal photocatalyst. *Appl. Catal. B Environ.* **69,** 133–137 (2007).

146. Kim, S. & Ehrman, S. H. Photocatalytic activity of a surface-modified anatase and rutile titania nanoparticle mixture. *J. Colloid Interface Sci.* **338,** 304–7 (2009).

147. Zhang, Y., Crittenden, J. C., Hand, D. W. & Perram, D. L. Fixed-bed photocatalysts for solar decontamination of water. *Environ. Sci. Technol.* **28,** 435–42 (1994).

148. Ahmaruzzaman, M. A review on the utilization of fly ash. *Prog. Energy Combust. Sci.* **36,** 327–363 (2010).

149. Joshi, R. C. & Lohita, R. *Fly ash in concrete: production, properties and uses*. (CRC Press, 1997).

150. Yasui, A., Kamiya, Y., Sugiyama, S., Ono, S., Noda, H. & Ichikawa, Y. Synthesis of Carbon Nanotubes on Fly Ashes by Chemical Vapor Deposition Processing. *Ieej Trans. Electr. Electron. Eng.* **4,** 787–789 (2009).

151. Qian, G., Cao, Y., Chui, P. & Tay, J. Utilization of MSWI fly ash for stabilization/solidification of industrial waste sludge. *J. Hazard. Mater.* **129,** 274–81 (2006).

152. Iyer, R. The surface chemistry of leaching coal fly ash. *J. Hazard. Mater.* **93,** 321–329 (2002).

153. Gitari, W. M., Fatoba, O. O., Petrik, L. F. & Vadapalli, V. R. K. Leaching characteristics of selected South African fly ashes: effect of pH on the release of major and trace species. *J. Environ. Sci. Health. A. Tox. Hazard. Subst. Environ. Eng.* **44,** 206–20 (2009).

154. Apak, R., Tütem, E., Hügül, M. & Hizal, J. Heavy metal cation retention by unconventional sorbents (red muds and fly ashes). *Water Res.* **32,** 430–440 (1998).

155. Ahmaruzzaman, M. Industrial wastes as low-cost potential adsorbents for the

treatment of wastewater laden with heavy metals. *Adv. Colloid Interface Sci.* **166,** 36–59 (2011).

156. Blissett, R. S. & Rowson, N. A. A review of the multi-component utilisation of coal fly ash. *Fuel* **97,** 1–23 (2012).

157. Williams, R. P. & van Riessen, A. Determination of the reactive component of fly ashes for geopolymer production using XRF and XRD. *Fuel* **89,** 3683–3692 (2010).

158. McCarthy, M. J. & Dhir, R. K. Development of high volume fly ash cements for use in concrete construction. *Fuel* **84,** 1423–1432 (2005).

159. Dermatas, D. & Meng, X. Utilization of fly ash for stabilization/solidification of heavy metal contaminated soils. *Eng. Geol.* **70,** 377–394 (2003).

160. Kolias, S., Kasselouri-Rigopoulou, V. & Karahalios, A. Stabilisation of clayey soils with high calcium fly ash and cement. *Cem. Concr. Compos.* **27,** 301–313 (2005).

161. Yin, C.-Y., Mahmud, H. Bin & Shaaban, M. G. Stabilization/solidification of lead-contaminated soil using cement and rice husk ash. *J. Hazard. Mater.* **137,** 1758–1764 (2006).

162. Prabakar, J., Dendorkar, N. & Morchhale, R. K. Influence of fly ash on strength behavior of typical soils. *Constr. Build. Mater.* **18,** 263–267 (2004).

163. Green, J. B. & Manahan, S. E. Cupric ion binding by coal humic acids at pH's 1-3. *Can. J. Chem.* **55,** 3284–3254 (1977).

164. Bayat, B. Comparative study of adsorption properties of Turkish fly ashes I . The case of nickel (II), copper (II) and zinc (II). *J. Hazard. Mater.* **95,** 251–273 (2002).

165. Bayat, B. Combined Removal of Zinc (II) and Cadmium (II) From Aqueous Solutions By Adsorption Onto High-Calcium. *Water, Air, and Soil Pollution,* **136**, 69–92 (2001).

166. Rao, M., Parwate, A. V & Bhole, A. G. Removal of Cr^{6+} and Ni^{2+} from aqueous solution using bagasse and fly ash. *Waste Manag.* **22,** 821–30 (2002).

167. Cetin, S. & Pehlivan, E. The use of fly ash as a low cost, environmentally friendly alternative to activated carbon for the removal of heavy metals from aqueous solutions. *Colloids Surfaces A Physicochem. Eng. Asp.* **298,** 83–87 (2007).

168. Cho, H., Oh, D. & Kim, K. A study on removal characteristics of heavy metals from aqueous solution by fly ash. *J. Hazard. Mater.* **127,** 187–195 (2005).

169. Weng, C.-H. & Huang, C. P. Adsorption characteristics of Zn(II) from dilute aqueous solution by fly ash. *Colloids Surfaces A Physicochem. Eng. Asp.* **247,** 137–143 (2004).

170. Bertocchi, A. F., Ghiani, M., Peretti, R. & Zucca, A. Red mud and fly ash for remediation of mine sites contaminated with As, Cd, Cu, Pb and Zn. *J. Hazard. Mater.* **134,** 112–119 (2006).

171. López, E., Soto, B., Arias, M., Núñez, A., Rubinos, D. & Barral, M T Adsorbent properties of red mud and its use for wastewater treatment. *Water Res.* **32,** 1314–1322 (1998).

172. Banerjee, S. S., Joshi, M. V. & Jayaram, R. V. Removal of Cr(VI) and Hg(II) from Aqueous Solutions Using Fly Ash and Impregnated Fly Ash. *Sep. Sci. Technol.* **39,** 1611–1629 (2005).

173. Srivastava, V. C., Mall, I. D. & Mishra, I. M. Modelling Individual and Competitive Adsorption of Cadmium(II) and Zinc(II) Metal Ions from Aqueous Solution onto Bagasse Fly Ash. *Sep. Sci. Technol.* **41,** 2685–2710 (2006).

174. Akar, G., Polat, M., Galecki, G. & Ipekoglu, U. Leaching behavior of selected trace elements in coal fl y ash samples from Yenikoy coal- fi red power plants. *Fuel Process. Technol.* **104,** 50–56 (2012).

175. Kumar, S., Upadhyay, S. N. & Upadhya, Y. D. Removal of phenols by adsorption on fly ash. *J. Chem. Technol. Biotechnol.* **37,** 281–287 (1987).

176. Srivastava, V. C., Swamy, M. M., Mall, I. D., Prasad, B. & Mishra, I. M. Adsorptive removal of phenol by bagasse fly ash and activated carbon: Equilibrium, kinetics and thermodynamics. *Colloids Surfaces A Physicochem. Eng. Asp.* **272,** 89–104 (2006).

177. Aksu, Z. & Yener, J. The usage of dried activated sludge and fly ash wastes in phenol biosorption/adsorption: Comparison with granular activated carbon. *J. Environ. Sci. Heal. Part a-Toxic/Hazardous Subst. Environ. Eng.* **34,** 1777–1796 (1999).

178. Chen, Q., Luo, Z., Hills, C., Xue, G. & Tyrer, M. Precipitation of heavy metals from wastewater using simulated flue gas: Sequent additions of fly ash, lime and carbon dioxide. *Water Res.* **43,** 2605–2614 (2009).

179. Seidel, A. & Zimmels, Y. Mechanism and kinetics of aluminum and iron leaching from coal fly ash by sulfuric acid. *Chem. Eng. Sci.* **53,** 3835–3852 (1998).

180. Pelaez, M., Nolan, N. T., Pillai, S. C., Seery, M. K., Falaras, P., Kontos, A. G., Dunlop, P. S. M., Hamilton, J. W. J., Byrne, J. A., O'Shea, K., Entezari, M. H. & Dionysiou, D. D. A review on the visible light active titanium dioxide photocatalysts for environmental applications. *Appl. Catal. B Environ.* **125,** 331–349 (2012).

181. Turner, M., Golovko, V. B., Vaughan, O. P. H., Abdulkin, P., Berenguer-Murcia, A., Tikhov, M. S., Johnson, B. F. G. & Lambert, Richard M. Selective oxidation with dioxygen by gold nanoparticle catalysts derived from 55-atom clusters. *Nature* **454,** 981–983 (2008).

182. Sacchi, M. C., Zucchi, D., Tritto, I., Locatelli, P. & Dall'Occo, T. Silica-supported

metallocenes: stereochemical comparison between homogeneous and heterogeneous catalysis. *Macromol. Rapid Commun.* **16,** 581–590 (1995).

183. Astruc, D., Lu, F. & Aranzaes, J. R. Nanoparticles as Recyclable Catalysts: The Frontier between Homogeneous and Heterogeneous Catalysis. *Angew. Chemie Int. Ed.* **44,** 7852–7872 (2005).

184. Bell, A. T. The impact of nanoscience on heterogeneous catalysis. *Science* **299,** 1688–1691 (2003).

185. Wang, S. & Lu, G. Q. Effect of chemical treatment on Ni/fly-ash catalysts in methane reforming with carbon dioxide. *Stud. Surf. Sci. Catal.* **167,** 275–280 (2011).

186. Huo, P., Yan, Y., Li, S., Li, H. & Huang, W. Floating photocatalysts of fly-ash cenospheres supported $AgCl/TiO_2$ films with enhanced Rhodamine B photodecomposition activity. *Desalination* **256,** 196–200 (2010).

187. Kastner, J. R., Das, K. C. & Melear, N. D. Catalytic oxidation of gaseous reduced sulfur compounds using coal fly ash. **95,** 81–90 (2002).

188. Khatri, C., Mishra, M. K. & Rani, A. Synthesis and characterization of fly ash supported sulfated zirconia catalyst for benzylation reactions. *Fuel Process. Technol.* **91,** 1288–1295 (2010).

189. Khatri, C. & Rani, A. Synthesis of a nano-crystalline solid acid catalyst from fly ash and its catalytic performance. *Fuel* **87,** 2886–2892 (2008).

190. Chaudhuri, S. K. & Sur, B. Oxidative decolorization of reactive dye solution using fly ash as catalyst. *J. Environ. Eng.* **126,** 583–594 (2000).

191. van Jaarsveld, J. G., van Deventer, J. S. & Lukey, G. . The effect of composition and temperature on the properties of fly ash- and kaolinite-based geopolymers. *Chem. Eng. J.* **89,** 63–73 (2002).

192. Arroyo, F. & Fernández-Pereira, C. Hydrometallurgical Recovery of Germanium

from Coal Gasification Fly Ash. Solvent Extraction Method. *Ind. Eng. Chem. Res.* **47,** 3186–3191 (2008).

193. Zheng, F., Fang, Z. & Gesser, H. D. Recovery of gallium from coal fly ash. *Hydrometallurgy* **41,** 187–200 (1996).

194. Anderson, C. & Bard, A. J. Improved Photocatalytic Activity and Characterization of Mixed TiO_2 / SiO_2 and TiO_2 / Al_2O_3 Materials. **5647,** 2611–2616 (1997).

195. Machida, M., Norimoto, K. & Watanabe, T. The effect of SiO_2 addition in super-hydrophilic property of TiO_2 photocatalyst. *J. Mater. Sci.* **4,** 2569–2574 (1999).

196. Tanabe, K. The Acidic Properties of TiO_2-SiO_2 and Its Catalytic Activities for the Amination of Phenol , the Hydration of Ethylene and the lsomerization of Butene. *J. Catal.* **231,** 225–231 (1974).

197. Dlugi, R. & Gusten, H. The Catalytic and Photocatalytic Activity of Coal Fly Ashes. *Atmos. Environ.* **17,** 1765–1771 (1983).

198. Zhang, J., Cui, H., Wang, B., Li, C., Zhai, J. P. & Li, Q Fly ash cenospheres supported visible-light-driven $BiVO_4$ photocatalyst: Synthesis, characterization and photocatalytic application. *Chem. Eng. J.* **223,** 737–746 (2013).

199. Wang, B., Li, C., Pang, J., Qing, X., Zhai, J. & Li, Qin Novel polypyrrole-sensitized hollow TiO_2/fly ash cenospheres: Synthesis, characterization, and photocatalytic ability under visible light. *Appl. Surf. Sci.* **258,** 9989–9996 (2012).

200. Wang, B., Li, Q., Wang, W., Li, Y. & Zhai, J. Preparation and characterization of Fe^{3+}-doped TiO_2 on fly ash cenospheres for photocatalytic application. *Appl. Surf. Sci.* **257,** 3473–3479 (2011).

201. Querol, X., Moreno, N., Umaña, J. C., Alastuey, A., Hernández, E., López-Soler, A. & Plana, F. Synthesis of zeolites from coal fly ash: an overview. *Int. J. Coal Geol.* **50,** 413–423 (2002).

202. Shigemoto, N., Sugiyama, S., Hayashi, H. & Miyaura, K. Characterization of Na-X, Na-A, and coal fly ash zeolites and their amorphous precursors by IR, MAS NMR and XPS. *J. Mater. Sci.* **30,** 5777–5783 (1995).

203. Jha, B. & Singh, D. N. Formation of meso- And micro-pores in fly-ash zeolites using a three-step activation. *Acta Geotech. Slov.* **11,** 63–69 (2014).

204. Khaleghian-Moghadam, R. & Seyedeyn-Azad, F. A study on the thermal behavior of low silica X-type zeolite ion-exchanged with alkaline earth cations. *Microporous Mesoporous Mater.* **120,** 285–293 (2009).

205. Holler, H. & Wirsching, U. Zeolite formation from fly-ash. *Fortschritte der Mineral.* **63,** 21–43 (1985).

206. Shigemoto, N., Hayashi, H. & Miyaura, K. Selective formation of Na-X zeolite from coal fly ash by fusion with sodium hydroxide prior to hydrothermal reaction. *J. Mater. Sci.* **28,** 4781–4786 (1993).

207. Jha, B. & Singh, D. N. A three step process for purification of fly ash zeolites by hydrothermal treatment. *Appl. Clay Sci.* **90,** 122–129 (2014).

208. Ojha, K., Pradhan, N. C. & Samanta, A. N. Zeolite from fly ash: Synthesis and characterization. *Bull. Mater. Sci.* **27,** 555–564 (2004).

209. Koukouzas, N., Vasilatos, C., Itskos, G., Mitsis, I. & Moutsatsou, A. Removal of heavy metals from wastewater using CFB-coal fly ash zeolitic materials. *J. Hazard. Mater.* **173,** 581–8 (2010).

210. Wang, C. F., Li, J. S., Wang, L. J. & Sun, X. Y. Influence of NaOH concentrations on synthesis of pure-form zeolite A from fly ash using two-stage method. *J. Hazard. Mater.* **155,** 58–64 (2008).

211. Molina, A. & Poole, C. A comparative study using two methods to produce zeolites from fly ash. *Miner. Eng.* **17,** 167–173 (2004).

212. Fukahori, S., Ichiura, H., Kitaoka, T. & Tanaka, H. Capturing of bisphenol A photodecomposition intermediates by composite TiO_2–zeolite sheets. *Appl. Catal. B Environ.* **46,** 453–462 (2003).

213. Ichiura, H., Kitaoka, T. & Tanaka, H. Preparation of composite TiO_2 -zeolite sheets using a papermaking technique and their application to environmental improvement. *J. Mater. Sci.* **37,** 2937–2941 (2002).

214. Ichiura, H., Kitaoka, T. & Tanaka, H. Removal of indoor pollutants under UV irradiation by a composite TiO_2-zeolite sheet prepared using a papermaking technique. *Chemosphere* **50,** 79–83 (2003).

215. Anpo, M., Yamashita, H., Ichihashi, Y., Fujii, Y. & Honda, M. Photocatalytic Reduction of CO_2 with H_2O on Titanium Oxides Anchored within Micropores of Zeolites: Effects of the Structure of the Active Sites and the Addition of Pt. *J. Phys. Chem. B* **101,** 2632–2636 (1997).

216. Smalley, R. Discovering the fullerenes. *Rev. Mod. Phys.* **69,** 723–730 (1997).

217. Iijima, S. Helical microtubules of graphitic carbon. *Nature* **354,** 56–58 (1991).

218. Ferrari, A. C. Raman spectroscopy of graphene and graphite: Disorder, electron–phonon coupling, doping and nonadiabatic effects. *Solid State Commun.* **143,** 47–57 (2007).

219. Chen, J., Li, B., Zheng, J., Zhao, J. & Zhu, Z. Role of Carbon Nanotubes in Dye-Sensitized TiO_2 -Based Solar Cells. *J. Phys. Chem. C* **116,** 14848–14856 (2012).

220. Santangelo, S., Messina, G., Faggio, G., Donato, A., De Luca, L., Donato, N., Bonavita, A. & Neri, G.Micro-Raman analysis of titanium oxide/carbon nanotubes-based nanocomposites for hydrogen sensing applications. *J. Solid State Chem.* **183,** 2451–2455 (2010).

221. Kedem, S., Schmidt, J., Paz, Y. & Cohen, Y. Composite Polymer Nanofibers with

Carbon Nanotubes and Titanium Dioxide Particles. *Langmuir* 5600–5604 (2005).

222. Leary, R. & Westwood, A. Carbonaceous nanomaterials for the enhancement of TiO_2 photocatalysis. *Carbon* **49,** 741–772 (2011).

223. Nxumalo, E. N. & Coville, N. J. Nitrogen Doped Carbon Nanotubes from Organometallic Compounds: A Review. *Materials.* **3,** 2141–2171 (2010).

224. Iijima, S. Helical microtubules of graphitic carbon. *Nature* **354,** 56–58 (1991).

225. Dupius, A. The catalyst in the CCVD of carbon nanotubes—a review. *Prog. Mater. Sci.* **50,** 929–961 (2005).

226. O'Byrne, J. P. Justin, P. Li, Z., Jones, S. L. T., Fleming, P. G., Larsson, J. A., Morris, M. A. & Holmes, J. D. Nitrogen-doped carbon nanotubes: Growth, mechanism and structure. *ChemPhysChem* **12,** 2995–3001 (2011).

227. Chizari, K., Vena, A., Laurentius, L. & Sundararaj, U. The effect of temperature on the morphology and chemical surface properties of nitrogen-doped carbon nanotubes. *Carbon* **68,** 369–379 (2013).

228. Couteau, E., Hernadi, K., Seo, J. W., Thiên-Nga, L., Mikó, C., Gaál, R. & Forró, L. CVD synthesis of high-purity multiwalled carbon nanotubes using $CaCO_3$ catalyst support for large-scale production. *Chem. Phys. Lett.* **378,** 9–17 (2003).

229. Dunens, O.M., MacKenzie, K.J. & Harris, A. T. Synthesis of Multiwalled Carbon Nanotubes on Fly Ash Derived Catalysts. *Environ. Sci. Technol*. **43,** 7889–7894 (2009).

230. Magrez, A., Seo, J. W., Smajda, R., Mionić, M. & Forró, L. Catalytic CVD synthesis of carbon nanotubes: Towards high yield and low temperature growth. *Materials* **3,** 4871–4891 (2010).

231. Nagaraju, N., Fonseca, A., Konya, Z. & Nagy, J. B. Alumina and silica supported metal catalysts for the production of carbon nanotubes. *J. Mol. Catal. A: Chem.* **181,**

57–62 (2002).

232. Nath, D. C. D. & Sahajwalla, V. Application of fly ash as a catalyst for synthesis of carbon nanotube ribbons. *J. Hazard. Mater.* **192,** 691–7 (2011).

233. Hintsho, N., Shaikjee, A., Masenda, H., Naidoo, D., Billing, D., Franklyn, P. & Durbach, S. Direct synthesis of carbon nanofibers from South African coal fly ash. *Nanoscale Res. Lett.* **9,** 2-11 (2014).

234. Hintsho, N., Shaikjee, A., Franklyn, P. & Durbach, S. The effect of CO_2 on the CVD synthesis of carbon nanomaterials using fly ash as a catalyst. *RSC Adv.* **5,** 53776–53781 (2015).

235. Ayala, P., Arenal, R., Rümmeli, M., Rubio, A. & Pichler, T. The doping of carbon nanotubes with nitrogen and their potential applications. *Carbon* **48,** 575–586 (2010).

236. Hlekelele, L., Tripathi, P., Franklyn, P. J. & Durbach, S. H. Morphological and crystallinity differences in Nitrogen- Doped Carbon Nanotubes grown by Chemical Vapor Deposition Decomposition of Melamine over Coal Fly Ash. *RSC Adv.* **6,** 76773–76779 (2016).

237. Maldonado, Stephen Stephen, M. & Stevenson, K. J. Structure, composition, and chemical reactivity of carbon nanotubes by selective nitrogen doping. *Carbon* **44,** 1429–1437 (2006).

238. Stephan, O., Ajayan, P. M., Colliex, C., Redlich, P., Lambert, J. M. & Bernier, P. Doping graphitic and carbon nanotube structures with boron and nitrogen. *Science* **266,** 1683–16855 (1994).

239. Terrones, M. Ajayan, P. M., Banhart, F., Blase, X., Carroll, D. L., Charlier, J. C., Czerw, R., Foley, B. & Grobert. N-doping and coalescence of carbon nanotubes: synthesis and electronic properties. *Appl. Phys. A* **74,** 355–361 (2002).

240. Dingshan, Y., Yuhua, X. & Dai, L. Vertically aligned carbon nanotube arrays co-doped with phosphorus and nitrogen as efficient metal-free electrocatalysts for oxygen reduction. *J. Phys. Chem. Lett.* **3,** 2863–2870 (2012).

241. Panchakarla, L. S., Subrahmanyam, K. S., Saha, S. K. & Govindaraj, A. Synthesis , Structure and Properties of Boron and Nitrogen Doped Graphene.

242. Koós, A. A., Dowling, M., Jurkschat, K., Crossley, A. & Grobert, N. Effect of the experimental parameters on the structure of nitrogen-doped carbon nanotubes produced by aerosol chemical vapor deposition. *Carbon* **47,** 30–37 (2009).

243. Sharifi, T., Nitze, F., Barzegar, H. R., Tai, C. W., Mazurkiewicz, M., Malolepszy, Stobinski, L. & Wagberg, T. Nitrogen doped multi walled carbon nanotubes produced by CVD-correlating XPS and Raman spectroscopy for the study of nitrogen inclusion. *Carbon* **50,** 3535–3541 (2012).

244. Luo, Z., Lim, S., Tian, Z., Shang, J., Lai, L., MacDonald, B., Fu, C., Shen, Z., Yu, T. & Lin, Jianyi Pyridinic N doped graphene: synthesis, electronic structure, and electrocatalytic property. *J. Mater. Chem.* **21,** 8038 (2011).

245. Wang, H., Maiyalagan, T. & Wang, X. Review on recent progress in nitrogen-doped graphene: Synthesis, characterization, and its potential applications. *ACS Catal.* **2,** 781–794 (2012).

246. Lee, Y. T., Kim, N. S., Bae, S. Y. & Park, J. Growth of Vertically Aligned Nitrogen-Doped Carbon Nanotubes : Control of the Nitrogen Content over the Temperature Range. 900 - 1100 ° C. *J. Phys. Chem. B*, **107**, 12958–12963 (2003).

247. Czerw, R., Terrones, M., Charlier, J. C., Blase, X., Foley, B., Kamalakaran, R., Grobert, N., Terrones, H., Tekleab, D., Ajayan, P. M., Blau, W., Rühle, M. & Carroll, D. L. Identification of Electron Donor States in N-Doped Carbon Nanotubes. *Nano Lett.* **1,** 457–460 (2001).

248. Terrones, M. Terrones, H., Grobert, N., Hsu, W. K., Zhu, Y. Q. & Hare, J. P. Efficient route to large arrays of CNx nanofibers by pyrolysis of ferrocene/melamine mixtures. *Appl Phys Lett* **76,** 3932–3934 (1999).

249. Terrones, M., Ajayan, P. M., Banhart, F., Blase, X., Carroll, D. L., Charlier, J. C., Czerw, R., Foley, B. & Grobert, N N-doping and coalescence of carbon nanotubes. *Science* **361,** 355–361 (2002).

250. Ghosh, K., Kumar, M., Maruyama, T. & Ando, Y. Tailoring the field emission property of nitrogen-doped carbon nanotubes by controlling the graphitic/pyridinic substitution. *Carbon* **48,** 191–200 (2010).

251. Van Dommele, S., Romero-Izquirdo, A., Brydson, R., de Jong, K. P. & Bittera, J. H. Nitrogen-containing carbon nanotubes as solid base catalysts. *Carbon* **46,** 138–148 (2008).

252. Van Dommele, S., Van de Jong, K. P. & Bitter, J. H. Tuning nitrogen functionalities in catalytically grown nitrogen-containing carbon nanotubes. *Chem. Commun.* **46,** 4859–4861 (2006).

253. Wang, Z., Jia, R., Zheng, J., Zhao, J., Li, L., Song, J. & Zhu, Z. Nitrogen-Promoted Self-Assembly of N-Doped Carbon Nanotubes and their Intrinsic Catalysis for Oxygen Reduction in Fuel Cells. *ACS nano*. **5**, 1677–1684 (2011).

254. Gao, B., Chen, G. Z. & Li Puma, G. Carbon nanotubes/titanium dioxide ($CNTs/TiO_2$) nanocomposites prepared by conventional and novel surfactant wrapping sol-gel methods exhibiting enhanced photocatalytic activity. *Appl. Catal. B Environ.* **89,** 503–509 (2009).

255. Yu, Y., Jia, R., Zheng, J., Zhao, J., Li, L., Song, J. & Zhu, Z. Enhancement of adsorption and photocatalytic activity of TiO_2 by using carbon nanotubes for the treatment of azo dye. *Appl. Catal. B Environ.* **61,** 1–11 (2005).

256. Eder, D. & Windle, A. H. Carbon-inorganic hybrid materials: The carbon-nanotube/TiO_2 interface. *Adv. Mater.* **20,** 1787–1793 (2008).

257. Hintsho, N., Petrik, L., Nechaev, A., Titinchi, S. & Ndungu, P. Photo-catalytic activity of titanium dioxide carbon nanotube nano-composites modified with silver and palladium nanoparticles. *Appl. Catal. B Environ.* **156–157,** 273–283 (2014).

258. Perera, S. D., Sanjaya D. Mariano, R. G., Vu, K., Nour, N., Seitz, O., Chabal, Y. & Balkus, K. J. Hydrothermal synthesis of graphene-TiO_2 nanotube composites with enhanced photocatalytic activity. *ACS Catal.* **2,** 949–956 (2012).

259. Woan, K., Pyrgiotakis, G. & Sigmund, W. Photocatalytic Carbon-Nanotube-TiO_2 Composites. *Adv. Mater.* **21,** 2233–2239 (2009).

260. Liu, H., Zhang, Y., Li, R., Sun, X., De, S., Abou-rachid, H., Jaidann, M. & Lussier, L. Structural and morphological control of aligned nitrogen-doped carbon nanotubes. *Carbon* **48,** 1498–1507 (2010).

261. Dai, K., Peng, T., Ke, D. & Wei, B. Photocatalytic hydrogen generation using a nanocomposite of multi-walled carbon nanotubes and TiO_2 nanoparticles under visible light irradiation. *Nanotechnology* **20,** 125603 (2009).

262. Wang, W., Serp, P., Kalck, P. & Faria, J. L. Visible light photodegradation of phenol on MWNT-TiO_2 composite catalysts prepared by a modified sol–gel method. *J. Mol. Catal. A Chem.* **235,** 194–199 (2005).

263. Pyrgiotakis, G., Lee, S.H. & Wolfgang, S. Advanced photocatalysis with anatase nano-coated multi-walled carbon nanotubes. *MRS Proc.* **876,** 5–7 (2005).

CHAPTER 3:

EXPERIMENTAL

3.1 Introduction

This chapter serves to provide information on the characterization techniques that were used in order to execute the work described in this thesis. **Chapter 3** includes 1) Characterization techniques, 2) Instrument information, 3) Specimen preparation procedure and 4) The photocatalytic procedure. However, more of the experimental specifics are covered in the subsequent Results and Discussion chapters, i.e. Chapters 4 to 7**.**

3.2 Characterization of materials

In order to understand the properties of a photocatalyst, a series of different types of characterization techniques are routinely used. The most common of these, used for morphological studies of nanoparticles are scanning electron microscopy (SEM) and transmission electron microscopy (TEM). TEM can also be used for measuring the crystallite size as well as for studying the structural properties of photocatalyst nanoparticles. Powder X-ray diffraction (PXRD) like TEM can also be used for the purposes of elucidating crystallite information, such as the arrangement of atoms and their spacing as well as their crystalline phase. When TEM or SEM are coupled with energy dispersive spectroscopy (EDS) this allows for qualitative and semi-quantitative elemental analyses to be performed. This is vital, especially when the photocatalyst consists of more than one element, as is the case in doped and supported catalyst systems. Adsorption-desorption isotherms are equally vital for

studying the surface characteristics of photocatalysts, such as surface area and pore volumes. Several of these techniques will now be discussed in further detail.

3.2.1 Transmission electron microscopy (TEM)

TEM operates through the utilization of collimated rays of electrons that are accelerated by high voltages.[1-3] Here a beam of electrons is focused through a sequence of lenses which can either be electrostatic or magnetic.[2,3] The focused beam of electrons then goes through the sample and is fixated on a detector plate.[2,3] The electrons interact with the various atoms situated in different positions in the sample and then micrographs are formed based on these interactions.[2,4] TEM is very useful when the sample being viewed is thin because in that way not only the particle arrangement and geometry therein can be determined but also its morphology. Electron diffraction is also very convenient for determining the crystallinity and crystal orientation of separate nanoparticles rather than powder X-ray diffraction which gives the crystallinity of many particles.[5] In such TEM analyses digital micrographs and diffraction patterns can be obtained with the aid of a digital camera and specialized software that is associated directly with the instrument.

One of the key reasons for using TEM is that the interactions of a beam of electrons with matter are generally superior to those that occur between matter and X-rays or neutrons with similar wavelengths.[1–4] Here the most reliable results obtained are for sample depths that are similar to the mean free path of the electrons, i.e. the average distance moved by the electrons between scattering procedures.[5,4,6,7] In this technique, the suggested depth of the sample differs from a few nanometers for

samples comprising of light elements to tens or hundreds of nanometers for samples consisting of heavy elements.[4] Indeed, the hypothetical resolving strength of high-resolution TEM is subatomic, while resolutions of approximately 1 Å have been obtained experimentally.[6,3]

In this work, an FEI Tecnai T12 transmission electron microscope (**Figure 3.1**) was used to study some of the above-stated properties of nanoparticles.

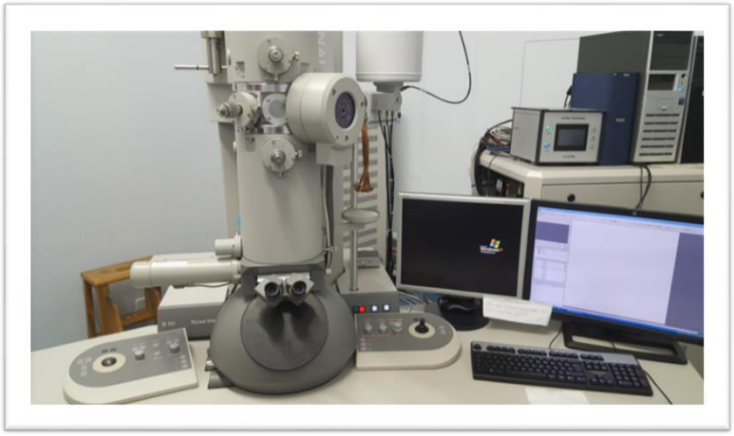

Figure 3.1. A photograph of the FEI TECNAI T12 TEM that was used in these studies.

Samples were prepared for TEM analysis by sonicating a mass of *ca*. 2 mg of each in ethanol in a small glass vial for 30 min. Thereafter a small amount of the dispersed sample was dropped onto a holey carbon-coated copper grid using a Pasteur pipette and allowed to dry under an incandescent lamp for 5 min. Each sample was then loaded into the FEI TECNAI T12 TEM and analyzed.

3.2.2 Scanning electron microscopy (SEM)

SEM is one of the prevailing methods that are used for studying the surfaces of materials. Here a beam of electrons is condensed and narrowed down, through a sequence of the condenser and objective lenses, in order to eradicate high-angle electrons before they are focused onto the sample being analyzed.[5,4,6,3] The number of backscattered electrons and/or the secondary electrons that are produced by the beam that arises from the sample, hinges on its local composition and topography.[4] The resulting electrons are gathered by an electron detector and a micrograph is then obtained by plotting the detector signal as a function of the beam location.[2,4]

In this work, an FEI Nova Nanolab 600 FEG-SEM, operated at 30 kV with a spot size of 0.63 nA, was used (**Figure 3.2**). In each case, a small mass of fine powder sample (*ca*. 5 mg) was placed onto a double-sided adhesive carbon tape which was then mounted onto an aluminum stub.[4] In some instances, to avoid surface charging, the materials were coated with a 40-60 nm layer of Ag/Pd and/or carbon by sputter coating.[4]

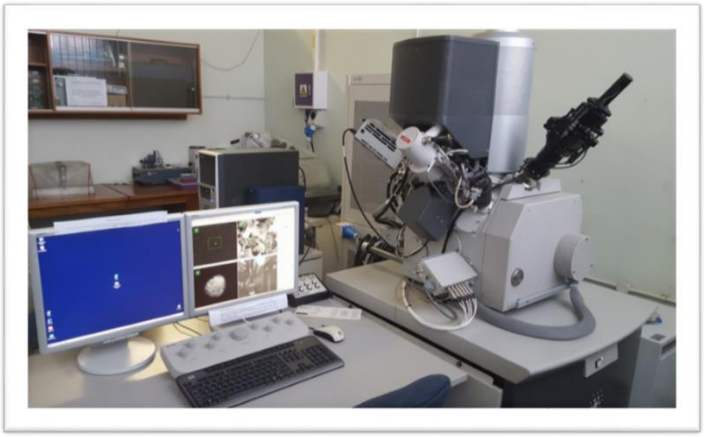

Figure 3.2. A photograph of the FEI Nova Nanolab FEG-SEM that was used in these studies.

3.2.3 Energy dispersive X-ray spectroscopy (EDS)

In many cases, both the TEM and SEM are coupled to an energy dispersive X-ray spectroscopy (EDS) detector. Here the composition of a sample can be quantified and mapped.[1,3,4] In addition to EDS, an electron back-scattered diffraction detector (EBSD) can be coupled to an SEM instrument allowing the use of SEM to examine and map crystal grain boundaries in materials down to about 100 nm.[4] In these studies, an EDS detector was attached to both the FEI TECNAI T12 TEM and the FEI Nova Nanolab FEG-SEM and was used for such analyses where appropriate.

3.2.4 Powder X-ray diffraction (PXRD) crystallography

An approximation of the degree of crystallinity, the identification of crystalline phases, the determination of particle sizes and the stress or strain experienced by the particles can all be studied using PXRD.

In this technique, electrons are accelerated at a high voltage (ranging between 10–100 kV) to bombard a target material e.g. Cu, Mo, Cr, Co or Fe in order to dislodge its inner-shell electrons and produce X-rays. It is these X-rays that are then collimated and concentrated onto samples that are then analyzed. If the atoms in these samples are arranged in a periodic or organized way then the X-rays are scattered in such a way that diffraction patterns are generated.[2,4] Each pattern that arises this way has a variety of peaks of diverse intensities at definite angles of diffraction.[4] The arrangement of atoms in a crystal structure enforces strong constraints on the X-ray diffraction pattern that is yielded.[3] Hence an individual diffraction pattern can be used to determine the crystallographic structure and thus the identity of a sample. Consequently, PXRD can be used as a quantitative and qualitative method for studying the fingerprint categorization of materials that are crystalline.[3] Moreover, PXRD can also be used to study and measure the: 1) Size of the crystallites, 2) Extent of the micro-stresses and strains, 3) Inter-planar differences, 4) Miller indices, 5) Charge distribution around atoms, and 6) Orientation distribution.[2]

In this project, the solid materials that were synthesized were analyzed by a Bruker D2-Phaser PXRD as shown in **Figure 3.3**.

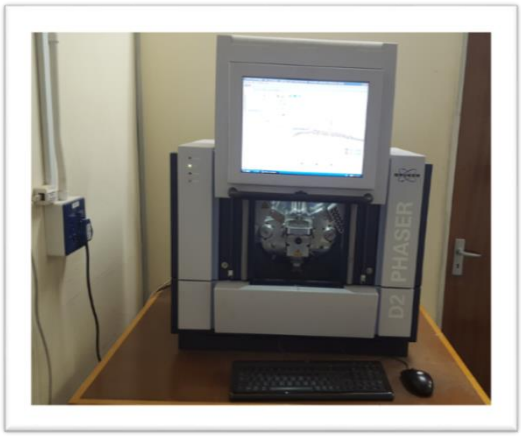

Figure 3.3. A photograph of the Bruker D2-Phaser PXRD that was used in these studies.

The Bruker D2-Phaser PXRD used Co-Kα radiation that utilized a 30 kV X-ray tube and was run at a current of 30 mA over a 2θ range of 10-90 °. Each powder sample that was analyzed was carefully loaded onto a specialized zero diffraction holder which had the following proportions: 32 mm in diameter and 2.0 mm in thickness with a cavity that was 10 mm in diameter and 0.2 mm in thickness.

3.2.5 Laser Raman spectroscopy

Laser Raman spectroscopy is a technique which is named after an Indian scientist i.e. Sir Chandrasekhara Venkata Raman, who was the first to experimentally observe the inelastic scattering of monochromatic radiation.[8,9] Here the Raman effect or Raman scattering, is the resultant inelastic scattering of light that is observed after incident photons interact with vibrating molecules of a given material.[8] Throughout these interactions, photons either transfer energy to or receive energy from molecular vibrations, which produce what is respectively called stokes and anti-stokes scattering signals.[6,3,8] The energy change of these scattered photons

parallels that of the vibrational energy heights of the molecules in the sample.[8,10] Given that the vibrational energy spectrum hinges on the chemical composition and characteristics of a particular sample (e.g. types of atoms, bond strengths, bond angles, and crystallographic symmetries), this means a Raman spectrum is chemically specific and can be used for qualitative measurements of molecules with vibrating bonds.[3,6,8,9] Hence laser Raman spectroscopy can be used for the purposes of studying: 1) Phases and crystalline polymorphs as well as, 2) Strain and symmetries of molecular and crystalline materials that are molecular or crystalline.[10–13]

In these studies, a Bruker Senterra laser Raman spectrometer (as shown in **Figure 3.4**), fitted with a 50x objective lens for imaging was used at an excitation wavelength of 532 nm (green light). In each case, a mass of *ca*. 5 mg of sample was placed onto a glass slide and then under the 50x objective lens before being analyzed by the Bruker Senterra laser Raman spectrometer.

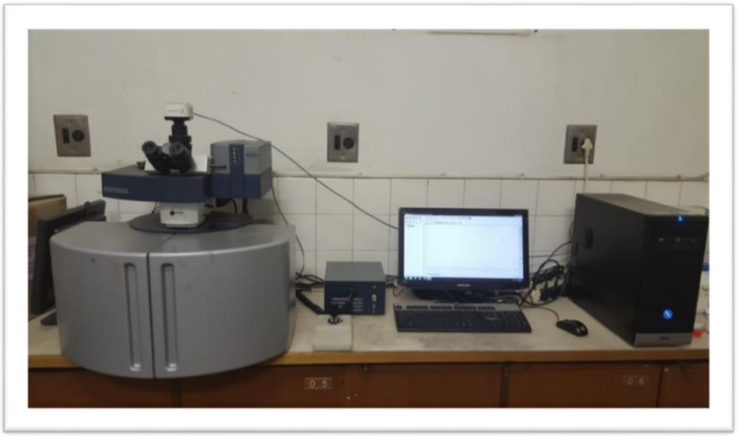

Figure 3.4. A photograph of the Bruker Senterra laser Raman spectrometer that was used in these studies.

3.2.6 Fourier transform infrared (FTIR) spectroscopy

The FTIR technique can be conducted on solid, liquid and gas samples and is used for studying chemical bonding in molecules as well as the molecular structure of both organic and inorganic compounds.[1,3,14] In this technique infrared radiation (i.e. 10 000 cm^{-1} to 100 cm^{-1}) is used (wherever energetically possible) to induce transitions between vibrational and rotational states in molecules. Indeed, the wavelengths at which molecules and functional groups absorb infrared light are determined by their molecular potential energy surfaces, their weights (identities) of the atoms and by their related vibrionic coupling.[6,3] Hence infrared spectroscopy can be used for compositional analyses of samples due to the absorption wavelengths related to particular bond types.[3] In these studies, a Bruker Tensor 27 FTIR spectrometer as shown in **Figure 3.5**, was used**.**



Figure 3.5. A photograph of the Bruker Tensor 27 FTIR spectrometer that was used in these studies.

3.2.7 Thermogravimetric analysis (TGA)

TGA is a thermal analysis technique that is used mainly to study the thermal properties of materials. Here the stability of materials when exposed to heat is measured i.e. the mass of a given sample is monitored as a function of temperature in a given atmosphere and plotted on a thermogram.[1,3,15] Hence a mass loss observed on the thermogram is indicative of the presence of volatile substances in the sample.[1] For this reason, TGA can be used to quantify and detect the presence of volatile components of a sample (in a specific temperature range and atmosphere). In these studies, a Perkin Elmer Pyris 1 TGA (**Figure 3.6**) was used for these analyses.



Figure 3.6. A photograph of the Perkin Elmer Pyris 1 TGA that was used in these studies.

In each case, a small mass of fine powder sample (*ca*. 10 mg) was placed into a sample pan and the sample was then heated at 10 ml/min from 25 °C to 900 °C.

3.2.8 Brunauer Emmett and Teller (BET) surface area measurement

BET is a technique used for studying the surface properties of materials e.g. specific surface area, pore size distribution and percentage porosity.[1] In practice a gas (e.g. N_2, Ar or CO_2) is physisorbed onto the surface of a solid sample being analyzed and assuming a monolayer interaction, the amount of adsorbate in correspondence to its surface is used to evaluate its specific surface area. Here physisorption results from moderately weak van der Waals forces that exist between the adsorbate gas molecules and the surface of the powder sample.[1] In these studies, a Micromeritics RS232 Brunauer-Emmett-Teller (BET) surface area analyzer (**Figure 3.7**) was used for the BET surface area and pore volume analyses.

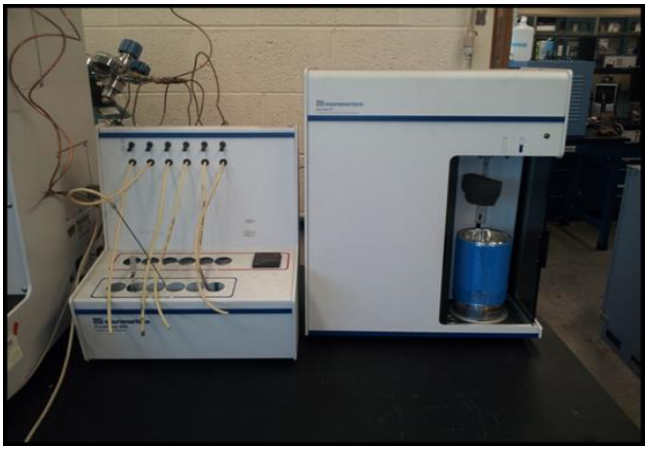

Figure 3.7 A photograph of the Micromeritics RS232 BET surface area analyzer that was used in these studies.

In each case, a small mass of fine powder sample (*ca*. 200 mg) was placed into a glass sample holder and deoxygenated at 150 °C under a nitrogen stream. The sample was then inserted into the instrument chambers and analyzed.

3.2.9 Elemental analysis

The elemental analysis offers the means for rapid quantification of carbon, hydrogen, nitrogen, and sulphur (CHNS) in complex inorganic and inorganic matrices.[16] Here the state of matter of the sample being analyzed can either be liquid or solid; while samples can be viscous or volatile.[1] In order to conduct CHNS analyses, on the basis of the Pregl-Dumas technique, high temperatures are required to effect combustion of samples in oxygen-rich atmospheres.[1] In these analyses the combustion process can either occur in static or dynamic oxygen conditions.[1] In the former case this involves introducing a fixed volume of oxygen into the reaction chamber, whereas in the latter case this involves a constant flow of oxygen.[1] Usually in these analyses the furnace where the sample is combusted is set to temperatures up to 1000 °C.[1] Thus in the CHNS analyses this results in carbon being converted into CO_2, hydrogen into water vapor, nitrogen into N_2 gas and sulphur into SO_2.[1] As these gaseous products are formed (during combustion) they are carried out of the vessel by an inert carrier gas (e.g. He). Thereafter these gases are then passed over a high purity copper wire which is heated to temperatures up to 600 °C to remove the unreacted oxygen and to convert the elements into their oxides. The combustion gases are then separated using GC and measured using a thermal conductivity detector.

In these studies, a Carlo Erba EA 1108 Organic Elemental Analyzer (like the one shown in **Figure 3.8**) was used for the CNHS analyses.



Figure 3.8. A photograph of a Carlo Erba EA 1108 Organic Elemental Analyzer like the one that was used in these studies.

In each case, a small mass of fine powder sample (*ca*. 2 mg) was placed into a polymer-based specimen holder and placed into the instrument for analysis.

3.2.10 Ultra-violet diffuse reflectance spectroscopy (UV-DRS)

UV-DRS operates on the principles of the excitation of electrons in the valence orbitals into empty orbitals and the relative difference in the amount of light reflected off the surfaces of the samples.[1,3,17] For instance, a sample that possesses components whose electronic energy (band gap) levels are equivalent to quanta in the visible or ultraviolet region, will absorb some of the incident rays of radiation energy resulting in the excitation of electrons from the valence band into the unoccupied conduction band.[1,3,17] This results in a reduction in the quantity of radiation at that particular wavelength which is measured relative to the incident light. Indeed it can be said that the % transmission/reflectance of the incident light has decreased.

The percentage of diffuse reflectance data can be converted into Kubelka-Munk units, for an infinitely thick layer. This is achieved by using the Kubelka-Munk equation:[6,18]

$$K = \frac{(1-R)^2}{2R} = F(R) \qquad \textbf{(3.2.10.1)}$$

Where:

K is the reflectance according to Kubelka-Munk

R is the percentage of reflectance (%)

$F(R)$ is the Kubelka-Munk function

The absorption coefficient (α) and band gap energy (E_g) are then connected in accordance to the equation:

$$\alpha h\nu = A(h\nu - E_g)^n \qquad \textbf{(3.2.10.2)}$$

Where:

The absorption coefficient is given by α

A is a constant value

E_g is the band gap

hν is the band gap

n is a constant governed by the nature of the band-gap transition mode, where $n = 2$ for titanium dioxide.

In the case of crystalline materials that scatter light in a perfectly diffused way, the value of K equals that of α, and thus equation **3.2.10.2** can be written as follows:

$$A(hv - E_g)^n = [F(R)hv]^{1/n} \quad \textbf{(3.2.10.3)}$$

In these studies the band gaps of the potential photocatalysts that were synthesized were evaluated from Tauc plots, i.e. $[F(R)hv]^n$ against the photon energy, where the zero intercept on the plot is the band edge of the material.[1] Analyses of these potential photocatalysts were carried out using a Praying Mantis Cary 500 UV-DRS, (**Figure 3.9**). In each case, the powder samples of these potential photocatalysts were analyzed without any preparation.



Figure 3.9. A photograph of the Praying Mantis Cary 500 UV-DRS that was used in these studies.

3.3 Photocatalytic degradation

The performances of the various potential photocatalysts that were synthesized were assessed by monitoring the rate of the photodegradation of BPA under simulated sunlight conditions using a Newport model 69911 solar simulator (**Figure 3.10**). The radiation used in these photocatalytic experiments was supplied by a 300 W Xe short arc lamp (Eurolux), with 3 W of radiant flux, which was kept 15 cm from the quartz reaction vessel. In this way, radiation of 1000 $W.m^{-2}$ was supplied to the quartz reaction vessel (with an 80 mL capacity). An Oriel PV reference cell system, consisting of a 2 cm × 2 cm monocrystalline silicon photovoltaic cell, was used to set the Newport solar simulator irradiance to an equivalence of 1 sun.



Figure 3.10. A photograph of the Newport model 69911 solar simulator that was used in these studies.

Various masses of potential photocatalysts were added to 50 ml of BPA that was kept at different concentrations in the reactor vessel. Each suspension, that was prepared in this way, was magnetically stirred in the dark for 2 h prior to photocatalytic experiments. This was done to ensure that an adsorption-desorption equilibrium had been attained. The

details of the concentrations and reaction times are supplied in the subsequent results chapters. During photocatalytic experiments (i.e. illumination), 1 ml of the suspension was sampled periodically using a syringe which was fitted with 0.25 µl syringe filters (PALL, life sciences Acrodis PSF syringe filters). These samples were analyzed by high-performance liquid chromatography (HPLC) coupled with a Photodiode Array Detector (UltiMate 3000). In all cases, the photodegradation of BPA was monitored at 225 nm. Samples were eluted using a gradient method at a flow rate of 0.2 ml/min using a Phenomenex LUNA 5µ C18 reverse phase column (150 µm x 4.60 mm). Initially, 70 % ultra-pure water and 30 % acetonitrile were used for 6 min. Thereafter a gradual increase from 30 % acetonitrile to 90 % was scheduled over 2 min, which was then held constant for 1 min. This was then followed by an 8 min decrease in the ratio of acetonitrile from 90 % to 30 % that was finally held for 3 min.

3.4 References

1. Kuvarega, A. T. Photocatalytic performance of nitrogen-platinum group metal co-doped TiO_2 supported on carbon nanotubes for visible-light degradation of organic pollutants in water. (University of Johannesburg, 2012).

2. Franklyn, P. Hydrothermal synthesis and characterisation of titania nanoparticles. (University of the Witwatersrand, 2004).

3. Dlamini, N. L. Doped nanotitanium dioxide for photocatalytic applications. (University of Johannesburg, 2012).

4. Egerton, R. F. *Physical principles of electron microscopy: an introduction to TEM, SEM, and AEM*. (2006). Springer Science & Business Media

5. Franklyn, P. Synthesis, Characterization and Structural Investigations of Nanoparticulate forms of selected (W,Ti,Al,Ba) Mixed Metal Oxides. (University of Cambridge, 2011).

6. Gareth, T. & Goringe, M. J. *Transmission electron of microscopy of materials*. (1979).

7. Yin H, Wada Y, Kitamura T, Kambe S, Murasawa S, Mori H, Sakata T, Yanagida S. Hydrothermal synthesis of nanosized anatase and rutile TiO_2 using amorphous phase TiO_2. *Chem. Mater.* **11**, 1694-703 (2001)

8. Kademani BS, Kalyane VL, Kademani AB. Scientometric Portrait of Nobel Laureate Dr. CV Raman. *Indian Journal of Information Library and Society*. **7**, 215-49 (1994).

9. Singh R. CV Raman and the Discovery of the Raman Effect. *Physics in Perspective*.

4. 399-420 (2002).

10. Hodkiewicz, J. & Scientific, T. F. Characterizing Carbon Materials with Raman Spectroscopy. *Thermo Scientific Application Note* (2010).

11. Zhang, W. F., He, Y. L., Zhang, M. S., Yin, Z. & Chen, Q. Raman scattering study on anatase TiO_2 nanocrystals. *J. Phys. D. Appl. Phys.* **33,** 912–916 (2000).

12. Ravindran T. R., Jackson B. R., Badding J. V. UV Raman spectroscopy of single-walled Carbon nanotubes. *Chem. Mater.* **13**, 4187-91 (2001).

13. Dresselhaus, M. S., Dresselhaus, G, Saito, R, Jorio, A. Raman spectroscopy of carbon nanotubes. *Physics reports* **409**, 47-99 (2005).

14. Misra, A., Tyagi, P. K., Singh, M. K. & Misra, D. S. FTIR studies of nitrogen doped carbon nanotubes. *Diam. Relat. Mater.* **15,** 385–388 (2006).

15. Dixon Dikio, E. & Shooto, N. D. Raman and TGA Study of Carbon Nanotubes Synthesized Over Mo/Fe Catalyst on Aluminium Oxide, Calcium Carbonate and Magnesium Oxide Support. *Chem Sci Trans* **2,** 1160–1173 (2013).

16. Khatri, C., Mishra, M. K. & Rani, A. Synthesis and characterization of fly ash supported sulfated zirconia catalyst for benzylation reactions. *Fuel Process. Technol.* **91,** 1288–1295 (2010).

17. Tetana, Z. N. Boron and nitrogen doped carbons for photochemical degradation reactions. (University of the Witwatersrand, 2013).

18. Murphy, A. B. Band-gap determination from diffuse reflectance measurements of semiconductor films and applications to photoelectrochemical water splitting. *Sol. Energy Mater. Sol. Cells* **91,** 1326–1337 (2007).

CHAPTER 4:

Morphological and crystallinity differences in NCNTs synthesized by CVD of melamine over coal fly ash†

† Parts of this chapter were published in *RSC Advances* 6 (80), 76773-76779 (2016)

4.1 Introduction

Coal fly ash (CFA) is an industrial by-product that is generated during the combustion of ground coal in thermoelectric coal powered stations.[1,2] Inorganic minerals form the major part of CFA, accounting for 90-99 % of its matrix, whereas organic and fluid components account for 1-9 % and 0.5 % respectively.[3–5] CFA is a powdery material consisting of mainly spherically-shaped porous solid and hollow aluminosilicate particles.[5] The chemical composition of CFA consists of inorganic oxides such as silica, alumina, haematite, lime, magnesium oxide, potassium oxide and titania amongst others.[3–6] The reclamation of CFA is vital because of the 800 Mt of CFA produced globally each year only 25 % is reused, with the rest being disposed of in landfills and ash ponds.[7]

Several researchers have demonstrated that CFA can be used in catalysis.[3,8–12] For instance Xiaoping Xuan *et al*. investigated the selective catalytic reduction of NO with NH_3 using Fe, V, Ni and Cu supported on CFA.[8] CFA has also been shown to be a visible light photocatalyst and has been used to degrade 60% of 0.1 mM thionine solution in 4 hrs.[9] However, few reports on the synthesis of carbon nanomaterials (CNMs) from CFA have been made. Dunens *et al*. reported on the fixed bed catalytic CVD synthesis of carbon nanotubes (CNTs) through the decomposition of acetylene on Fe-impregnated CFA.[10] On the other hand, various

carbon nanomaterial morphologies: ropes, branches, whiskers, and graphene sheets have been observed when polyvinyl alcohol and fly ash films were subjected to pyrolysis at 500 °C for 10 min in a nitrogen atmosphere.[11] Carbon nanofibers (CNFs) have been synthesized by the decomposition of acetylene on fly ash in a reducing gas atmosphere by CVD.[12] On the other hand, in our group, it has been shown that the yields of CNFs can be enhanced by pre-treating CFA with CO_2 before the introduction of C_2H_2 and H_2.[13] Saudi Arabian and Japanese CFA have also been used to synthesize CNTs.[14,15] Salah *et al*. have also optimized the synthesis parameters such as temperature, gas pressure, growth times, and gas flow rates for the decomposition of C_2H_2 in the presence of H_2 for the growth of MWCNTs on carbon-rich CFA by low-pressure chemical vapor deposition (LPCVD).[14]

Since the rediscovery of carbon nanotubes (CNTs) by Iijima in 1991,[16] a great deal of research has been focused on fine-tuning the chemical properties of CNTs for various applications. One method which has been employed has been the manipulation of the chemical properties of CNTs by doping them with heteroatoms such as nitrogen and boron.[17] For instance, NCNTs have been shown to have a strong affinity to metals, which has resulted in good dispersion of metal nanoparticles on their surfaces for applications in catalysis.[18] The optical and electronic properties of CNTs have also been shown to be improved by N-doping.[19] Chemicals such as pyridine, aniline, ammonia, melamine, and acetonitrile have been used, amongst others, as precursors for the synthesis of NCNTs.[20,21] In this study, melamine was used as a lone carbon and nitrogen source. Melamine is an organic molecule which has 67 % nitrogen by mass, similar to that of carbon nitride (C_3N_4).[22]

Low-cost production of NCNTs is a desirable prospect as the current methodologies require the use of expensive precursors and catalysts. Since the cost of melamine is relatively low and fly ash is practically free, this serves as an opportunity to deal with the above-mentioned limitations. In this chapter, a two-stage CVD synthesis of NCNTs from melamine over CFA has been reported for the first time. Here the effects of synthesis temperature on the morphology, crystallinity, and amount of nitrogen incorporated into these NCNTs were also investigated.

4.2 Experimental

4.2.1 Preparation of materials

In this study, a two-stage furnace with separate controllers was used for the CVD synthesis of NCNTs (refer to **A.3.1.** for a schematic diagram of the two-stage furnace CVD synthesis). A mass 1 g of melamine was weighed into a quartz boat which was placed into a quartz reactor tube and inserted in the middle of the first-stage furnace. A second quartz boat containing a mass of 0.5 g of unreacted CFA (i.e. used as supplied by ESKOM before being exposed to acetylene and hydrogen) was placed in the middle of the second-stage furnace. Nitrogen gas (carrier gas) was introduced into the quartz reactor tube through the inlet at a flow rate of 50 ml/min throughout the duration of the experiment. The second-stage furnace was initially heated, at a heating rate of 10 °C/min, to 800, 850 or 900 °C for the three separate experiments. Once the second-stage furnace had reached its set temperature, then the first-stage furnace with melamine was always rapidly heated to 350 °C at 35 °C/min in order to vaporize melamine. Gaseous melamine was then carried by

nitrogen gas into the second stage furnace to react with CFA (**A.3.1**). Black product was collected in the second stage furnace (CFA furnace).

CFA is an inhomogeneous material, as such, there were slight inconsistencies in the results obtained. Nevertheless, the results reported in this chapter are the best representation of the triplicate experiments that were conducted. For comparison, NCNTs were also synthesized using a more traditional catalyst i.e. 5 % Fe/$CaCO_3$ instead of CFA using exactly the same conditions as described previously. The catalyst was prepared by incipient wet impregnation. Herewith, $FeCl_2$ was dissolved in water and added slowly to solid $CaCO_3$, whilst stirring thus creating a slurry. The slurry was then oven dried at 110 °C before calcining at 500 °C for 2 h.

4.2.2 Material characterization

The materials synthesized in this study were characterized using several different techniques as described in **Section 3.2**.

4.3 Results and discussion

4.3.1 Fly ash characterization

The CFA used in this study, which came from the ESKOM's power station in South Africa (hereafter referred to as CFA), was analyzed by XRF (**Table 1**). Based upon the chemical abundance of silica, alumina and iron oxide that was detected by the XRF analysis of the unreacted CFA it was determined to belong to the pozzolanic class F category. Class F CFA is usually obtained from the combustion of anthracite and bituminous coal, which is South Africa's main export coal.[23,24] Of great

importance to this study was the observation from the XRF analysis that iron-related materials (i.e. Fe_2O_3 and FeO) together with silica and alumina were present (**Table 1**). This was desirable as iron has been shown to be an active catalyst in the CVD synthesis of CNMs, while silica and alumina have been used as catalyst supports in such reactions.[25–27]

Table 4.1. Composition of unreacted CFA as determined by XRF spectroscopy.

Mineral	%/mass
SiO_2	58.14
Al_2O_3	28.79
Fe_2O_3	0.57
FeO	4.64
MnO	0.047
MgO	1.04
CaO	3.5
Na_2O	0.05
K_2O	0.77
TiO_2	1.57
P_2O_5	0.7

PXRD is one of the most common and widely used techniques for the quantitative and qualitative analysis of CFA. It is mostly used to characterize the mineral matter and to a lesser extent, to study the inorganic amorphous matter and organic matter present in CFA. The advantage of using PXRD for the analysis of CFA is the detection of the amount and degree of crystallinity of the major and some of the minor minerals that form. **Figure 4.1** is a PXRD pattern that was obtained and which indicated that the main mineralogical constituents of the unreacted CFA were: quartz, mullite, hematite, and magnetite. Peaks which could be correlated to magnesium oxide, potassium oxide, and sodium oxide were also observed. The peaks were not identified on the diffraction pattern because they were

small relative to the identified peaks. The percentage mass reported here did not include that of C, H, and N because of the limitations of XRF with regards to these elements.

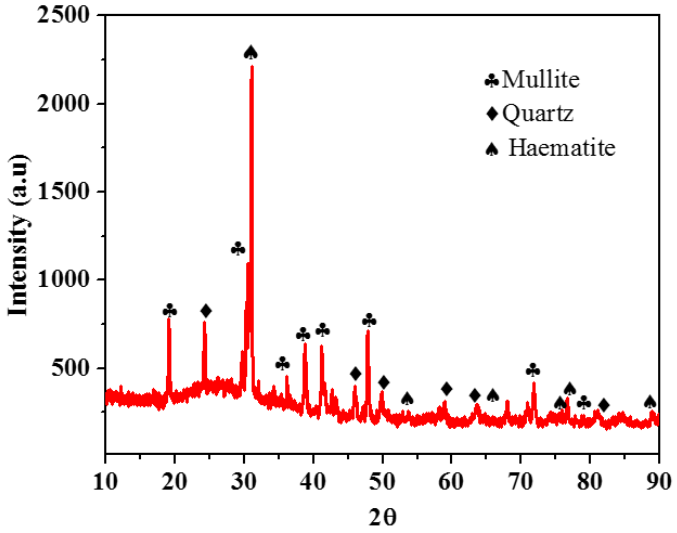

Figure 4.1 PXRD pattern of unreacted CFA.

TEM and SEM are of the best and of the most widely used techniques for studying CFA. Studies have shown that the morphology of CFA has been determined by the pyrolysis and cooling temperatures of coal.[4] SEM micrographs revealed that unreacted CFA was mostly dominated by spherical particulates which had diameters that ranged between 1- 15 µm (**Figures 4.2 (a)-(c)**). Particulates which were suspected to have been soot aggregates (**Figure 4.2 (d)**) were found to be smaller than the spheres, with diameters which ranged between 20 nm and 1000 nm and have been reported to have formed during the quenching and homogeneous condensation of carbonaceous materials at high temperature in the presence of oxygen.[25]

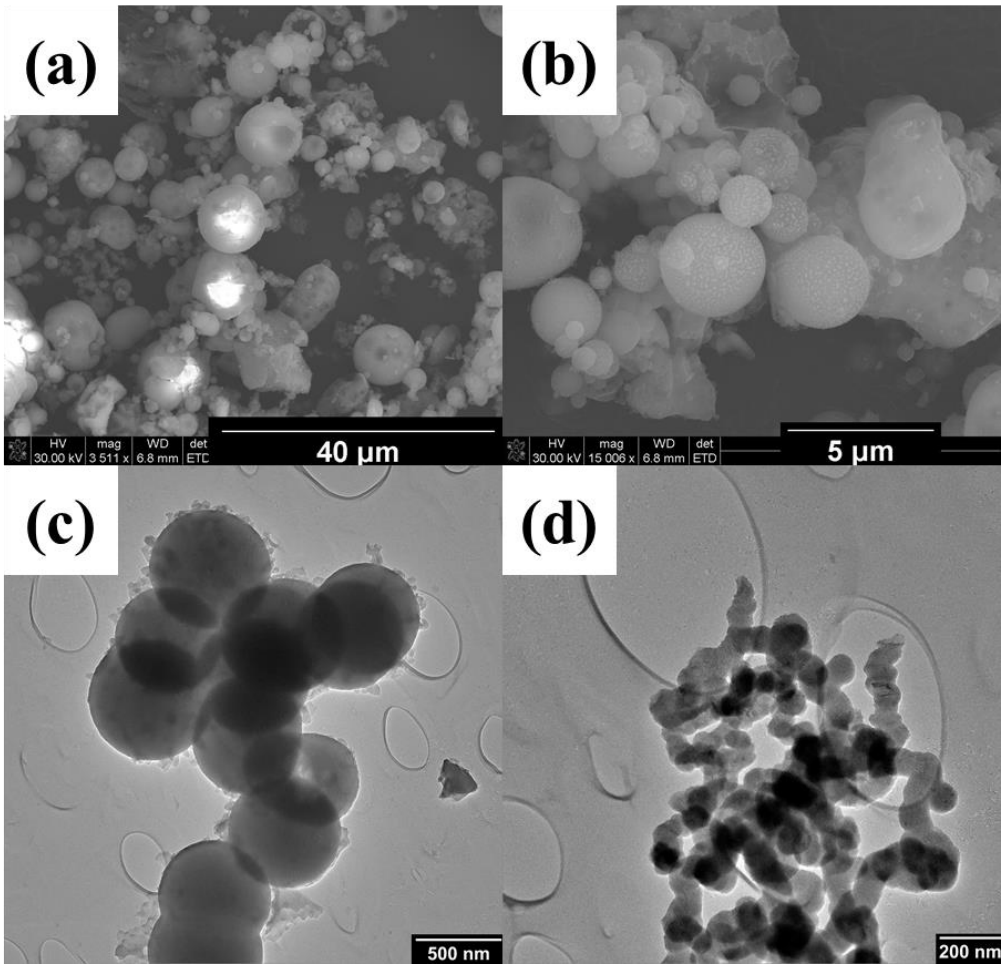

Figure 4.2 (a)-(b) SEM micrographs of CFA and (c)-(d) TEM micrographs of unreacted CFA and soot aggregates therein.

The chemical composition of unreacted CFA was found to be complex as it was composed of many different types of oxides. As such the resulting laser Raman spectrum was found to be complicated and had overlapping peaks. Nevertheless, several of these were identified and indexed when the laser-Raman analysis was performed (**Figure 4.3**). These peaks reflected the presence of quartz, iron oxide, calcite (a crystalline calcium carbonate phase) and hydroxides of aluminum and calcium.

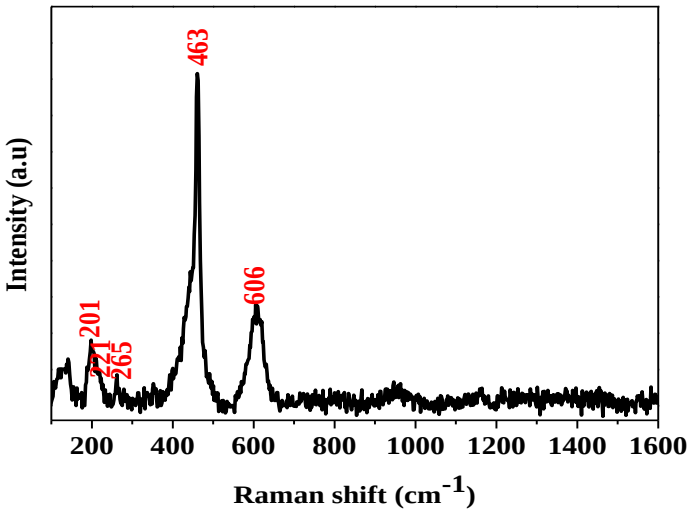

Figure 4.3. Laser Raman spectroscopy spectrum showing inorganic constituents of unreacted CFA.

For instance, the main peak in the Raman spectrum shown in **Figure 4.3** appeared at 463 cm^{-1} which was attributed to quartz (SiO_2). Additional peaks characteristic of SiO_2 were also observed at 202 and 265 cm^{-1}. Similarly, as identified by XRF, a major peak for haematite was observed at 606 cm^{-1}, with a minor peak at 221 cm^{-1}. While these results were consistent with those of Guedes *et al*., who analyzed low sulphur coals from South Africa, Colombia, and Australia, it was noted that due to compositional differences in these coals several of the peaks that they observed for other constituents were not present in the CFA.[28]

Laser Raman analysis of the unreacted CFA in areas dominated by carbonaceous materials yielded a spectrum with two peaks which have previously been used to study and characterize carbonaceous materials.[29–32] Here the D peak was observed to have had a centroid at 1367 cm^{-1} and the G peak one at 1607 cm^{-1} (**Figure 4.4**). As can be observed in **Figure 4.4** the intensities of these peaks were very low. This was as expected as it is known that only minute traces of carbon remain after the combustion of coal, to result in

CFA. It was also observed that these peaks were "skewed". This was particularly true for the D peak (i.e. the distorted peak at 1367 cm^{-1}) which suggested that low levels of fairly crystalline carbonaceous material were present. This too was consistent with results obtained by Guedes *et al*., who identified that different types of carbon (e.g. char, soot, etc.) were present in CFA, after the coal combustion process.[28]

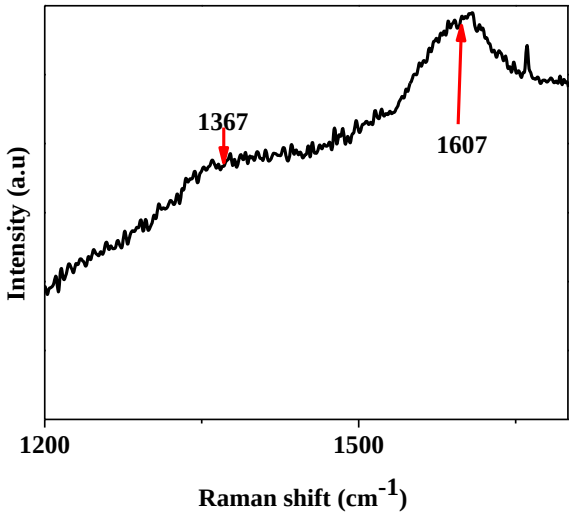

Figure 4.4. A laser Raman spectrum showing the D and G peaks of carbonaceous materials in unreacted CFA.

The FTIR spectrum of CFA consisted of two main peaks, which were intense and broad at wavenumbers of 787 cm^{-1} and 1090 cm^{-1} (**Figure 4.5**). The two peaks were characteristic of internal vibrations in MO_4 tetrahedra, where, M was Al or Si .[33] The peak with a centroid at 787 cm^{-1} was attributed to the vibrations of the M-O bond which signified the inner distortion vibration modes.[33] Similarly, the peak observed at 1090 cm^{-1} was attributed to the asymmetric stretching vibrations of the M-O bond.

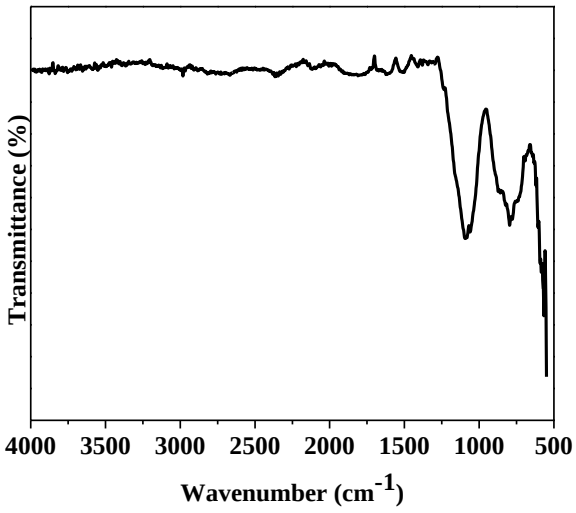

Figure 4.5 A FTIR spectrum of unreacted CFA.

The wide bands that were seen in **Figure 4.5** have been reported before. For instance, Criado *et al*., have conducted a detailed study of CFA to identify which bands may have overlapped to give rise to these characteristic broad and intense peaks.[33] Here they reported that the presence of SiO_2 in CFA gave rise to a succession of bands situated at 1150, 1084, 796–778, 697, 668, 522 and 460 cm^{-1}.[33] The presence of mullite, in turn, was accountable for a sequence of bands at approximately 1180–1130 cm^{-1} and 560–550 cm^{-1}.[33] Similarly it was found that the bands generated by quartz, mullite and the vitreous phase of the CFA overlapped in the area between 1200 and 900 cm^{-1}.[33] Since quartz and mullite were both present in the unreacted CFA (see **Figure 4.1**) it was concluded that the broad peaks observed in **Figure 4.5** were consistent with those identified by Criado *et al*. [33]

Unreacted CFA was also characterized by TGA in order to study its thermal properties. The thermogram and weight derivative plot of the unreacted CFA are shown in **Figures 4.6 and 4.7** respectively. The thermogram **(Figure 4.6)** showed

that the unreacted CFA was thermally stable, as less than 7 % of it burned when it was heated from 30 °C to 900 °C in air. Indeed, even this mass loss was attributed to the unburned carbon that was present in unreacted CFA (which originated from the combustion of coal), as was previously identified by TEM and laser Raman spectroscopy.

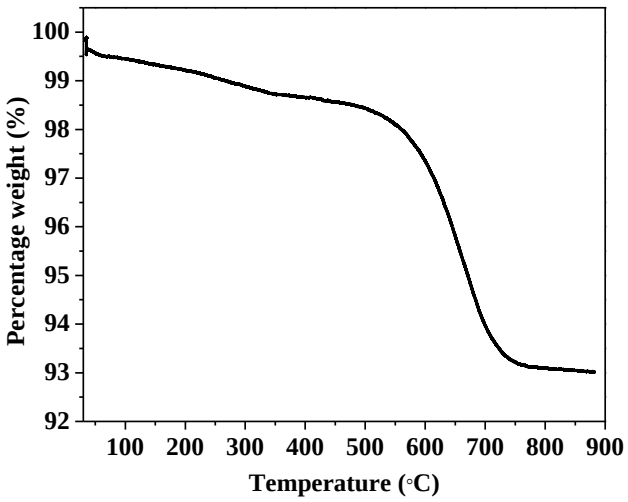

Figure 4.6. A thermogram of unreacted CFA

The maximum combustion temperature of the unburned carbonaceous materials that were present in the unreacted CFA (i.e. c.a. 675 °C) was obtained from the weight derivative plot (**Figure 4.7**). This showed that the carbonaceous material in the unreacted CFA was highly stable and crystalline, as was confirmed by laser Raman spectroscopy.

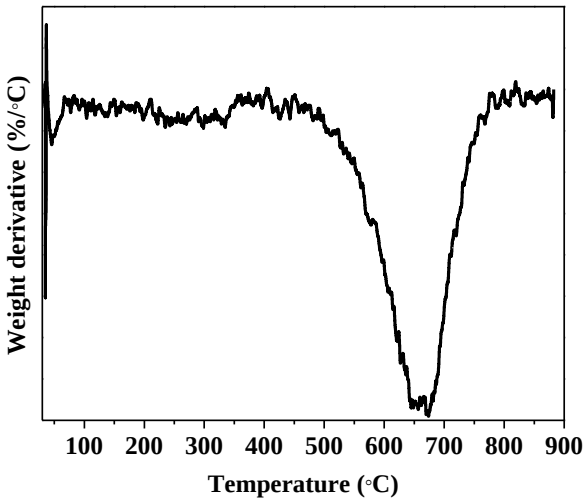

Figure 4.7 Weight derivative plot of unreacted CFA

4.3.2 Characterization of the products formed over CFA in the two-stage CVD reactor

When melamine was decomposed on the surface of CFA in a two-stage CVD setup at various temperatures (800, 850 and 900 °C), a black product was formed. This black product was collected and analyzed using a variety of techniques. All through these experiments, it was observed that the typical masses of these black products, that were synthesized, increased as a function of the synthesis temperature (**Table 4.2**). This was attributed to the increased rate of decomposition of melamine on the CFA catalyst surface at higher temperatures. It is noteworthy that the yields calculated included the amount of unburned carbon that was already present in CFA, nevertheless, the trends reported were accurate as the "same" CFA was used for the synthesis of all samples.

Table 4.2. Masses and percentage yields of black products that were formed.

Synthesis temperature/°C	**Mass/g**	**Yield/%**
800	55	24
850	112	31
900	310	44

The percentage yield of the black products which had formed at various temperatures was calculated using **equation 4.1**. The percentage yields as a function of temperature were also shown in **Table 4.3**.

$$\%\ \boldsymbol{yield} = \frac{\boldsymbol{M_1 - (M_2 + M_3)}}{\boldsymbol{M_1}} \times \mathbf{100}\ \% \qquad \mathbf{4.1}$$

Where,

M_1= initial mass of melamine weighed into furnace 1 (**A.3.1**)

M_2= mass of black product collected from furnace 2, excluding that of CFA (**A.3.1**)

M_3= mass of melamine unused weighed from furnace 1 after reaction (**A.3.1**)

The resultant samples were characterized as they were without the dissolution of CFA to separate it from the black product. The PXRD patterns of the CFA together with the black products (which had been synthesized at various temperatures) are shown in **Figure 4.8**. Here it was observed that the patterns were similar irrespective of the reaction temperature and that they strongly resembled those of the unreacted CFA (**Figure 4.1**). However, in each case a broad peak at 27° (2θ), which has been attributed to carbonaceous materials,

was observed.[12] Hence it was suspected that the black products, which had formed once melamine had decomposed over CFA, were carbonaceous. It is noteworthy that a broad shoulder was observed on the PXRD pattern of CFA (**Figure 4.1**), it less intense relative to those of the products formed by the decomposition of melamine on the CFA surface.

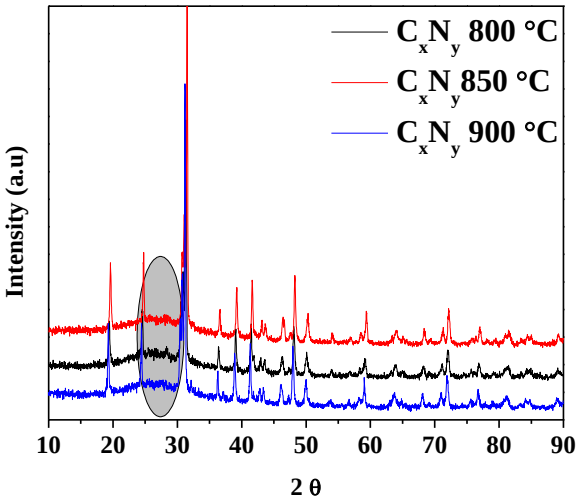

Figure 4.8. PXRD pattern of CFA together with the black products which had been synthesized at 800, 850 and 900 °C.

The products issued by decomposition of melamine were then analyzed by CHNS elemental analysis in order to ascertain if nitrogen from the melamine (67 % nitrogen by mass), had been incorporated into them when they formed. The results shown in **Table 4.3** indicated that the black products which had formed were composed of both carbon and nitrogen. Furthermore, it was found that the carbonaceous products synthesized at 850 °C contained the most nitrogen, whereas the nitrogen content of the carbonaceous materials synthesized at 800 °C had the least. The carbonaceous materials synthesized at 900 °C were found to have a nitrogen content that was intermediate between the other two.

Table 4.3. Percentage nitrogen present in the carbonaceous materials as determined by the CHNS analysis.

Synthesis temperature/°C	Nitrogen content/%
800	1.10 (±0.12)
850	3.16 (±0.11)
900	1.95 (±0.09)

The nitrogen-containing carbonaceous (i.e. C_xN_y) materials were then analyzed by FTIR (**Figure 4.10**).

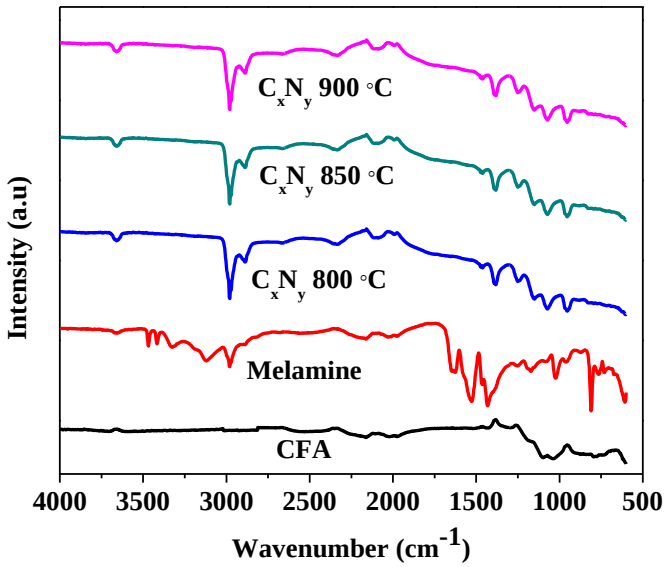

Figure 4.9. FTIR spectra of unreacted CFA, melamine and the C_xN_y materials that were synthesized at different temperatures.

Here it was found that the FTIR spectra of the C_xN_y materials were substantially different from that of melamine or unreacted CFA (the latter was discussed in detail in **section 4.3.1**). For instance, the bands that were present in the melamine absorption spectra in the 3000-3500 cm^{-1} region were not present in the spectra of the C_xN_y materials. This suggested that all the N-H bonds present in melamine had been destroyed during the decomposition of melamine over the surface of CFA. On the other hand, a few more absorption bands in the 1000-1800 cm^{-1} were present in the FTIR spectrum of the C_xN_y materials. This confirmed that these black colored products were not unreacted melamine, but were, in fact, new nitrogen-containing carbonaceous products. Indeed Y.C. Zhao *et al.* made the same observation when they compared the FTIR spectra of melamine and turbostratic carbon nitride that had been prepared from melamine.[35] Here Y.C. Zhao *et al* attributed the extra absorption peaks to the condensation of the melamine triazine skeletal structure.[35]

The C_xN_y materials were then characterized using SEM in order to study their morphological and structural properties. The SEM micrographs of the C_xN_y materials that were synthesized at various temperatures are shown in **Figure 4.10**. Based upon these micrographs it was observed that the C_xN_y materials were tubular in shape and were, in fact, nitrogen-doped carbon nanotubes or NCNTs. The NCNTs synthesized at 800 °C (**Figure 4.10 (a)**) were found to be 'smooth surfaced', with tube diameters that ranged between 40-100 nm (average tube diameter 85 nm). On the other hand, the NCNTs synthesized at 850 and 900 °C (**Figure 4.10 (b)-(c)**) were "irregular" and had groves on their surfaces. The tube diameters of the NCNTs synthesized at 850 °C (**Figure 4.10 (e)**) ranged between 28 and 44 nm (average tube diameter of 40 nm). In the case of NCNTs synthesized at

900 °C, their tube diameters (**Figure 4.10 (f)**) were found to range between 35 and 75 nm (average tube diameter of 45 nm).

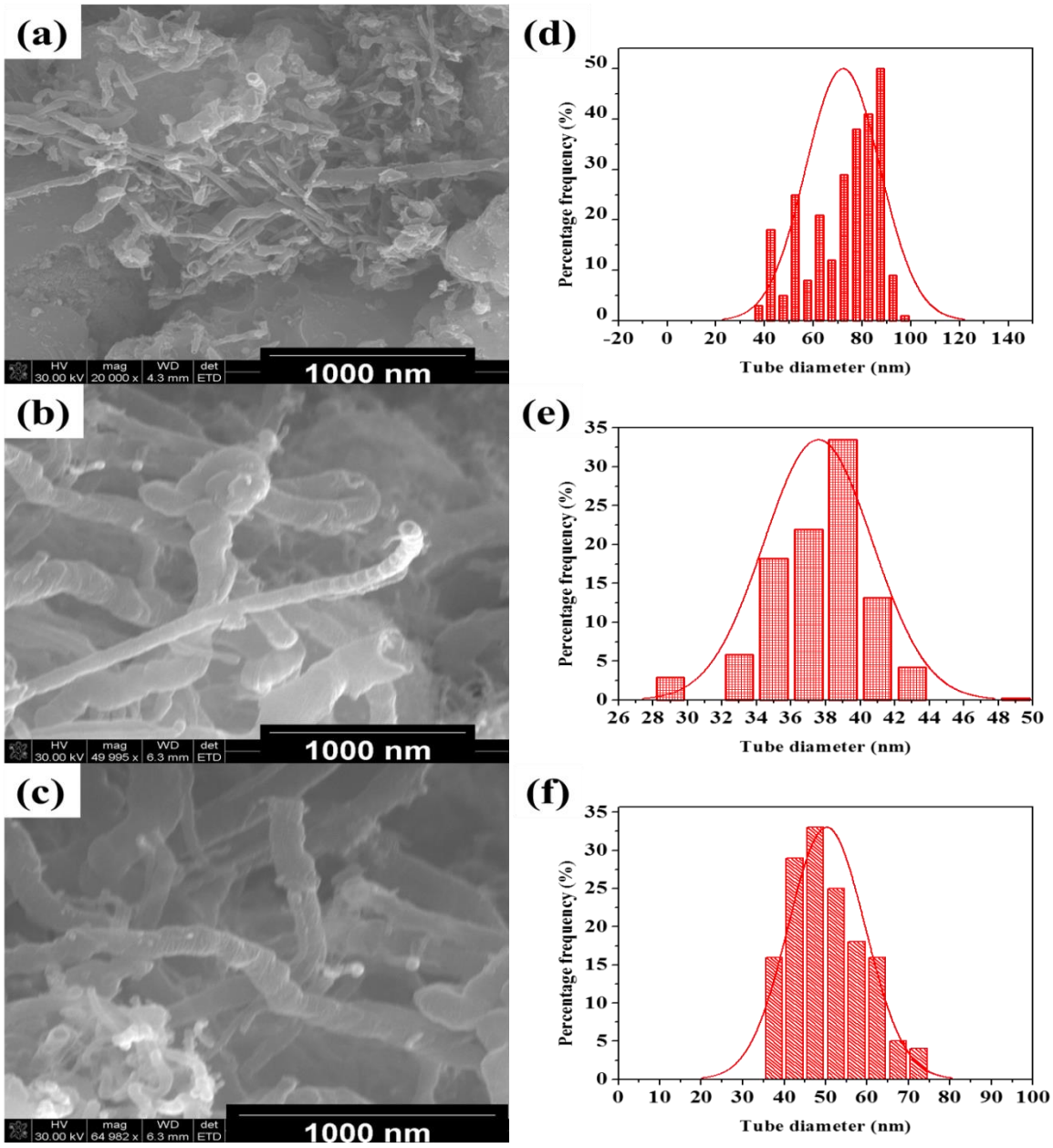

Figure 4.10. SEM micrographs and tube diameter ranges of the NCNTs that were synthesized at: 800 °C (a) & (d), 850 °C (b) & (e), 900 °C (c) & (f).

These NCNTs were also analyzed using TEM in order to further study their morphological properties (**Figure 4.11 (a)-(f)**).

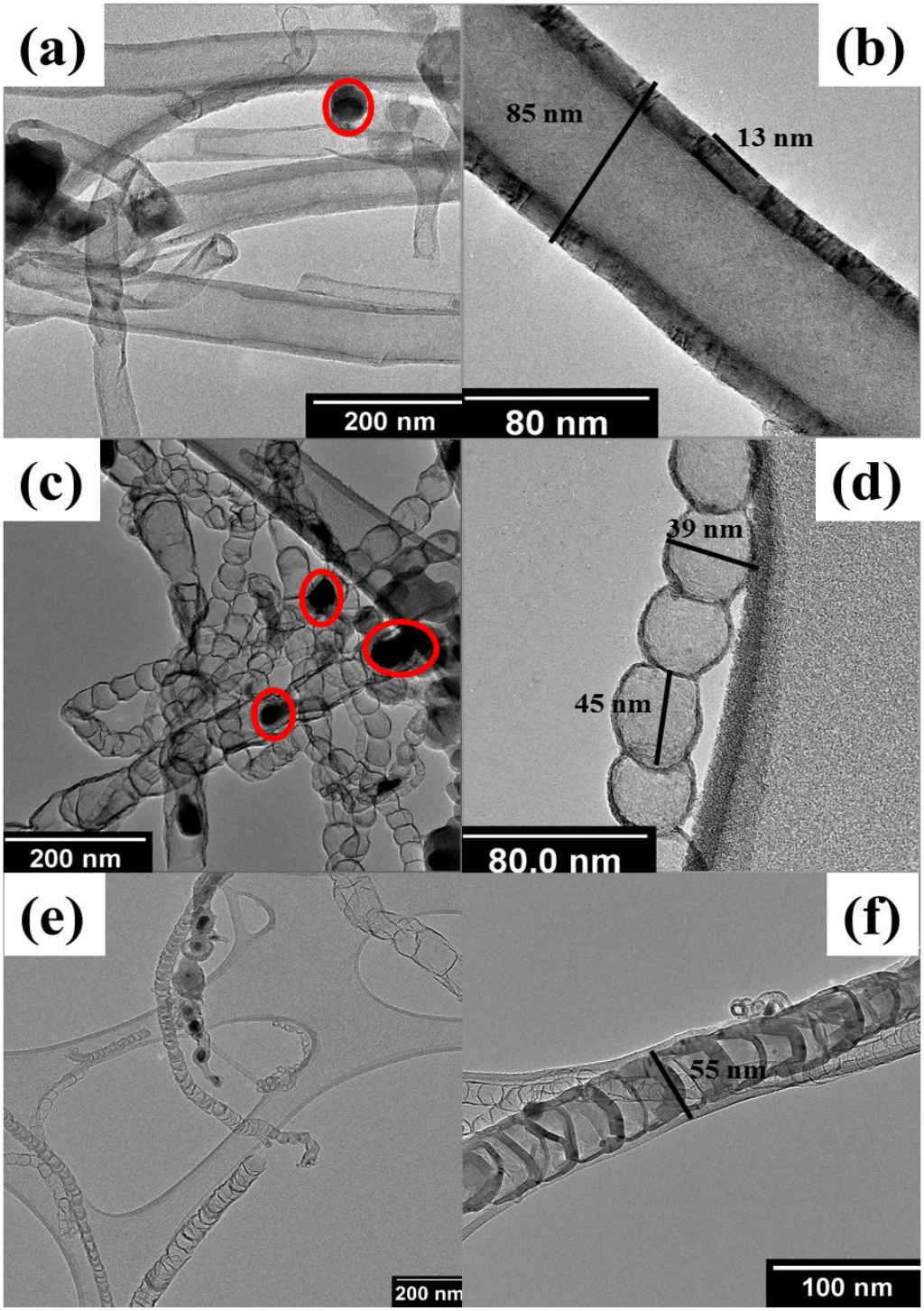

Figure 4.11. TEM micrographs of NCNTs that were synthesized at: 800 °C (a)-(b), 850 °C (c)-(d) and 900 °C (e)-(f).

Since CHNS analysis (**Table 4.3**) had already confirmed that the CNTs that were synthesized at 800 °C contained nitrogen i.e. they were NCNTs, it was considered unusual that they appeared to have had morphologies that were similar to those of MWCNTs i.e. without bamboo segments (**Figure 4.11 (a)-(b)**). However, these same morphologies have been observed when low levels of N were found to have been incorporated into such tubes after iron had been used as a catalyst.[19] Similarly, NCNTs without the typical bamboo morphology have also been observed from Ni and Co catalysts.[36] The walls of the NCNTs synthesized at 800 °C were thick i.e. an average of 13 nm, appeared crystalline and had diameters which ranged between 74 and 96 nm.

In the case of the NCNTs that were synthesized at 850 °C and 900 °C (**Figure 4.11(c)-(f)**), these had the typical morphology of NCNTs, i.e. they were compartmentalized. [37–42] However, differences in the morphologies of the NCNTs synthesized at 850 and 900 °C were noted. The majority of the NCNTs synthesized at 850 °C were found to have a morphology that could be likened to that of a chain that had circular hollow compartments strung together to form a tube (**Figure 4.11 (c)-(d)**). On the other hand, the majority of the NCNTs synthesized at 900 °C consisted of tubes with what appeared to be well-ordered walls and separate hollow cone-like bamboo compartments (**Figure 4.11 (e)-(f)**).

Hao Liu *et al*. have observed similar morphological differences to these and attributed them to the amount of nitrogen incorporated into the cylindrical graphene materials that formed.[45] The more irregular morphologies (formed as a consequence of nitrogen replacing carbon), which were less crystalline, were reported to have contained higher concentrations of nitrogen.[38,43–45]

Likewise, Jang *et al*. showed that compartments like those seen in this research were attributable to the inclusion of C=N bonds in the graphene network.[43] Nxumalo *et al*. have also reported that the effects of nitrogen incorporation into the graphene network were more pronounced in the inner layers of such tubes i.e. their bamboo characteristics became more pronounced.[19] This was consistent with Jang *et al*. who showed that as the amount of nitrogen incorporated in the sp^2 graphene cylinders increased, the size of the bamboo compartments inside the tube decreased with an increased number.[43] In this research, both types of tubes synthesized at 850 and 900 °C had compartments which were typical of NCNTs, but the former was more well-spaced apart and appeared less crystalline than the latter, while their diameters ranged between 30 and 55 nm respectively. A schematic conceptualizing the differences in the morphology of the NCNTs synthesized at the different temperatures is given in **Figure 4.12**.

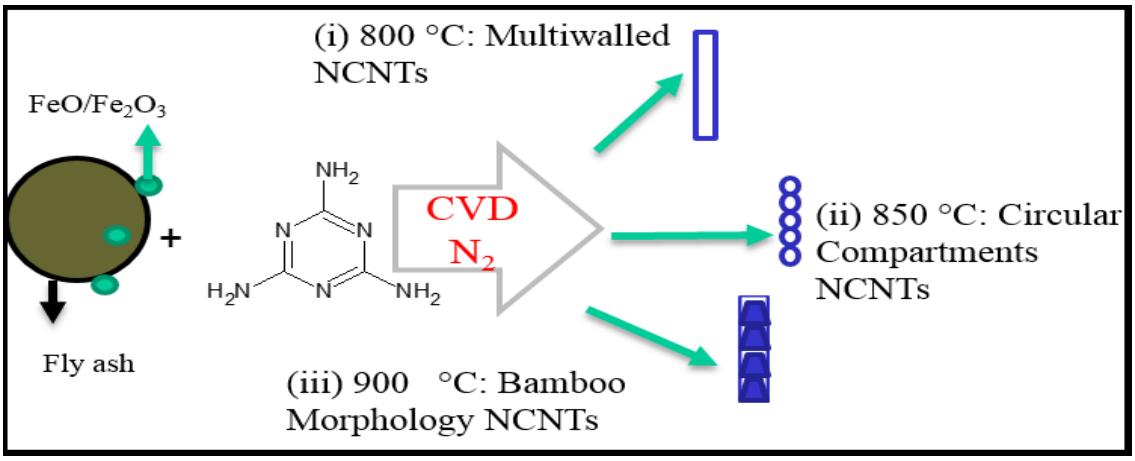

Figure 4.12. Schematic of reactions conducted at: (i) 800 °C where multiwalled NCNTs were formed, (ii) 850 °C where NCNTs with circular compartments were formed and (iii) 900 °C where NCNTs with typical bamboo morphology was formed.

The morphology of the NCNTs synthesized at 850 °C was considered to be interesting and therefore TEM was used to further study this. In **Figure 4.11 (c) & (d)** it was observed that these NCNTs were circular with hollow compartments. Indeed, when a tube with a broken compartment was examined by TEM (**Figure 4.13 (a))** it was confirmed that these compartments were hollow. Furthermore, it was observed that wherever each circular compartment ended a layer of graphitic walls, which separated each compartment from the next, was present (see red arrows in **Figure 4.13 (a) & (b))**. It was also observed (**Figure 4.13 (b)**) that the thickness of the outer walls (12 nm) was almost the same size as those of the groves that separated the hollow compartments i.e. 10 nm.

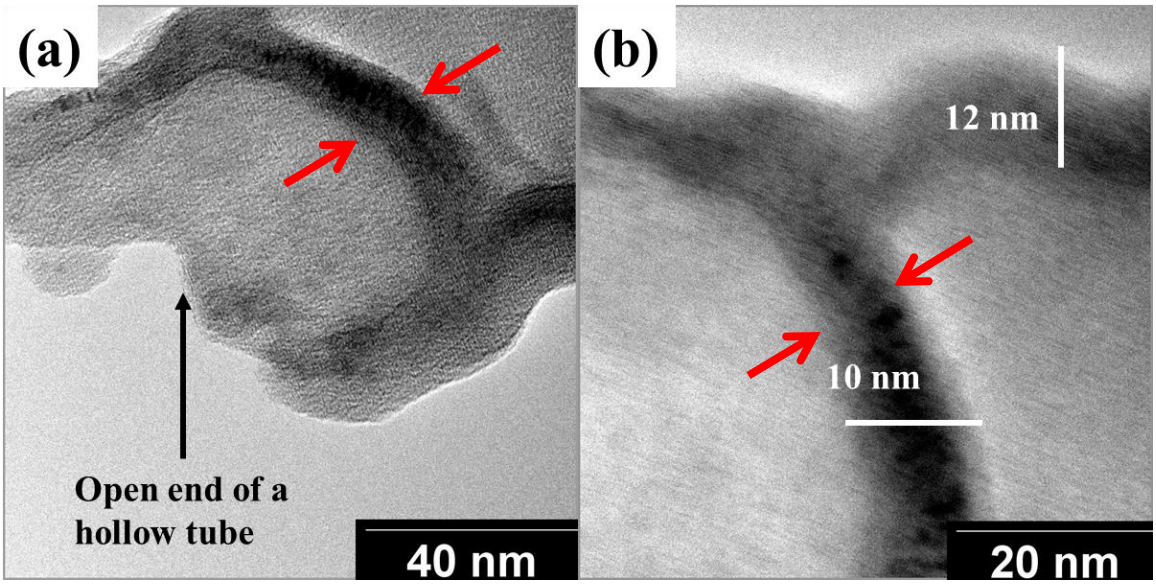

Figure 4.13. TEM micrographs of NCNTs synthesized at 850 °C

The exact mechanism by which these NCNTs had formed on the surfaces of the CFA catalysts, under these conditions, has not yet been fully determined. However, based on the observation that catalyst nanoparticles were detected inside and at the

tips of the NCNTs that had formed (circled in red in **Figure 4.11(a) & (c)**), it was hypothesized that the most probable mechanism for the growth of NCNTs by the decomposition of melamine on the surface of the CFA catalyst was tip growth.[12] Furthermore, since iron was present in the CFA (in the form of Fe_2O_3 and FeO), it is most likely that this catalyzed the tip growth of NCNTs by the decomposition of melamine. Indeed in a related study in our research laboratories, where acetylene was used as the carbon source and CFA as the catalyst, Hintsho *et al*. were able to show that Fe_3C (which had originated from the same iron oxides) had been linked to the tip growth of CNFs.[12] Similarly, Nath *et al*. have suggested the tip-growth of bundles of aligned NCNTs that were formed by the pyrolysis of pyridine on Fe/Co supported on silica, while several authors have reported the same for various catalysts.[46–48]

The NCNTs that were synthesized at different temperatures were then analyzed by laser Raman spectroscopy because this technique has been demonstrated to be useful for studying the irregularities and crystallinities of graphene-based materials.

The Raman spectra of the NCNTs that were synthesized at different temperatures are shown in **Figure 4.14**. In these spectra, the strong bands in the region of 1350 cm^{-1} were assigned as the D-bands, which have been reported to have arisen as a result of defects in graphene-based materials and have been affiliated with optical phonons close to the K-point of their Brillouin zone.[49] The bands that were observed in the region of 1580 cm^{-1} were denoted as the G-bands, which were Raman allowed and associated with the optical phonon modes of the E_{2g} symmetry in graphene-based materials.[40]

The integration of the normalized D and G-bands, to give an intensity ratio i.e. I_G/I_D, has been found to be dependent on the defects present in carbon nanomaterials and has been used to measure their crystallinity and defect-density.[50] The incorporation of nitrogen into the lattice of graphene-based materials is known to have resulted in the formation of defects in their structures.[18] Hence this has made it possible to use laser Raman spectroscopy to study the crystallinity, as well as to estimate the extent of nitrogen incorporation in the NCNTs that were formed in this study. Indeed, D and G bands were observed on the laser Raman spectra of the NCNTs (**Figure 4.14**) that were synthesized at various temperatures and the I_G/I_D ratio values were plotted and are shown in **Figure 4.15**.

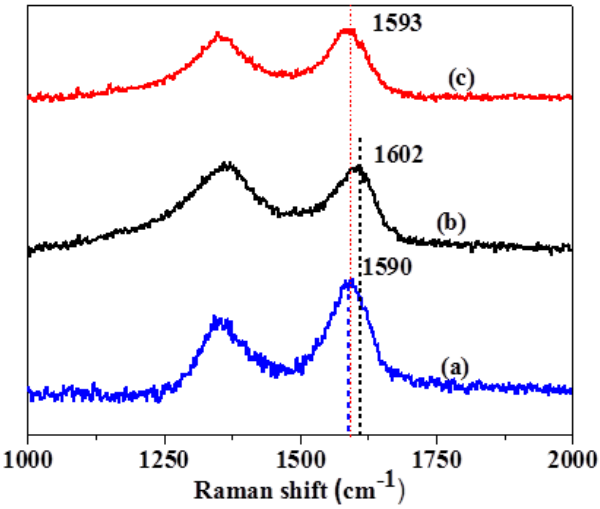

Figure 4.14. Laser Raman spectra of the NCNTs that were synthesized at (a) 800, (b) 850 and (c) 900 °C.

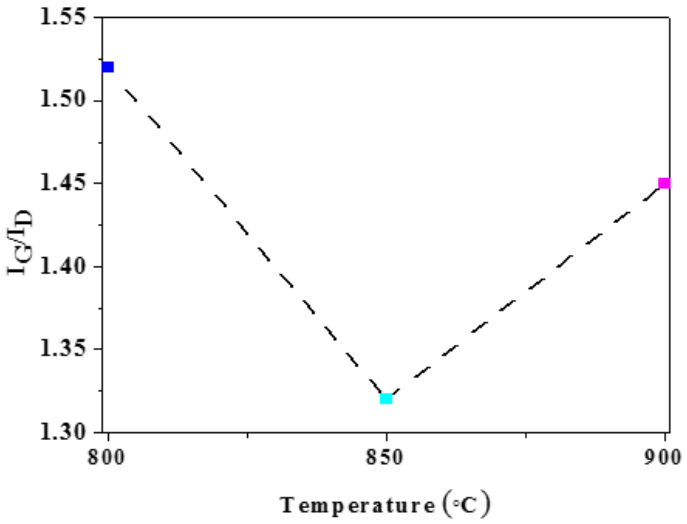

Figure 4.15. I_G/I_D values of the NCNTs that were synthesized at various temperatures.

Here it was found that the NCNTs that were synthesized at 800 °C had the highest I_G/I_D ratio indicating that they had the least defects and were the most crystalline. When the I_G/I_D ratios of the NCNTs synthesized at 850 °C and 900 °C were compared, it was found that the ratio for the NCNTs synthesized at 850 °C was the lowest, while for those at 900 °C it was intermediate relative to the other two. Based on these ratios, these results suggested that the crystallinity of the NCNTs decreased as the % of nitrogen incorporated increased. The Raman results were found to be consistent with the data obtained by elemental analysis (**Table 4.4**). Significantly these results were consistent with those of Liu *et al*. who observed that the I_D/I_G ratio increased (i.e. I_G/I_D ratio decreased) with the increased % nitrogen incorporated in the NCNTs that was formed when a floating catalyst system was used with melamine as the nitrogen source.[45]

Referring back to **Figure 4.14**, it was also observed that the G-bands appeared to shift to higher wavenumbers (i.e. from 1590 to 1602 cm^{-1}) with increased % nitrogen incorporation (i.e. from 1.1% to 3.16%) (**Figure 4.13 and Table 4.4**), for the three NCNTs that were synthesized at the various temperatures.

Referring back to **Figure 4.14**, it was observed that the G-bands for NCNTs from CFA appeared to reach a maximum and then decrease in wavenumber (i.e. from 1590 cm^{-1} to 1602 cm^{-1} and then back down to 1593 cm^{-1}) with increased % N incorporated (i.e. from 1.1% to 3.16% and then back down to 1.95%) (**Figure 4.13 and Table 4.4**), for the NCNTs that were synthesized at the various temperatures. Concomitantly as this wavenumber shift occurred the morphology of these products changed from tubes (most crystalline) to chain-like structures (least crystalline) and back to tubes which were compartmentalized (intermediate crystallinity). Shifts in laser Raman peaks, in relation to the % N incorporated into a carbon network, have been reported to have taken place due to charge-transfer from the nitrogen dopants to the carbon.[52] However, in contrast to the results in our research, Liu *et al*. have noted a shift to lower wavenumbers in the G-band as the % N incorporated into the graphene structure increased.[45] Three possible explanations could be postulated for this variance: The first is that Liu *et al*. performed their experiments at a fixed temperature (while the reaction temperature was varied in this research and did not reach 950 °C as it did in their case), the second is that ethylene and melamine were used in their study (while only melamine was used in this research), the third was that varying masses of melamine were used in their study (while a fixed mass of melamine was used in this research). This was considered plausible as different precursors decompose on different catalysts differently at different temperatures.

The thermal stabilities of different types of carbon nanomaterials can be evaluated using TGA in oxygen. **Figure 4.16** is a TGA derivative profile of the various NCNTs that were synthesized at the different temperatures. Here it was observed that NCNTs synthesized at 850 °C started decomposing at a lower temperature, followed by the NCNTs synthesized at 900 and then 800 °C respectively.

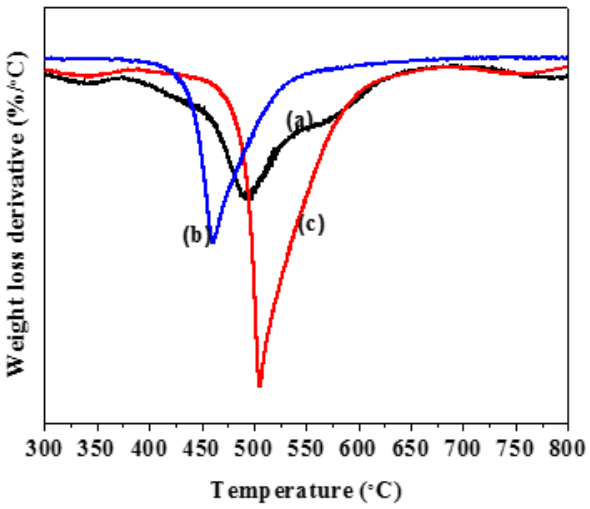

Figure 4.16. TGA derivatives of NCNTs synthesized at (a) 800, (b) 850 and (c) 900 °C.

The data obtained from the TGA thermograms revealed that as the % N incorporated in the NCNTs increased (i.e. from 1.1% to 3.16%), the decomposition temperature at which these materials burned decreased. This observation was consistent with Villalpando-Paez *et al.*, who showed that the decomposition temperature of NCNTs decreased when the concentration of nitrogen incorporated in these materials increased.[51]

Moreover, from the TGA thermograms (**Figure 4.17**), information on the quantities of the products that were formed could be obtained. Based upon this it was determined that 60 % of the products synthesized at 900 °C combusted, whereas 11 % and 22 % of the products synthesized at 800 and 850 °C were combusted respectively. This trend was consistent with the percentage yields that were reported earlier in **Table 4.3**. The remainder of the material (unburned residue) was that of the CFA catalyst.

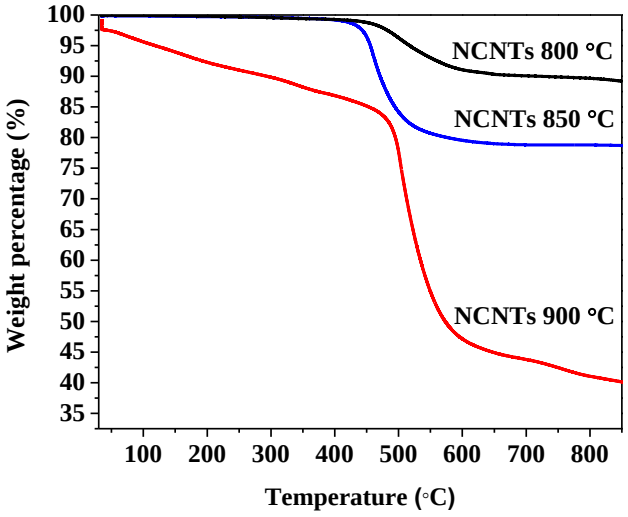

Figure 4.17. TGA thermograms of NCNTs that were synthesized at various temperatures.

CFA is a fairly inhomogeneous material, as such, it is unlikely that its catalytic products would be homogeneous. Even so, the data reported here accounted >80% of the samples, determined using TEM and SEM micrographs. TEM micrographs of the structural features of variants in tube morphology are shown in **Figure 4.18**.

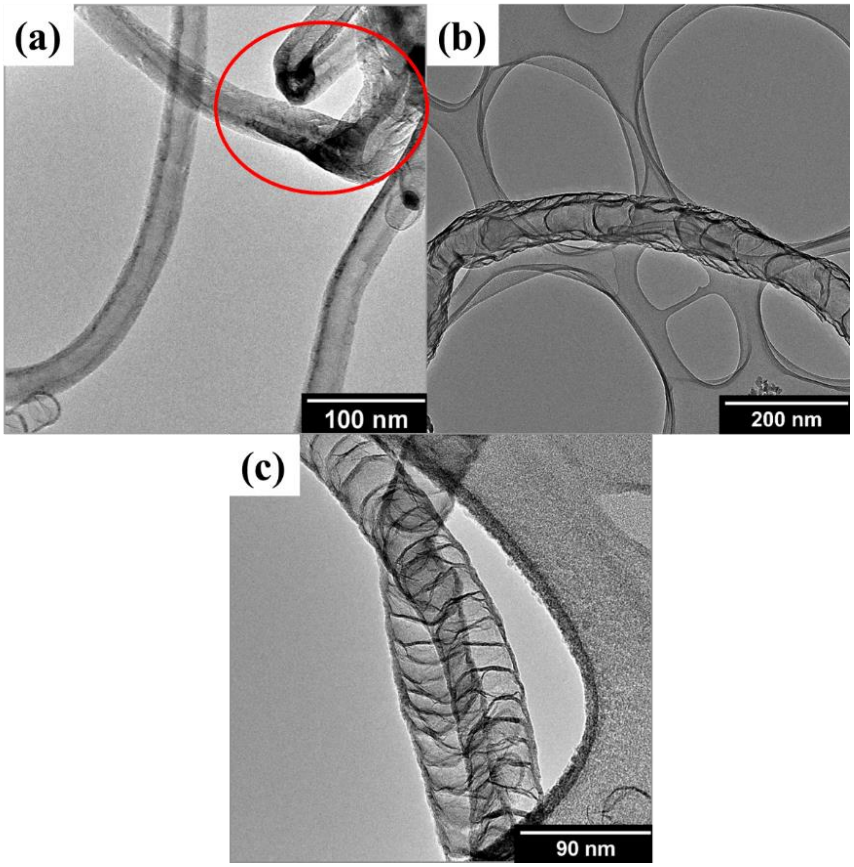

Figure 4.18. TEM micrographs of the morphological variations of NCNTs that were synthesized at (a) 800 °C, (b) 850 °C and (c) 900 °C.

For example, at 800 °C it was observed that apart from the majority product i.e. NCNTs which looked like MWCNTs (**Figure 4.11. (a) & (b))**, a small minority of the tubes that were synthesized showed some signs of the beginning of internal segmentation (see encircled region in **Figure 4.18 (a)**). In the case of NCNTs that were synthesized at 850 °C (**Figure 4.18 (b)**), a minority of the products (**Figure 4.11 (b)**) showed tubular morphology that did not resemble the majority chain-like tubular product **(Figure 4.11 (c) & (d))**. Similarly, with the NCNTs synthesized at 900 °C about 20 % of the NCNTs that were produced did not have the cone-like

bamboo compartments (**Figure 4.18 (c))** that were observed in the majority product (**Figure 4.11. (e) & (f))**.

4.3.3 Characterization of NCNTs synthesized from 5 % Fe/$CaCO_3$.

In order to assess the quality of the NCNTs synthesized over CFA, a more conventional catalyst i.e. 5% Fe/$CaCO_3$ was used for comparison under the same reaction conditions. The TEM micrographs of the NCNTs synthesized at various temperatures i.e. 800 °C, 850 °C and 900 °C, are shown in **Figure 4.19 (a)-(c)**.

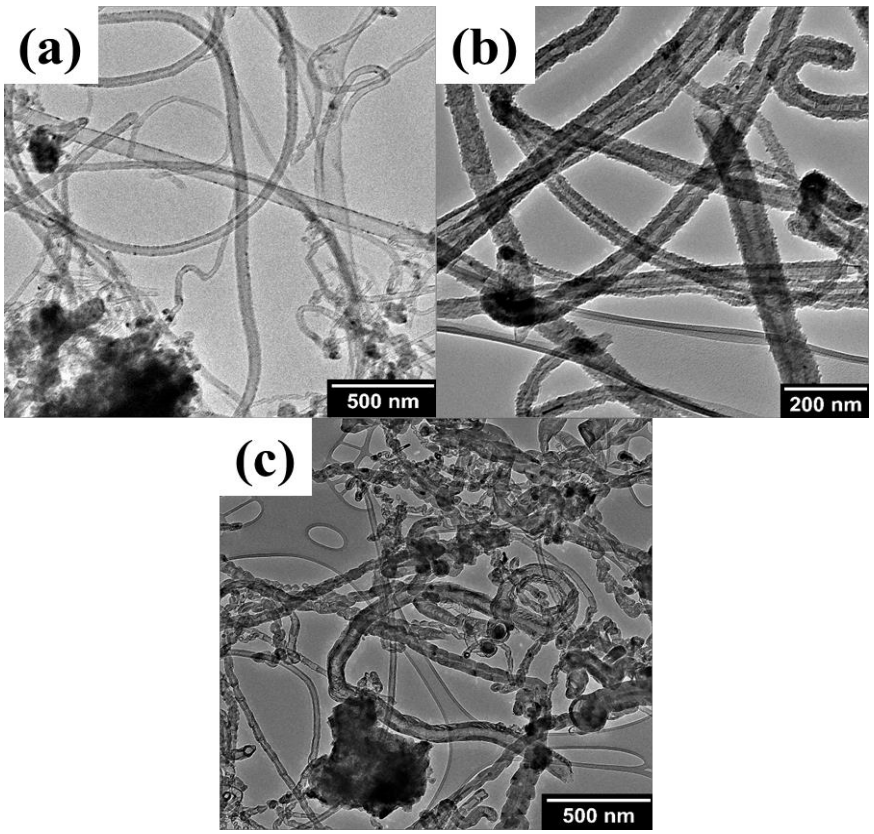

Figure 4.19. TEM micrographs of the NCNTs that were synthesized from the reaction of melamine over 5% Fe/$CaCO_3$ at: (a) 800 °C, (b) 850 °C and (c) 900 °C.

The morphology of the NCNTs that were synthesized at 800 °C using 5% Fe/$CaCO_3$ (**Figure 4.19 (a**)) was similar to that of the NCNTs synthesized at 800 °C from CFA (**Figure 4.11(a)-(b)**), however the former NCNTs were found to be more uniform in shape, while their tube diameter range was narrower (i.e roughly 35-65 nm **Table 4.5**). The NCNTs synthesized at 850 °C and 900 °C using 5% Fe/$CaCO_3$ (**Figure 4.19 (b)-(c)**) had morphologies that were similar to each other and had bamboo compartments. In the main, it was found that the morphologies of the NCNTs from the 5% Fe/$CaCO_3$ catalyst were less varied than those that were synthesized over CFA (**Figure 4.11(a)-(f)**).

The NCNTs grown from 5% Fe/$CaCO_3$ were also subjected to CHNS analysis to determine the % N incorporated into the tubes. Here it was found that the % N incorporated increased with increased reaction temperature (**Table 4.4**). It was also observed that the % N present was higher than that for the NCNTs that were synthesized over CFA (**Table 4.3**).

Table 4.4. Percentage N incorporated into tubes and their diameter range

Sample	% N	Diameter range (nm)
NCNTs 800 °C	5.55	40-60
NCNTs 850 °C	6.53	35-65
NCNTs 900 °C	10.92	35-65

Laser Raman spectroscopy was also used to study the NCNTs that were synthesized from the 5% Fe/$CaCO_3$ catalyst (**Figure 4.20**). Here similar bands as those that were observed in the case of the NCNTs synthesized from CFA were observed (please see **Figure 4.14**). The I_G/I_D ratios of the NCNTs synthesized at 800 °C and 850 °C

were found to be similar but differed slightly to that of the I_G/I_D ratio for the NCNTs synthesized at 900 °C. Here the I_G/I_D ratio (**Figure 4.20**) was found to have increased with increased reaction temperature which was contrary to that which was observed for the NCNTs synthesized from CFA (refer to **Figure 4.15**).

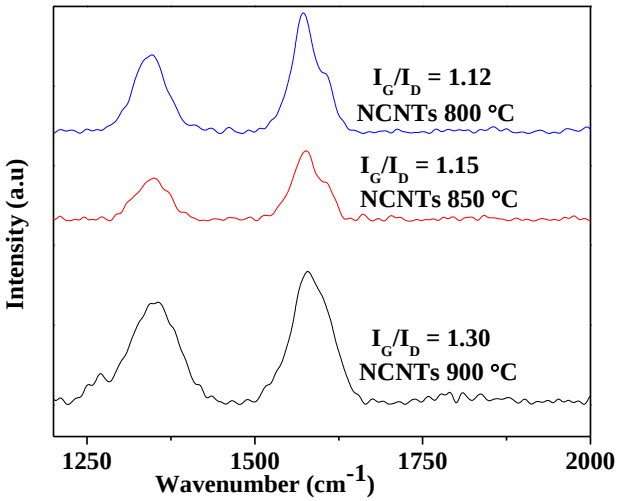

Figure 4.20. Laser Raman spectra of the NCNTs synthesized from the reaction of melamine over 5% $Fe/CaCO_3$ at various synthesis temperatures.

Thermogravimetric analyses were also conducted on the NCNTs grown from 5% $Fe/CaCO_3$ to investigate their thermal properties. It was observed from the weight derivative plots of both the NCNTs synthesized from CFA and 5% $Fe/CaCO_3$, shown in **Figure 4.16** and **Figure 4.21** respectively, that the latter were more thermally stable. It was also observed that the thermal stability trends were different, as in the case of the NCNTs synthesized from 5% $Fe/CaCO_3$, it was observed that their thermal stability increased with increasing synthesis temperature. This observation was however consistent with what was deduced from laser Raman spectra of these NCNTs, that the crystallinity of these materials increased with

increasing synthesis temperature. The second peaks that were observed on the thermograms of the NCNTs were attributed to $CaCO_3$, which decomposes to CO_2 and CaO.

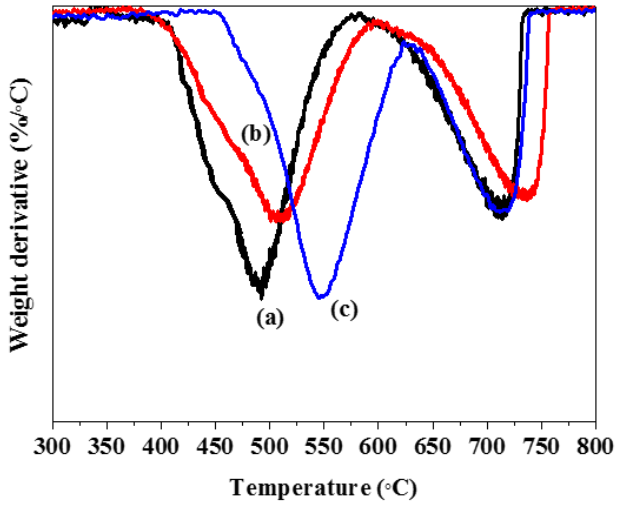

Figure 4.21. TGA weight derivative plots of NCNTs synthesized using 5 % $Fe/CaCO_3$ at (a) 800 °C, (b) 850 °C and (c) 900 °C.

4.4 Conclusions

CFA was characterized by various analytical techniques. It was determined by XRF and PXRD that the CFA was primarily composed of silica and aluminum oxides, with iron based oxides accounting for approximately 5 % of the chemical composition.

This CFA was used as a catalyst for the decomposition of melamine to synthesize NCNTs by a two-stage chemical vapor deposition setup at various temperatures (i.e. 800, 850 and 900 °C). It was observed that the morphologies, crystallinity and the

amount of nitrogen incorporated into these tubes varied as a function of synthesis temperature. An inverse relationship between the degree of crystallinity and the amount of nitrogen incorporated was observed i.e. the greater the % N incorporated into the tubes, the less crystalline they were.

Since CFA is not a homogeneous material, morphological variations were observed in the products that were synthesized. However, these variants accounted for less than 20 % of the NCNTs that were formed.

A comparison of the CFA catalyst with a standard catalyst i.e. 5% Fe/$CaCO_3$ was made. Here the same reaction conditions were used in order to validate the synthesis procedure and assess the quality of the NCNTs that formed. Discrepancies were observed in the crystallinity trends and also in the morphological consistency, where the NCNTs synthesized on CFA had a more uniform morphology.

Even so, this research showed that CFA was a potentially versatile catalyst, where synthesis conditions (i.e. synthesis temperature) could be varied in order to control the morphology and crystallinity of the resulting nitrogen-doped carbon nanotubes.

The NCNTs synthesized in this **CHAPTER** were used in **CHAPTER 5** and **CHAPTER 7.**

4.5 References

1. Silva, L. F. O. Jasper, A., Andrade, M. L., Sampaio, C. H., Dai, S., Li, X., Li, T., Chen, W., Wang, X., Liu, H., Zhao, L., Hopps, S. G., Jewell, R. F. & Hower, J. C. Applied investigation on the interaction of hazardous elements binding on ultrafine and nanoparticles in Chinese anthracite-derived fly ash. *Sci. Total Environ.* **419,** 250–64 (2012).

2. Kostova, I., Vassileva, C., Dai, S., Hower, J. C. & Apostolova, D. Influence of surface area properties on mercury capture behaviour of coal fly ashes from some Bulgarian power plants. *Int. J. Coal Geol.* **116-117,** 227–235 (2013).

3. Vassilev, S. V & Vassileva, C. G. Methods for Characterization of Composition of Fly Ashes from Coal-Fired Power Stations : A Critical Overview. *Energy and fuels* **19,** 1084–1098 (2005).

4. Blissett, R. S. & Rowson, N. A. Review article A review of the multi-component utilisation of coal fly ash. *Fuel* **97,** 1–23 (2012).

5. Ahmaruzzaman, M. A review on the utilization of fly ash. *Prog. Energy Combust. Sci.* **36,** 327–363 (2010).

6. Basu, M., Pande, M., Bhadoria, P. B. S. & Mahapatra, S. C. Potential fly-ash utilization in agriculture : A global review. *Prog. Nat. Sci.* **19,** 1173–1186 (2009).

7. Panias, D., Giannopoulou, I. P. & Perraki, T. Effect of synthesis parameters on the mechanical properties of fly ash-based geopolymers. *Colloids Surfaces A Physicochem. Eng. Asp.* **301,** 246–254 (2007).

8. Xuan, X., Yue, C., Li, S. & Yao, Q. Selective catalytic reduction of NO by ammonia

with fly ash catalyst. *Fuel* **82,** 575–579 (2003).

9. Chatterjee, D., Ruj, B. & Mahata, A. Adsorption and photocatalysis of colour removal from waste water using flyash and sunlight. *Catal. Commun.* **2,** 113–117 (2001).

10. Dunens, O. M., MacKenzie, K. J. & Harris, A. T. Synthesis of multiwalled carbon nanotubes on fly ash derived catalysts. *Environ. Sci. Technol.* **43,** 7889–94 (2009).

11. Nath, D. C. D. & Sahajwalla, V. Growth mechanism of carbon nanotubes produced by pyrolysis of a composite film of poly (vinyl alcohol) and fly ash. *Appl. Phys. A* **104,** 539–544 (2011).

12. Hintsho, N. Shaikjee, A., Masenda, H., Naidoo, D., Billing, D., Franklyn, P. & Durbach, S. Direct synthesis of carbon nanofibers from South African coal fly ash. *Nanoscale Res. Lett.* **9,** 387 (2014).

13. Hintsho, N., Shaikjee, A., Franklyn, P. & Durbach, S. The effect of CO_2 on the CVD synthesis of carbon nanomaterials using fly ash as a catalyst. *RSC Adv.* **5,** 53776–53781 (2015).

14. Salah, N., Al-ghamdi, A. A., Memic, A., Habib, S. S. & Khan, Z. H. Formation of Carbon Nanotubes from Carbon-Rich Fly Ash: Growth Parameters and Mechanism. *Mater. Manuf. Process.* **31,** 146–156 (2016).

15. Yasui, A., Kamiya, Y., Sugiyama, S., Ono, S., Noda, H. & Ichikawa, Y. Synthesis of Carbon Nanotubes on Fly Ashes by Chemical Vapor Deposition Processing. *Ieej Trans. Electr. Electron. Eng.* **4,** 787–789 (2009).

16. Iijima, S. Helical microtubules of graphitic carbon. *Nature* **354,** 56–58 (1991).

17. Ghosh, K., Kumar, M., Maruyama, T. & Ando, Y. Tailoring the field emission property of nitrogen-doped carbon nanotubes by controlling the graphitic/pyridinic substitution. *Carbon* **48,** 191–200 (2010).

18. Stoyanov, S. R., Titov, A. V. & Kral, P. Transition metal and nitrogen doped carbon nanostructures. *Coord. Chem. Rev.* **253,** 2852–2871 (2009).

19. Nxumalo, E. N. & Coville, N. J. Nitrogen Doped Carbon Nanotubes from Organometallic Compounds: A Review. *Materials.* **3,** 2141–2171 (2010).

20. Wang, X. Li, X., Zhang, L., Yoon, Y., Weber, P. K., Wang, H., Guo, J. & Dai, Hongjie N-doping of graphene through electrothermal reactions with ammonia. *Science* **324,** 768–71 (2009).

21. Ewels, C. P. & Glerup, M. Nitrogen doping in carbon nanotubes. *J. Nanosci. Nanotechnol.* **5,** 1345–1363 (2005).

22. Montigaud, H., Tanguy, B., Gérard Demazeau, I., Alves, M. B. & Dunogues, J. Solvothermal synthesis of the graphitic form of C_3N_4 as macroscopic sample. *Mater. Sci. Forum* **325,** 31–36 (2000).

23. Jeffrey, L. S. Characterization of the coal resources of South Africa. *J. South African Inst. Min. Metall.* **105,** 95–102 (2005).

24. Pone, J. D. N., Hein, K. A. A., Stracher, G. B., Annegarn, H. J., Finkleman, R. B., Blake, D. R., McCormack, J. K. & Schroeder, Paul The spontaneous combustion of coal and its by-products in the Witbank and Sasolburg coalfields of South Africa. *Int. J. Coal Geol.* **72,** 124–140 (2007).

25. Cassell, A. M., Raymakers, J. A., Kong, J, Dai, H. Large scale CVD synthesis of single-walled carbon nanotubes. *J. Phys. Chem. B* **103**, 6484-92 (1999).

26. Bachilo, S.M., Balzano, L., Herrera, J.E., Pompeo, F., Resasco, D.E. and Weisman, R.B. Narrow (n, m)-distribution of single-walled carbon nanotubes grown using a solid supported catalyst. *JACS*, **125** (2003).

27. Nagaraju, N., Fonseca, A., Konya, Z. & Nagy, J. B. Alumina and silica supported metal catalysts for the production of carbon nanotubes. *J. Mol. Catal*. **181,** 57–62 (2002).

28. Guedes, A., Valentim, B., Prieto, A. C., Sanz, A., Flores, D. & Noronha, F. Characterization of fly ash from a power plant and surroundings by micro-Raman spectroscopy. *Int. J. Coal Geol.* **73,** 359–370 (2008).

29. Ravindran, T.R., Jackson, B.R. and Badding, J.V. UV Raman spectroscopy of single-walled Carbon nanotubes. *Chem. Mater*. **13**, 4187-4191 (2001).

30. Zhang, L. Li, H., Yue, K., Zhang, S., Wu, X., Zi, J., Shi, Z. & Gu, Z. Effects of intense laser irradiation on Raman intensity features of carbon nanotubes. *Phys. Rev. B* **65,** 073401 (2002).

31. Santangelo, S., Messina, G., Faggio, G., Donato, A., De Luca, L., Donato, N., Bonavita, A. & Neri, G.Micro-Raman analysis of titanium oxide/carbon nanotubes-based nanocomposites for hydrogen sensing applications. *J. Solid State Chem.* **183,** 2451–2455 (2010).

32. Jorio, A. Pimenta, M A., Filho, A. G. S. & Saito, R. Characterizing carbon nanotube samples with resonance Raman scattering. *New Journal of Physics*, **5**, 139 (2003).

33. Criado, M., Fernández-Jiménez, A. & Palomo, A. Alkali activation of fly ash: Effect

of the SiO_2/Na_2O ratio. Part I: FTIR study. *Microporous Mesoporous Mater.* **106,** 180–191 (2007).

34. May, H. Pyrolysis of melamine. *Journal of Applied Chemistry*. **9**, 340-344 (1959).

35. Zhao, Y. C., Yu, D. L., Zhou, H. W. & Tian, Y. J. Turbostratic carbon nitride prepared by pyrolysis of melamine. *J. Mater. Sci.* **40,** 2645–2647 (2005).

36. Kudashov, A. G. Okotrub, A. V., Bulusheva, L. G., Asanov, I. P., Shubin, Yu. V., Yudanov, N. F., Yudanova, L. I., Danilovich, V. S. & Abrosimov, O. G. Influence of Ni−Co Catalyst Composition on Nitrogen Content in Carbon Nanotubes. *J. Phys. Chem. B* **108,** 9048–9053 (2004).

37. Stephan, O., Ajayan, P. M., Colliex, C., Redlich, P., Lambert, J. M. & Bernier, P. Doping graphitic and carbon nanotube structures with boron and nitrogen. *Science* **266,** 1683–16855 (1994).

38. Ayala, P., Arenal, R., Rümmeli, M., Rubio, A. & Pichler, T. The doping of carbon nanotubes with nitrogen and their potential applications. *Carbon* **48,** 575–586 (2010).

39. Glerup, M., Castignolles, M., Holzinger, M., Hug, G., Loiseau, A. & Bernier, P. Synthesis of highly nitrogen-doped multi-walled carbon nanotubes. *Chem. Comm*. **33,** 2542–2543 (2003).

40. Yadav, R. M., Dobal, P. S., Shripathi, T., Katiyar, R. S. & Srivastava, O. N. Effect of Growth Temperature on Bamboo-shaped Carbon-Nitrogen (C-N) Nanotubes Synthesized Using Ferrocene Acetonitrile Precursor. *Nanoscale Res. Lett.* **4,** 197–203 (2008).

41. Keru, G., Ndungu, P. G. & Nyamori, V. O. Nitrogen-Doped Carbon Nanotubes

Synthesised by Pyrolysis of (4-{[(pyridine-4-yl)methylidene]amino}phenyl) ferrocene. *J. Nanomater.* **2013,** 1–7 (2013).

42. Tang, C., Bando, Y., Golberg, D. & Xu. Structure and nitrogen incorporation of carbon nanotubes synthesized by catalytic pyrolysis of dimethylformamide. *Carbon* **42,** 2625–2633 (2004).

43. Jang, J. W., Lee, C. E., Lyu, S. C., Lee, T. J. & Lee, C. J. Structural study of nitrogen-doping effects in bamboo-shaped multiwalled carbon nanotubes. *Appl. Phys. Lett.* **84,** 2877 (2004).

44. Chizari, K., Vena, A., Laurentius, L. & Sundararaj, U. The effect of temperature on the morphology and chemical surface properties of nitrogen-doped carbon nanotubes. *Carbon* **68,** 369–379 (2014).

45. Liu, H., Zhang, Y., Li, R., Sun, X., De, S., Abou-rachid, H., Jaidann, M. & Lussier, L. Structural and morphological control of aligned nitrogen-doped carbon nanotubes. *Carbon* **48,** 1498–1507 (2010).

46. Nath, M., Satishkumar, B. C., Govindaraj, A., Vinod, C. P. & Rao, C. N. R. Production of bundles of aligned carbon and carbon-nitrogen nanotubes by the pyrolysis of precursors on silica-supported iron and cobalt catalysts. *Chem. Phys. Lett.* **322,** 333–340 (2000).

47. Sharifi, T., Nitze, F., Barzegar, H. R., Tai, C. W., Mazurkiewicz, M., Malolepszy, Stobinski, L. & Wagberg, T. Nitrogen doped multi walled carbon nanotubes produced by CVD-correlating XPS and Raman spectroscopy for the study of nitrogen inclusion. *Carbon* **50,** 3535–3541 (2012).

48. O'Byrne, J. P. Justin, P. Li, Z., Jones, S. L. T., Fleming, P. G., Larsson, J. A.,

Morris, M. A. & Holmes, J. D. Nitrogen-doped carbon nanotubes: Growth, mechanism and structure. *ChemPhysChem* **12,** 2995–3001 (2011).

49. Thomsen, C. & Reich, S. Raman Scattering in Carbon Nanotubes. **232,** 115–232 (2007).

50. Czerw, R., Terrones, M., Charlier, J. C., Blase, X., Foley, B., Kamalakaran, R., Grobert, N., Terrones, H., Tekleab, D., Ajayan, P. M., Blau, W., Rühle, M. & Carroll, D. L. Identification of Electron Donor States in N-Doped Carbon Nanotubes. *Nano Lett.* **1,** 457–460 (2001).

51. Villalpando-Paez, F. Zamudio, A., Elias, A.L., Son, H., Barros, E. B., Chou, S. G., Kim, Y. A., Muramatsu, H., Hayashi, T., Kong, J., Terrones, H., Dresselhaus, G., Endo, M., Terrones, M. & Dresselhaus, M. S. Synthesis and characterization of long strands of nitrogen-doped single-walled carbon nanotubes. *Chem. Phys. Lett.* **424,** 345–352 (2006).

52. Lim, S., Elim, H., Gao, X., Wee, A., Ji, W., Lee, J., Lin, J. Electronic and optical properties of nitrogen-doped multiwalled carbon nanotubes. Phys. Rev. B 73, 454021-454026 (2006).

CHAPTER 5:

Photodegradation of BPA on purified fly ash synthesized CNFs and NCNTs composited with TiO_2 prepared by the surfactant wrapping sol-gel/hydrothermal method

5.1 Introduction

The threat posed to natural water systems by various anthropological processes and chemicals is increasing. Some chemicals used as drugs, pesticides, household products, and cosmetics are suspected to be endocrine disruptors.[1–5] Endocrine disrupting chemicals (EDCs) can affect the hormonal system by blocking, inducing or mimicking certain natural hormones in the body. Several reports have demonstrated that EDCs are responsible for the occurrence of various sexual and reproductive irregularities.[6–8]

Bisphenol-A ([2,2-Bis(4-hydroxyphenyl)propane]) i.e. BPA is a common chemical that is used industrially mainly for the production of polycarbonate plastics that are used for making baby bottles, amongst other plastic applications.[9,10] It is also used as a major constituent of the epoxy resin used for lining food cans and dental sealants.[9,11]

BPA has been reported to cause cancer[12] and mimic estrogen.[13] It was shown through clinical trials that BPA decreases sperm production in male rats.[14] EDCs including BPA have been detected in wastewater, surface water and drinking water as such it is, important that water treatment methods be improved.[15–18]

Several techniques have been investigated for the treatment of EDCs in water, these include adsorption, biological, sonochemical, chemical reaction processes, electrochemical oxidation reactions, and photocatalysis amongst other techniques.[19–21] Photocatalysis has been shown as the most encouraging technique for the removal of organic contaminants in

water because it is a relatively easy and cheap technique.[22,23] Furthermore, it has high mineralization efficiency and sunlight can be used as a source of energy.[24,25]

TiO_2 is one of the most commonly used semiconductors as a photocatalyst for the oxidation of organic compounds because of its low cost, availability and unique physical and chemical properties.[26,27] However, the quantum efficiency of TiO_2 as a photocatalyst is limited by the high rate of the electron/hole recombination.[28–30] Therefore a lot of research has been aimed at improving the photocatalytic efficiency of TiO_2 using techniques that include: doping with precious metals (Au, Rh, Ru, Os, etc.), non-metal doping (C, F, N etc.), coupling with semiconductors (Fe_2O_3, ZnO, etc.) and photosensitization.[19,31–33]

Research has shown that coupling TiO_2 with carbon nanomaterials (CNMs) enhances the photocatalytic quantum efficiency of TiO_2.[34] The addition of CNMs introduces irregularities on the TiO_2 surface that act as trap sites for electrons thus reducing the electron and hole recombination rate.[34,35] Another way of increasing the quantum efficiency is through the formation of a semiconductor-metal (SM) junction or Schottky barrier.[34] At the SM junction electrons flow from the material with a higher Fermi level to the material with a lower Fermi level thus achieving charge separation.[34] This principle is usually observed at the interface of precious metals and an n-type semiconductor, such as TiO_2, where electrons move from the semiconductor to the metal.[34]

CNTs can be tailored to possess metallic properties like precious metals, where they can act as sinks for electrons as they have a large electron storage capacity.[34,36] CNTs can possess metallic, n-type or p-type semiconductor properties.[37] This can be achieved through substitutional doping of heteroatoms such as nitrogen or boron into the graphene-based lattices of CNTs.[38–40] Doping CNTs with N (which contains an extra electron compared to C) can lead to the formation of NCNTs often with n-type semiconductor

properties.[37,41,42] This can possibly enhance the function of NCNTs as a functional supporting material for TiO_2 photocatalyst relative to the more pristine CNFs.

It is important that CFA is reused as 800 Mt of it is produced annually during the combustion of coal in the thermoelectric coal powered stations and only 200 Mt is reused.[43] In prior research in our laboratory it has been shown that NCNTs and CNFs could be synthesized from CFA using melamine as a lone carbon and nitrogen source in the former case and acetylene as the carbon source in the latter one.[44–46] This was achieved by exploiting the moderate concentration of iron and high concentration of aluminosilicates contained in CFA.[44,46] Iron is one of the most commonly used catalysts for synthesizing CNMs by CVD and aluminosilicates spheres are often used as catalyst supports. CFA is essentially free and makes the process of synthesizing CNFs and NCNTs cheaper while at the same time also taking away an environmental contaminant.

In order to appropriately use CNMs along with TiO_2 for photocatalysis, it is important they are purified so that their potential beneficial effect on activity could be attributed to the CNMs alone. In this chapter the purification of NCNTs and CNFs synthesized from CFA, using dilute HF and a combination of dilute HNO_3/H_2SO_4 separately is discussed.

Here TiO_2 in the anatase phase was synthesized in the presence of these purified CNFs or NCNTs at various loadings (i.e. 1, 5 and 20 % m/m SCNMs) to form composites. The BPA photodegradation efficiencies of these composite catalysts and pure TiO_2 were compared at experimental conditions which were optimized by using pure TiO_2. Although literature exists on the photodegradation of different dyes and other organic contaminants using TiO_2 and CNMs[47–50], to the best of our knowledge this is the first report that focuses on comparing the efficiency for the photodegradation of BPA from TiO_2 composited with two different types of CNMs that were synthesized from CFA.

5.2 Experimental

5.2.1 Chemicals

Bisphenol A (99 % purity) and melamine were purchased from Sigma-Aldrich and were used as-received without any modifications. CFA was obtained from the Electricity Supply Commission (Eskom) Research and Innovation Centre in Rosherville, South Africa. Ethanol (96 % purity) was purchased from Merck, 2-propanol (97 %) and the ammonium hydroxide solution (25 %) were purchased from Fluka. Hydrofluoric acid (40 %) was purchased from Associated chemicals and titanium isopropoxide (99.9 %) was purchased from Sigma-Aldrich. Sodium dodecylbenxenesulfonate, nitric acid (55 %) and sulphuric acid (95-98 %) were also purchased from Sigma-Aldrich. Distilled water was used except for HPLC analysis where the water was both distilled and treated with UV light. HPLC grade acetonitrile (CHROMASOLV®) was purchased from Sigma-Aldrich. Acetylene and argon gas were both purchased from Afrox.

5.2.2 Synthesis and purification of NCNTs and CNFs

The method followed for the synthesis of NCNTs at 850 °C was described in detail in **section 4.2.1**. The NCNTs synthesized at 850 °C were selected because the NCNTs contained the highest amount of nitrogen. One of the objectives in CHAPTER 5 was to compare NCNTs and CNFs.

In the case of CNFs, these were synthesized using CFA as a catalyst at 850 °C by CVD in a single tube furnace. The temperature of the furnace was heated to 850 °C in 85 min (10 °C/min). Argon gas was used as a carrier gas and was passed through

the reaction tube throughout the duration of the reaction at 100 ml/min (including the temperature ramping stage). In our previous study, it was shown that argon gas was an effective carrier (inert) gas for the CVD synthesis of CNFs using CFA as a catalyst as opposed to nitrogen. Upon reaching the synthesis temperature (850 °C) acetylene, the carbon source was added into the reaction chamber at a flow rate of 50 ml/min. The reaction was allowed to run for 60 min after which the flow of acetylene was discontinued and the tube furnace was allowed to cool down to room temperature under a flow of argon gas.

The CNFs and NCNTs synthesized from CFA still contained CFA as it was not removed post-synthesis. For the purification of the CNMs (both NCNTs and CNFs, separately), 3 g each of these was stirred in 20 ml of 5 % HF aqueous solution for 24 h at room temperature. The solutions were diluted with 150 ml of water, centrifuged and then washed a further five times with water. The wet samples were then transferred into round bottom flasks, each containing 30 ml HNO_3, 10 ml H_2SO_4, and 60 ml water. They were then heated at 60 °C for 12 h. The mixtures were transferred into beakers, diluted with 200 ml of water and filtered. The solid residue samples were dried in an oven set at 60 °C for 12 h.

5.2.3 Synthesis of CNF/NCNTs-TiO_2 composites by the surfactant wrapping sol-gel/hydrothermal method.

The CNFs/NCNTs-TiO_2 composites were synthesized by the surfactant wrapping sol-gel/hydrothermal method. The method was hydrothermally adapted from the previously reported surfactant wrapping sol-gel gel technique by Gao *et al.*[47] Typically, a predetermined mass of purified CNFs/NCNTs was dispersed in a 0.5 % sodium dodecylbenxenesulfonate aqueous solution by sonication for 60 min. The suspension was then added to 20 ml ethanol and stirred for 30 min to homogenize it.

A predetermined amount of titanium isopropoxide was then added to 15 ml isopropanol and stirred for 30 min. The titanium isopropoxide solution was added dropwise to the CNFs/NCNTs suspension whilst stirring vigorously. Ammonium hydroxide solution (5 ml, 1 M) was added to the mixture dropwise to complete the hydrolysis of the metal precursor. The suspension was then transferred into a pressure autoclave lined with a Teflon reaction vessel. The reaction was completed by heating the reaction mixture in the sealed pressure autoclave at 120 °C for 24 h. The resulting gray precipitate was then centrifuged, washed with ethanol, oven dried at 80 °C for 24 h and then calcined at 500 °C for 2 h. The materials were calcined at 500 °C for a short period of time to fully crystallize TiO_2 (anatase) without phase transformation to rutile and combusting NCNTs or CNFs. TiO_2 was synthesized following the same procedure but without the addition of CNMs. The composites reported in this chapter consisted of 1, 5 and 20 % (m/m) CNMs as such were labeled as shown in **Table 5.1**.

Table 5.1. CNM ratios in composites and sample labeling.

Sample	% NCNTs	% CNFs
TiO_2	0	0
TiO_2/1%_NCNTs	1	0
TiO_2/5%_NCNTs	5	0
TiO_2/20%_NCNTs	20	0
TiO_2/1%_CNFs	0	1
TiO_2/5%_CNFs	0	5
TiO_2/20%_CNFs	0	20

5.2.4 Materials characterization

The materials synthesized in this chapter (i.e. unbound TiO_2 and the various TiO_2_NCNT/CNFs composites) were all characterized in accordance with the details that were discussed in **Section 3.2**.

5.2.5 Photocatalytic testing

The photocatalytic performances of the various materials were assessed by monitoring the rate of photodegradation of BPA under simulated sunlight conditions. Several photocatalytic measurements were conducted in this study; consequently, experimental details specific to the different experiments are discussed in detail in **Section 5.3**.

5.3 Results and discussion

5.3.1 Materials characterization

The morphological properties of the raw (i.e. as-synthesized) and purified CNFs, as well as NCNTs, were studied by SEM (**Figure 5.1**). As expected, since CFA was used as a catalyst for the growth of these materials, spherical CFA particulates were observed in the SEM micrographs of the raw CNFs and NCNTs (please see encircled regions in **Figure 5.1 (a)** and **Figure 5.1 (b)** respectively). In order to ascertain the influence of the CNMs in the photocatalytic efficiency of TiO_2, it was important that the catalyst material (i.e. CFA) be removed from them. **Figure 5.1 (b)** and **Figure 5.1 (d)**, SEM micrographs of purified CNFs and NCNTs respectively) showed that the majority (> 95% see TGA analyses - **Figure 5.3**) of the spherical aluminosilicates particles had been removed upon sequential treatment with 5 % HF and dilute HNO_3/H_2SO_4. The use of HF was necessary as CFA is

primarily composed of aluminosilicates which form gaseous fluorides upon reaction with HF. These gaseous products escape, ridding the composites formed of aluminosilicates. The dilute HNO_3/H_2SO_4 combination was used in order to solubilize the metals that were contained in the CFA and to introduce functional groups to the materials.

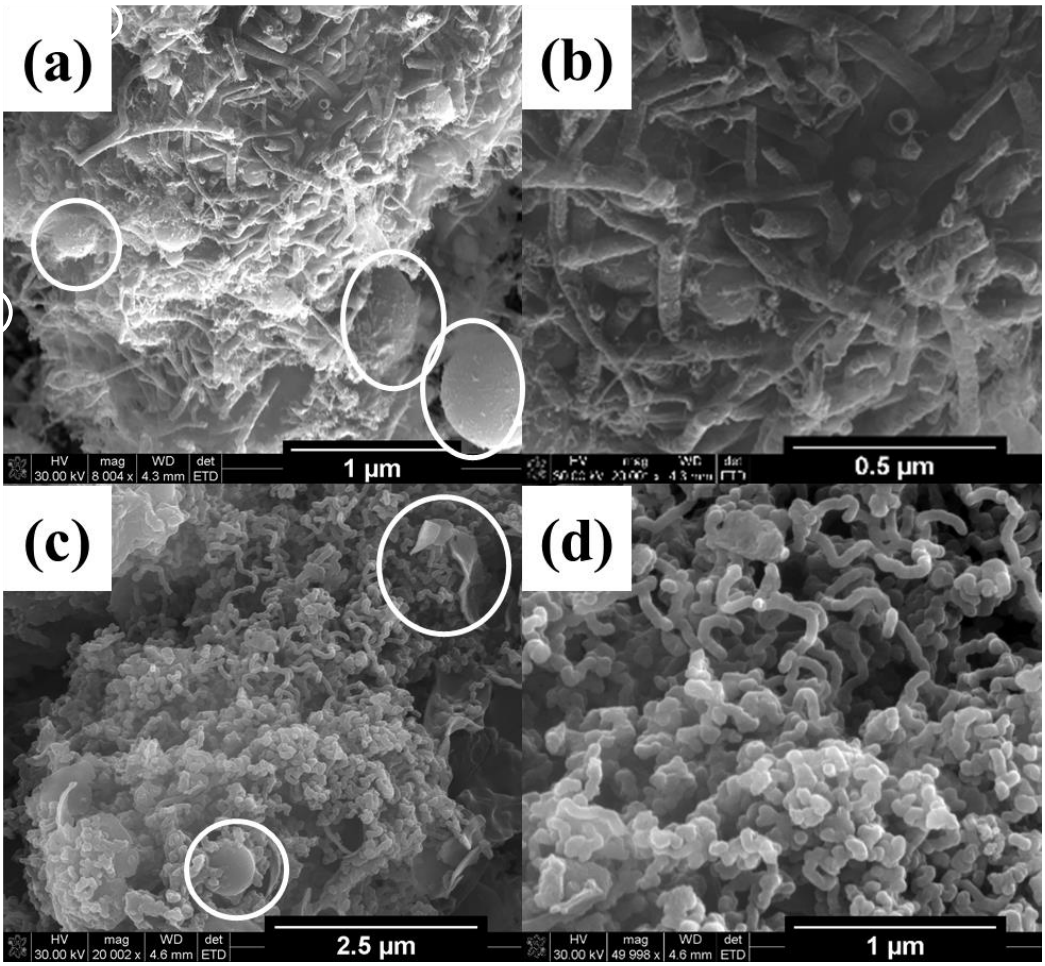

Figure 5.1. SEM micrographs of (a) Raw NCNTs, (b) Purified NCNTs, (c) Raw CNFs and (d) Purified CNFs.

Electron microscopy (TEM and SEM) were also used to study the morphological properties of the TiO_2, NCNTs/CNFs as well as their composites with TiO_2 as

shown in **Figure 5.2**. The morphological properties of NCNTs and CNFs that were observed from the TEM micrographs (**Figure 5.2 (a)** and **Figure 5.2 (b)** respectively) were consistent with those that had been observed with SEM (**Figure 5.1**). The CNFs had some fibers which were intertwined, with a narrow diameter range (average diameter of 40 nm). As shown before (**Figure 4.11 (c)-(d)**), the NCNTs had a chain-like morphology with circular compartments and multiple-walls. The average diameter of these NCNTs was 39 nm.

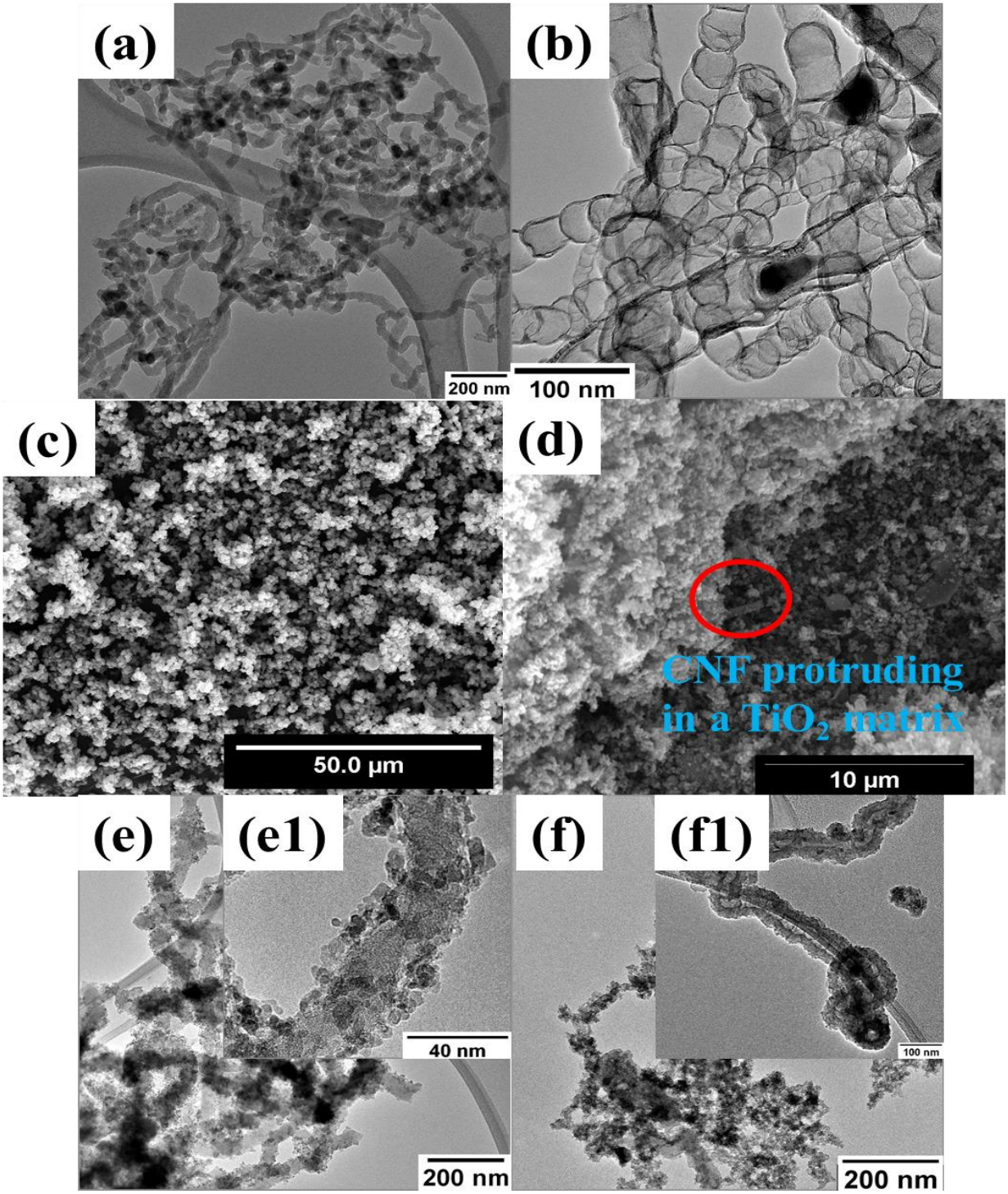

Figure 5.2. TEM micrographs of: (a) CNFs, (b) NCNTs, (c) TiO_2, (e,e1) TiO_2/20_%_CNFs, (f,f1) TiO_2/_20_%_NCNTs and (d) is an SEM micrograph of TiO_2.

The TiO_2 nanoparticles were found to be agglomerated and a particle size that ranged between 10 and 13 nm (**Figure 5.2 (c)**). As expected the SEM micrograph of the TiO_2/1%_CNFs composite (**Figure 5.2 (d)**) showed that the material predominantly consisted of TiO_2; a CNF protruding from the TiO_2 matrix was highlighted (circled in red). In the case of composites consisting of 20 % (i.e. TiO_2/20%_CNFs and TiO_2/20%_NCNTs), the connection between TiO_2 and the carbonaceous nanomaterial was more evident. The CNFs were completely coated with TiO_2 nanoparticles as observed in **Figure 5.2 (e,e1);** the same was observed in the case of NCNTs (**Figure 5.2 (f,f1)**). Gao *et al*., have demonstrated that compositing TiO_2 and CNTs by the surfactant wrapping sol-gel technique yielded CNTs which were uniformly coated with TiO_2 nanoparticles.[47] In this work it was shown that modifying the afore-mentioned method by completing the reaction hydrothermally, yielded carbonaceous materials that were completely coated with TiO_2. It was therefore suspected that chemical interactions between the materials had occurred. Indeed physical and chemical interactions between such materials have been reported to be responsible for electron mobility between them and resulted in charge separation.[51–54] Largely the physical and chemical properties of CNMs/TiO_2 combinations depend on their interactions, which in turn depend on their method of synthesis.[47] However, in this research the presence of aggregated TiO_2 nanoparticles on the walls of the CNFs and NCNTs provided evidence that the carbon nanomaterials had played a role in the deposition and evolution of these particles during hydrolysis, as supported by the literature. [47] Indeed the introduction of the functional groups (carboxylic acid groups as it is the norm with acid functionalization of CNMs, and possibly amide groups in the case of NCNTs) on the surfaces of the CNFs and NCNTs was achieved during the purification of these

materials. This most likely explained the clustering of TiO_2 nanoparticles along their walls, where these functional groups were located.

TGA analyses were performed in order to investigate the effectiveness of the sequential treatment of NCNTs/CNFs with HF and a combination of dilute HNO_3 and H_2SO_4 at removing CFA from the carbonaceous materials. The thermograms of raw NCNTs and CNFs showed that approximately 29 % and 18 % of CNFs and NCNTs respectively were combusted (**Figure 5.3 (a)-(b)**). This meant that over two-thirds of the carbonaceous materials consisted of thermally stable CFA (**refer to Figure 4.6**). It is noteworthy that the same CFA was used for the synthesis of the NCNTs and CNFs. Since this was the case the positive bias brought about by the residual carbonaceous material in CFA is accounted for. The thermograms of the purified NCNTs and CNFs showed that 99 % and 97 % of the respective materials had combusted which indicated that almost complete removal of catalyst material (i.e. CFA) had occurred.

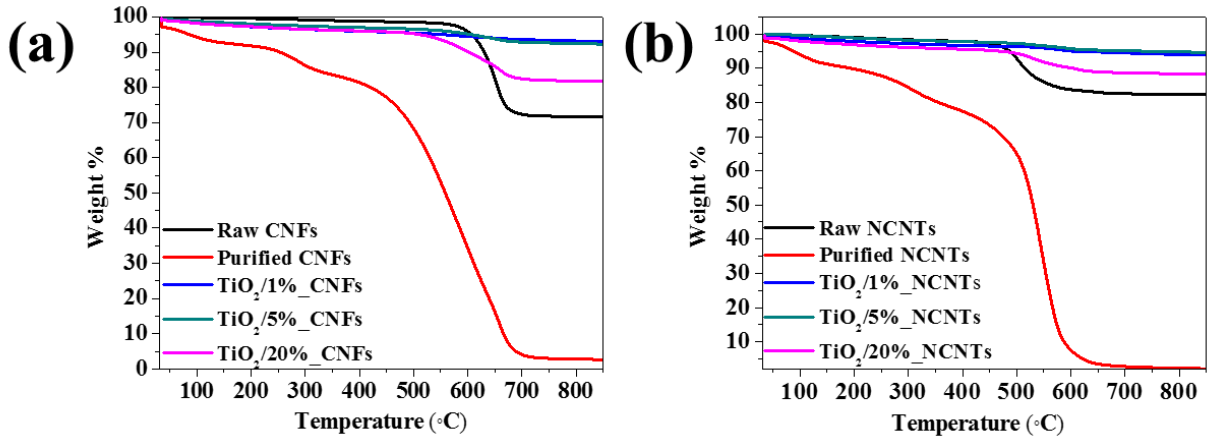

Figure 5.3. TGA thermograms of: (a) Raw CNFs, purified CNFs, TiO_2/CNFs based composites and (b) Raw NCNTs, purified NCNTs, TiO_2/NCNTs based composites.

Furthermore, from the thermograms, it was observed that raw CNFs and NCNTs combusted at higher temperatures as opposed to their purified counterparts. Here the raw NCNTs and purified NCNTs combusted at 640 °C and 530 °C respectively, while for the CNFs, the raw CNFs combusted at 650 °C and the functionalized CNFs at 590 °C. Since the purification process had involved acid treatment, the reduction in combustion temperatures acted as an indirect confirmation that functional groups had been introduced onto the surfaces of these carbonaceous materials and had thus distorted their graphicity. This, in turn, made them easier to combust. TGA was also used to approximate the weight fractions of CNMs relative to TiO_2 in the composites. The values that were obtained were found to be close to the TiO_2 loadings that were sought (i.e. 1, 5 and 20%) (**Table 5.2**).

The Surface area properties of the various samples were determined using BET (**Table 5.2**). The purified CNFs and NCNTs were determined to have higher BET

surface areas than pristine CNFs and NCNTs, indicating that the removal of low surface area CFA improved the surface area of the CNMs. The surface area of TiO_2 was found to be 37 m^2/g, lower than expected for nano-TiO_2 particles. The low surface area was attributed to that TiO_2 was calcined at high temperature and had agglomerated. The surface areas of the composites varied between 65-123 m^2/g and were higher than those of the purified carbonaceous materials and pristine TiO_2. The surface areas of the composites increased with an increasing weight percentage of NCNTs or CNFs. This allowed for the conclusion that the presence of CNFs or NCNTs during the hydrolysis of TiO_2 lessened or prevented the agglomeration of TiO_2 nanoparticles hence the increased surface area.

Table 5.2. Surface areas of the various samples and the CNMs weight percentages along with their I_D/I_G values.

Sample	S_{BET} m^2/g	I_D/I_G	% CNMs
CFA	3(±0.5)	-	-
Raw CNFs	17(±0.9)	1.21	29
Raw NCNTs	22(±1.2)	1.03	18
Purified CNFs	48(±2.5)	1.09	98
Purified NCNTs	52(±3.1)	0.99	98
TiO_2	37(±1.6)	-	-
TiO_2/1%_CNFs	68(±3.3)	1.05	1.5
TiO_2/5%_CNFs	108(±9.5)	1.03	6.3
TiO_2/20%_CNFs	124(±6.9)	0.99	19.3
TiO_2/1%_NCNTs	65(±5.8)	0.95	1.9
TiO_2/5%_NCNTs	78(±4.4)	0.93	5.2
TiO_2/20%_NCNTs	123(±9.5)	0.92	19.2

Laser Raman spectroscopy was used to investigate the extent of the graphitization of the CNFs and NCNTs, before and after purification. The D and G bands of the CNMs

appeared at approximately 1358 cm^{-1} and 1600 cm^{-1} respectively (**Figure 5.4 and Table 5.2**). The ratio of the normalized G and D (I_D/I_G) peak was used to estimate the extent of distortions present in the CNMs.

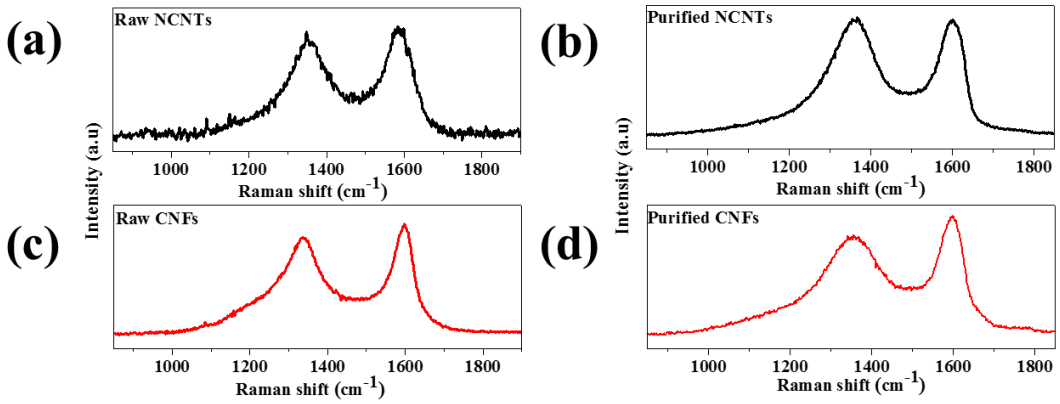

Figure 5.4. Laser Raman spectra of: (a) raw NCNTs, (b) purified NCNTs, (c) raw CNFs and (d) purified CNFs.

The I_D/I_G of raw NCNTs was smaller than that of the purified NCNTs (**Figure 5.4 (a), Figure 5.4 (b) and Table 5.2**) indicating increased extent of defects present in the NCNTs after purification. This trend was also observed in the case of CNFs (**Figure 5.4 (c), Figure 5.4 (d) and Table 5.2**). The decrease in the I_G/I_D ratio for purified CNFs and NCNTs indicates increased defects in the tubes because acid treatment resulted in the introduction of carboxylic functional groups. It was also deduced from the laser Raman spectra that the CNFs were more graphitic than the NCNTs. Incorporation of N into the sp^2 carbon network results in defects. Indeed, TGA data also gave evidence for this observation as the onset combustion temperature of CNFs was higher than that of NCNTs.

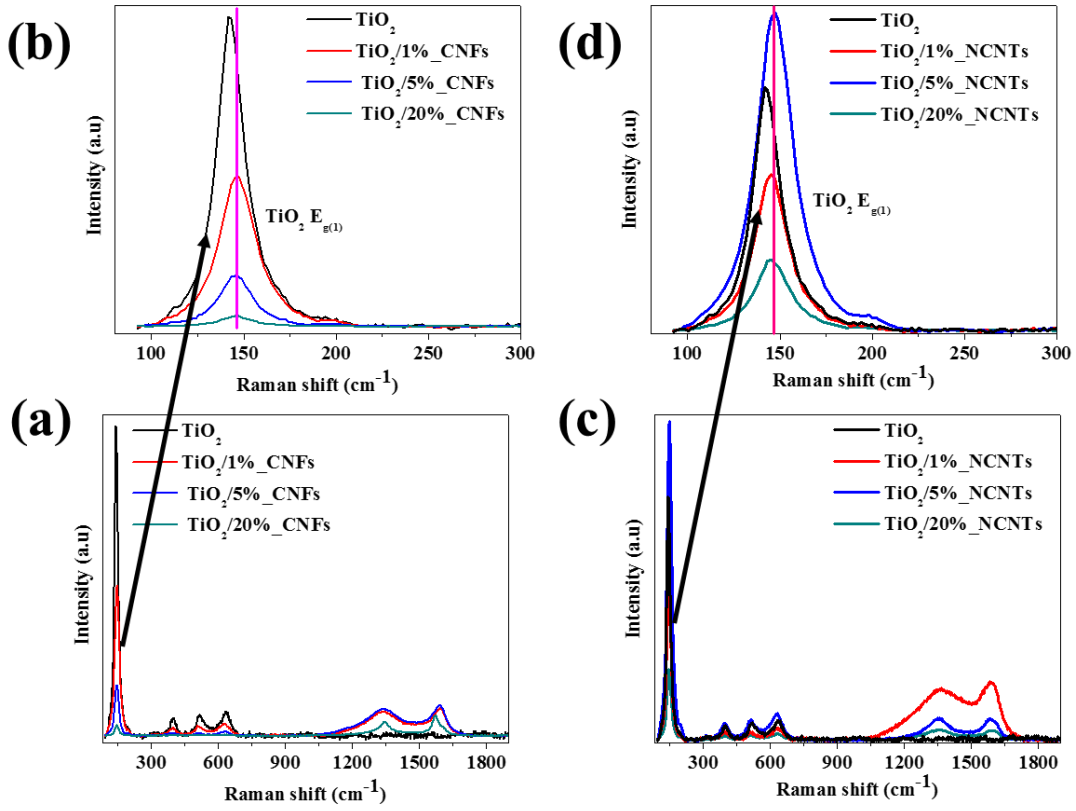

Figure 5.5. Laser Raman spectra of: (a) TiO_2 and CNFs based composites, (b) Expansion of the TiO_2 $E_{g(1)}$ peak of TiO_2 and CNFs based composites, (c) TiO_2 and NCNTs based composites and (d) Expansion of the TiO_2 $E_{g(1)}$ peak of TiO_2 and NCNTs based composites.

Laser Raman spectroscopy was also used to confirm the presence of TiO_2 (anatase phase) and study what effect the compositing of the two materials had had on their crystallinity. On the laser Raman spectrum of TiO_2 (**Figure 5.5 (a)**), four well-resolved peaks were observed at Raman shifts of 142, 399, 517 and 640 cm^{-1}. These were indexed as (E_g), (B_{1g}), (A_{1g}) and (E_g) respectively.[55–58] All of these modes were also observed for the composites, which confirmed the presence of TiO_2 (anatase phase) therein. It was also observed that the most intense TiO_2 peak (E_g) for all composites was broader and blue-shifted relative to that

of unbound TiO_2 (142 to 147 cm^{-1}). The broadening and positioning of Raman peaks have been reported to be primarily affected by the size and defects of the nanomaterial, the temperature at which measurements were recorded and also the effect of laser-induced local heating on the sample.[55,59,60] All the laser Raman analyses in this study were conducted using the same laser source and under exactly the same conditions. This meant that the temperature and laser-induced localized heating of these samples could be disregarded as potential sources of peak shifting and broadening. Consequently, the peak broadening and blue-shifting of the E_g peak were ascribed to be as a result of the surface pressure or phonon confinement.[55] Compromised crystallinity and change in the crystallite size of nanomaterials have been reported to be responsible for the phonon confinement effects .[55] Moreover these same observations have been previously reported for composites of titanium nanotubes and graphene oxide (TNTs/hGO) as well as for CNTs/TiO_2 where they were used to propose the existence of strong chemical interactions between TiO_2 and CNMs.[55,61] In this research chemical interactions were desired as they increased the likelihood of charge separation in the TiO_2_CNs/NCNTs composites and hence their potential applicability in photocatalysis.

PXRD analyses were also conducted on the carbonaceous materials before and after purification to further qualify the observations made from SEM and TGA analysis that the purification process had been effective at removing CFA particles. It was observed from the PXRD patterns (**Figure 5.6**) that the patterns of the raw CNMs were similar to that of CFA, indicating that the materials were dominated by the presence of CFA. On the other hand, the PXRD patterns of purified CNMs were different from those of CFA and the raw CNMs, indicating that the removal of the CFA had been achieved. The results agreed with those obtained from TGA analysis (**Figure 5.3**) and SEM (**Figure 5.1**). Only peaks that were attributed to graphitic

carbon reflections at 2θ values of 31 and 50 ° (i.e. the (002) and (100) reflections, respectively) were observed on the PXRD patterns of purified CNMs. The (002) peak of CNMs appeared at a 2θ value corresponding to that of quartz in CFA. Nevertheless, the peak was assigned to CNMs because: i) the other quartz peaks were not observed and ii) the corresponding (100) peak was observed confirming that the materials were CNMs.

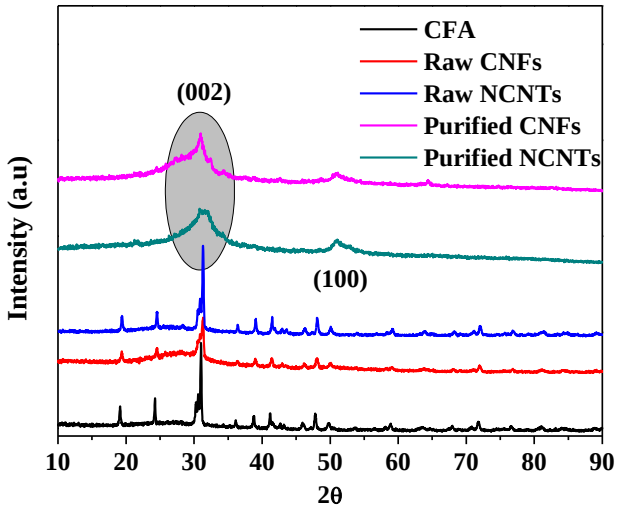

Figure 5.6. PXRD patterns of CFA as well as raw and purified CNMs.

PXRD analyses were also performed in order to investigate the effects that CNMs had on the crystallinity of TiO_2 upon compositing the two materials. The PXRD patterns of TiO_2 and the composites with varying compositions revealed peaks characteristic of the anatase phase of TiO_2 (**Figure 5.7**). These reflections were indexed as: (101), (004), (200), (105), (211), (204), (116), (220) and (215), as they appeared on the diffraction pattern from the lowest to the highest 2θ value (JCPDS PDF#: 00-021-1272). Characteristic peaks of carbonaceous materials were not observed on the PXRD patterns of the composites in the range that was examined

because of the: i) Overlap of the intense (101) TiO_2-anatase reflection with the (002) reflection of CNM, ii) Higher scattering from TiO_2 and the large difference in mass of TiO_2 and CNMs in the composites.

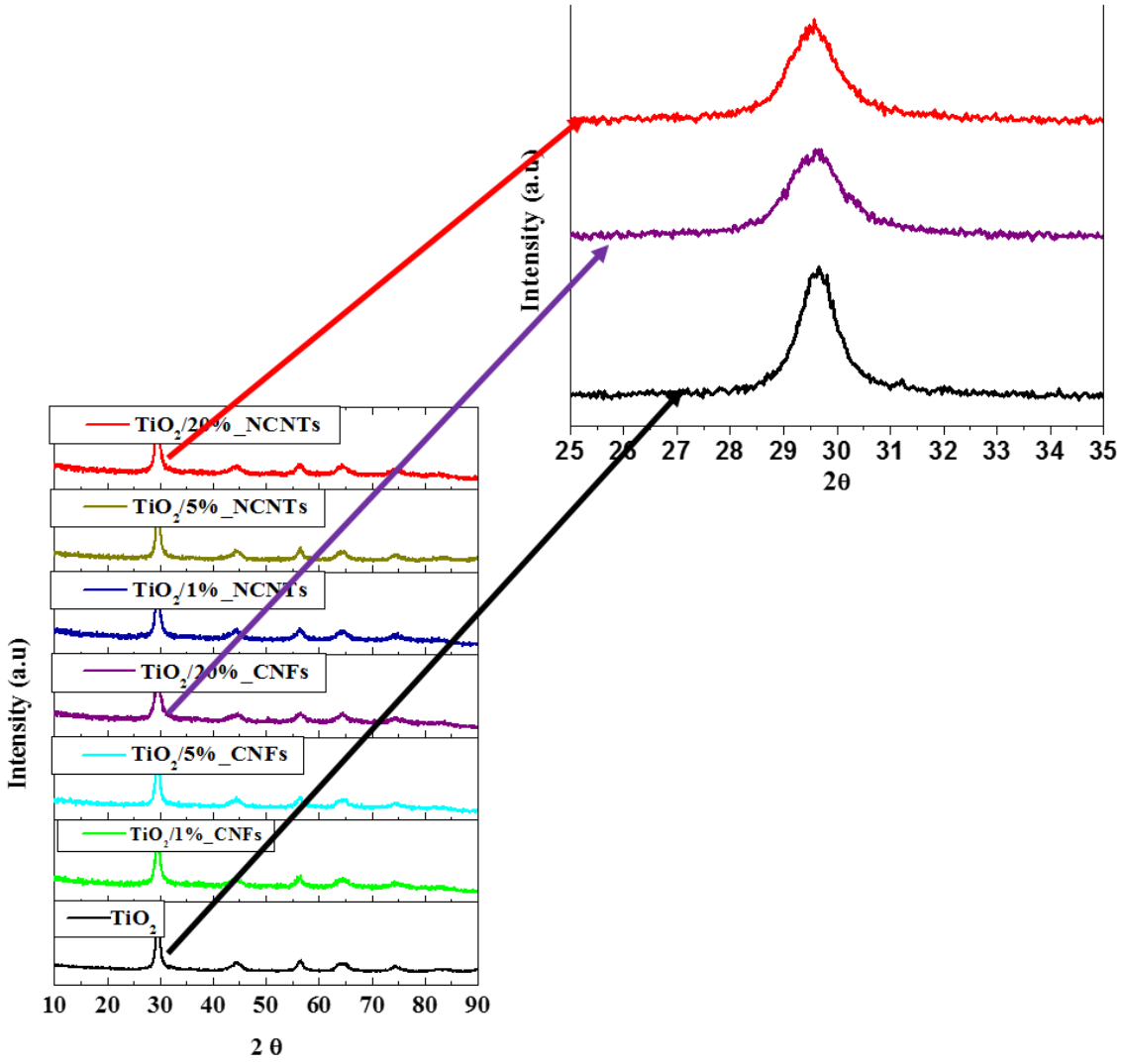

Figure 5.7. PXRD patterns of TiO_2 and TiO_2_CNFs/NCNTs composites.

As was the case with laser Raman spectroscopy (**refer to Figure 5.5**), the (101) TiO_2-anatase reflection for the composites, TiO_2/20%_CNFs and TiO_2/20%_NCNTs (**inset in Figure 5.7**) was found to have been broader relative to

that of unbound TiO_2. Perera *et al*.,[55] have observed similar results upon compositing TNTs and reduced graphene oxide, where they cited work by Sun *et al*.[62] and attributed their own observations to two things: 1) Lattice distortions which occurred in TiO_2 as a result of compositing with CNMs and 2) The more developed crystal structure of unbound TiO_2 as compared to TiO_2 in composites.[55] The average crystallite size of unbound TiO_2 and TiO_2 in composites was calculated by Scherer's equation using the (101) reflection. The crystal size of bound TiO_2 (9-12 nm) was found to be smaller than that of TiO_2 which was found to be 14 nm by Scherrer's equation. These results were consistent with the laser Raman data which showed that the presence of CNMs had had an influence on the crystallization of TiO_2.

In order to investigate the trapping, migration and transfer properties of the photoinduced charge carriers, photoluminescence measurements were conducted on unbound TiO_2 and the TiO_2_CNFs/NCNTs composites. This was possible as the photoluminescence emission of semiconductors has been shown to arise as a result of the recombination of charge carriers.[52,50,63] Excitation at a wavelength of 290 nm resulted in an emission spectrum with a broad peak from 350 nm to 429 nm (which consisted of several peaks) and two other distinct peaks at 444 and 486 nm (**Figure 5.8**).

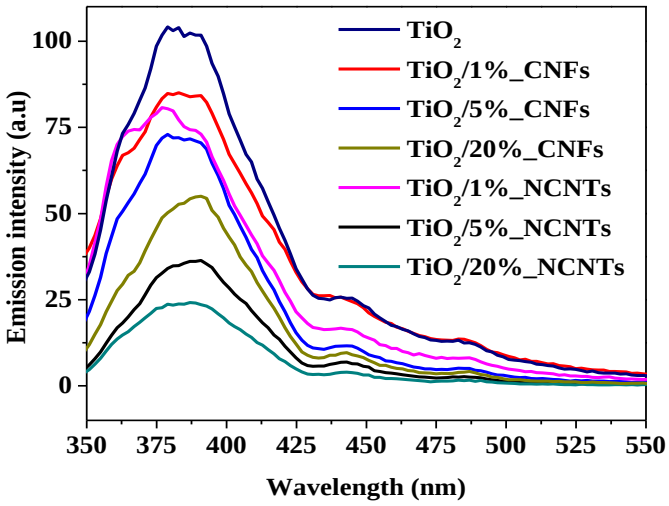

Figure 5.8. Photoluminescence spectra of unbound TiO_2 and various composites.

These features have been reported to be characteristic of the recombination of charge carriers at the surface trap sites of the semiconductor (TiO_2).[50] The emission peaks of unbound TiO_2 were found to be higher than those of the TiO_2_CNFs/NCNTs composites. **Table 5.2** shows the intensity values of the main broad emission peaks of TiO_2 and the TiO_2_CNFs/NCNTs composites. The reduction in the intensity in the case of composites was ascribed to the reduced recombination of electrons and holes, thus indicating that the carbonaceous materials had increased the lifetime of the charge carriers.[47,58,50,48,49,28] The emission intensities of the composites that were modified with CNFs were observed to have been reduced as a function of the amount of CNFs contained therein. The same trend was observed in the case of the NCNTs-based composites. Hence that the greater the number of CNMs in the composites, the more effective the charge separation appeared to get. Furthermore, it was observed that the emission intensities of NCNTs-based composites were lower than those for CNFs-based composites. Here the NCNTs had more intrinsic

functional groups, due to the presence of nitrogen species, than the CNFs which had been surface functionalized by acid treatment during purification. Either way, the functional groups on the CNMs had increased chemical contact between TiO_2 and CNMs, and hence had increased the lifetime of the charge carriers (**Figure 5.8**). Indeed, Wang *et al*. have attributed the superior photoactivity of TiO_2 composited with NCNTs over TiO_2 and TiO_2-CNTs composites to strong linkages between these CNMs and TiO_2.[32]

Diffuse reflectance UV-vis spectra of the various potential photocatalysts, expressed in terms of the Tauc's plot in equivalent absorption units, are presented in **Table 5.3** and **Figure 5.9**.

Table 5.3. PL emission intensities and band gap energies (Tauc's plot) of the various potential photocatalysts

Material	PL emission intensity (a.u)	Band gap (eV)
TiO_2	101	3.25
TiO_2/1%_CNFs	85	3.19
TiO_2/5%_CNFs	72	3.19
TiO_2/20%_CNFs	55	3.19
TiO_2/1%_NCNTs	80	3.24
TiO_2/5%_NCNTs	36	3.19
TiO_2/20%_NCNTs	24	3.12

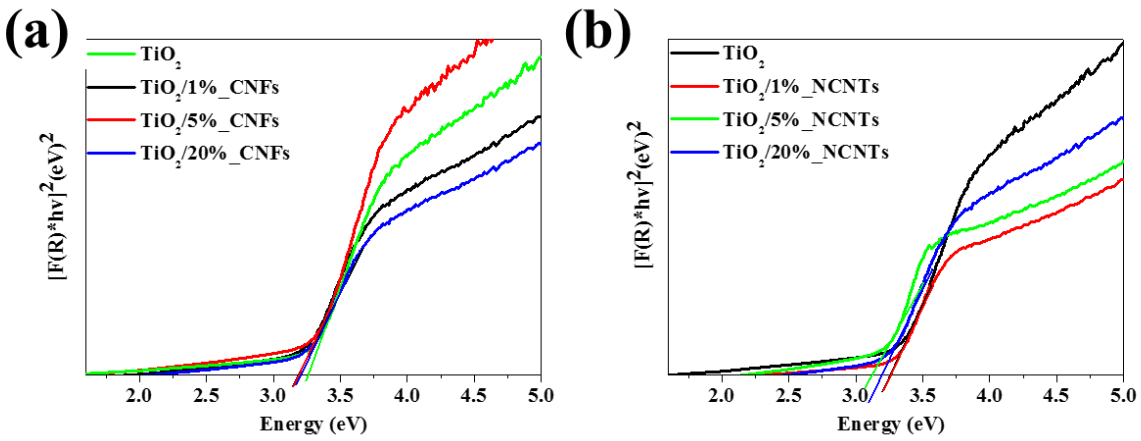

Figure 5.9. UV-DRS Tauc's plots of TiO_2 and various potential photocatalysts.

The characteristic band energy of TiO_2 nanoparticles was observed at 3.25 eV, while the band energies of the TiO_2_CNFs/NCNTs composites were found to be slightly lower. For instance, the TiO_2_CNFs composites showed the least improvement i.e. all had band energies of 3.19 eV. On the other hand, the TiO_2_NCNTs composites had lower band energies as the % NCNT in the composite was increased (i.e. they decreased from 3.24 to 3.12 eV as the % NCNT was increased from 1% to 20%).

5.4 Photodegradation studies

The photocatalytic activity of each of the potential photocatalytic materials was evaluated by studying their efficiency at removing BPA in water under solar simulated conditions using a Newport model 69911 solar simulator. A full radiation spectrum was used, i.e. UV and Vis light. The experimental conditions under which these reactions were conducted were optimized using unbound TiO_2. In order to ascertain that the results obtained were as a result of photocatalysis, two kinds of

control experiments were conducted: 1) Irradiation of BPA in the absence of any potential photocatalyst material, and 2) Stirring BPA in the presence of each potential photocatalyst material, but without irradiation. Here it was found that there was no significant reduction in the amount of BPA upon its irradiation in the absence of any potential photocatalyst material. However, it was found that an adsorption equilibrium was reached after 2 h when BPA was stirred in the presence of the various potential photocatalyst materials without being subject to irradiation. An insignificant amount of BPA was adsorbed onto the surface of the materials.

5.4.1.1 Effect of the mass of catalyst in solution.

The kinetics of the photocatalytic decomposition of organic contaminants assumes the form of a simple pseudo-first-order reaction, where the rate limiting step is the rate at which the active radical species are produced.[62] Indeed, this is true but in photocatalysis, the depth at which light can penetrate is another important factor to be considered.[62] Therefore in order to avoid using an excessive quantity of catalyst, it is necessary to optimize the mass of catalyst used for the efficient photodegradation of BPA. The effect of the mass of catalyst (using unbound TiO_2) for the photodegradation of BPA (120 ppm BPA, pH 7 in 2 h) was investigated in the range of 20-100 mg per 50 ml BPA solution.

Here it was observed that the % BPA that was photodegraded increased with increased mass of catalyst (i.e. unbound TiO_2) in the range from 20-60 mg per 50 ml solution, with the optimum catalyst mass being 60 mg (**Figure 5.10**). However, the photodegradation efficiencies of unbound TiO_2 catalyst at 80 and 100 mg per 50 ml BPA solution were lower than those that were obtained at 40 and 60 mg per 50 ml.

Indeed, several studies have found that increasing the mass of photocatalyst per volume of solution did not necessarily always result in increased efficiency. For example, Muruganandham *et al*. have reported an increase in the photocatalytic decolorization of reactive yellow 14 azo dye as a function of increased catalyst mass/volume at a range of 1-4 g/l, whereas at between 4 and 6 g/l, they observed that the activity had plateaued off.[66] Similarly, it has been reported that the photodegradation efficiency of BPA increased as a function of increased mass of catalyst per volume of solution i.e. up to 500 mg, after which it plateaued off and then decreased from 600 to 1000 mg.[62]

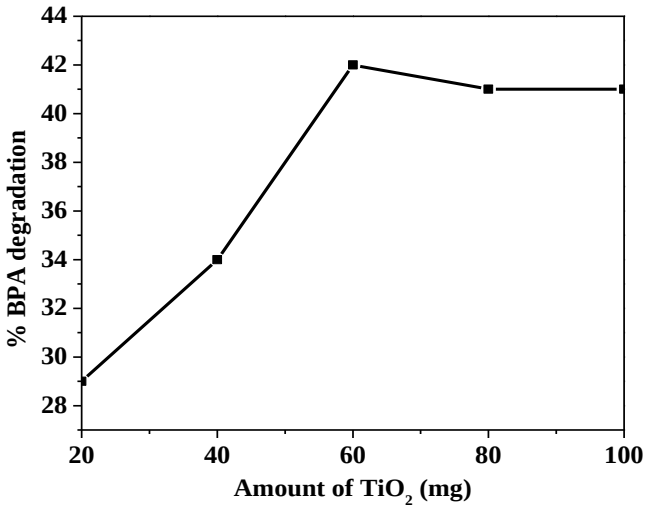

Figure 5.10. The effect of the mass of photocatalyst (i.e. unbound TiO_2) on the photodegradation of 50 ml of 120 ppm solution (pH 7) of BPA in water at 22 °C.

The initial solution pH in photocatalysis is important as TiO_2, like most other semiconductors, is amphoteric and its surface charge is influenced by pH.[64] The point of zero charge or pH_{zpc} of TiO_2 nanoparticles has been reported to be

approximately 6.[64,65] This, therefore, means that the surface of TiO_2 is positively charged at a pH below 6 and negatively charged at a pH above 6. Also given that photocatalytic reactions are REDOX in nature, they are sensitive to the surface charge of the catalyst. Similarly, the adsorption of BPA onto TiO_2 would be influenced by changes in pH. Indeed, in this research, the photodegradation of BPA with TiO_2 was found to have been significantly influenced by the solution pH, where the efficiency was found to have increased with increased solution pH (**Figure 5.11**).

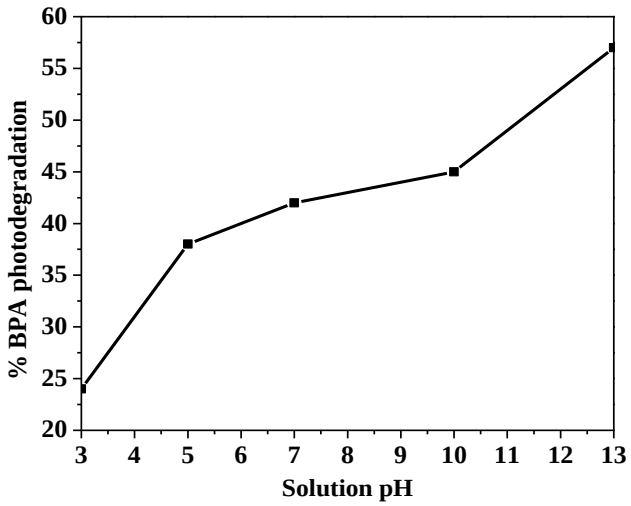

Figure 5.11. The effect of solution pH on the % BPA of 50 ml of 120 ppm that was photodegraded in water using 60 mg TiO_2 as a photocatalyst, at 22 °C.

5.4.1.2 Effect of solution pH

Here reactions were conducted in the pH range of 3 to 13, where the highest photoactivity that was measured was for the solution at pH 13. This was attributed to that fact that at high pH there are more hydroxyl ions which upon interaction with

photogenerated positively charged holes yield hydroxyl radicals.[66] In photocatalysis hydroxyl radicals are the foremost oxidizing agents when created in abundance, hence the rate at which BPA was photodegraded at pH 13 increased. This conclusion has been reached by several authors.[66–69] Consequently, pH 13 was selected as the optimum pH for the photodegradation of BPA, which also happened to be the pH at which BPA was the most soluble in water. It is noteworthy that the optimal pH obtained in this study would not be applicable in real life applications.

5.4.1.3 Effect of initial BPA concentration

The concentration of pollutants in water systems vary. This, therefore, necessitates a determination of the photocatalyst efficiency at different substrate (e.g. BPA) concentrations. Thus the effect of the initial BPA concentration on the ability of unbound TiO_2 to photodegrade it, in the range of 40 ppm to 140 ppm, was investigated. Here an inverse relationship between the % BPA that was photodegraded and the BPA concentration was observed (**Figure 5.12**).

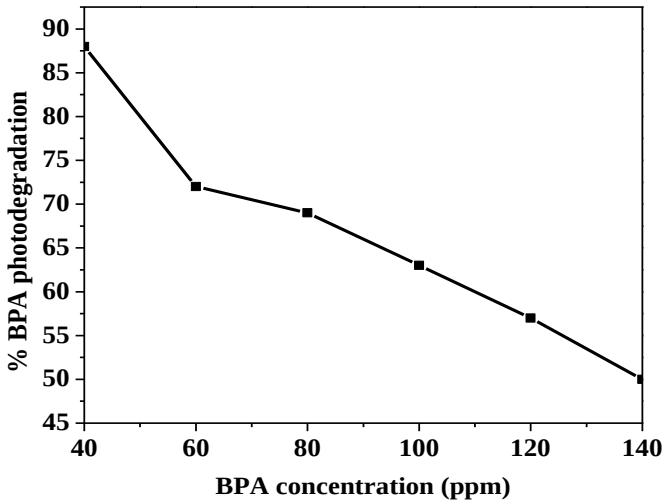

Figure 5.12. The effect of the initial concentration of BPA on the % BPA photodegraded in a 50 ml solution at pH 13 using 60 mg TiO_2 at 22 °C.

Here the least % BPA that was photodegraded was observed when the initial concentration of BPA was 140 ppm, while the highest was for when 40 ppm BPA was used. Here it is thought that when such large concentrations of BPA were used, they were adsorbed onto the catalyst surface and impeded light from reaching it and initiating photocatalytic reactions. Furthermore, it is suggested that with the catalyst so covered the BPA itself absorbed the incoming radiation. Indeed, several authors have observed similar trends to these.[66,67,23,70] Nevertheless, in view of the practical need to clean wastewater with high concentrations of BPA, 100 ppm was selected as the substrate concentration to be used for evaluating the photodegradation efficiencies of the various TiO_2_CNFs/NCNTs composites.

5.4.1.4 Effect of reaction temperature

Temperature is one of the environmental factors that could influence the photodegradation efficiency. Hence the effect of temperature was studied within the ranges of 22 and 50 °C using TiO_2 as was the case with all other optimization experiments. There was not much difference in the efficiencies of the experiments conducted at different temperatures to make any kind of conclusion (see **appendix (A5.1)).**

Therefore for the purposes of evaluating the photoactivity of the various potential TiO_2_CNFs/NCNTs catalysts, 22 °C (room temperature) was chosen. Thus the optimal conditions that were used for evaluating the photocatalytic efficiencies of the various potential TiO_2_CNFs/NCNTs catalysts are summarized in **Table 5.4**.

Table 5.4. Optimum conditions for evaluating the photocatalytic efficiencies of the various potential TiO_2_CNFs/NCNTs catalysts.

BPA conc.	100 ppm
Catalyst loading	60 mg
Solution volume	50 ml
pH	13
Temperature	22 °C
Reaction duration	4 h
Stirring speed	600 RPM

5.4.2 Evaluation of the photoactivity of the various materials

The photodegradation efficiencies of the various photocatalysts that were tested under the condition shown in **Table 5.4** are shown in **Figure 5.13** and **Table 5.5**.

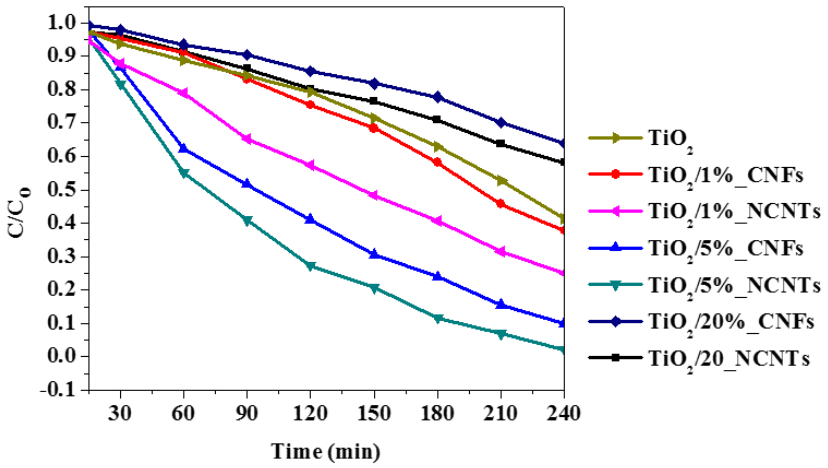

Figure 5.13. Photodegradation of BPA using the various TiO_2_CNFs/NCNTs photocatalysts at conditions given in **Table 5.5**.

Table 5.5. Summary of the photodegradation efficiencies of the various TiO_2_CNFs/NCNTs photocatalysts after 4 h (X_{4h}, %).

Sample	X_{4h} (%)
TiO_2	59
TiO_2/1%_CNFs	64
TiO_2/5%_CNFs	90
TiO_2/20%_CNFs	36
TiO_2/1%_NCNTs	75
TiO_2/5%_NCNTs	98
TiO_2/20%_NCNTs	42

The photodegradation values on **Table 5.5** were expressed as X_{4h} which indicated the amount of BPA that had been removed after 4 h of photodegradation. Based upon these results the highest photodegradation activity observed was for

TiO_2/5%_NCNTs followed by TiO_2/5%_CNFs and TiO_2/1%_NCNTs. All of these had superior photoactivity when compared to unbound TiO_2.

The high photoactivity of these composites was likely due to the collective effect of several factors: i) The TiO_2_CNFs/NCNTs composites were found to have higher surface areas compared to unbound TiO_2 (**Table 5.2**). This most probably translated into increased adsorption capacity, meaning that there was a higher chance of reactive photogenerated species coming into contact with BPA, and ii) The close proximity of the CNFs/NCNTs with TiO_2 had resulted in the chemical interactions between them and thus the formation of a heterojunction that consequently caused a decrease in the recombination rate of photoinduced charge carriers. As previously indicated the evidence of this close proximity, through the surface coating of TiO_2 on these CNMs, has been noted in the TEM micrographs (**Figure 5.2**). Similarly, the evidence that chemical interactions between the two had occurred was observed both in the laser Raman spectra (**Figure 5.5**) and in the PXRD patterns (**Figure 5.7**). Indeed, the photoluminescence data (**Figure 5.8**) revealed that the recombination rate of electrons and holes had been reduced by compositing TiO_2 with these CNMs. Other possible reasons for the improvement in photoactivity, as postulated by other authors who have had similar observations when TiO_2 was composited with CNMs, include: i) A possible shift of the Fermi level to more positive potential values[47,36], and ii) possible photoionization of the CNMs causing electrons to be injected into the conduction band of TiO_2 and thus resulting in an increased generation of active radical species.[34,53] The photodegradation efficiency of TiO_2/1%_CNFs was found to be slightly higher than that of TiO_2, whereas the photo-activities of TiO_2/20%_CNFs and TiO_2/20%_NCNTs were found to be lower than that of

unbound TiO_2. The decreased photocatalytic efficiency of the composites consisting of 20 % CNFs/NCNTs was likely due to the higher proportion of CNMs relative to the actual photoactive material i.e. TiO_2. It is thought that this may have increased phonon scattering. Indeed, Gao *et al*. have observed similar trends like these, where the TiO_2/MWCNTs composites consisting of 10 % or more MWCNTs showed diminished photoactivity relative to unbound TiO_2.[47]

Furthermore, it was observed that NCNTs had more of an effect on the improvement of the photocatalytic efficiency of TiO_2 than CNFs. This was ascribed to a collective consequence of numerous concomitant influences: i) the surface areas of NCNTs and NCNTs-based composites were generally higher than those of CNFs and CNFs-based composites (**Table 5.2**). From this, it was inferred that the high surface areas were translated into increased surface interactions between the active photogenerated radicals and BPA. ii) Also, it was inferred from flatter PL emission spectra of the NCNTs-based composites that a greater separation of electrons and holes had been achieved by compositing them with TiO_2. iii) Furthermore, it was observed from UV-DRS measurements that the absorption wavelengths of NCNTs-based composites were more blue-shifted as compared to the unbound TiO_2, which meant that more light was harvested by NCNTs and hence the increased photoactivity. Similar observations were made by Wang *et al*., where it was reported that TiO_2-CN_x composites had superior photoactivities relative to TiO_2-CNTs composites and unbound TiO_2.[32] Here increased charge separation was proposed as the main reason for the observations.[32]

The additional functional groups in NCNTs over and above those that were introduced by acid functionalization (refer to **Figure 2.11** in **section 2.4.2**) played a

vital role in the increased photoactivity of NCNTs-based composites particularly in creating chemically reactive centers. These in addition to the functional groups that were introduced by acid treatment were vital in the creation of chemical interactions between the CNMs and TiO_2. Ultimately this meant that NCNTs had more defects than CNFs. Thus the photogenerated electrons could more easily be transferred into NCNTs than CNFs, which could act as better electron sinks to yield greater charge separation and hence superior photoactivity.

5.5 Conclusions

In this chapter, the irony of using hazardous waste material to synthesize useful materials for the removal of hazardous water contaminant, BPA was demonstrated. The synthesis of NCNTs as was demonstrated in **CHAPTER 4** were grown from CFA along with CNFs. The purification of NCNTs and CNFs that were synthesized from toxic waste material (CFA) was demonstrated as effective by various analytical techniques. The purified CNFs and NCNTs were used to form composites with TiO_2 with varying ratios by the surfactant wrapping sol-gel method that was modified by hydrothermal completion of the hydrolysis process. Founded on the information deduced from the characterization techniques, the modified synthetic procedure employed in this report was shown to be effective in the synthesis of TiO_2_CNFs/NCNTs composites, where the two components were in very close proximity to each other. Furthermore, it was observed that chemical interactions between TiO_2 and NCNTs/CNFs existed which translated into increased photoactivity. This enhancement was primarily attributed to the separation of electrons and holes that was achieved as a result of the chemical interfaces that had formed between the TiO_2 and NCNTs/CNFs through this synthetic method. It was

also found that the NCNTs-based composites had higher photoactivities as compared to their CNFs-based counterparts. This was most probably due to the greater number of functional groups in NCNTs than in CNFs, due to the presence of nitrogen, which had an increased affinity to TiO_2. However, it was found that compositing TiO_2 higher %'s of CNMs e.g. 20 % NCNTs or 20 % CNFs, resulted in a decrease in photoactivity relative to unbound TiO_2. This meant that there was a tradeoff to be made between the % of CNMs in composites with TiO_2, for use as photocatalysts, and their increase in photoactivity. Notwithstanding these observations, it is also possible that given that the amount of TiO_2 in the composite consisting of 20 % CNMs was low, it is possible that if normalized the values would improve.

Having demonstrated that CFA could be used for the synthesis of NCNTs and CNFs which were shown to be effective functional supports for TiO_2 photocatalyst, in **CHAPTER 5** we report the synthesis of zeolitic materials from CFA to be used for the same applications as was with the NCNTs and CNFs.

5.6 References

1. Boas, M., Feldt-Rasmussen, U. & Main, K. M. Thyroid effects of endocrine disrupting chemicals. *Mol. Cell. Endocrinol.* **355,** 240–248 (2012).
2. Sidhu, S., Gullett, B., Striebich, R., Klosterman, J., Contreras, J. & DeVito, Michael Endocrine disrupting chemical emissions from combustion sources: Diesel particulate emissions and domestic waste open burn emissions. *Atmos. Environ.* **39,** 801–811 (2005).
3. Shokrollahzadeh, S., Azizmohseni, F., Golmohammad, F., Shokouhi, H. & Khademhaghighat, F. Biodegradation potential and bacterial diversity of a petrochemical wastewater treatment plant in Iran. *Bioresour. Technol.* **99,** 6127–6133 (2008).
4. Gaspari, L., Sampaio, D. R., Paris, F., Audran, F., Orsini, M., Neto, J. B. & Sultan, C. High prevalence of micropenis in 2710 male newborns from an intensive-use pesticide area of Northeastern Brazil. *Int. J. Androl.* **35,** 253–264 (2012).
5. Tabb, M. M. & Blumberg, B. New modes of action for endocrine-disrupting chemicals. *Mol. Endocrinol.* **20,** 475–482 (2006).
6. Vandenberg, L. N. Colborn, T., Hayes, T. B., Heindel, J. J., Jacobs, D. R., Lee, D. H., Shioda, T., Soto, A. M., vom Saal, F. S., Welshons, W. V., Zoeller, R. T. & Myers, J. P. Hormones and endocrine-disrupting chemicals: Low-dose effects and nonmonotonic dose responses. *Endocr. Rev.* **33,** 378–455 (2012).
7. Schug, T. T., Janesick, A., Blumberg, B. & Heindel, J. J. Endocrine disrupting chemicals and disease susceptibility. *J. Steroid Biochem. Mol. Biol.* **127,** 204–215 (2011).
8. Rogers, J. A., Metz, L. & Yong, V. W. Review: Endocrine disrupting chemicals and

immune responses: A focus on bisphenol-A and its potential mechanisms. *Mol. Immunol.* **53,** 421–430 (2013).

9. Howdeshell, K. Peterman, P. H., Judy, B. M., Taylor, J. A., Orazio, C. E., Ruhlen, R. L., vom Saal, F. S. & Welshons, W. V. Bisphenol A is released from used polycarbonate animal cages into water at room temperature. *Environ. Health Perspect.* **111,** 1180–1187 (2003).
10. Carwile, J. L. Luu, H. T., Bassett, L. S., Driscoll, D. A., Yuan, C., Chang, J. Y., Ye, X., Calafat, A. M. & Michels, K. B. Polycarbonate Bottle Use and Urinary Bisphenol A Concentrations. *Environ. Health Perspect.* **117,** 1368–1372 (2009).
11. Vandenberg, L. N., Hauser, R., Marcus, M., Olea, N. & Welshons, W. V. Human exposure to bisphenol A (BPA). *Reprod. Toxicol.* **24,** 139–177 (2007).
12. Gould, J. C., Leonard, L. S., Maness, S. C., Wagner, B. L., Conner, K., Zacharewski, T., Safe, S., McDonnell, D. P. & Gaido, K. W. Bisphenol A interacts with the estrogen receptor α in a distinct manner from estradiol. *Mol. Cell. Endocrinol.* **142,** 203–214 (1998).
13. Paulose, T., Speroni, L., Sonnenschein, C. & Soto, A. M. Estrogens in the wrong place at the wrong time: Fetal BPA exposure and mammary cancer. *Reprod. Toxicol.* **54**, 27–29 (2014).
14. Wu, H. J., Liu, C., Duan, W. X., Xu, S. C., He, M. D., Chen, C. H., Wang, Y., Zhou, Z., Yu, Z. P., Zhang, L.& Chen, Y. Melatonin ameliorates bisphenol A-induced DNA damage in the germ cells of adult male rats. *Mutat. Res. - Genet. Toxicol. Environ. Mutagen.* **752,** 57–67 (2013).
15. Rahman, M. F., Yanful, E. K. & Jasim, S. Y. Occurrences of endocrine disrupting compounds and pharmaceuticals in the aquatic environment and their removal from drinking water: Challenges in the context of the developing world. *Desalination*

248, 578–585 (2009).

16. Nakada, N., Shinohara, H., Murata, A., Kentaro, K., Managaki, S., Nobuyuki, S. & Hideshige, T. Removal of selected pharmaceuticals and personal care products (PPCPs) and endocrine-disrupting chemicals (EDCs) during sand filtration and ozonation at a municipal sewage treatment plant. *Water Res.* **41,** 4373–4382 (2007).
17. Casajuana, N. & Lacorte, S. Presence and release of phthalic esters and other endocrine disrupting compounds in drinking water. *Chromatographia* **57,** 649–655 (2003).
18. Huerta-Fontela, M., Galceran, M. T. & Ventura, F. Occurrence and removal of pharmaceuticals and hormones through drinking water treatment. *Water Res.* **45,** 1432–1442 (2011).
19. Pelaez, M., Nolan, N. T., Pillai, S. C., Seery, M. K., Falaras, P., Kontos, A. G., Dunlop, P. S. M., Hamilton, J. W. J., Byrne, J. A., O'Shea, K., Entezari, M. H. & Dionysiou, D. D. A review on the visible light active titanium dioxide photocatalysts for environmental applications. *Appl. Catal. B Environ.* **125,** 331–349 (2012).
20. Mezohegyi, G., Erjavec, B., Kaplan, R. & Pintar, A. Removal of bisphenol A and its oxidation products from aqueous solutions by sequential catalytic wet air oxidation and biodegradation. *Ind. Eng. Chem. Res.* **52,** 9301–9307 (2013).
21. Daskalaki, V. M., Fulgione, I., Frontistis, Z., Rizzo, L. & Mantzavinos, D. Solar light-induced photoelectrocatalytic degradation of bisphenol-A on TiO_2/ITO film anode and BDD cathode. *Catal. Today* **209,** 74–78 (2013).
22. Kumar, S. G. & Devi, L. G. Review on Modified TiO_2 Photocatalysis under UV / Visible Light : Selected Results and Related Mechanisms on Interfacial Charge Carrier Transfer Dynamics. *J. phys. Chem. A* **115,** 13211–13241 (2011).

23. Kaneco, S., Rahman, M. A., Suzuki, T., Katsumata, H. & Ohta, K. Optimization of solar photocatalytic degradation conditions of bisphenol A in water using titanium dioxide. *J. Photochem. Photobiol. A Chem.* **163,** 419–424 (2004).

24. Chiang, K., Lim, T. M., Tsen, L. & Lee, C. C. Photocatalytic degradation and mineralization of bisphenol A by TiO_2 and platinized TiO_2. **261,** 225–237 (2004).

25. Zhou, X., Liu, G., Yu, J. & Fan, W. Surface plasmon resonance-mediated photocatalysis by noble metal-based composites under visible light. *J. Mater. Chem.* **22,** 21337 (2012).

26. Liu, Y., Guo, L., Yan, W. & Liu, H. A composite visible-light photocatalyst for hydrogen production. *J. Power Sources* **159,** 1300–1304 (2006).

27. Shan, A. Y., Ghazi, T. I. M. & Rashid, S. A. Immobilisation of titanium dioxide onto supporting materials in heterogeneous photocatalysis: A review. *Appl. Catal. A Gen.* **389,** 1–8 (2010).

28. Sobana, N., Muruganadham, M. & Swaminathan, M. Nano-Ag particles doped TiO_2 for efficient photodegradation of Direct azo dyes. *J. Mol. Catal. A Chem.* **258,** 124–132 (2006).

29. Li, X. ., Li, F. ., Yang, C. . & Ge, W. . Photocatalytic activity of WOx-TiO_2 under visible light irradiation. *J. Photochem. Photobiol. A Chem.* **141,** 209–217 (2001).

30. Iliev, V., Tomova, D., Bilyarska, L., Eliyas, a. & Petrov, L. Photocatalytic properties of TiO_2 modified with platinum and silver nanoparticles in the degradation of oxalic acid in aqueous solution. *Appl. Catal. B Environ.* **63,** 266–271 (2006).

31. Wang, P., Huang, B., Dai, Y. & Whangbo, M.-H. Plasmonic photocatalysts: harvesting visible light with noble metal nanoparticles. *Phys. Chem. Chem. Phys.* **14,** 9813–9825 (2012).

32. Wang, L., Shen, L., Li, Y., Zhu, L., Shen, J. & Wang, L. Enhancement of Photocatalytic Activity on TiO_2-Nitrogen-Doped Carbon Nanotubes Nanocomposites Enhancement of Photocatalytic Activity on TiO_2 -Nitrogen-Doped Carbon Nanotubes Nanocomposites. *Int. J. photoenergy* **2013,** 1–7 (2013).

33. Anandan, S., Sivasankar, T. & Lana-Villarreal, T. Synthesis of TiO_2/WO_3 nanoparticles via sonochemical approach for the photocatalytic degradation of methylene blue under visible light illumination. in *Ultrasonics Sonochemistry* **21,** 1964–1968 (2014).

34. Woan, K., Pyrgiotakis, G. & Sigmund, W. Photocatalytic Carbon-Nanotube-TiO_2 Composites. *Adv. Mater.* **21,** 2233–2239 (2009).

35. Leary, R. & Westwood, A. Carbonaceous nanomaterials for the enhancement of TiO_2 photocatalysis. *Carbon* **49,** 741–772 (2010).

36. Kongkanand, A. & Kamat, P. V. Electron Storage in Single Wall Carbon nanotubes. Fermi level equilibration in Semiconductor – SWCNT Suspensions. *ACS Nano* **1,** 13–21 (2007).

37. Czerw, R., Terrones, M., Charlier, J. C., Blase, X., Foley, B., Kamalakaran, R., Grobert, N., Terrones, H., Tekleab, D., Ajayan, P. M., Blau, W., Rühle, M. & Carroll, D. L. Identification of Electron Donor States in N-Doped Carbon Nanotubes. *Nano Lett.* **1,** 457–460 (2001).

38. Ayala, P., Arenal, R., Rümmeli, M., Rubio, A. & Pichler, T. The doping of carbon nanotubes with nitrogen and their potential applications. *Carbon* **48,** 575–586 (2010).

39. Voggu, R., Rout, C. S., Franklin, A. D., Fisher, T. S. & Rao, C. N. R. Extraordinary Sensitivity of the Electronic Structure and Properties of Single-Walled Carbon Nanotubes to Molecular Charge-Transfer. *J. Phys. Chem. C* **112**, 13053–13056

(2008).

40. Mao, Y., Duan, H., Xu, B., Zhang, L., Hu, Y., Zhao, C., Wang, Z., Chen, L. & Yang, Y. Lithium storage in nitrogen-rich mesoporous carbon materials. *Energy Environ. Sci.* **5,** 7950 (2012).

41. Nxumalo, E. N. & Coville, N. J. Nitrogen Doped Carbon Nanotubes from Organometallic Compounds: A Review. *Materials.* **3,** 2141–2171 (2010).

42. Terrones, M., Ajayan, P. M., Banhart, F., Blase, X., Carroll, D. L., Charlier, J. C., Czerw, R., Foley, B. & Grobert, N N-doping and coalescence of carbon nanotubes. *Science* **361,** 355–361 (2002).

43. Panias, D., Giannopoulou, I. P. & Perraki, T. Effect of synthesis parameters on the mechanical properties of fly ash-based geopolymers. *Colloids Surfaces A Physicochem. Eng. Asp.* **301,** 246–254 (2007).

44. Hintsho, N., Shaikjee, A., Masenda, H., Naidoo, D., Billing, D., Franklyn, P. & Durbach, S. Direct synthesis of carbon nanofibers from South African coal fly ash. *Nanoscale Res. Lett.* **9,** 2-11 (2014).

45. Hintsho, N., Shaikjee, A., Franklyn, P. & Durbach, S. The effect of CO_2 on the CVD synthesis of carbon nanomaterials using fly ash as a catalyst. *RSC Adv.* **5,** 53776–53781 (2015).

46. Hlekelele, L., Tripathi, P., Franklyn, P. J. & Durbach, S. H. Morphological and crystallinity differences in Nitrogen- Doped Carbon Nanotubes grown by Chemical Vapor Deposition Decomposition of Melamine over Coal Fly Ash. *RSC Adv.* **6,** 76773–76779 (2016).

47. Gao, B., Chen, G. Z. & Li Puma, G. Carbon nanotubes/titanium dioxide ($CNTs/TiO_2$) nanocomposites prepared by conventional and novel surfactant wrapping sol-gel methods exhibiting enhanced photocatalytic activity. *Appl. Catal.*

B Environ. **89,** 503–509 (2009).

48. Eder, D. & Windle, A. H. Carbon-inorganic hybrid materials: The carbon-nanotube/TiO_2 interface. *Adv. Mater.* **20,** 1787–1793 (2008).

49. Yu, Y., Jia, R., Zheng, J., Zhao, J., Li, L., Song, J. & Zhu, Z. Enhancement of adsorption and photocatalytic activity of TiO_2 by using carbon nanotubes for the treatment of azo dye. *Appl. Catal. B Environ.* **61,** 1–11 (2005).

50. Hintsho, N., Petrik, L., Nechaev, A., Titinchi, S. & Ndungu, P. Photo-catalytic activity of titanium dioxide carbon nanotube nano-composites modified with silver and palladium nanoparticles. *Appl. Catal. B Environ.* **156–157,** 273–283 (2014).

51. Dai, K., Peng, T., Ke, D. & Wei, B. Photocatalytic hydrogen generation using a nanocomposite of multi-walled carbon nanotubes and TiO_2 nanoparticles under visible light irradiation. *Nanotechnology* **20,** 125603 (2009).

52. Liu, J., Li, J., Sedhain, A., Lin, J. & Jiang, H. Structure and Photoluminescence Study of TiO_2 Nanoneedle Texture along Vertically Aligned Carbon Nanofiber Arrays. *J. Phys. Chem. C* **112,** 17127–17132 (2008).

53. Dahl, M., Liu, Y. & Yin, Y. Composite titanium dioxide nanomaterials. *Chem. Rev.* **114,** 9853–9889 (2014).

54. Liu, S., Sun, H., Liu, S. & Wang, S. Graphene facilitated visible light photodegradation of methylene blue over titanium dioxide photocatalysts. *Chem. Eng. J.* **214,** 298–303 (2013).

55. Perera, S. D., Sanjaya D. Mariano, R. G., Vu, K., Nour, N., Seitz, O., Chabal, Y. & Balkus, K. J. Hydrothermal synthesis of graphene-TiO_2 nanotube composites with enhanced photocatalytic activity. *ACS Catal.* **2,** 949–956 (2012).

56. Berger, H., Tang, H. & Levy, F. Growth and Raman spectroscopic characterization of TiO_2 anatase single crystals. *J. Cryst. Growth* **130,** 108–112 (1993).

57. Zhang, W. F., He, Y. L., Zhang, M. S., Yin, Z. & Chen, Q. Raman scattering study on anatase TiO_2 nanocrystals. *J. Phys. D. Appl. Phys.* **33,** 912–916 (2000).

58. Santangelo, S., Messina, G., Faggio, G., Donato, A., De Luca, L., Donato, N., Bonavita, A. & Neri, G.Micro-Raman analysis of titanium oxide/carbon nanotubes-based nanocomposites for hydrogen sensing applications. *J. Solid State Chem.* **183,** 2451–2455 (2010).

59. Balaji, S., Djaoued, Y. & Robichaud, J. Phonon confinement studies in nanocrystalline anatase-TiO_2 thin films by micro Raman spectroscopy. *J. Raman Spectrosc.* **37,** 1416–1422 (2006).

60. Sahoo, S., Arora, A. K. & Sridharan, V. Raman line shapes of optical phonons of different symmetries in anatase TiO_2 nanocrystals. *J. Phys. Chem. C* **113,** 16927–16933 (2009).

61. Solís, D., Vigueras-Santiago, E., Hernández-López, S., Gómez-Cortés, A., Aguilar-Franco, M. & Camacho-López, M. A. Textural, structural and electrical properties of TiO_2 nanoparticles using Brij 35 and P123 as surfactants. *Sci. Technol. Adv. Mater.* **9,** 25003 (2008).

62. Kim, S. W., Khan, R., Kim, T. & Kim, W. Synthesis, Characterization, and Application of Zr, S Co-doped TiO_2 as Visible-light Active Photocatalyst. *Bull. Chem. Soc.* **29,** 1217 (2008).

63. Gao, B., Ma, Y., Cao, Y., Yang, W. & Yao, J. Great enhancement of photocatalytic activity of nitrogen-doped titania by coupling with tungsten oxide. *J. Phys. Chem. B* **110,** 14391–7 (2006).

64. Ku, Y., Leu, R.-M. & Lee, K.-C. Decomposition of 2-chlorophenol in aqueous solution by UV irradiation with the presence of titanium dioxide. *Water Res.* **30,** 2569–2578 (1996).

65. Yang, H.-G., Li, C.-Z., Gu, H.-C. & Fang, T.-N. Rheological Behavior of Titanium Dioxide Suspensions. *J. Colloid Interface Sci.* **236,** 96–103 (2001).

66. Muruganandham, M., Shobana, N. & Swaminathan, M. Optimization of solar photocatalytic degradation conditions of Reactive Yellow 14 azo dye in aqueous TiO_2. *J. Mol. Catal. A Chem.* **246,** 154–161 (2006).

67. Al-Qaradawi, S. & Salman, S. R. Photocatalytic degradation of methyl orange as a model compound. *J. Photochem. Photobiol. A Chem.* **148,** 161–168 (2002).

68. Bianco Prevot, A., Vincenti, M., Bianciotto, A. & Pramauro, E. Photocatalytic and photolytic transformation of chloramben in aqueous solutions. *Appl. Catal. B Environ.* **22,** 149–158 (1999).

69. Sánchez, L., Peral, J. & Domènech, X. Photocatalyzed destruction of aniline in UV-illuminated aqueous TiO_2 suspensions. *Electrochim. Acta* **42,** 1877–1882 (1997).

70. Garcia, J. C. & Takashima, K. Photocatalytic degradation of imazaquin in an aqueous suspension of titanium dioxide. *J. Photochem. Photobiol. A Chem.* **155,** 215–222 (2003).

CHAPTER 6:

Titania anchored on CFA derived zeolites by resin gel technique decorated with Ag nanoparticles for UV and visible light photodegradation of BPA.

6.1 Introduction

Since the burning of coal in the 1920s for electricity generation scaled up globally this has led to increased production of coal by-products including coal CFA. It is estimated that only 16 % of the 600 Mt of coal fly ash (CFA) produced annually is utilized, the rest of it is disposed of in landfills and lagoons.[1,2]

CFA is a powdery material that is principally composed of glassy, hollow or solid spherical particles with diameters in the micron range. The chemical composition of CFA is 65-95 % alumina and silica whereas the other 5-15 % is made up of other metal oxides, elements, and unburned carbonaceous material.[1,2] The physical and chemical properties of CFA make it a potentially useful material for research. Indeed research has been performed on the potential uses of CFA to obviate an increasing threat to the environment while minimizing the costs associated with disposing of it.[1,3] For instance, different types of carbon nanomaterials have been synthesized from CFA when used as a catalyst in the chemical vapor deposition (CVD) method.[4–8] CFA has also been used as an adsorbent and catalyst support, amongst other applications.[9–14] Furthermore, zeolites have been derived from CFA using direct and non-direct techniques.[1,15,16]

Zeolites are aluminosilicates with group 1 and 2 metals as counter ions. The framework components that make up their structure are $[SiO_4]^{-4}$ and $[AlO_4]^{-5}$ and are arranged in tetrahedral geometries. They are linked to each other through the corners of the tetrahedrals, sharing oxygen atoms and the 3-D network that results has various sized cavities or voids. It is these voids that are responsible for the properties of zeolites and by

extension the large scope of their applications. The properties of zeolites that make them potentially suitable materials for photocatalysis include: i) photochemical stability, chemically unreactive and thermally stable, ii) high surface area, and iii) the capability of zeolites to contribute in electron-transfer progressions either as an electron acceptor.[71] Zeolites have mainly been used in catalysis, gas separation, ion exchange and adsorption of water pollutants.[2,17–20]

BPA is an example of an endocrine-disrupting chemical, which is industrially produced in large quantities and mainly used as a monomer for the production of polycarbonate plastics. It is reported to be toxic to living organisms because of its estrogenic effects and has been detected in water systems.[21–25] Numerous methods have been investigated for the removal of BPA and related compounds from water, including chemical oxidation, physical adsorption, and biological treatments.[25,26] The above-mentioned techniques are somewhat effective at removing BPA but they tend to be expensive and form toxic by-products.[27]

It is possible to use sunlight as a source of energy to drive a photocatalytic process as well as achieve mineralization of organic pollutants such as BPA.[28–32] It is for these reasons that photocatalysis is such a popular method for the decontamination of water.[28,29,33–35] TiO_2 is the most commonly used photocatalyst for such reactions because it is cheap, stable and has superior photocatalytic efficiency by comparison with other metal oxides.[33-35] However, the problem with TiO_2 photocatalysis is the high recombination rate of the active charge carriers.[36–40] Moreover, TiO_2 absorbs light in the UV region of the spectrum (large band gap) whereas the primary component of sunlight is visible light.[41,42] As such it is important that methods be investigated to improve the properties of TiO_2 in order to fully realize its potential as a photocatalyst in the visible portion of sunlight.

The photoactivity of TiO_2 has been shown to improve with the addition of noble metals (under both UV and visible light). For example, Hintsho *et al*. have shown that Pd and Ag improved the efficiency of TiO_2 for the photocatalytic removal of methylene blue under UV-radiation.[43] Similarly, Zhou *et al*. have reviewed harvesting visible light via the formation of surface plasmon resonance (SPR) by noble metals.[28] The wavelength at which the metal nanoparticles can absorb visible light can be tuned by controlling the size and shape of the metal nanoparticles and their environment. For instance, it was shown that the main resonance wavelength red-shifted as a function of the Ag nanocube edge length.[44] Here the centroid of the resonance wavelength of Ag nanocubes with an edge length of 36 nm was at 430 nm, whereas for 172 nm Ag nanocubes it was at 600 nm and spreading beyond 800 nm.[44]

Attempts have been made at improving the photoactivity of TiO_2 using metal oxides. For instance Fu *et al*. have formed binary metal oxides of TiO_2/ZrO_2 and TiO_2/SiO_2 using sol-gel synthesis.[45] These oxides were shown to have superior photoactivity as compared to pure TiO_2 under UV irradiation.[45] Similarly, there are several reports of composites consisting of TiO_2 and zeolites which were used as photocatalysts.[46,47] In this regard, Fukahori *et al*. have shown that the photocatalytic efficiencies of TiO_2-zeolites were superior to that of pure TiO_2 for the photodegradation of BPA under UV radiation.[48]

Several techniques have been used for the fabrication of composites of TiO_2 and other materials (including zeolites), including electrophoretic deposition, mechanical mixtures, sol-gel, electro-spinning, the paper-making technique, Pechini-based methods, and CVD.[45,48-53] The uniformity of the interactions between these composite materials as well as their physical and chemical properties have been found to differ according to the method of synthesis.[54]

Herewith, the feasibility of a novel resin-gel technique for the synthesis of CFA_Zeo coated uniformly with TiO_2 nanoparticles is demonstrated. The CFA_Zeo was derived from CFA using the modified alkali fusion hydrothermal method. Varying amounts of TiO_2 were loaded onto the synthesized zeolites using the resin gel method and modified with silver nanoparticles. Silver nanoparticles were deposited by deposition-precipitation with NaOH and urea. The photodegradation efficiencies of the resultant materials were determined using BPA under both full solar spectrum and visible light.

6.2 Experimental

6.2.1 Zeolite formation

The modified alkali fusion hydrothermal method of synthesizing zeolites from CFA was carried out as follows: 10 g of NaOH pellets (Sigma-Aldrich) was mixed with 10 g of CFA (as-received from the ESKOM, Research and Innovation Centre, Rosherville in South Africa). The mixture was ground into a fine powder and heated in a tempered iron jaffle maker to 700 °C. The resultant material was allowed to cool down to 350 °C and transferred into ice-cold water whilst stirring magnetically. The slurry was transferred into a Teflon cup, placed in an autoclave and heated to 200 °C for 12 h while stirring. The product was then centrifuged, washed with distilled water and then the precipitate was oven dried at 60 °C for 12 h. The dry powder was then calcined at 500 °C for 2 h. The product was labeled and referred to as CFA_Zeo in text.

6.2.2 Catalyst preparation

TiO_2 and CFA_Zeo composites were synthesized using the resin gel technique. A predetermined mass of CFA_Zeo was dispersed in 20 ml ethanol (96 %, Sigma-Aldrich) by sonication followed by vigorous magnetic stirring. The mixture was then kept in ice to

temperatures below 5 °C and 1 ml of titanium tetrachloride (Fluka) was added to the mixture slowly and then stirred for 30 min. Separately, 10 g of polyethylene glycol (PEG, M_w, 8000 Sigma-Aldrich) was added to 50 ml ethanol and heated to 100 °C to fully melt and dissolve the polymer. The ethanol molten polymer solution was added to the $TiCl_4$ and zeolite mixture whilst vigorously stirring and 5 ml of an ammonium hydroxide solution (25 %, Fluka) was added slowly and stirred for a further 30 min and kept under a 200 W IR lamp until a hard wax formed. The mixture was then transferred into a ceramic crucible, placed on a sand heating bath and heated to *ca*. 500 °C. A Bunsen burner was then used to ignite the sample and it was left to burn to completion. The black granular powder was collected, ground and calcined at 500 °C for 2 h. The samples were synthesized such that they contained 15 or 30 % CFA_Zeo relative to TiO_2 (m/m) and as such were labeled as TiO_2/CFA_Zeo(15 %) and TiO_2/CFA_Zeo(30 %) respectively. TiO_2 nanoparticles were synthesized using the same procedure except that the CFA_Zeo was not added.

Ag nanoparticles were deposited onto TiO_2 and both TiO_2/CFA_Zeo composites by the NaOH-urea deposition-precipitation technique as follows: A predetermined mass of one of the TiO_2/CFA_Zeo composites (i.e. either 15 % or 30 %) was dispersed in 100 ml distilled water by sonication for 30 min. A predetermined mass of silver nitrate (Sigma-Aldrich) to yield 1 % deposition of Ag nanoparticles was added to the mixture along with urea (Merck) at a molar concentration that was 20 times that of Ag^+. The pH of the mixture was then increased to 10 using a 0.1 M solution of NaOH (Sigma-Aldrich) which was then heated at 80 °C for 24 h. The product was washed with ethanol and centrifuged, then the resulting solid was dried at 60 °C for 12 h and calcined at 500 °C for 2 h. Ag nanoparticles were deposited on TiO_2/CFA_Zeo(15 %), TiO_2/CFA_Zeo(30 %) and on TiO_2 and as such the resulting composites were labeled Ag/TiO_2/CFA_Zeo(15 %), Ag/TiO_2/CFA_Zeo(15 %), Ag/TiO_2.

6.2.3 Catalyst characterization

The materials synthesized in this chapter were characterized as it was discussed in **Section 3.2**.

6.2.4 Photocatalytic measurements

The photoactivities of these materials were evaluated by monitoring the photodegradation of BPA. A slurry consisting of 25 mg of the materials and a BPA solution (50 ml, 60 ppm) was first magnetically stirred for 2 h in the dark to ensure adsorption equilibrium. Each mixture was then exposed to light for 60 min using a Newport model 69911 solar simulator. As the photocatalytic efficiency of the materials was tested under both UV and visible light, the visible light reactions were conducted with a UV-light filter ($\lambda > 400$ nm) whereas the visible light measurements were conducted using the full spectrum. The photocatalysis experimental details and the quantification of BPA details were discussed in detail in **section 3.2**.

6.3 Results and discussion

6.3.1 Materials characterization

The chemical composition of the unreacted CFA was determined by XRF (**Table 6.1**), where it was observed that silicon, aluminum and iron oxide accounted for more than 70 % of the CFA composition. Here the silica to alumina ratio was found to be 2.04. This meant that the raw CFA used was class F, according to the American society for testing of materials (ASTM).[3]

Table 6.1. The composition of CFA as determined by XRF.

Mineral	%/mass
SiO_2	58.14
Al_2O_3	28.79
Fe_2O_3	0.57
FeO	4.64
MnO	0.047
MgO	1.04
CaO	3.5
Na_2O	0.05
K_2O	0.77
TiO_2	1.57
P_2O_5	0.7

PXRD analyses were conducted in order to establish whether, after reacting the CFA, the zeolite phase had been formed (**Figure 6.1**). The PXRD pattern of CFA before being reacted showed that quartz (Q), mullite (M) and haematite (H) were the major minerals in CFA. After reaction of the CFA, the PXRD analysis revealed that a zeolitic material had formed i.e. sodium aluminum silicate hydrate.[56] In this regard, Molina and Poole investigated two methods of synthesizing zeolites from CFA where they found that the fusion process was crucial for the formation of zeolite X at short reaction times.[55] The PXRD pattern of the zeolite X they obtained, along with several others reported as zeolite X in literature [56–58], were similar to that which was reported in this work. This along with peak indexing led to the conclusion that the synthesis procedure adopted in this research had yielded zeolite X.

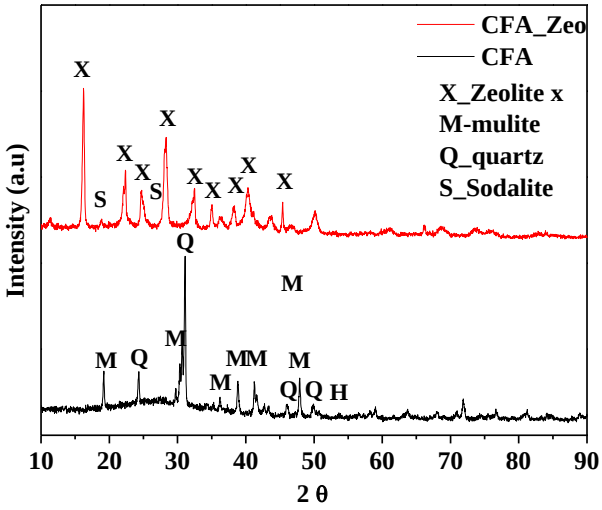

Figure 6.1. PXRD patterns of CFA and CFA_Zeo

EDS analyses confirmed that the major components of CFA were Si and Al, with very low Na content (**Table 6.2**). Upon zeolitization (i.e. the conversion of CFA to a zeolitic material), the amount of Na was observed to have increased significantly, having a Si/Na ratio of 1.31 as compared to 22.7 for that of unreacted CFA. The decrease in the Si/Na was plausible given that Na was used in the zeolization process. The Si/Al ratio of CFA_Zeo was found to be 1.87 (similar to that of CFA, 2.13) indicating that an insignificant amount of alumina and silica were lost during the zeolitization process.

Table 6.2. EDS Elemental composition of CFA and CFA_Zeo

Sample	Si/Na	Si/Al
CFA	22.7	1.57
CFA_Zeo	1.31	1.11

FTIR analyses were conducted on both the unreacted CFA and CFA_Zeo in order to further investigate if zeolitization had occurred (**Figure 6.2**).

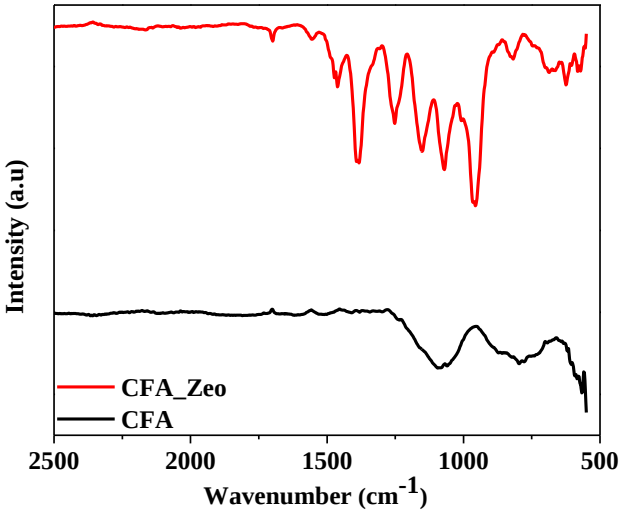

Figure 6.2 FTIR spectra of CFA and CFA_Zeo

The FTIR spectrum of the unreacted CFA comprised of two focal intense and wide peaks, typical of internal vibrations in MO_4 tetrahedra, where M=Si, Al. As before the peak centered at 1090 cm^{-1} was attributed to the vibrations of the M–O asymmetric stretching, which signified the extent of crystallinity of the material.[59] The other less intense band centered at 787 cm^{-1} was attributed to the presence of Al atoms in the tetrahedral form.[60] Individual types of zeolites have distinguishing IR signatures even though there some common characteristics exist.[59] The broad and intense peak observed in the FTIR spectra of CFA_Zeo, at 1001 cm^{-1} was attributed to the asymmetric stretching of bridge bonding between M–O–M, where M is Si or Al.[59] The smaller peak at 670 cm^{-1} was attributed to the symmetric stretching vibrations of bridge bonds of M–O–M .[59] The interpretations of the differences in the FTIR spectra of CFA and CFA_Zeo along with data obtained from EDS and PXRD established that zeolitization had occurred upon fusing CFA with NaOH and then hydrothermally treating the product.

SEM was also used to further investigate if zeolitization had occurred. The morphology of the unreacted CFA was found to be dominated by spherical particles with diameters that ranged between 1 and 100 μm (**Figure 6.3 (a)**). By contrast, the morphology of CFA_Zeo was found to be predominantly needle-like (**Figure 6.3 (b)**). Furthermore, these needles were aggregated together forming patterns that resembled a bundle of wool (see encircled regions in **Figure 6.3 (b)**.

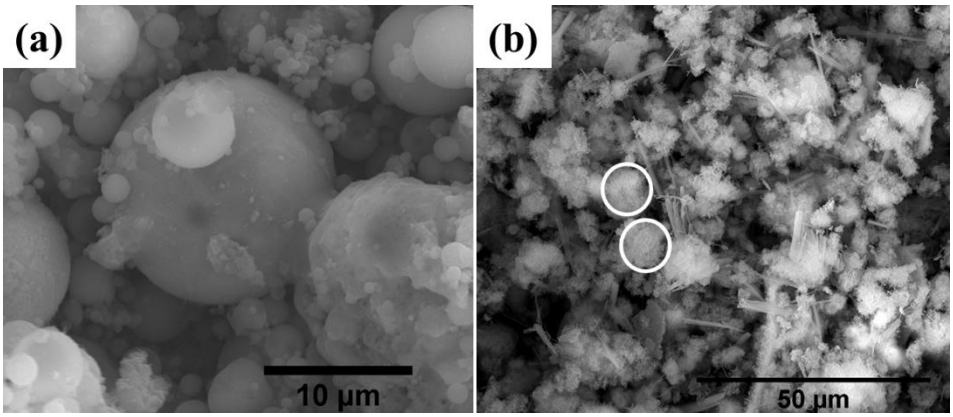

Figure 6.3. SEM images of (a) CFA and (b) CFA_Zeo

TEM was used to further investigate the structure of CFA_Zeo (**Figure 6.4**). Here it was observed that the needle-like morphology observed in SEM actually appeared to be more like that of nanorods (see the outlined area in **Figure 6.4 (a**)) and had an average width of 130 nm. On the other hand, TiO_2 nanoparticles had a grain-like morphology with particles that ranged between 8.5 to 12 nm, with an average size of 10 nm (**Figure 6.4 (b**)).

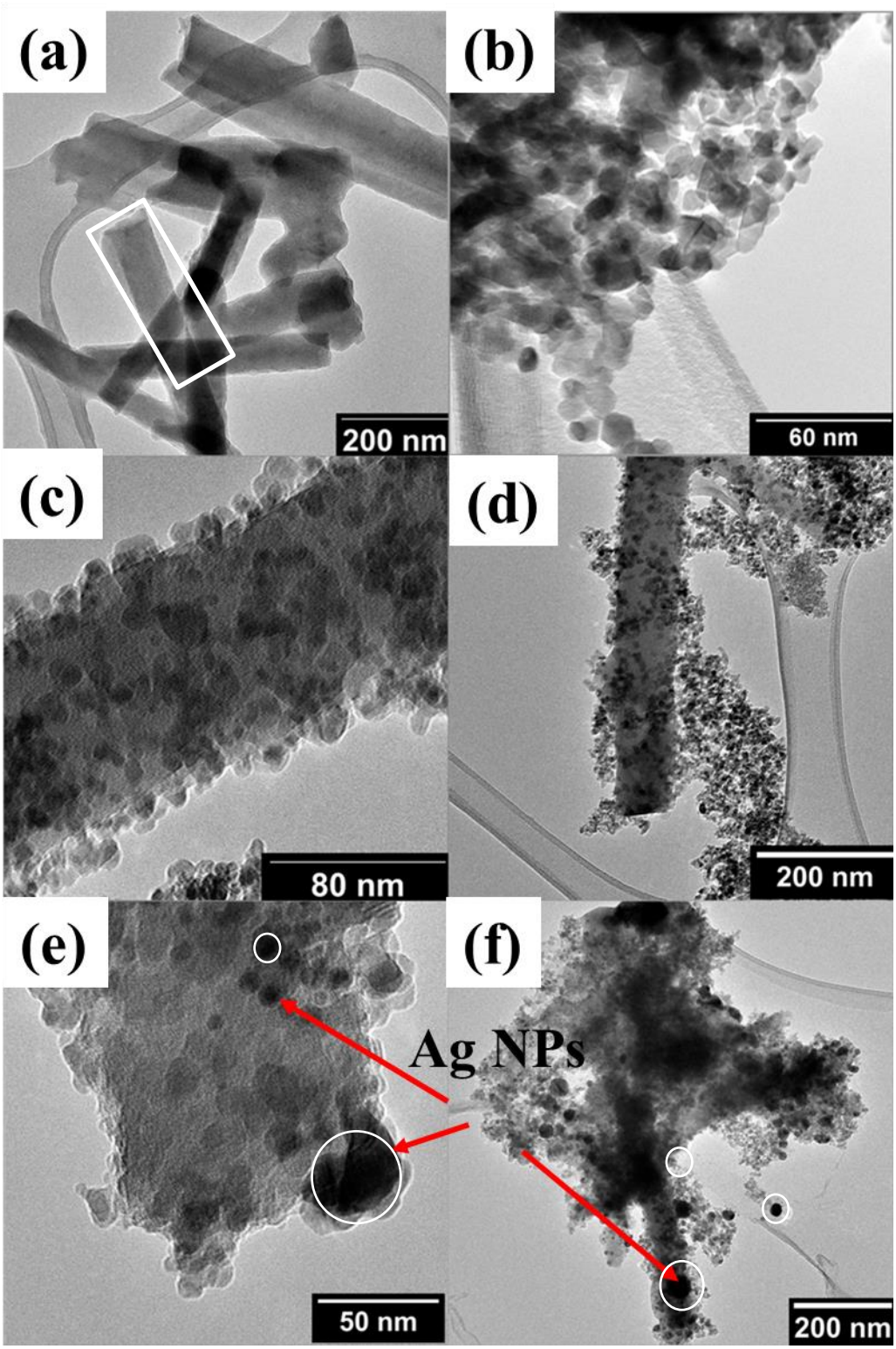

Figure 6.4. TEM micrographs of (a) CFA_Zeo, (b) TiO_2, (c) TiO_2/CFA_Zeo(30%), (d) TiO_2/CFA_Zeo(15%), (e) Ag/TiO_2/CFA_Zeo(30%) and (f) Ag/TiO_2/CFA_Zeo(15%).

In this research, TiO_2 was synthesized in the presence of the CFA_Zeo in order to maximize the likelihood of the complete coating of the CFA_Zeo nanorods with TiO_2 and to enable chemical interactions to form between the two materials. Indeed, it was observed using TEM that the CFA_Zeo nanorods were completely coated with TiO_2 (**Figure 6.4 (c)–(f)**). This occurred because these composites were composed of at least 70 % TiO_2. The reason for this high percentage was because TiO_2 was the photoactive material in these composites, so it was decided it should be used in greater proportion to the CFA_Zeo nanorods as the latter was being investigated as a functional support material for TiO_2 photocatalyst. The other reason why the CFA_Zeo nanorods appeared completely coated was due to the fact that the TiO_2 nanoparticles were significantly smaller (10 nm, **Table 6.3**) than them. The materials are shown in **Figure. 6.4 (c)** and **Figure 6.4 (d)** were TiO_2/CFA_Zeo(15 %) and TiO_2/CFA_Zeo(30 %) respectively. Here their morphologies were found to be similar and their close proximity to each other suggested that chemical interactions between TiO_2 and CFA_Zeo had occurred. These interactions are desirable in photocatalysis as they bring about Schottky barriers which enhance the separation of photo-generated charge carriers, that generally increase their photocatalytic efficiency.[44] However, the main difference between the TiO_2/CFA_Zeo(15 %) composite and the TiO_2/CFA_Zeo(30 %) composite was that some of the TiO_2 nanoparticles in the case of TiO_2/CFA_Zeo(15 %) were not supported. This is probably because of the amount of TiO_2 meaning the entire surface of CFA_Zeo was used up in TiO_2/CFA_Zeo(15 %).

TEM micrographs of composites loaded with Ag, i.e. Ag/TiO_2/CFA_Zeo(15 %) and TiO_2/CFA_Zeo(30 %) were shown in **Figure. 6.4 (e)** and **Figure. 6.4 (f)** respectively. The Ag nanoparticles were identified as the dark particles in these micrographs i.e. dark spots

because Ag is heavier than Ti (see encircled regions in **Figure 6.4 (e)-(f)**). The average particle size of these Ag nanoparticles (1 % loaded) was determined to be 9 nm from TEM micrographs, with several agglomerates which had particle sizes over 40 nm. An examination of **Figure 6.4 (e)-(f)** revealed that Ag nanoparticles were observed to have been deposited on the surface of TiO_2 nanoparticles. This was desirable because it increased the likelihood of SPR occurring and the likelihood that visible light would be absorbed. [51,61]

The surface properties of the samples were then analyzed. The BET surface area values are given in **Table 6.3**.

Table 6.3. BET surface areas and TiO_2 crystallite sizes.

Sample	BET surface area(m^2/g)	TiO_2 particle size (nm)
CFA	2.9	
CFA_Zeo	49	
TiO_2	82	9.2
Ag/TiO_2	79	9.2
TiO_2/CFA_Zeo(15 %)	123	7.5
TiO_2/CFA_Zeo(30 %)	131	7.4
Ag/TiO_2/CFA_Zeo(15 %)	169	7.4
Ag/TiO_2/CFA_Zeo(30 %)	174	7.3

The BET surface area of CFA_Zeo (49 m^2/g) was found to be much higher than that of CFA (2.9 m^2/g), while those of TiO_2 (82 m^2/g) and Ag/TiO_2 (79 m^2/g) were found to be similar. However, the surface areas of all of the rest of the composites were found to be significantly higher than that of TiO_2 and Ag/TiO_2. In addition, it was observed that the BET surface areas of the composites appeared to increase slightly with increased % CFA_Zeo therein. Similarly, CFA_Zeo composites that contained Ag nanoparticles had higher surface areas than those without Ag. The increase in the BET surface areas of the

composites suggested that the CFA_Zeo prevented the agglomeration of the TiO_2 nanoparticles during hydrolysis and hence it increased with an increasing amount of CFA_Zeo used.

The crystallite size of pristine TiO_2 nanoparticles and TiO_2 nanoparticles in Ag/TiO_2, as determined using the Scherrer equation (**Table 6.3**) was found to be larger than those of TiO_2 in composites. It was also observed that the peak width of the TiO_2 (101) reflection of unbound TiO_2 and Ag/TiO_2 was narrower than that of the composites (**Figure 6.5 (a)-(b)**). These observations indicated that the CFA_Zeo had a role in the crystallization of TiO_2 and had affected the crystal development of TiO_2.[62–64] This suggests that there was a possibility of chemical interactions between TiO_2 nanoparticles and CFA_Zeo, and that CFA_Zeo affects the crystal development of TiO_2.[64] The TiO_2 (101) reflection on the Ag/TiO_2 was not broadened as it was the case with the other composites because Ag nanoparticles were precipitated on the TiO_2 surface, after TiO_2 nanoparticles had already been crystallized. Apart from the broadening of the (101) reflection, there was no evidence of CFA_Zeo on the PXRD patterns of the composites probably because of the low crystallinity of CFA_Zeo as compared to TiO_2 nanoparticles. Also, this was attributed to that the composites consisted of at least 70 % TiO_2. Ag nanoparticles were loaded at low levels of 1 % which explains why their characteristic peaks were not observed.

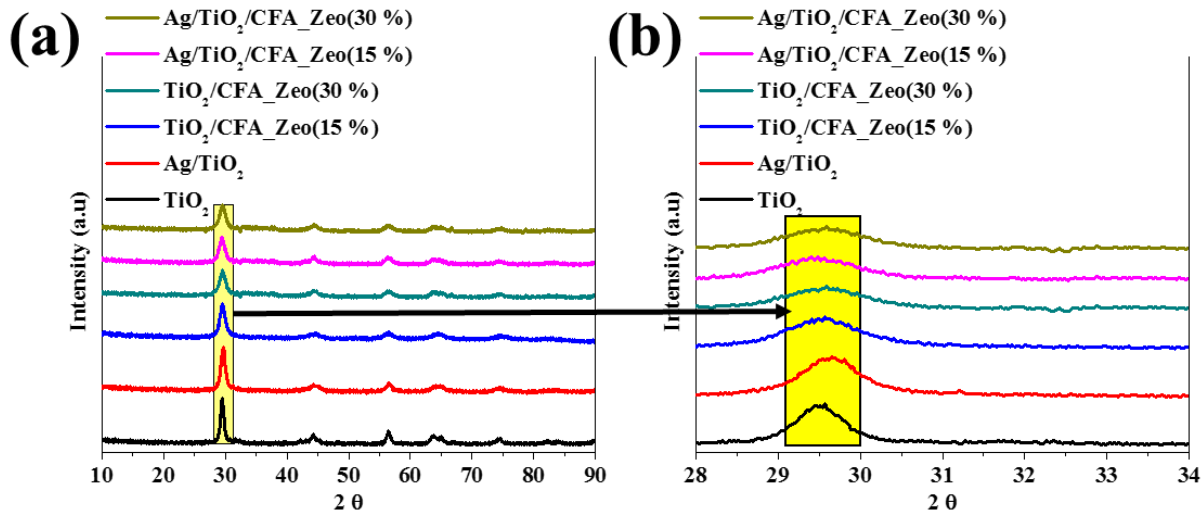

Figure 6.5. (a) PXRD pattern of TiO_2 and the composites and (b) insert showing the (101) reflection.

UV-vis DRS analysis was conducted in order to investigate the optical properties of TiO_2 and the composites, in order to ascertain if compositing TiO_2 with CFA_Zeo and Ag had any influence on its optical properties. A solitary band gap absorption with a steep absorption edge at the UV region (380 nm) was observed for TiO_2, TiO_2/CFA_Zeo(15 %) and TiO_2/CFA_Zeo(30 %) (**Figure 6.6 (a)**). The steep absorption edge is typical of TiO_2 nanoparticles, indicating that compositing TiO_2 with CFA_Zeo had no influence on the optical properties of TiO_2. The UV-vis DRS profiles of catalysts containing Ag nanoparticles i.e. Ag/TiO_2, Ag/TiO_2/CFA_Zeo(15 %) and Ag/TiO_2/CFA_Zeo(30 %) were similar as shown in **Figure 6.6 (b)** but different from those shown in Figure. 6.6a. The steep absorption edge was also present in Ag nanoparticles containing composites and also a band that extended from 600 nm in the visible range was observed. The wide absorption band was attributed to the SPR of Ag nanoparticles which have been reported to be

responsible for the improved photoactivity of noble metals based TiO_2 composites. [27,65,44,66–68]

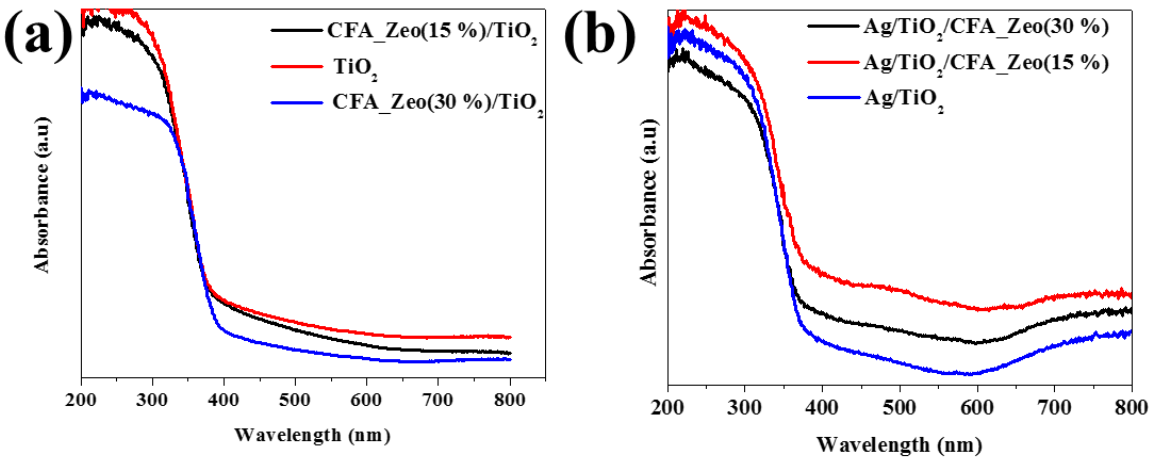

Figure 6.6. UV-vis DRS absorption spectra of TiO_2 and composites

Photoluminescence (PL) emission spectroscopy is a significant instrument for investigating the efficiency of charge carrier separation. The observed PL emission is primarily a consequence of the recombination of photogenerated electron-hole pairs, and inferior emission intensity signposts a reduction in the recombination rate [37,69,70]. In order to study the effect of CFA_Zeo and Ag nanoparticles on the recombination of electrons-holes produced by TiO_2, the PL profiles of the various photocatalysts were recorded (**Figure. 6.7**). In a control experiment, it was observed that CFA_Zeo showed no emission profile when excited at 290 nm. Unbound TiO_2 nanoparticles showed a broad and intense peak centered around 400 nm, indicative of high electron-hole recombination rate. TiO_2/CFA_Zeo(15 %) had a significantly lower emission peak compared to that of TiO_2, indicating that the CFA_Zeo was effective at reducing the recombination of electrons-holes. Indeed, the emission peak of TiO_2/CFA_Zeo(30 %) was further decreased, showing that the more CFA_Zeo used the lower the electrons-holes recombination rate. The PL

emission peak observed for Ag/TiO_2 was the same level as that TiO_2/CFA_Zeo(30 %), showing that Ag nanoparticles also have the ability to reduce the electrons-holes recombination rate. The emission peaks observed for composites containing Ag nanoparticles (i.e. Ag/TiO_2/CFA_Zeo(15 %) and Ag/TiO_2/CFA_Zeo(30 %)) were much lower than those of the other catalysts, with that of Ag/TiO_2/CFA_Zeo(30 %) being almost flat. This suggests the existence of a synergy between CFA_Zeo and Ag nanoparticles that is effective for reducing the electron-hole recombination rate.

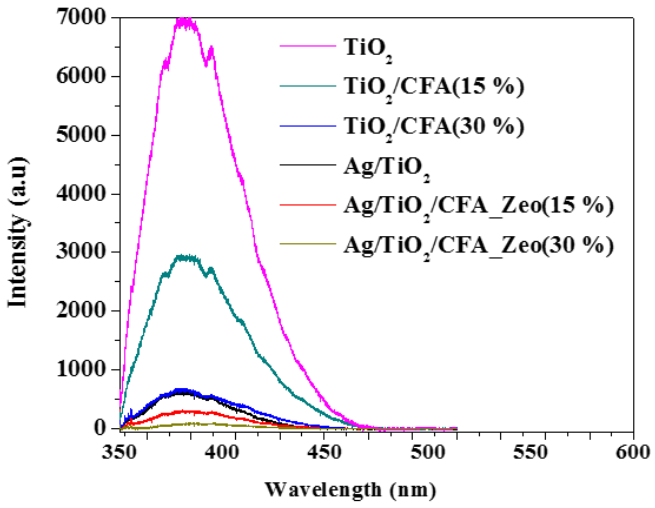

Figure 6.7. Photoluminescence spectrum of TiO_2 and composites

6.3.2 Photocatalytic measurements

The adsorption equilibrium at 2 h (Q) was determined (Table 6.4). It was found that TiO_2 and Ag/TiO_2 adsorbed the least amount of BPA at equilibrium, 0.8 ppm, and 0.9 ppm respectively. TiO_2/CFA_Zeo(15 %) and Ag/TiO_2/CFA_Zeo(15 %) adsorbed 1.2 and 1.4 ppm, respectively. The composites consisting of 30 % CFA_Zeo showed the largest adsorption capacity values, where 1.9 ppm was recorded for TiO_2/CFA_Zeo(30 %) and 2.3 ppm for Ag/TiO_2/CFA_Zeo(30 %). Composites consisting of 30 % had the highest

absorption capacity towards BPA, it was even higher for those with Ag nanoparticles. The trend observed is consistent with the surface properties of the materials, in a sense that the materials with larger surface areas adsorbed more BPA at equilibrium. Furthermore, it has been reported that the adsorption of organic compounds in zeolites occur via: i) Van der Waals connections with lattice oxygens of zeolitic materials, ii) electrostatic interactions of organic compounds with extra-framework cations present in the zeolitic materials, and iii) π-π interactions of unsaturated bonds of organic compounds with transition metal cations if present as extra-framework cations.[71] The possibility of the 3rd explanation wasn't applicable in our study as the zeolitic materials reported in this work had sodium as cations for charge balance. However, the other two possibilities were applicable in our study and were considered as possible mechanisms. It is noteworthy that the adsorption of organic compounds contributes to enhancing the photocatalytic activity of the coated TiO_2 as it brings the organic molecules

Prior to photodegradation experiments, control experiments were conducted in order to check the ability of the photocatalysts to degrade BPA in the absence of radiation from the solar simulator (UV and Vis irradiation). There was no reduction in the amount of BPA in solution. BPA was also irradiated with the solar simulator (UV and Vis irradiation) for 60 min in the absence of TiO_2 and the composites, it was also found that the amount of BPA in solution had not changed. The photoactivity of CFA_Zeo under solar simulator irradiation (with and without a filter) was also determined where it was found that the CFA_Zeo were inert.

Table 6.4. Adsorption equilibrium and photocatalytic activities of the various photocatalysts

Sample	Q (ppm)	X_{60min_UV} (%)	X_{60min_Vis} (%)
TiO_2	0.8	49	24
Ag/TiO_2	0.9	69	91
TiO_2/CFA_Zeo(15 %)	1.2	64	24
TiO_2/CFA_Zeo(30 %)	1.9	33	21
Ag/TiO_2/CFA_Zeo(15 %)	1.4	96	67
Ag/TiO_2/CFA_Zeo(30 %)	2.3	89	46

The photocatalytic activity of TiO_2 and the composites was evaluated for the photodegradation of BPA under full solar light spectrum and visible light ($\lambda > 400$). The curves for BPA degradation under full solar light radiation are shown in **Figure 6.8,** and the results are tabulated in Table 6.4. The photocatalytic activity of unbound TiO_2 was found to be 49 %, superior to the 33 % obtained for TiO_2/CFA_Zeo(30 %) but inferior to the 64 % obtained for TiO_2/CFA_Zeo(15 %). The improved photoactivity observed for TiO_2/CFA_Zeo(15 %) was attributed to the reduced electrons/holes recombination rate (**Figure 6.7**). The discrepancy was observed for TiO_2/CFA_Zeo(30 %), where an inferior photoactivity relative to that of TiO_2 was observed. This was attributed to that the ratio of the photoactive TiO_2 was reduced and the photo-inactive CFA_Zeo blocked the light from reaching TiO_2. Photoactivity of 69 % obtained for Ag/TiO_2, 89 % gotten for Ag/TiO_2/CFA_Zeo(30 %) and 96 % obtained for Ag/TiO_2/CFA_Zeo(15 %). The superior photoactivity of composites containing both Ag nanoparticles and CFA_Zeo was attributed to the significantly reduced electrons/hole recombination rate.

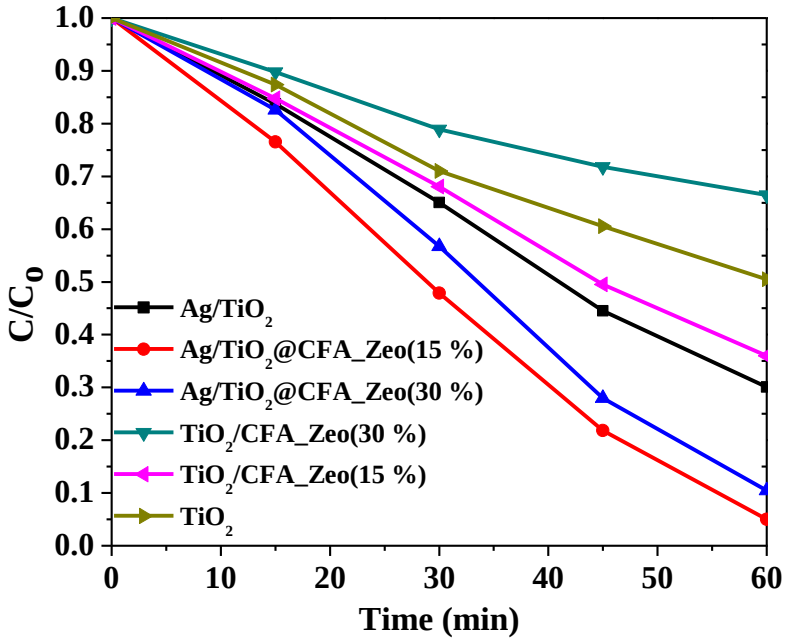

Figure 6.8. Photodegradation of BPA under full solar simulator spectrum.

Apart from the reduction of the propensity of electrons and holes to recombine by the use of CFA_Zeo, the photocatalytic enhancement observed when BPA was photodegraded with TiO_2/CFA_Zeo(15 %), both under visible and ultraviolet light was also attributed to enhanced surface area and improved adsorption capacity. CFA_Zeo have negligible photocatalytic activity but the compositing them with TiO_2 nanoparticles at the right amount have been shown to increase the photoactivity considerably under visible light [47,48,71,72]. Anpo and co-workers hydrothermally included TiO_2 nanoparticles within the framework of mesoporous zeolites [73]. The material was reported to exhibit an enhanced photocatalytic reduction of CO_2 with water for the production of methanol and methane [73]. Fukahori *et al*. prepared TiO_2-zeolites sheets and they reported that the composite TiO_2-zeolite sheets showed an upper efficiency for BPA photodegradation than the zeolite-free TiO_2 sheet [48]. They attributed the improved photoactivity to the synergistic effect of

compositing TiO_2 and zeolites in a sheet-like configuration, which is said to accelerate the photodegradation of BPA [48]. In a separate study, it was found that TiO_2-zeolite composites could photodegrade acetaldehyde more efficiently than unbound TiO_2 [72].

The photoactivity curves of the photocatalysts under visible light is shown in **Figure 6.9** and Table 6.4. The photoactivity of composites consisting of TiO_2 and CFA_Zeo, i.e. TiO_2/CFA_Zeo(15 %) and TiO_2/CFA_Zeo(30 %) showed photocatalytic activities of 24 and 21 % respectively, similar to that obtained for unbound TiO_2 (24 %). The low activity was attributed to that the illumination energy is lower than the band gap energy of the materials (**Figure. 6.6 (a**)). The composites containing Ag nanoparticles and CFA_Zeo were shown to have modest photoactivity. Ag/TiO_2/CFA_Zeo(15 %) and Ag/TiO_2/CFA_Zeo(30 %) were recorded to have photoactivity of 67 % and 46 %. The relatively large photoactivity (compared to TiO_2, TiO_2/CFA_Zeo(15 %) and TiO_2/CFA_Zeo(30 %)) observed was attributed to the ability of the composites to absorb visible light as a result of SPR which enables Ag nanoparticles to absorb visible light (**Figure. 6.6 (b**)).[44,74–76] The superior photoactivity of Ag/TiO_2/CFA_Zeo(15 %) compared to Ag/TiO_2/CFA_Zeo(30 %) was justified by that the large amounts of the CFA_Zeo meant lower amounts of TiO_2 thus decrease the amount of irradiation for photoionization. Ag/TiO_2 (91 %) was found to have the highest photocatalytic activity than all the other composites under visible light irradiation. This was attributed to that photoionization occurs in the bulk of Ag nanoparticles where electrons are transferred from Ag nanoparticles into TiO_2 nanoparticles.

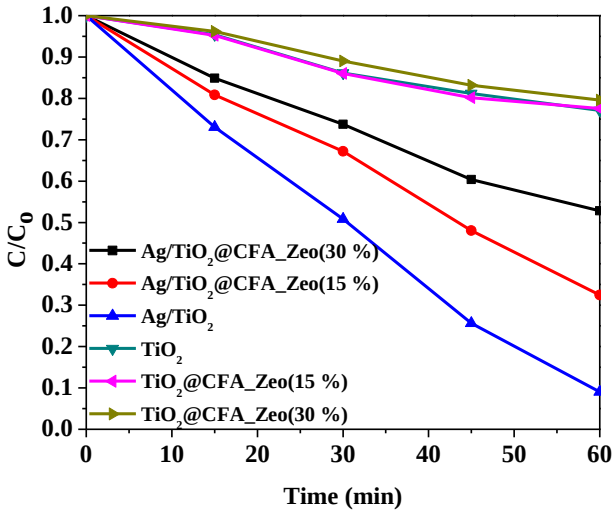

Figure 6.9. Photodegradation of BPA under visible light.

This phenomenon also exists in Ag/TiO_2/CFA_Zeo(15 %) and Ag/TiO_2/CFA_Zeo(30 %), but in the case of these composites, TiO_2 nanoparticles are anchored on CFA_Zeo, thus the presence of CFA_Zeo was suspected to have adverse effects on the visible light photoactivity. This was also qualified by that the visible light photoactivity of Ag/TiO_2/CFA_Zeo(30 %) was lower than that of Ag/TiO_2/CFA_Zeo(15 %), indicating that the more CFA_Zeo used the inferior the photoactivity. The low photoactivity of these composites, compared to the superior of Ag/TiO_2 was also attributed to that since the same amount of catalyst (25 mg) was used in all experiments, the ratio of Ag and TiO_2 nanoparticles were lower in these composites. This was determined to be crucial since both Ag and TiO_2 nanoparticles are required for SPR, the phenomenon responsible for the visible light photoactivity.

Mindful of the different observations, postulations, and conclusions made as to how the CFA_Zeo and Ag nanoparticles improve the photodegradation efficiency of BPA, two separate mechanisms were proposed: In order to account for the enhanced

photodegradation under UV-light brought about by CFA_Zeo, the following mechanism was proposed. Upon UV-light irradiation of TiO_2/CFA_Zeo(15 %), the valence band electrons were excited into the conduction band where they were quickly removed from the TiO_2 surface before they could recombine with the holes as shown in **Figure 6.10**. This is possible because of the electron-rich surface of zeolites which act as an electron scavenger [46,77,78] and the lower work function of Ag nanoparticles, as it is typical of noble metals [74,79,80]. In the case of Ag containing composites, Ag/TiO_2/CFA_Zeo(15 %) and Ag/TiO_2/CFA_Zeo(30 %), the visible light excitation occurs in the bulk of Ag nanoparticles as shown in **Figure 6.1**1 as a result of SPR, the photogenerated electrons are injected into the valence band of the semiconductor from Ag, thus leaving the positively charged holes that partake in oxidative reactions with BPA [27,28,65,44,67,81,82].

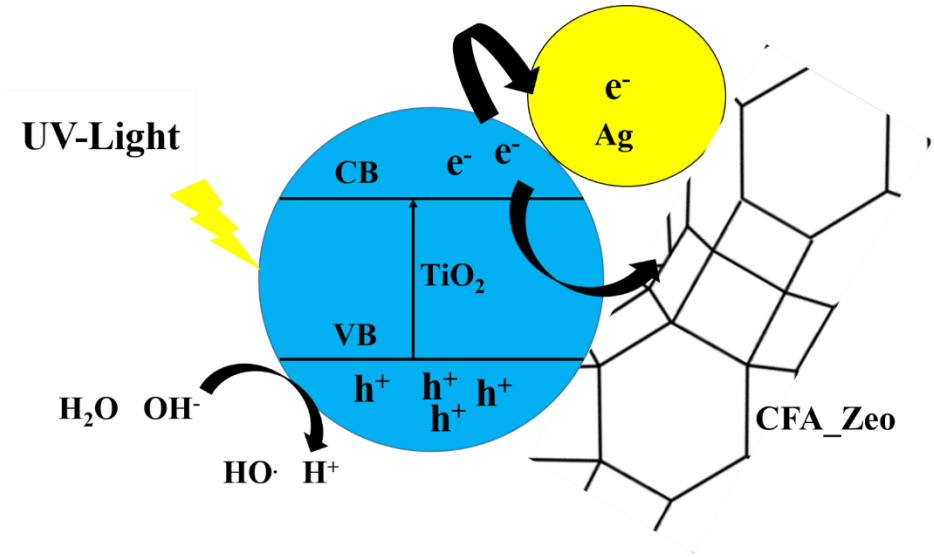

Figure 6.10.Schematic diagram of charge separation by Ag and CFA_Zeo under UV-light.

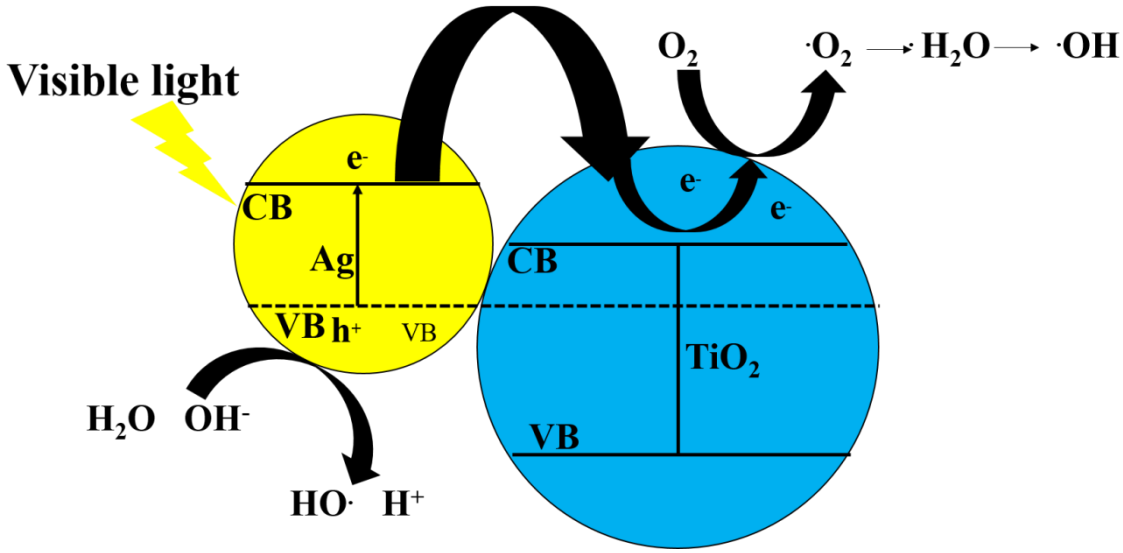

Figure 6.11. Schematic representation of visible light excitation of Ag nanoparticles.

6.4 Conclusions

The alkali fusion hydrothermal method was modified in order to synthesize zeolitic materials (CFA_Zeo) from coal fly ash. The material which consisted of nanorods as it was observed by TEM, was found to be sodium aluminum silicate hydrate (zeolite-X) by PXRD. CFA_Zeo was used as a support for TiO_2 nanoparticles by a novel resin-gel synthesis technique. To the materials, Ag nanoparticles were loaded by DPU, precipitated using NaOH and urea. CFA_Zeo nanorods were found to be coated completely with TiO_2 nanoparticles and Ag nanoparticles were on top of TiO_2 nanoparticles. UV-Vis DRS spectra indicated that CFA_Zeo had no influence on the band energy structure of TiO_2 whereas the deposition of Ag nanoparticles resulted in the formation of a wide absorption band in the visible part of the spectrum. Photoluminescence experiments showed that loading TiO_2 onto CFA_Zeo and decorating with Ag nanoparticles reduced the recombination photoinduced

charge. The photoactivities of the materials were assessed by measuring the efficiencies at which they photodegraded bisphenol-A under both UV and visible irradiation. The highest photocatalytic activity was observed for $Ag/TiO_2/CFA_Zeo(15\ \%)$ under both UV and visible irradiation whereas pure TiO_2 showed the least activity.

This **CHAPTER** along with **CHAPTER 4** demonstrated that useful materials could be synthesized from CFA which aided in the improvement of the photocatalytic activity of TiO_2. In this **CHAPTER** it was further shown that visible light could be harvested by decorating the materials with Ag nanoparticles. In **CHAPTER 7** we continue on the same principle of using CFA based materials (NCNTs synthesized and purified in **CHAPTER 4** and **CHAPTER 5**) to enhance the photocatalytic activity of TiO_2. Furthermore, we investigate the effects of incorporating tungsten and zinc ions into the crystal lattice of TiO_2 with the aim of harvesting visible light.

6.5 References

1. Ahmaruzzaman, M. A review on the utilization of fly ash. *Prog. Energy Combust. Sci.* **36,** 327–363 (2010).

2. Ahmaruzzaman, M. Industrial wastes as low-cost potential adsorbents for the treatment of wastewater laden with heavy metals. *Adv. Colloid Interface Sci.* **166,** 36–59 (2011).

3. Blissett, R. S. & Rowson, N. A. A review of the multi-component utilisation of coal fly ash. *Fuel* **97,** 1–23 (2012).

4. Nath, D. C. D. & Sahajwalla, V. Growth mechanism of carbon nanotubes produced by pyrolysis of a composite film of poly (vinyl alcohol) and fly ash. *Appl. Phys. A* **104,** 539–544 (2011).

5. Yasui, A., Kamiya, Y., Sugiyama, S., Ono, S., Noda, H. & Ichikawa, Y. Synthesis of Carbon Nanotubes on Fly Ashes by Chemical Vapor Deposition Processing. *Ieej Trans. Electr. Electron. Eng.* **4,** 787–789 (2009).

6. Hintsho, N., Shaikjee, A., Masenda, H., Naidoo, D., Billing, D., Franklyn, P. & Durbach, S. Direct synthesis of carbon nanofibers from South African coal fly ash. *Nanoscale Res. Lett.* **9,** 2-11 (2014).

7. Salah, N., Al-ghamdi, A. A., Memic, A., Habib, S. S. & Khan, Z. H. Formation of Carbon Nanotubes from Carbon-Rich Fly Ash: Growth Parameters and Mechanism. *Mater. Manuf. Process.* **31,** 146–156 (2016).

8. Dunens, O.M., MacKenzie, K.J.& Harris, A.T., Synthesis of Multiwalled Carbon Nanotubes on Fly Ash Derived Catalysts. *Environ. Sci. Technol*. **43,** 7889–7894

(2009).

9. Banerjee, S. S., Joshi, M. V. & Jayaram, R. V. Removal of Cr(VI) and Hg(II) from Aqueous Solutions Using Fly Ash and Impregnated Fly Ash. *Sep. Sci. Technol.* **39,** 1611–1629 (2005).

10. Konstantinou, I. K. & Albanis, T. A. Adsorption-desorption studies of selected herbicides in soil-Fly ash mixtures. *J. Agric. Food Chem.* **48,** 4780–90 (2000).

11. Srivastava, V. C., Swamy, M. M., Mall, I. D., Prasad, B. & Mishra, I. M. Adsorptive removal of phenol by bagasse fly ash and activated carbon: Equilibrium, kinetics and thermodynamics. *Colloids Surfaces A Physicochem. Eng. Asp.* **272,** 89–104 (2006).

12. Huo, P., Yan, Y., Li, S., Li, H. & Huang, W. Floating photocatalysts of fly-ash cenospheres supported AgCl/TiO_2 films with enhanced Rhodamine B photodecomposition activity. *Desalination* **256,** 196–200 (2010).

13. Wang, S. & Lu, G. Q. Effect of chemical treatment on Ni/fly-ash catalysts in methane reforming with carbon dioxide. *Stud. Surf. Sci. Catal.* **167,** 275–280 (2011).

14. Saputra, E. Muhammad, S., Sun, H., Ang, H. M., Tadé, M. O. & Wang, ShaobinRed mud and fly ash supported Co catalysts for phenol oxidation. *Catal. Today* **190,** 68–72 (2012).

15. Hollman, G., Steenbruggen, G. & Janssen-Jurkovičová, M. A two-step process for the synthesis of zeolites from coal fly ash. *Fuel* **78,** 1225–1230 (1999).

16. Shigemoto, N., Sugiyama, S., Hayashi, H. & Miyaura, K. Characterization of Na-X, Na-A, and coal fly ash zeolites and their amorphous precursors by IR, MAS NMR and XPS. *J. Mater. Sci.* **30,** 5777–5783 (1995).

17. Freese, U., Heinrich, F. & Roessner, F. Acylation of aromatic compounds on H-Beta zeolites. *Catal. Today* **49,** 237–244 (1999).

18. Shigemoto, N., Hayashi, H. & Miyaura, K. Selective formation of Na-X zeolite from coal fly ash by fusion with sodium hydroxide prior to hydrothermal reaction. *J. Mater. Sci.* **28,** 4781–4786 (1993).

19. Bayat, B. Combined Removal of Zinc (II) and Cadmium (II) From Aqueous Solutions By Adsorption Onto High-Calcium. *Nano* 69–92 (2001).

20. Lee, K. T., Bhatia, S., Mohamed, A. R. & Chu, K. H. Optimizing the specific surface area of fly ash-based sorbents for flue gas desulfurization. *Chemosphere* **62,** 89–96 (2006).

21. Gould, J. C., Leonard, L. S., Maness, S. C., Wagner, B. L., Conner, K., Zacharewski, T., Safe, S., McDonnell, D. P. & Gaido, K. W. Bisphenol A interacts with the estrogen receptor α in a distinct manner from estradiol. *Mol. Cell. Endocrinol.* **142,** 203–214 (1998).

22. Kang, J.-H., Kondo, F. & Katayama, Y. Human exposure to bisphenol A. *Toxicology* **226,** 79–89 (2006).

23. Gatidou, G., Thomaidis, N. S., Stasinakis, A. S. & Lekkas, T. D. Simultaneous determination of the endocrine disrupting compounds nonylphenol, nonylphenol ethoxylates, triclosan and bisphenol A in wastewater and sewage sludge by gas chromatography-mass spectrometry. *J. Chromatogr. A* **1138,** 32–41 (2007).

24. Liu, Z., Kanjo, Y. & Mizutani, S. Removal mechanisms for endocrine disrupting compounds (EDCs) in wastewater treatment — physical means , biodegradation , and chemical advanced oxidation : A review. *Sci. Total Environ.* **407,** 731–748

(2008).

25. Ying, G. G., Kookana, R. S. & Dillon, P. Sorption and degradation of selected five endocrine disrupting chemicals in aquifer material. *Water Res.* **37,** 3785–3791 (2003).

26. Koelmans, A. A. Sorption of Polycyclic Aromatic Hydrocarbons and Polychlorinated Biphenyls to Soot and Soot-like Materials in the Aqueous Environment : Mechanistic Considerations. *Environ. Sci. Technol*. **36**, 3725–3734 (2002).

27. Pelaez, M., Nolan, N. T., Pillai, S. C., Seery, M. K., Falaras, P., Kontos, A. G., Dunlop, P. S. M., Hamilton, J. W. J., Byrne, J. A., O'Shea, K., Entezari, M. H. & Dionysiou, D. D. A review on the visible light active titanium dioxide photocatalysts for environmental applications. *Appl. Catal. B Environ.* **125,** 331–349 (2012).

28. Zhou, X., Liu, G., Yu, J. & Fan, W. Surface plasmon resonance-mediated photocatalysis by noble metal-based composites under visible light. *J. Mater. Chem.* **22,** 21337-21354 (2012).

29. Kaneco, S., Rahman, M. A., Suzuki, T., Katsumata, H. & Ohta, K. Optimization of solar photocatalytic degradation conditions of bisphenol A in water using titanium dioxide. *J. Photochem. Photobiol. A Chem.* **163,** 419–424 (2004).

30. Chiang, K., Lim, T. M., Tsen, L. & Lee, C. C. Photocatalytic degradation and mineralization of bisphenol A by TiO_2 and platinized TiO_2. *Appl. Catal. A: Gen.* **261,** 225–237 (2004).

31. Gitari, W. M., Fatoba, O. O., Petrik, L. F. & Vadapalli, V. R. K. Leaching

characteristics of selected South African fly ashes: effect of pH on the release of major and trace species. *J. Environ. Sci. Health. A. Tox. Hazard. Subst. Environ. Eng.* **44,** 206–220 (2009).

32. Iliev, V., Tomova, D., Rakovsky, S., Eliyas, A. & Puma, G. L. Enhancement of photocatalytic oxidation of oxalic acid by gold modified WO_3/TiO_2 photocatalysts under UV and visible light irradiation. *J. Mol. Catal. A Chem.* **327,** 51–57 (2010).

33. Chatterjee, D., Ruj, B. & Mahata, A. Adsorption and photocatalysis of colour removal from waste water using flyash and sunlight. *Catal. Commun.* **2,** 113–117 (2001).

34. Zhang, Y., Crittenden, J. C., Hand, D. W. & Perram, D. L. Fixed-bed photocatalysts for solar decontamination of water. *Environ. Sci. Technol.* **28,** 435–442 (1994).

35. Li Puma, G., Bono, A. & Collin, J. G. Preparation of titanium dioxide photocatalyst loaded onto activated carbon support using chemical vapor deposition: A review paper. *J. Hazard. Mater.* **157,** 209–219 (2008).

36. Iliev, V., Tomova, D., Bilyarska, L., Eliyas, a. & Petrov, L. Photocatalytic properties of TiO_2 modified with platinum and silver nanoparticles in the degradation of oxalic acid in aqueous solution. *Appl. Catal. B Environ.* **63,** 266–271 (2006).

37. Liu, J., Li, J., Sedhain, A., Lin, J. & Jiang, H. Structure and Photoluminescence Study of TiO_2 Nanoneedle Texture along Vertically Aligned Carbon Nanofiber Arrays. *J. Phys. Chem. C* **112,** 17127–17132 (2008).

38. Shi, J., Zheng, J., Hu, Y. & Zhao, Y. Photocatalytic degradation of methyl orange in water by samarium-doped TiO_2. *Environ. Eng. Sci.* **25,** 489–496 (2008).

39. Yu, Y., Yu, J. C., Chan, C. Y., Che, Y. K., Zhao, J. C., Ding, L., Ge, W. Kun. & Wong, P. K. Enhancement of adsorption and photocatalytic activity of TiO_2 by using carbon nanotubes for the treatment of azo dye. *Appl. Catal. B Environ.* **61,** 1–11 (2005).

40. Kim, H., Kim, J., Kim, W. & Choi, W. Enhanced Photocatalytic and Photoelectrochemical Activity in the Ternary Hybrid of $CdS/TiO_2/WO_3$ through the Cascadal Electron Transfer. *J. Phys. Chem. C* **115,** 9797–9805 (2011).

41. Asahi, R., Taga, Y., Mannstadt, W. & Freeman, A. Electronic and optical properties of anatase TiO_2. *Phys. Rev. B* **61,** 7459–7465 (2000).

42. Yamashita, H., Nishiguchi, H. & Kamada, N. Photocatalytic reduction of CO_2 with H_2O on TiO_2 and Cu/TiO_2 catalysts. *Res. Chem. Intermed.* **20,** 815–823 (1994).

43. Hintsho, N., Petrik, L., Nechaev, A., Titinchi, S. & Ndungu, P. Photo-catalytic activity of titanium dioxide carbon nanotube nano-composites modified with silver and palladium nanoparticles. *Appl. Catal. B Environ.* **156–157,** 273–283 (2014).

44. Zhang, Q., Li, W., Moran, C., Zeng, J., Chen, J., Wen, L. P. & Xia, Y. Seed-mediated synthesis of Ag nanocubes with controllable edge lengths in the range of 30-200 nm and comparison of their optical properties. *J. Am. Chem. Soc.* **132,** 11372–11378 (2010).

45. Fu, X., Clark, L. A., Yang, Q. & Anderson, M. A. Enhanced Photocatalytic Performance of Titania-Based Binary Metal Oxides: TiO_2/SiO_2 and TiO_2/ZrO_2. *Environ. Sci. Technol.* **30,** 647–653 (1996).

46. Xu, Y. & Langford, C. H. Photoactivity of titanium dioxide supported on MCM41, zeolite X, and zeolite Y. *J. Phys. Chem. B* **101,** 3115–3121 (1997).

47. Takeda, N., Torimoto, T., Sampath, S., Kuwabata, S. & Yoneyama, H. Effect of inert supports for titanium dioxide loading on enhancement of photodecomposition rate of gaseous propionaldehyde. *J. Phys. Chem.* **99,** 9986–9991 (1995).

48. Fukahori, S., Ichiura, H., Kitaoka, T. & Tanaka, H. Photocatalytic Decomposition of Bisphenol A in Water Using Composite TiO_2 -Zeolite Sheets Prepared by a Papermaking Technique. *Environ. Sci. Technol.* **37,** 1048–1051 (2003).

49. Subramanian, V., Wolf, E. & Kamat, P. V. Semiconductor - Metal Composite Nanostructures . To What Extent Do Metal Nanoparticles Improve the Photocatalytic Activity of TiO_2 Films. *J. Phys. Chem. B* **105,** 11439–11446 (2001).

50. Stampfl, S. R., Chen, Y., Dumesic, J. A., Niu, C. & Hill, C. G. Interactions of molybdenum oxide with various oxide supports: Calcination of mechanical mixtures. *J. Catal.* **105,** 445–454 (1987).

51. Liu, Z., Sun, D. D., Guo, P. & Leckie, J. O. An efficient bicomponent TiO_2/SnO_2 nanofiber photocatalyst fabricated by electrospinning with a side-by-side dual spinneret method. *Nano Lett.* **7,** 1081–1085 (2007).

52. Saeidi, M., Sarpoolaky, H. & Mirkazemi, S. M. Characterization and microstructure investigation of novel ternary ZrO_2–Al_2O_3–TiO_2 composites synthesized by citrate–nitrate process. *J. Sol-Gel Sci. Technol.* **76,** 436–445 (2015).

53. Barreca, D., Comini, E., Ferrucci, A. P., Gasparotto, A., Maccato, C., Maragno, C., Sberveglieri, G. & Tondello, Eugenio First Example of ZnO−TiO_2 Nanocomposites by Chemical Vapor Deposition: Structure, Morphology, Composition, and Gas Sensing Performances. *Chem. Mater.* **19,** 5642–5649 (2007).

54. Gao, B., Chen, G. Z. & Li Puma, G. Carbon nanotubes/titanium dioxide

($CNTs/TiO_2$) nanocomposites prepared by conventional and novel surfactant wrapping sol-gel methods exhibiting enhanced photocatalytic activity. *Appl. Catal. B Environ.* **89,** 503–509 (2009).

55. Molina, A. & Poole, C. A comparative study using two methods to produce zeolites from fly ash. *Miner. Eng.* **17,** 167–173 (2004).

56. Wajima, T. & Ikegami, Y. Synthesis of zeolitic materials from waste porcelain at low temperature via a two-step alkali conversion. *Ceram. Int.* **33,** 1269–1274 (2007).

57. Ozdemir, O. D. & Pişkin, S. Zeolite X Synthesis with Different Sources. *International J. Chem. Environ. Biol. Sci.* **1,** 229–232 (2013).

58. Khaleghian-Moghadam, R. & Seyedeyn-Azad, F. A study on the thermal behavior of low silica X-type zeolite ion-exchanged with alkaline earth cations. *Microporous Mesoporous Mater.* **120,** 285–293 (2009).

59. Criado, M., Fernández-Jiménez, A. & Palomo, A. Alkali activation of fly ash: Effect of the SiO_2/Na_2O ratio. Part I: FTIR study. *Microporous Mesoporous Mater.* **106,** 180–191 (2007).

60. Mohan, S. & Gandhimathi, R. Removal of heavy metal ions from municipal solid waste leachate using coal fly ash as an adsorbent. *J. Hazard. Mater.* **169,** 351–359 (2009).

61. Fu, X., Clark, L. A., Yang, Q. & Anderson, M. A. Enhanced Photocatalytic Performance of Titania-Based Binary Metal Oxides: TiO_2/SiO_2 and TiO_2/ZrO_2. *Environ. Sci. Technol.* **30,** 647–653 (1996).

62. Kim, S. W., Khan, R., Kim, T. & Kim, W. Synthesis, Characterization, and

Application of Zr, S Co-doped TiO_2 as Visible-light Active Photocatalyst. *Bull. Chem. Soc.* **29,** 1217 (2008).

63. Zhang, W. F., He, Y. L., Zhang, M. S., Yin, Z. & Chen, Q. Raman scattering study on anatase TiO_2 nanocrystals. *J. Phys. D. Appl. Phys.* **33,** 912–916 (2000).

64. Perera, S. D., Sanjaya D. Mariano, R. G., Vu, K., Nour, N., Seitz, O., Chabal, Y. & Balkus, K. J. Hydrothermal synthesis of graphene-TiO_2 nanotube composites with enhanced photocatalytic activity. *ACS Catal.* **2,** 949–956 (2012).

65. Link, S. & El-sayed, M. A. Spectral Properties and Relaxation Dynamics of Surface Plasmon Electronic Oscillations in Gold and Silver Nanodots and Nanorods. *J. Phys. Chem. B* **103,** 8410–8426 (1999).

66. Liu, R., Wang, P., Wang, X., Yu, H. & Yu, J. UV-and Visible-Light Photocatalytic Activity of Simultaneously Deposited and Doped Ag/Ag(I)-TiO_2 Photocatalyst. *J. Phys. Chem. C* **116,** 17721–17728 (2012).

67. Dahl, M., Liu, Y. & Yin, Y. Composite titanium dioxide nanomaterials. *Che. Rev.* **114,** 9853–9889 (2014).

68. Kumar, S. G. & Devi, L. G. Review on Modified TiO_2 Photocatalysis under UV/ Visible Light : Selected Results and Related Mechanisms on Interfacial Charge Carrier Transfer Dynamics. *J. phys. Chem. A* **115,** 13211–13241 (2011).

69. Anpo, M., Yamashita, H., Ichihashi, Y., Fujii, Y. & Honda, M. Photocatalytic Reduction of CO_2 with H_2O on Titanium Oxides Anchored within Micropores of Zeolites: Effects of the Structure of the Active Sites and the Addition of Pt. *J. Phys. Chem. B* **101,** 2632–2636 (1997).

70. Xu, Y., Zhuang, Y. & Fu, X. New Insight for Enhanced Photocatalytic Activity of

TiO_2 by Doping Carbon Nanotubes: A Case Study on Degradation of Benzene and Methyl Orange. *J. Phys. Chem. C* **114,** 2669–2676 (2010).

71. Tayade, R. J., Kulkarni, R. G. & Jasra, R. V. Enhanced Photocatalytic Activity of TiO_2 -Coated NaY and HY Zeolites for the Degradation of Methylene Blue in Water. *Society* **46,** 369–376 (2007).

72. Ichiura, H., Kitaoka, T. & Tanaka, H. Preparation of composite TiO_2 -zeolite sheets using a papermaking technique and their application to environmental improvement. *J. Mater. Sci.* **37,** 2937–2941 (2002).

73. Anpo, M., Yamashita, H., Ichihashi, Y., Fujii, Y. & Honda, M. Photocatalytic Reduction of CO_2 with H_2O on Titanium Oxides Anchored within Micropores of Zeolites: Effects of the Structure of the Active Sites and the Addition of Pt. *J. Phys. Chem. B* **101,** 2632–2636 (1997).

74. Sobana, N., Muruganadham, M. & Swaminathan, M. Nano-Ag particles doped TiO_2 for efficient photodegradation of Direct azo dyes. *J. Mol. Catal. A Chem.* **258,** 124–132 (2006).

75. Hirakawa, T. Charge separation and catalytic activity of Ag/ TiO_2 core-shell composite clusters under UV-irradiation. *J. Am. Chem. Soc.* **127,** 3928–3934 (2005).

76. Wu, F., Hu, X., Fan, J., Liu, E., Sun, T., Kang, L., Hou, W., Zhu, C. & Liu, H. Photocatalytic Activity of Ag/TiO_2 Nanotube Arrays Enhanced by Surface Plasmon Resonance and Application in Hydrogen Evolution by Water Splitting. *Plasmonics* **8,** 501–508 (2013).

77. Kim, Y. & Yoon, M. TiO_2/Y-zeolite encapsulating intramolecular charge transfer molecules: A new photocatalyst for photoreduction of methyl orange in aqueous

medium. *J. Mol. Catal. A Chem.* **168,** 257–263 (2001).

78. Anpo, M., Yamashita, H., Ichihashi, Y., Fujii, Y. & Honda, M. Photocatalytic Reduction of CO_2 with H_2O on Titanium Oxides Anchored within Micropores of Zeolites: Effects of the Structure of the Active Sites and the Addition of Pt. *J. Phys. Chem. B* **101,** 2632–2636 (1997).

79. Subramanian, V., Wolf, E. E. & Kamat, P. V. Catalysis with TiO_2/Gold Nanocomposites. Effect of Metal Particle Size on the Fermi Level Equilibration. *J. Am. Chem. Soc.* **126,** 4943–4950 (2004).

80. Linsebigler, Amy L., Guangquan, L. & Yates, J. J. T. Photocatalysis on TiO_2 surfaces: principles, mechanisms, and selected results. *Chem. Rev.* **95,** 735–758 (1995).

81. Liu, Z., Hou, W., Pavaskar, P., Aykol, M. & Cronin, S. B. Plasmon resonant enhancement of photocatalytic water splitting under visible illumination. *Nano Lett.* **11,** 1111–1116 (2011).

82. Wang, P., Huang, B., Dai, Y. & Whangbo, M.-H. Plasmonic photocatalysts: harvesting visible light with noble metal nanoparticles. *Phys. Chem. Chem. Phys.* **14,** 9813–9825 (2012).

CHAPTER 7:

Synthesis of TiO_2 based quaternary mixed metal oxides by incorporating W^{6+} and Zn^{2+} into its anatase lattice structure loaded on coal fly ash synthesized NCNTs for photodegradation of BPA.

7.1 Introduction

Nanoscale applications of TiO_2 are principally derived from its semiconductor properties, one prime example is that of UV-light aided H_2 production on a TiO_2 anode.[1] Research on nanoscale TiO_2 has also been expanded to areas such as photovoltaics, photo-electrochemical sensors, medical and biomedical applications and as photocatalysts for environmental conservation and water splitting.[2–5]

The photoactivity of TiO_2 has been shown to be reliant on a few important factors, which include: morphology, polymorphic phase, surface area, lattice defects, extent of crystallinity, the presence of uncoordinated surface sites and exposed crystal facets.[5–7] The control and fine-tuning of most of these properties lie with the morphology of TiO_2, which can be directed by the synthesis procedure and post-synthesis treatment.

Furthermore, the photoactivity of TiO_2 can be fine-tuned by compositing or doping it with materials such as other semiconductors, anions, cations, SCNMs, and zeolites.[8–10] Some of the resultant combinations of TiO_2 and these materials have been reported to have yielded composites that absorbed in the visible part of the spectrum and/or introduced a heterojunction that aided in charge trapping.[5–7,11,12] This is important as the photoactivity of TiO_2 is limited by its large band gap and high charge carrier recombination rate. Extensive research on compositing TiO_2 in order to enhance its photoactivity has been carried out.[5,6,8,11–14]

One such method is synthesizing composites of TiO_2 with other metal oxides such as ZnO, NiO, WO_3 and Fe_2O_3.[5,15] WO_3 is one of the key semiconductors that has attracted much attention for compositing with TiO_2. Both Do *et al*. and Know *et al*. have tested the photoactivity of TiO_2/WO_3 for the photodegradation of dichlorobenzene under UV-light, and reported superior activities for these composites compared to that of TiO_2 alone.[16,17] Here the enhanced activity was due to the band gap positions of WO_3 and TiO_2 having been favorably positioned for charge separation. The photoactivity of TiO_2/WO_3 composites have also been measured under visible radiation, as the band gap of WO_3 is narrower (2.8 eV), and was shown to be superior to that of TiO_2 under visible light.[5,18,19]

ZnO is another semiconductor which has UV-light photoactivity that has rivaled that of TiO_2, however, it has suffered from photocorrosion which significantly reduced its activity and stability.[20,21] Fang-Xing Xiao synthesized ZnO-TiO_2 nanotubes (TNTs) that were highly ordered and had photoactivity that was higher than that of ZnO and TiO_2 separately.[22] Here the increased activity was attributed to better charge separation. It was suggested that holes accumulated at the valence band of ZnO and electrons accumulated at the conduction band of TiO_2 so that migration could occur with minimal recombination.[5,21–23] The formation of binary-semiconductors as previously discussed has shown promising results, but these have lacked homogeneity and have been insufficiently stable for catalysis.[24]

The abovementioned examples have focused on the formation of mixtures of metal oxides, where a great deal of research has been performed. On the contrary, less research has been focused on the synthesis and use of mixed metal oxides based on TiO_2 by introducing foreign metal ions into its crystal lattice structure for use in photocatalysis. In order to achieve this, it is important that the crystal structure of TiO_2 be understood in order to systematically introduce foreign metal ions into its crystal lattice. One of the important

crystal structural properties of anatase is that the atoms are comparatively loosely packed with fairly large vacancies. The anatase phase has the ability to hold multiple cation oxidation states and environments.[25–28] This makes it possible to introduce other metal ions into the anatase crystal, through replacement of Ti ions and/or vacancy occupation.

In this research, the incorporation of Zn^{2+} and W^{6+} into the crystal lattice of TiO_2 using a novel resin gel method to form quaternary mixed metal oxides (QMMOs) is reported. Franklyn and Narrandes have demonstrated the applicability of the above-mentioned novel resin gel synthesis technique and by its use reported the synthesis of TiO_2.[29]

The ionic radius of Ti^{4+} when coordinated to six species is 60.5 pm, with a crystal radius of 74.5 pm. In the case of Zn^{2+} and W^{6+}, their respective ionic radii are 60 and 55 pm, comparable to that of Ti^{4+}.[25] Therefore, the three metal ions should be compatible when in a single crystal structure. This therefore allowed for the systematic manipulation of the crystal structure of TiO_2 and thus its electronic and optical properties. It is for this reason that this novel method was employed in this study to deliberately introduce both Zn^{2+} and W^{6+} into the anatase crystal structure to form quaternary mixed metal oxides (QMMOs), with the aim of making materials that absorb visible radiation and improve charge separation.

There other ways of improving the photoactivity of TiO_2 as was mentioned earlier. In particular, there is a growing interest in the combination of carbon-based materials and TiO_2 to enhance photocatalytic efficiency. It has been reported that TiO_2-carbon nanotube composites show enhanced photocatalytic activity because of electron transfer from TiO_2 to carbon nanotubes (CNTs), which promotes charge separation and stabilization. Part of this work involved the use of CFA to synthesize NCNTs (as was described in **Chapter 4**) which were then used to form composites with TiO_2 and these above-mentioned QMMOs.

7.2 Experimental

7.2.1 Synthesis of QMMOs.

The principles of the resin gel technique are described by Franklyn and Narrandes.[29] An appropriate volume of $TiCl_4$ (Fluka/Sigma Aldrich) was measured and dissolved in 10 ml ethanol (Sigma Aldrich) kept at 0 °C using ice whilst stirring magnetically. An appropriate mass of $Zn(NO_3)_2.4H_20$ (Merck) was weighed and dissolved in 10 ml ethanol by stirring. Having made the ethanoic Zn^{2+} solution, 50 g of polyethylene glycol, M_w 8.000 g/mol (Sigma Aldrich) was added to it, heated to 150 °C whilst stirring until all the polymer had dissolved. The W^{6+} solution was prepared by dissolving an appropriate mass of H_2WO_4 (Sigma Aldrich) in 10 ml NH_4OH. The Ti^{4+} solution was added to the W^{6+} solution and stirred for 5 min and the solution consisting of Zn^{2+} and PEG was added to the mixture and stirred for a further 60 min. The white homogenous suspension that formed was then placed under a 200 W infrared lamp until it was completely desolvated and a hard wax had formed. The samples were then transferred into a ceramic crucible, placed on a sand bath and heated to 300 °C. Here they liquefied and then ignited by burning from above with a Bunsen burner. This was allowed to burn until a black powder had formed and the flames had died. The samples were then calcined at 400 °C for 6 h in the air to crystallize the particles and remove the soot. The calcination conditions were optimized where it was realized that 400 °C for 6 h was optimal because higher temperatures resulted in undesirable phase transformation whereas lower temperatures were not suitable for the complete removal of soot. The metal ion ratios (Ti^{4+}: W^{6+}: Zn^{2+}) of the samples prepared were: (9:1:0), (9:0:1), (8:2:0), (8:1:1), (8:0:2), (7:3:0), (7:2:1), (7:1:2) and (7:0:3). The pure metal oxides were prepared following the same procedure as for the mixed metal oxides except that the solvents were added without the other metal precursors, i.e. TiO_2 was

synthesized in exactly the same way as QMMOs except for that H_2WO_3 and $Zn(NO_3)_2.4H_2O$ were not added to the mixture. Such was the case for the synthesis of WO_3 and ZnO. The pure metal oxides and QMMOs that were calcined at 400 °C for 6 h in the air were labeled as described in **Table 7.1**.

Table 7.1. Sample names and calcination temperatures applied for the concentration study of the various QMMOs.

Sample name	% Ti^{4+}	W^{6+}	Zn^{2+}	Calcination temperature
TiO_2	100	0	0	400
WO_3	0	100	0	400
ZnO	0	0	100	400
TWZ910	90	10	0	400
TWZ901	90	0	10	400
TWZ820	80	20	0	400
TWZ811	80	10	10	400
TWZ802	80	0	20	400
TWZ730	70	30	0	400
TWZ721	70	20	10	400
TWZ712	70	10	20	400
TWZ703	70	0	30	400

7.2.2 Synthesis of QMMOs and NCNTs composites

The description of the synthesis and purification processes of the NCNTs that were used in this study have been described in **Chapter 4** and **Chapter 5**. The resin gel procedure was modified to synthesize various Ti:W:Zn composites. The resins were synthesized as described above except that in these instances they were prepared in the presence of NCNTs and were not ignited as it was the case with QMMOs without NCNTs. An amount of NCNTs corresponding to 10 % (m/m) of NCNTs relative to that of the various QMMOs/TiO_2, was added to the white homogeneous mixture of QMMOs or TiO_2 and

stirred magnetically for 2 h until a grey homogeneous mixture was formed. The mixture was then transferred into a pressure sealed autoclave lined with Teflon to complete the reaction at 150 °C for 12 h. The grey precipitates were collected, centrifuged and washed with distilled water. The resulting materials were then calcined at 400 °C for 6 h.

7.2.3 Materials characterization

The procedures and instrumentation used for the characterization of the materials synthesized in this chapter were discussed in section **3.3**.

7.2.4 Photocatalytic measurements

The photo-activities of these materials were evaluated by the photodegradation of BPA. A slurry consisting of 25 mg of the materials and a BPA solution (50 ml, 60 ppm) was first magnetically stirred for 2 h in the dark to ensure adsorption equilibrium. Each mixture was then exposed to light for 60 min with a solar simulator. In this chapter, the photocatalytic experiments were conducted using visible light, where a UV-light filter (λ> 400 nm) was used. The experimental details of the photocatalysis and the quantification of BPA were discussed in detail in **section 3.2**

7.3 Results and discussion

7.3.1 Characterization of pure metal oxides

7.3.1.1 PXRD characterization of pure metal oxides

PXRD analyses were performed in order to study the crystallographic structure of the pure materials and the mixtures. The PXRD patterns of the annealed pure metals, TiO_2, ZnO,

and WO_3 were shown in **Figure 7.1**. It was deduced from the PXRD of ZnO that the material was exclusively hexagonal wurtzite (Zincite, JCPDS 5-0664), with reflections at 2θ positions of 37.136; 40.069; 42.566; 56.102; 66,949, 74.655; 78.933; 80.971 and 82.322°, indexed as (100), (002), (101), (102), (110), (103), (200), (112) and (201). There were no other peaks observed which were not accounted for, indicating that the procedure had yielded pure ZnO.

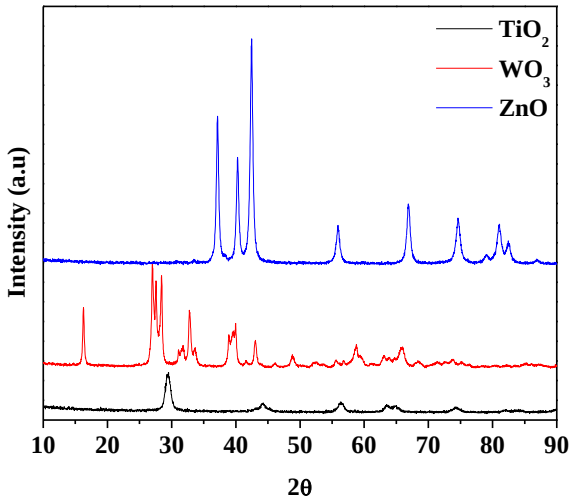

Figure 7.1. PXRD patterns of TiO_2, WO_3, and ZnO.

In the case of WO_3, a series of peaks, some of which were overlapping were observed on its PXRD pattern (**Figure 7.1**). The peaks were generally narrow and strong which was attributed to that the materials were highly crystalline and had fairly big particles. The main peaks at 2θ positions: 16.340; 26.967; 28.763; 32.153; 32.831; 33.509; 40.069; 43.001; 48.882; 58.813; and 65.831 °, were indexed as: (100), (001), (110), (101), (200), (111), (201), (300), (002), (220), (202), (221) and (400) respectively (PDF card, 75-2187). All the diffraction peaks were that of hexagonal WO_3, indicating that the material synthesized was pure.

The PXRD of TiO_2 showed a series of peaks at 29.441; 44.356; 55.340; 63.797, 64.915; 74.286; 82.185; 83.568 and 86.247 °, indexed as: (101), (004), (200), (105), (211), (204), (116), (220) and (215), and as it was the case with ZnO and WO_3, all the peaks were accounted for indicating that the synthesized material was pure TiO_2 anatase.

7.3.1.2 Raman analyses of pure metal oxides

Laser Raman spectroscopy analyses were conducted in order to confirm what was observed by PXRD. The laser Raman spectrum of ZnO nanoparticles (**Figure. 7.2 (a)-(b)**) was observed to have been dominated by the two intense E_2 modes at 108 and 438 cm^{-1}. In addition, two more peaks were observed at 376 and 582 cm^{-1} which corresponded to the A_1 and E_1 symmetry modes of ZnO. As it was the case with PXRD data, the laser Raman spectrum showed that the material was pure wurtzite.

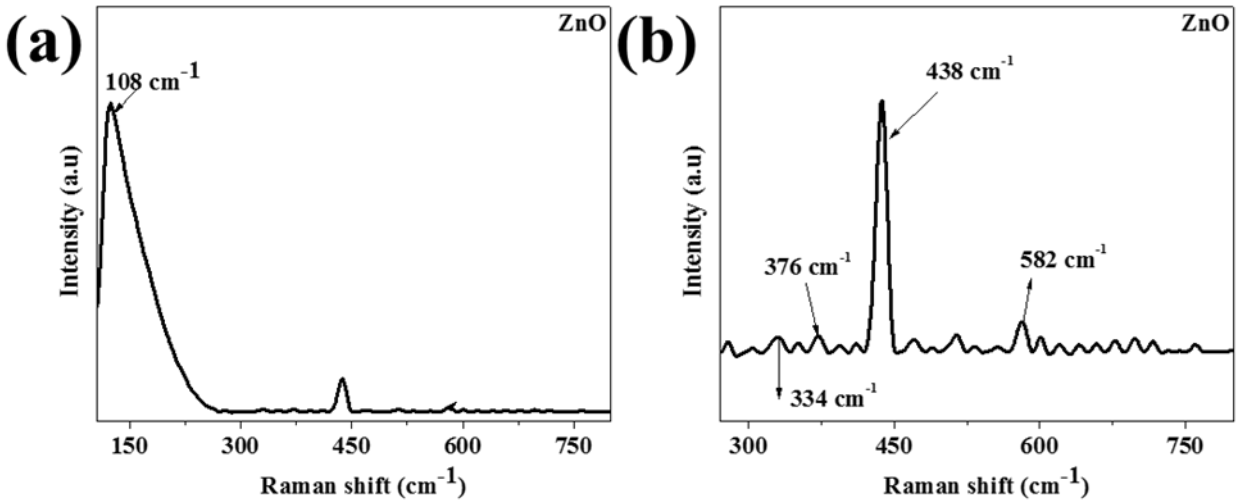

Figure. 7.2. Laser Raman spectrum of (a) ZnO and (b) expansion of the laser Raman spectrum of ZnO to show the low-intensity peaks.

Laser Raman spectroscopy was also used to confirm that pure WO_3 was synthesized using the resin gel synthesis. Several peaks were observed on the laser Raman spectrum of WO_3,

which were all accounted for, thus further confirming that the material synthesized was indeed pure hexagonal WO_3 (**Figure 7.3**). The peaks observed at 131 and 194 cm^{-1} were attributed to the lattice vibration modes. The peak at 260 and 326 cm^{-1} were attributed to the W^{6+}=O stretching vibrations. The peak observed at 702 cm^{-1} was attributed to the asymmetric stretching vibration of W-O-W whereas that which was observed at 803 cm^{-1} was attributed to the symmetry stretching of the same bond.

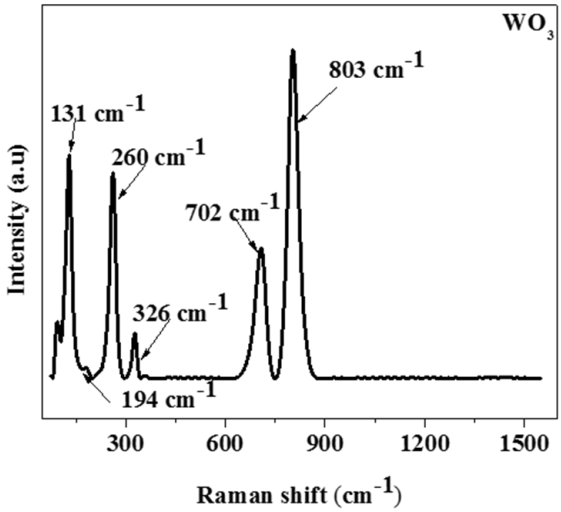

Figure. 7.3. Laser Raman spectrum of WO_3.

The crystal structure of TiO_2 nanoparticles was also investigated by laser Raman spectroscopy as shown in **Figure 7.4**. The Raman active modes observed at 146 $cm^{-1}(E_g)$, 396 $cm^{-1}(B_{1g})$, 518 $cm^{-1}(A_{1g})$, and 641 $cm^{-1}(E_g)$ were all typical of the anatase phase of TiO_2, in agreement with PXRD data.

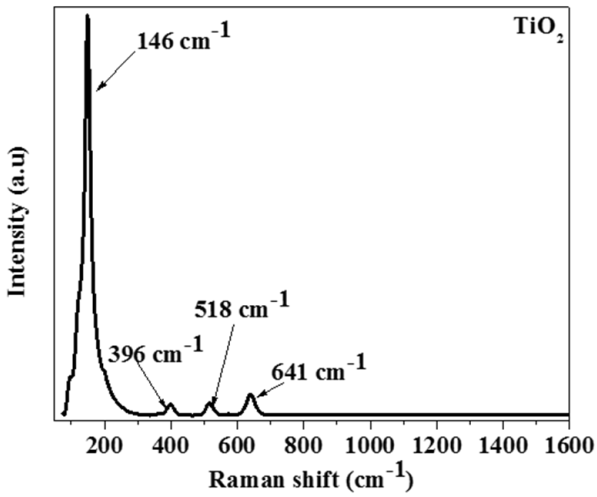

Figure. 7.4. Laser Raman spectrum of TiO_2.

7.3.1.3 TEM and EDX analyses of pure metal oxides

The pure metal oxides and the QMMOs were then analyzed by EDS to determine their elemental composition. TEM was used in order to study their morphological properties and particle size distribution. Here it was observed that the WO_3 nanoparticles were predominantly hexagonal, which was consistent with PXRD and laser Raman data (**Figure 7.5 (a)**). The particle size of the WO_3 nanoparticles ranged between 45 and 75 nm, with an average size of 55 nm as determined from TEM micrographs (**Figure 7.5 (b)**). EDS conducted on the particle shown in **Figure 7.5 (d)** showed that the material consisted of tungsten and oxygen (**Figure 7.5 (c)**). The copper peaks were present because a copper grid was used for specimen preparation (**Figure 7.5 (c)**). The EDS spectra that were recorded on several other particles were consistent with the results that were reflected here.

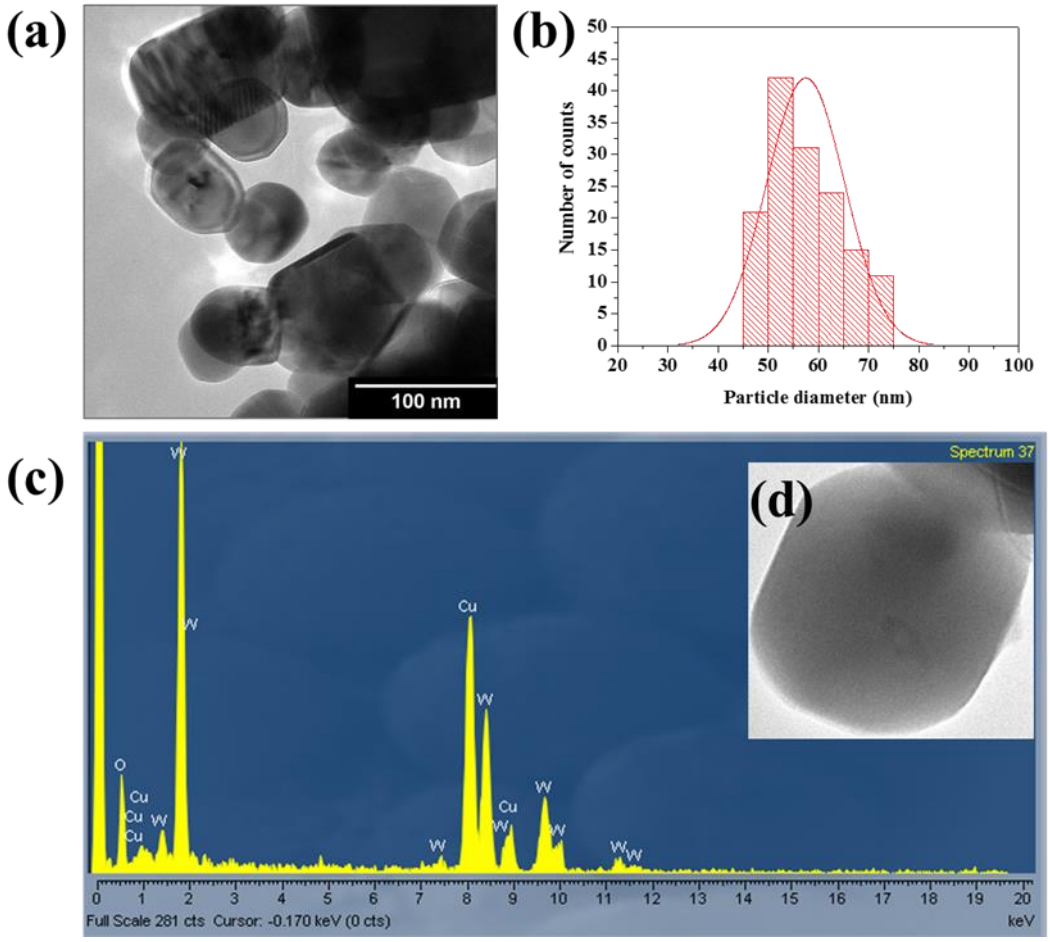

Figure 7.5. (a) TEM image of WO_3, (b) WO_3 particle size distribution, (c) EDS spectra of WO_3 nanoparticles and (d) TEM image of particle which the EDS spectra was recorded on.

In the case of ZnO particles, its morphology was found to inhomogeneous where some were found to be spherical and hexagonal in shape, whereas others had irregular facets (**Figure 7.6 (a**)). The diameter distribution of these particles ranged between 70-100 nm whilst most had a diameter of 85 nm as was determined from TEM micrographs by measuring ca. 100 particles from different images (**Figure 7.6 (b)**). As was the case with WO_3 nanoparticles, the EDS spectrum of ZnO (**Figure 7.6 (c)**) conducted on the particle shown in **Figure 7.6 (d)** showed that the material consisted of only Zn and O. A small

carbon peak was also observed, which was attributed to carbon soot that resisted the annealing/calcination step. It is noteworthy that EDS spectra were recorded on several other particles and these were similar to the spectrum shown in **Figure 7.6 (c)**.

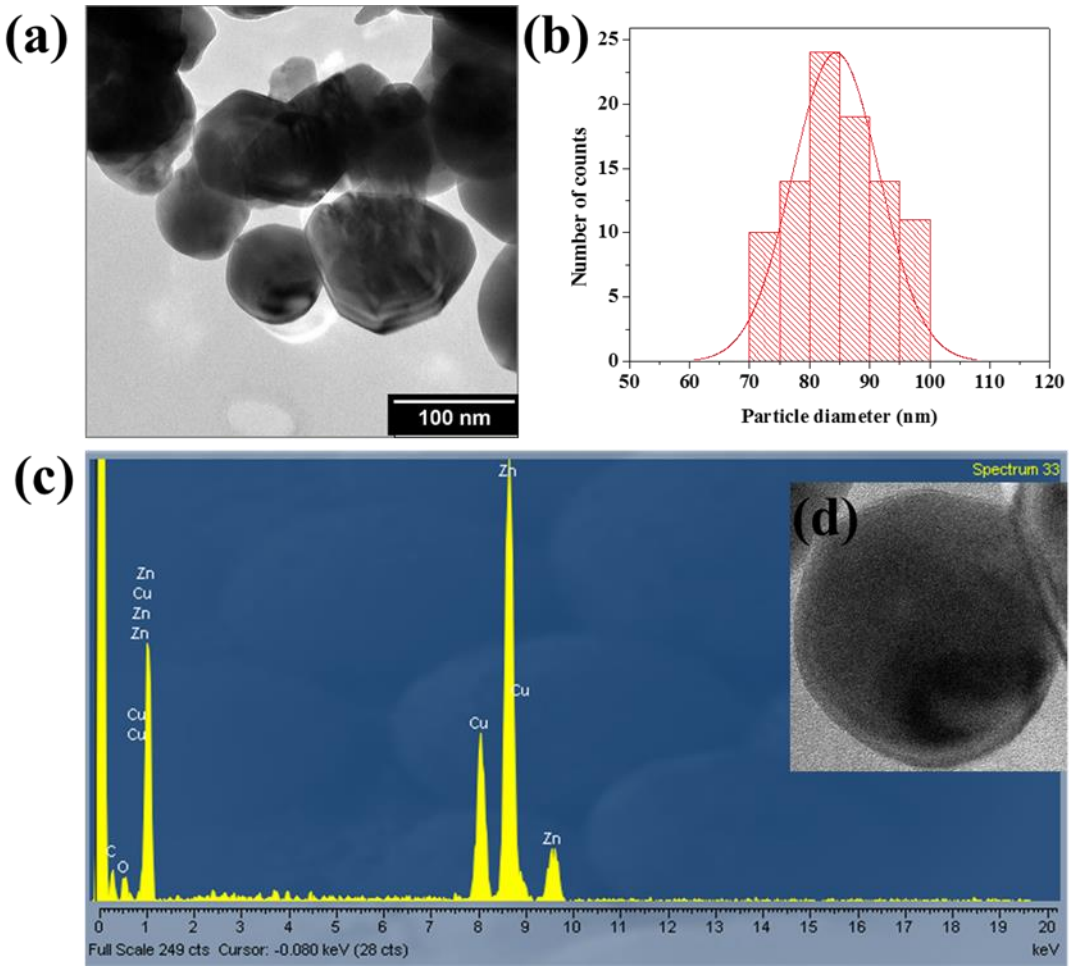

Figure 7.6. (a) TEM image of ZnO, (b) ZnO particle size distribution, (c) EDS spectra of ZnO nanoparticles and (d) TEM image of particle which the EDS spectra was recorded on.

The morphological properties of TiO_2 nanoparticles were also studied by TEM. The TEM image of TiO_2 nanoparticles showed that it consisted mostly of grain-like nanoparticles (**Figure 7.7 (a)**). These particles had sizes that ranged between 8 nm to 15 nm but were predominantly smaller than 11 nm (**Figure 7.7 (b)**). The EDS spectrum of TiO_2 (**Figure**

7.7 (c)) recorded on the particle shown in **Figure 7.7 (d)** showed that the material consisted of only Ti and O atoms, while a carbon peak was also observed. The carbon peak observed was due to the unburned carbon during the combustion and subsequent calcination process.

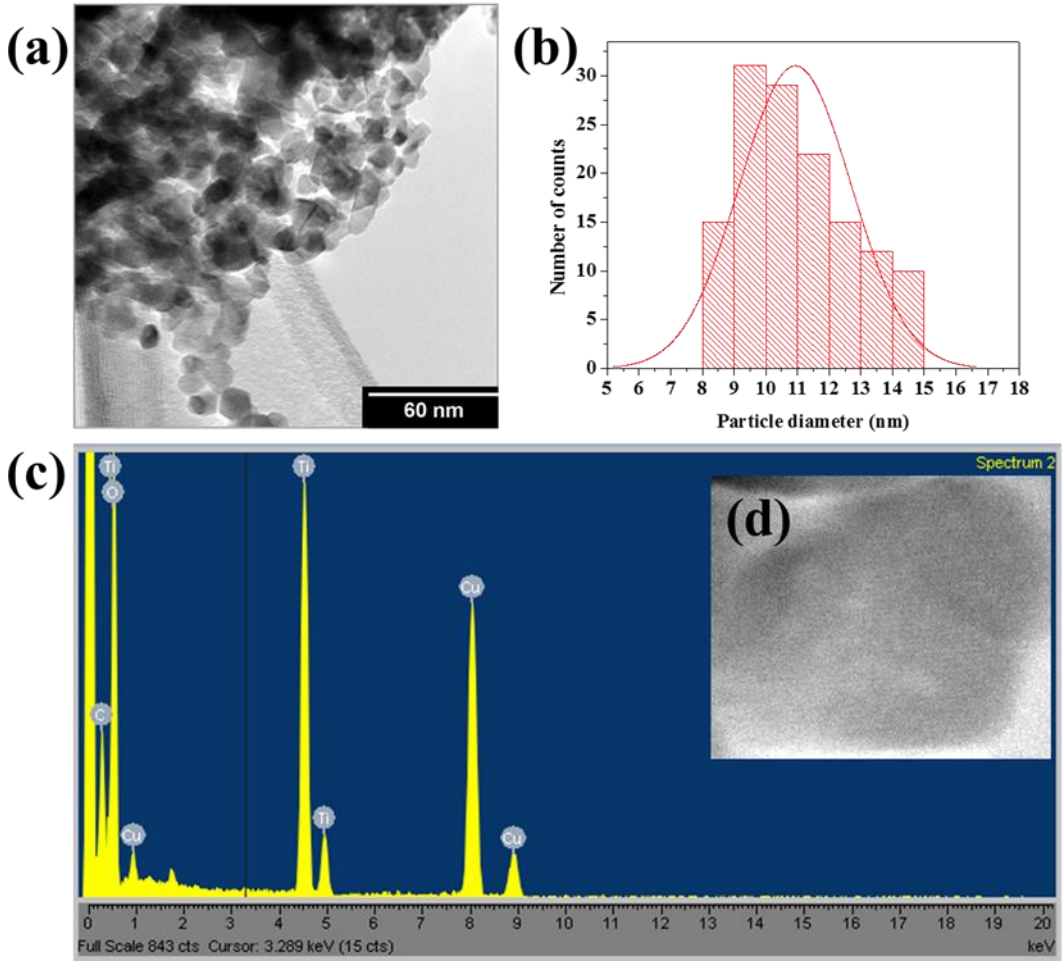

Figure 7.7. (a) TEM image of TiO_2, (b) TiO_2 particle size distribution, (c) EDS spectra of TiO_2 nanoparticles and (d) TEM image of particle which the EDS spectra was recorded on.

7.3.2 Characterization of QMMOs

7.3.2.1 PXRD analyses of QMMOs

PXRD analyses were conducted on the QMMOs and compared to that of TiO_2. The PXRD patterns of the QMMOs were similar to that of the anatase phase, indicating that Zn^{2+} and W^{6+} were incorporated into the TiO_2 crystal lattice without any phase change (**Figure 7.8 (a)**). This was justified on the basis of the argument put forward by Franklyn.[24] The crystal radii of Ti^{4+}, W^{6+} and Zn^{2+} are similar when in six coordination geometry.[24] Therefore, the three metal ions should be entirely harmonious with each other when in one crystal structure.[25] Franklyn went on to suggest that it was likely that the incorporation of W^{6+} and Zn^{2+} with different charges to that of Ti^{4+} should change the crystal radius of oxygen ions because of basic electronic effects. This then led to the assumption that the incorporation of these metal ions into the TiO_2 (anatase) should bring about changes in the unit cell i.e. the local lattice should be distorted. Indeed, this was confirmed by that the (101) reflection of the QMMOs appeared at higher 2θ values relative to that of TiO_2 (**Figure 7.8 (b)**).

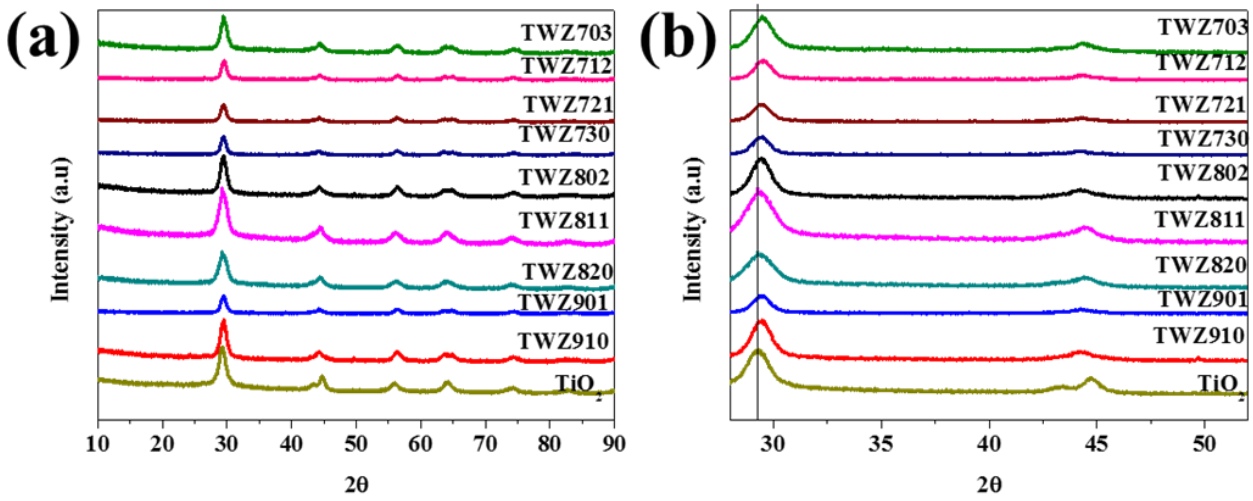

Figure 7.8. (a) PXRD patterns of TiO_2 and various QMMOs and (b) insert showing the (101) and (004) reflections of TiO_2 and various QMMOs.

In addition to the variation in the 2θ position of the (101) of QMMOs relative to those of QMMOs, similar variations were also observed amongst the different QMMOs (**Figure 7.8 and Table 7.2**). Herewith it was observed that the 2θ value of the (101) reflection of the QMMOs increased with an increasing percentage of dopants. The (101) reflections of QMMOs containing 90 % Ti^{4+} appeared at 2θ values closer to those of TiO_2 whereas those that contained 70 % Ti^{4+} were further from that of TiO_2. Furthermore, it was observed that the (101) reflection of QMMOs containing more W^{6+} relative to Zn^{2+} appeared at higher 2θ values (**Table 7.2**). This indicated that W^{6+} ions distorted the TiO_2 lattice at a higher degree than Zn^{2+}.

Table 7.2. Summary of the particle sizes, (101) reflection positions and lattice parameters of TiO_2 and the various QMMOs.

Sample	2θ (004)/°	2θ (101)/°	Particle size (nm)	a (pm)	c (pm)
TiO_2	44.732	29.275	10.5	490.077	808.121
TWZ910	44.416	29.338	11.7	485.644	815.854
TWZ901	44.479	29.316	11.2.	486.603	814.757
TWZ820	44.469	29.465	12.3	483.547	812.555
TWZ811	44.606	29.461	12.8	482.811	814.930
TWZ802	44.484	29.405	12.6	484.694	813.663
TWZ730	44.479	29.576	13.3	481.053	815.087
TWZ721	44.479	29.546	13.4	480.983	815.070
TWZ712	44.460	29.531	13.2	480.713	814.757
TWZ703	44.461	29.528	13.2	479.955	814.757

The degree of distortions that occurred on the crystal lattice of TiO_2 as a result of incorporating W^{6+} and Zn^{2+} into it was estimated by means of calculating the lattice constants/parameters. The lattice parameters were calculated by measuring accurately the 2θ positions of the (004) and (001) peaks. The a lattice parameter of the QMMOs was

different from that of TiO_2. The a lattice parameter of the QMMOs varied amongst themselves. The QMMOs that contained 90 % Ti^{4+} had lattice parameters that were closer to that of TiO_2, followed by those that contained 80 % Ti^{4+} and those that contained 70 % Ti^{4+} differed the most to that of TiO_2. Furthermore, the a lattice parameters of the QMMOs were observed to vary with varying amounts of W^{6+} and Zn^{2+} when comparing a series of QMMOs with the same Ti^{4+} concentration, e.g. the a lattice parameter of TWZ730 is lower than that of TWZ721 (**Table 7.2** and **Figure 7.9**).

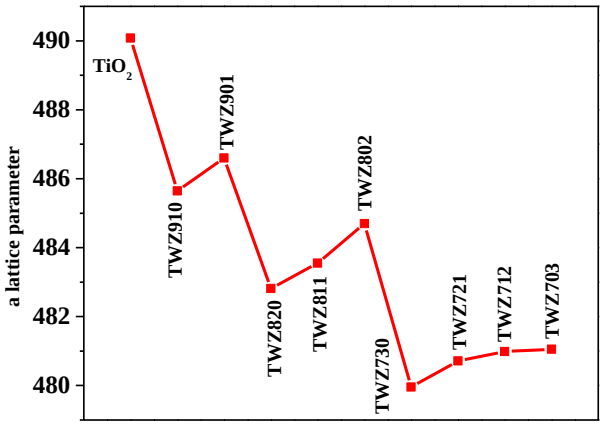

Figure 7.9. Graph showing the variation of the a lattice parameters of TiO_2 and QMMOs

The trend observed was that with increasing concentration of W^{6+} (decreasing concentration of Zn^{2+}), the a lattice parameter of the materials decreased. Similar trends were observed with the particle sizes of the materials **Table 7.2**. The average particle size of TiO_2 was the smallest and increased with increasing concentration of incorporated metal ions. As it was the case with the (101) peak positions and the a lattice parameters, the particle size of the QMMOs increased with increasing concentration of W^{6+}.

7.3.2.2 Laser Raman analyses of QMMOs

Major variations relative to TiO_2 were observed in the case of QMMOs that contained 70 % Ti^{4+} and as such further characterizations were conducted on these materials. The laser Raman signatures of the QMMOs consisting of 70 % Ti^{4+} were studied. Herewith it was observed that they were similar to that of TiO_2 (**Figure 7.10 (a)**). This was consistent with what was observed with PXRD. Furthermore, when the most intense peak was further investigated, it was observed that those of the QMMOs had shifted to shorter wavelengths relative to that TiO_2 as it was the case with the (101) PXRD reflection. This indicated that the inclusion of W^{6+} and Zn^{2+} into the lattice of TiO_2 resulted in lattice distortions (**Figure 7.10 (b)**).

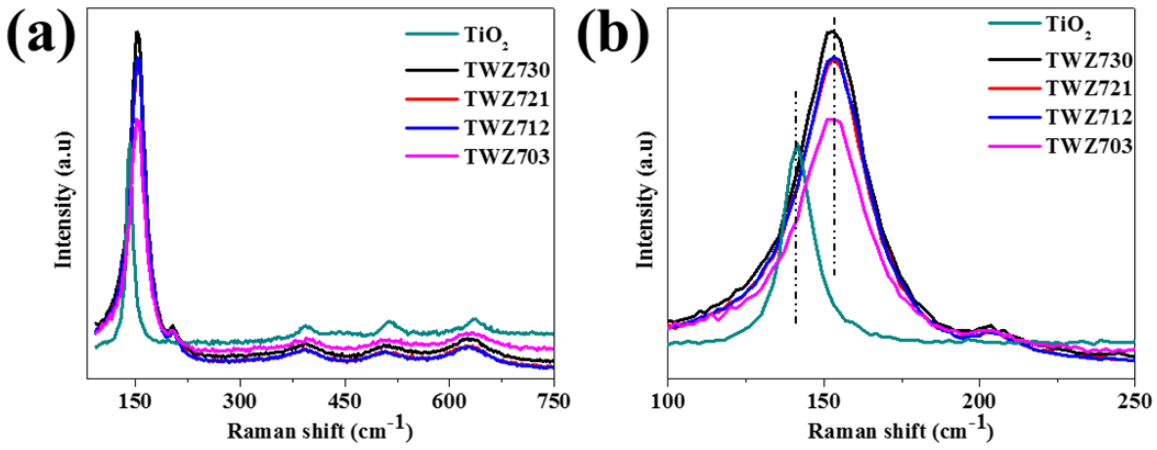

Figure 7.10. (a) Laser Raman spectra of TiO_2 and QMMOs and (b) insert showing the Eg peak

TEM and EDS analyses were also conducted on QMMOs consisting of 70 % Ti^{4+} as shown in **Figure 7.11**. The QMMOs were found to all have similar morphologies (**Figure 7.11a-d**). Furthermore, the morphology of the QMMOs was found to be similar to that of TiO_2 (**Figure 7.7a**). This was consistent with laser Raman and PXRD data where it was

found that TiO_2 and the QMMOs had similar Raman spectral and diffraction features. This further confirmed that W^{6+} and Zn^{2+} ions were incorporated into the lattice of TiO_2 as opposed to forming a mixture of metal oxides as metal oxides of these metal ions have morphological properties that vary with those of TiO_2 and QMMOs (**Figure 7.5** and **Figure 7.6**).

On the other hand, the EDS spectra of the QMMOs were found to differ amongst themselves and were different from that of TiO_2 (**Figure 7.11** (**e)-(f**)). It was observed on the EDS spectra of TWZ730 that it consisted of elemental Ti, W, and O (**Figure 7.10 (e)**). Indeed the same case was observed with the other QMMOs, whereas in the case of TWZ703 no peaks associated with W were present but those allied with Zn were observed. The other two QMMOs, TWZ712 and TWZ721 had similar EDS spectra showing the presence of elemental Ti, W, Zn, and O. EDS data further confirmed what was postulated from peak shifting and peak broadening of laser Raman and PXRD peaks of QMMOs relative to that of TiO_2, that W^{6+} and Zn^{2+} ions were inside the lattice of TiO_2.

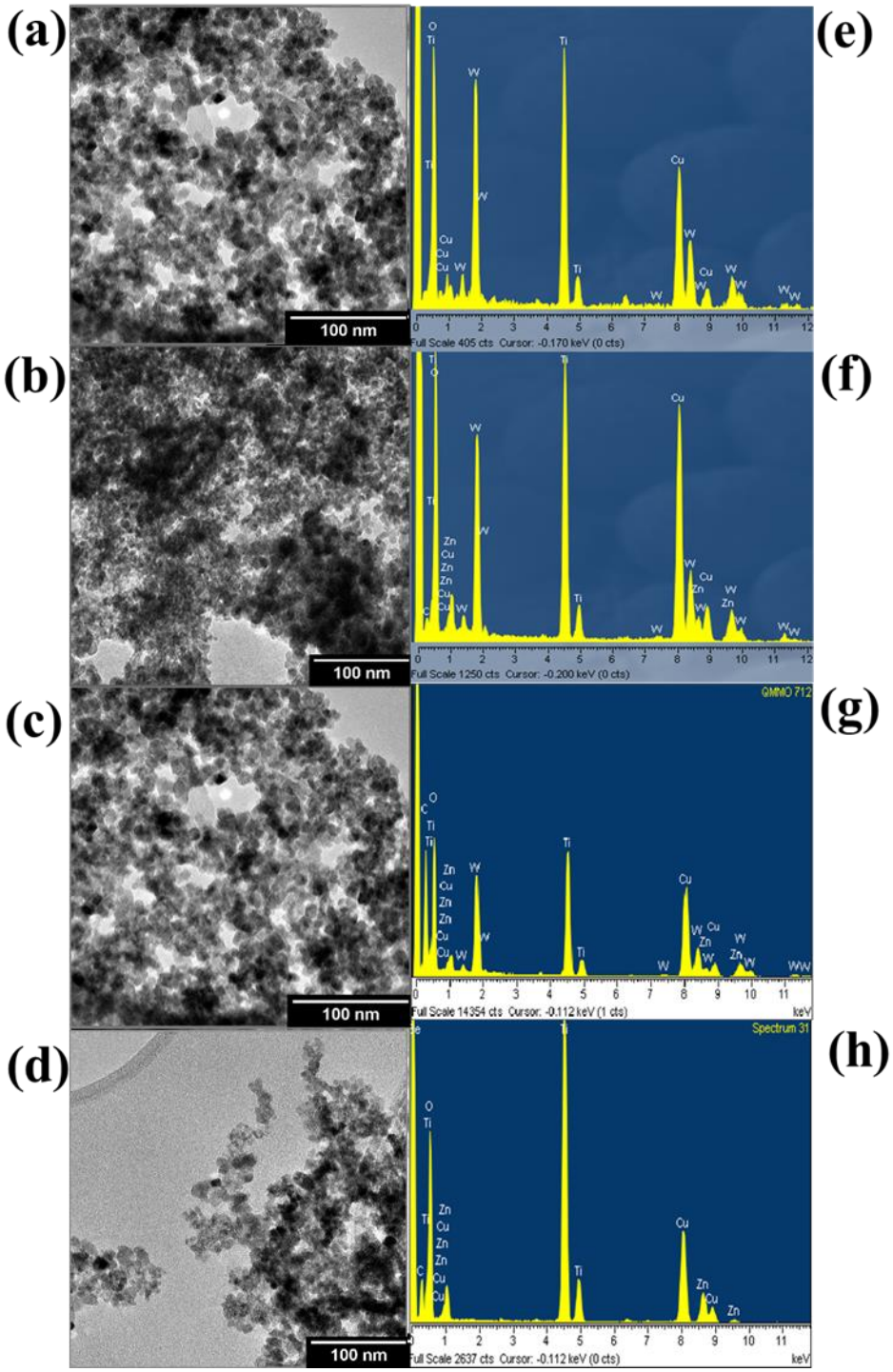

Figure 7.11. TEM images of (a) TWZ703, (b) TWZ712, (c) TWZ721 and (d) TWZ730. EDS spectra of (e) TWZ703, (f) TWZ712, (g) TWZ721 and TWZ730.

The QMMOs were found to all have similar morphologies (**Figure 7.11 (a)-(d)**). Furthermore, the morphology of the QMMOs was found to be similar to that of TiO_2 (**Figure 7.7 (a)**). This was consistent with laser Raman and PXRD data where it was found that TiO_2 and the QMMOs had similar Raman spectral and diffraction features. This further confirmed that W^{6+} and Zn^{2+} ions were incorporated into the lattice of TiO_2 as opposed to forming a mixture of metal oxides as metal oxides of these metal ions have morphological properties that vary with those of TiO_2 and QMMOs (**Figure 7.5** and **Figure 7.6**).

On the other hand, the EDS spectra of the QMMOs were found to differ amongst themselves and were different from that of TiO_2 (**Figure 7.11 (e)-(f)**). It was observed on the EDS spectra of TWZ730 that it consisted of elemental Ti, W, and O (**Figure 7.11 (e)**). Indeed the same case was observed with the other QMMOs, whereas, in the case of TWZ703 no peaks associated with W were present but those allied with Zn were observed. The other two QMMOs, TWZ712 and TWZ721 had similar EDS spectra showing the presence of elemental Ti, W, Zn, and O. EDS data further confirmed what was postulated from peak shifting and peak broadening of laser Raman and PXRD peaks of QMMOs relative to that of TiO_2, that W^{6+} and Zn^{2+} ions were inside the lattice of TiO_2.

The preceding discussed data gave a strong indication that the incorporation of W^{6+} and Zn^{2+} had been achieved. In order to ascertain if this had any effect on the optical properties of TiO_2, UV-DRS analyses were conducted. It was observed from the UV-DRS spectra of TiO_2 and the QMMOs that all the materials had a sharp absorption edge in the 380 nm region which is typical of TiO_2 (anatase phase) as shown in **Figure 7.12**. Furthermore, it was observed that the UV-DRS spectrum of TiO_2 was flat from 400 nm whereas those of the QMMOs had a wide absorption band extending up to 600 nm. This indicated that the presence of W^{6+} and Zn^{2+} in the lattice of TiO_2 influenced its electronic structure such that

a new conduction band was created. This is desirable as it meant that it was possible that the materials could harvest visible light and as such could be used for visible light driven photocatalysis.

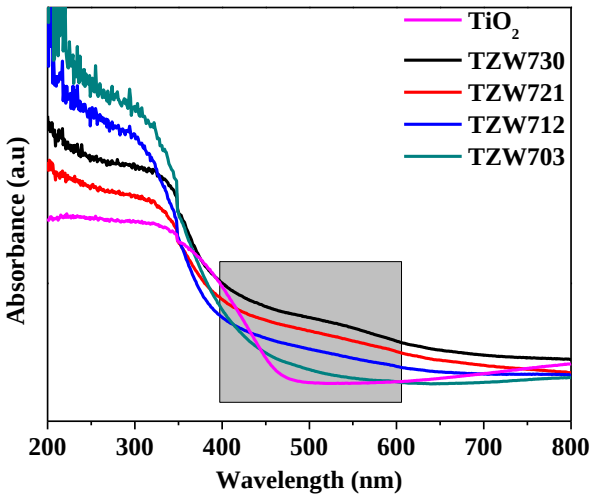

Figure 7.12. UV-DRS spectra of TiO_2 and QMMOs

7.3.3 Characterization of TiO_2 and QMMOs loaded on 10 % NCNTs

PXRD analyses were also done on the TiO_2/QMMOs and NCNTs composites in order to investigate the crystallographic properties of the materials. The PXRD patterns of the composites were found to be similar to those of TiO_2 and QMMOs, suggesting that the addition of NCNTs and the modified synthesis procedure did not alter the formation of QMMOs and TiO_2 (**Figure 7.13 (a)**). Moreover, the centroid of the (101) reflection of TiO_2 was observed at a lower 2θ values relative to those of QMMOs as it was the case with QMMOs (not supported on NCNTs) as shown in **Figure 7.13 (b)**. This was an indication that even the modified synthesis method yielded QMMOs. This was further demonstrated by calcining the materials to 800 °C to induce phase transformation from anatase to rutile (see appendix **A.7**) which is more stable and could not accommodate the high

concentration incorporation of Zn and W ions. Herewith it was observed that the QMMOs were turned into a mixture of W, Ti and Zn oxides.

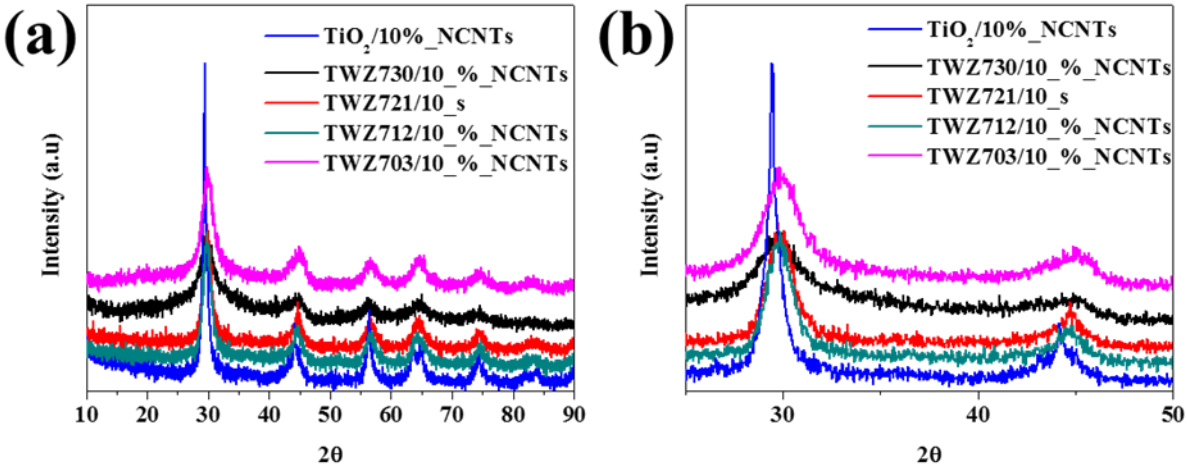

Figure 7.13. (a) PXRD patterns of TiO_2/QMMOs and 10 % NCNTs composites and (b) insert showing the (101) reflection.

TEM analyses were also conducted on the composites in order to ascertain if the coating of the NCNTs with TiO_2 or QMMOs nanoparticles was achieved as shown in **Figure 7.14.** It was observed that the NCNTs were coated uniformly with nanoparticles. This was deemed to be desirable as it increased the possibility of forming a heterojunction between the NCNTs and QMMOs/TiO_2 that could possibly reduce the recombination of electrons and holes thus increasing the photocatalytic efficiency of the materials.[30]

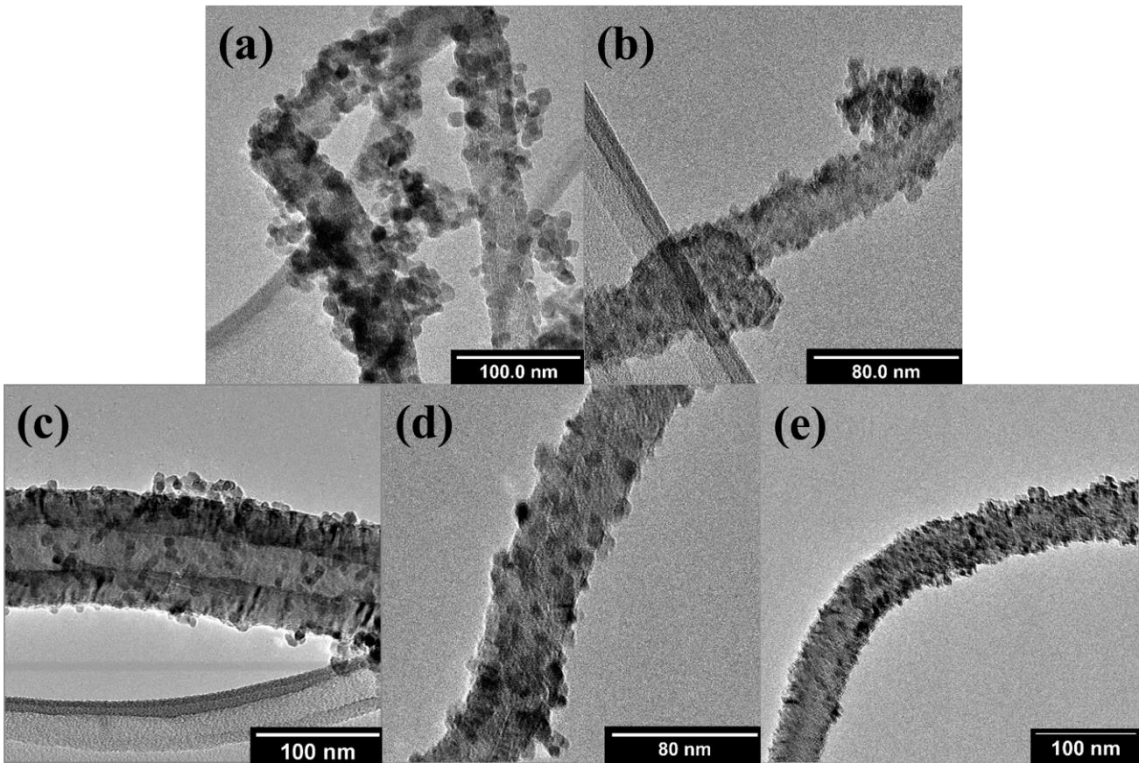

Figure 7.14. TEM images of (a) TiO_2/10%NCNTs, (b) TWZ730/10%NCNTs, (c) TWZ721/10%NCNTs, (d) TWZ712/10%NCNTs and (e) TWZ703/10%NCNTs

TGA analyses were conducted on the composites in order to determine if NCNTs were part of the composites as it was observed by TEM (**Figure 7.14**). The thermograms showed that the materials were thermally stable with less than 15 % of the material combusting at temperatures between 32 and 900 °C in oxygen (**Figure 7.15**). The stability of the materials is typical of metal oxides as they are able to withstand high temperatures without combusting. The small amount of material (>15 %) was attributed to the NCNTs onto which TiO_2 and the QMMOs were loaded onto. During the synthesis of the samples, 10 % of the materials were NCNTs, the small discrepancies observed on the thermograms were attributed to the inhomogeneity of the samples. Nevertheless, the amounts combusted were estimated to be between 7-14 % of the materials from the thermograms which were close

to the pre-calculated 10 %. Further evidence of that NCNTs were the ones combusted was that the combustion occurred at around 530 °C which was consistent with NCNTs (refer to **Figure 4.17**).

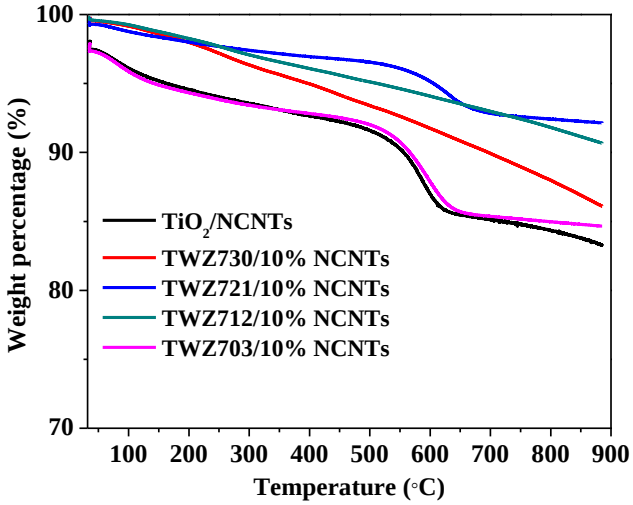

Figure 7.15. Thermograms of TiO_2 and QMMOs loaded onto 10 % NCNTs.

Having established that TiO_2 and QMMOs were successfully loaded onto NCNTs, photoluminescence analyses were conducted in order to ascertain if they had any effect on the recombination of the photoinduced charge carriers. The photoluminescence emission peaks of TiO_2, QMMOs, and composites were compared against each other (**Figure 7.16**). The emission peaks were observed upon exciting the materials with radiation with a wavelength of 290 nm. The emission intensity of TiO_2 was the highest observed indicating the lifetime of its electrons and holes was short. The intensities of the QMMOs were lower than that of TiO_2 indicating that the incorporation of W^{6+} and Zn^{2+} decreased the recombination rate of the photoinduced charge carriers.

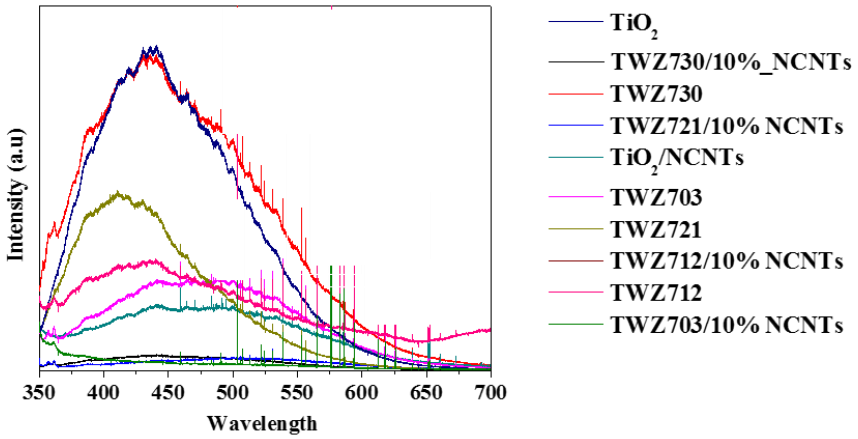

Figure 7.16. Photoluminescence emission spectra of TiO_2, QMMO and composites.

Furthermore, it was observed that the emission intensity of QMMOs decreased with an increasing amount of W^{6+} (increasing amount of Zn^{2+}) such that the emission intensity of the QMMO without W^{6+} TWZ703 was significantly lower than that of the QMMO with 30 % W^{6+} TWZ730. This indicated that the incorporation of Zn^{2+} was more effective at reducing the charge carriers' recombination rate. The materials composited with 10 % NCNTs had significantly lower than those of QMMOs and TiO_2. This was attributed to the NCNTs which are able to quench photoinduced electrons thus reducing the possibility of these electron recombining with holes.[8,31–33]

There was evidence of that the optical properties of TiO_2 were altered by the incorporation of W^{6+} and Zn^{2+} into the crystal lattice of TiO_2 and supporting the materials on NCNTs: i) It was observed from UV-DRS data that the incorporation of W^{6+} and Zn^{2+} into the lattice of TiO_2 resulted in mid-band gap energies (**Figure 7.12**), ii) It was observed from photoluminescence data the incorporation of W^{6+} and Zn^{2+} into the lattice of TiO_2 reduced the recombination of the photoinduced charge carriers (**Figure 7.16**). Moreover, from photoluminescence data, it was observed that the emission peaks of TiO_2/QMMO and 10 % NCNTs composites were significantly lower than those of the materials without

NCNTs. These were beneficial as they would be expected to be better photocatalysts than TiO_2 because: i) Sunlight which is primarily composed of visible light can be used to excite materials which absorb visible light and ii) The lower emission peaks suggest that the active charge carriers have a longer lifetime thus can interact with pollutants for longer consequently increasing the photocatalytic quantum efficiency. In order to test these postulates, the photoactivities of these materials were tested by measuring the efficiency at which they photodegrade BPA under visible light.

7.3.4 Photocatalytic testing

Prior to all photodegradation experiments, several experiments were conducted: i) BPA (80 ppm, 50 ml) was stirred in the presence of the various photocatalysts in the dark for 6 h. Herewith, it was observed that the adsorption equilibrium of BPA onto the various photocatalysts was 2 h. The various equilibrium concentrations are given in **Table 7.3** (Q_{60min}).

Prior to each photocatalytic experiments, BPA (80 ppm, 50 ml) was stirred in the presence of the photocatalysts to ensure that adsorption equilibrium had been reached preceding irradiation. ii) BPA (80 ppm, 50 ml) was irradiated using a solar simulator with a filter that cuts off radiation with wavelengths lower than 400 nm ensuring that UV was cut off. It was observed that radiation without a photocatalyst did not have any effect on the concentration of BPA.

Table 7.3. Adsorption equilibria concentrations of BPA on various photocatalysts.

Photocatalyst	X_{120min} (ppm)
TiO_2	0.9
TWZ730	0.7
TWZ721	0.8
TWZ712	0.8
TWZ703	0.9
TiO_2/10% NCNTs	1.4
TWZ730/10 % NCNTs	1.5
TWZ721/10 % NCNTs	1.4
TWZ712/10 % NCNTs	1.4
TWZ703/10 % NCNTs	1.5

The photocatalytic activity of TiO_2 (X_{60min} = 24 %) was found to be lowest when compared to those of the QMMOs and composites (**Figure 7.17**).

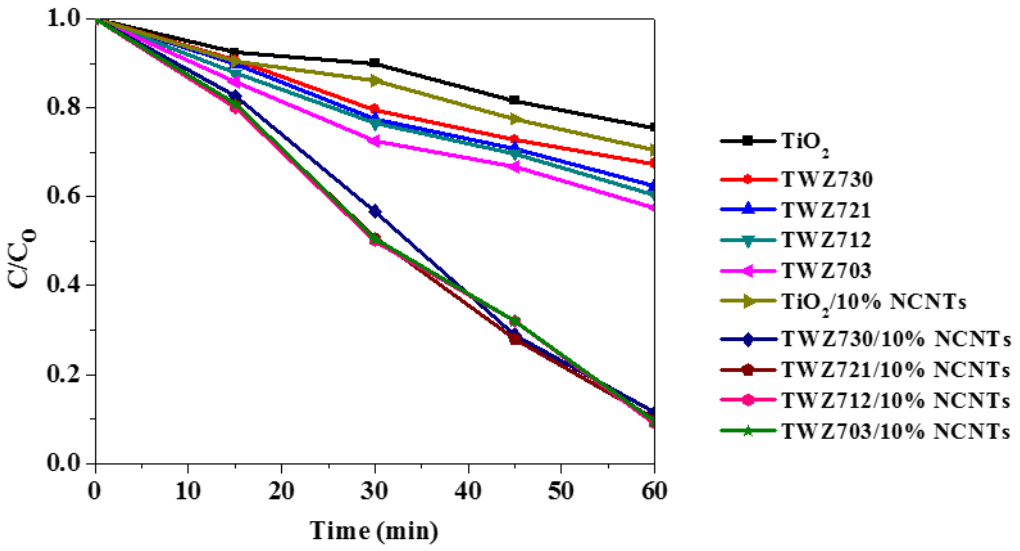

Figure 7.17. Photocatalytic efficiencies of TiO_2, QMMOs, and composites.

The low photoactivity was attributed to the fact that unmodified TiO_2 does not absorb visible light. Furthermore, it was observed that loading TiO_2 onto NCNTs only increased by 6 % (X_{60min} = 30 %). The slight increase in photoactivity was attributed to the decreased propensity of active charge carriers to recombine, evidence being that the photoluminescence emission peak of TiO_2/10% NCNTs was significantly lower than that of TiO_2. In the case of QMMOs, it was observed that their photoactivities (ranged between 32 and 46 %) were higher than that of TiO_2 and its NCNTs composite. The increased photocatalytic activity was attributed to the QMMOs which absorbed light in the visible part of the spectrum (**Figure 7.12**) and the significantly lower photoluminescence emission peaks (**Figure 7.16**). Furthermore, herewith it was observed that the photoactivities of the QMMOs increased with increasing amounts of Zn^{2+} incorporated (decreasing amount of W^{6+} incorporated) as shown in **Figure 7.17**. This was consistent with what was observed from photoluminescence where the emission peak of TWZ730/10 % NCNTs had the intensity that was almost as intense as that of TiO_2 and decreased with decreasing amounts of W^{6+}, with TWZ703/10 % NCNTs having the least intense photoluminescence emission peak. The QMMOs supported on NCNTs had the highest photoactivities ranging between 89-91 %.

It was hypothesized that the superior photoactivities observed for the QMMOs loaded onto NCNTs was as a result of the combined effect of that incorporating Zn^{2+} and W^{6+} introduced mid-band gap energies thus making it possible for the materials to absorb visible light (**Figure 7.12**) and the increased lifetime of charge carriers.

7.4 Conclusion

W^{6+} and Zn^{2+} ions were successfully incorporated into the crystal lattice of TiO_2 (anatase phase) using the resin gel technique to form QMMOs. This was confirmed using various characterization techniques, including PXRD, EDX, TEM, and laser Raman spectroscopy. The calcination of the QMMOs at 800 °C in air resulted in the material decomposing into tungsten trioxide, zinc oxide and the rutile phase of TiO_2, further confirming that mixed metal oxides were formed (see **Appendix A.7**). The incorporation of these metal ions into the lattice of TiO_2 did not alter the band edge of TiO_2 as was shown by UV-DRS but a wide absorption band was observed in the case of the QMMOs which wasn't there for TiO_2.

Composites consisting of QMMOs/TiO_2 and NCNTs (10 % loading) were successfully synthesized by modified resin gel synthesis. It was observed that the NCNTs were completely and homogeneously coated with QMMOs/TiO_2 nanoparticles. The photoluminescence emission peaks of NCNTs containing NCNTs were lower than that of the QMMOs and TiO_2, indicating retardation of the recombination of the electrons and holes.

The photocatalytic efficiencies of the materials were tested by monitoring the efficiency at which they photodegraded BPA under visible-light irradiation ($\lambda > 400$ nm). The QMMOs had higher photocatalytic efficiency relative to that of TiO_2. The photocatalytic efficiency of QMMOs increased with decreasing amounts of W^{6+} incorporated into TiO_2. The photocatalytic efficiency of TiO_2 was not improved by much when was loaded onto NCNTs (TiO_2/10 %NCNTs) but that of the QMMOs loaded on NCNTs was significantly increased. These remarks ratify that incorporation of W^{6+} and Zn^{2+} and compositing the

materials with TiO_2 resulted in unique materials with the potential of being viable photocatalysis.

7.5 References

1. Fujishima, A. & Honda, K. Photolysis-decomposition of water at the surface of an irradiated semiconductor. *Nature* **238,** 37–38 (1972).
2. Hara, K., Dan-oh, Y., Kasada, C., Ohga, Y., Shinpo, A., Suga, S., Sayama, K. & Arakawa, H. Effect of additives on the photovoltaic performance of coumarin-dye-sensitized nanocrystalline TiO_2 solar cells. *Langmuir* **20,** 4205–4210 (2004).
3. Wang, Y. Q., Hu, G. Q., Duan, X. F., Sun, H. L. & Xue, Q. K. Microstructure and formation mechanism of titanium dioxide nanotubes. *Chem. Phys. Lett.* **365,** 427–431 (2002).
4. Tahir, M. N. Natalio, F., Therese, H. A., Yella, A., Metz, N., Shah, M. R., Mugnaioli, E., Berger, R., Theato, P., Schröder, H. C., Müller, W. E. G. & Tremel, Wolfgang Enzyme-mediated deposition of a TiO_2 coating onto biofunctionalized WS_2 chalcogenide nanotubes. *Adv. Funct. Mater.* **19,** 285–291 (2009).
5. Dahl, M., Liu, Y. & Yin, Y. Composite titanium dioxide nanomaterials. *Chemical Reviews* **114,** 9853–9889 (2014).
6. Linsebigler, Amy L., Guangquan, L. & Yates, J. J. T. Photocatalysis on TiO_2 surfaces: principles, mechanisms, and selected results. *Chem. Rev.* **95,** 735–758 (1995).
7. Hoffmann, M. R., Martin, S. T., Choi, W. & Bahnemannt, D. W. Environmental Applications of Semiconductor Photocatalysis. *Chem. Rev.* **95,** 69–96 (1995).
8. Woan, K., Pyrgiotakis, G. & Sigmund, W. Photocatalytic Carbon-Nanotube-TiO_2 Composites. *Adv. Mater.* **21,** 2233–2239 (2009).

9. An, G., Ma, W., Sun, Z., Liu, Z., Han, B., Miao, S., Miao, Z. & Ding, KunlunPreparation of titania/carbon nanotube composites using supercritical ethanol and their photocatalytic activity for phenol degradation under visible light irradiation. *Carbon* **45,** 1795–1801 (2007).

10. Tayade, R. J., Kulkarni, R. G. & Jasra, R. V. Enhanced Photocatalytic Activity of TiO_2-Coated NaY and HY Zeolites for the Degradation of Methylene Blue in Water. *Ind. Eng. Chem. Res.* **46,** 369–376 (2007).

11. Ni, M., Leung, M. K. H., Leung, D. Y. C. & Sumathy, K. A review and recent developments in photocatalytic water-splitting using TiO_2 for hydrogen production. *Renew. Sustain. Energy Rev.* **11,** 401–425 (2007).

12. Fujishima, A., Rao, T. N. & Tryk, D. A. Titanium dioxide photocatalysis. *J. Photochem. Photobiol. C Photochem. Rev.* **1,** 1–21 (2000).

13. Leary, R. & Westwood, A. Carbonaceous nanomaterials for the enhancement of TiO_2 photocatalysis. *Carbon* **49,** 741–772 (2011).

14. Xu, Y., Zhuang, Y. & Fu, X. New Insight for Enhanced Photocatalytic Activity of TiO_2 by Doping Carbon Nanotubes: A Case Study on Degradation of Benzene and Methyl Orange. *J. Phys. Chem. C* **114,** 2669–2676 (2010).

15. Zhang, Z., Wang, W., Wang, L. & Sun, S. Enhancement of Visible-Light Photocatalysis by Coupling with Narrow-Band-Gap Semiconductor: A Case Study on Bi_2S_3/Bi_2WO_6. *ACS Appl. Mater. Interfaces* **4,** 593–597 (2012).

16. Ying, G. G., Kookana, R. S. & Dillon, P. Sorption and degradation of selected five endocrine disrupting chemicals in aquifer material. *Water Res.* **37,** 3785–3791 (2003).

17. Do, Y. R., Lee, W., Dwight, K. & Wold, A. The effect of WO_3 on the photocatalytic activity of TiO_2. *J. Solid State Chem.* **108,** 198–201 (1994).

18. Chai, S. Y., Kim, Y. J. & Lee, W. I. Photocatalytic WO_3/TiO_2 nanoparticles working under visible light. in *Journal of Electroceramics* **17,** 909–912 (2006).

19. Iliev, V., Tomova, D., Rakovsky, S., Eliyas, A. & Puma, G. L. Enhancement of photocatalytic oxidation of oxalic acid by gold modified WO_3/TiO_2 photocatalysts under UV and visible light irradiation. *J. Mol. Catal. A Chem.* **327,** 51–57 (2010).

20. Fu, H., Xu, T., Zhu, S. & Zhu, Y. Photocorrosion inhibition and enhancement of photocatalytic activity for ZnO via hybridization with C60. *Environ. Sci. Technol.* **42,** 8064–8069 (2008).

21. Vu, T. T., del Río, L., Valdés-Solís, T. & Marbán, G. Fabrication of wire mesh-supported ZnO photocatalysts protected against photocorrosion. *Appl. Catal. B Environ.* **140–141,** 189–198 (2013).

22. Xiao, F. X. Construction of highly ordered ZnO-TiO_2 nanotube arrays (ZnO/TNTs) heterostructure for photocatalytic application. *ACS Appl. Mater. Interfaces* **4,** 7055–7063 (2012).

23. Rajbongshi, B. M., Samdarshi, S. K. & Boro, B. Multiphasic bi-component TiO_2 – ZnO nanocomposite: synthesis, characterization and investigation of photocatalytic activity under different wavelengths of light irradiation. *J Mater. Sci. Mater. Electron* **26,** 377–384 (2015).

24. Franklyn, P. Synthesis, Characterisation and Structural Investigations of Nanoparticulate Forms of Selected (W,Ti,Al,Ba) Mixed MetalOxides. (University of Cambridge, 2011).

25. Asahi, R., Taga, Y., Mannstadt, W. & Freeman, A. Electronic and optical properties of anatase TiO_2. *Phys. Rev. B* **61,** 7459–7465 (2000).

26. Scanlon, D. O. Dunnill, C. W., Buckeridge, J. Shevlin, S. A., Logsdail, A. J., Woodley, S. M., Catlow, C. R. A., Powell, M. J., Palgrave, R. G., Parkin, I. P.,

Watson, G. W., Keal, T. Sherwood, P., Walsh, A. & Sokol, A. A. Band alignment of rutile and anatase TiO_2. *Nat. Mater.* **12,** 798–801 (2013).

27. Sanjinés, R., Tang, H., Berger, H., Gozzo, F., Margaritondo, G. & Lévy, F. Electronic structure of anatase TiO_2 oxide. *J. Appl. Phys.* **75,** 2945 (1994).

28. Franklyn, P. J. & Narrandes, A. Unlocking the Secrets Behind the Resin-Gel Synthesis for the Controlled Formation of Anatase and Rutile. *Proc. Int. Conf. Nanomater. Appl. Prop.* **1,** 1–17 (2012).

29. Perera, S. D., Sanjaya D. Mariano, R. G., Vu, K., Nour, N., Seitz, O., Chabal, Y. & Balkus, K. J. Hydrothermal synthesis of graphene-TiO_2 nanotube composites with enhanced photocatalytic activity. *ACS Catal.* **2,** 949–956 (2012).).

30. Wang, L., Shen, L., Li, Y., Zhu, L., Shen, J. & Wang, L. Enhancement of Photocatalytic Activity on TiO_2-Nitrogen-Doped Carbon Nanotubes Nanocomposites Enhancement of Photocatalytic Activity on TiO_2-Nitrogen-Doped Carbon Nanotubes Nanocomposites. *Int. J. photoenergy* **2013,** 1–7 (2013).

31. Gao, B., Chen, G. Z. & Li Puma, G. Carbon nanotubes/titanium dioxide ($CNTs/TiO_2$) nanocomposites prepared by conventional and novel surfactant wrapping sol-gel methods exhibiting enhanced photocatalytic activity. *Appl. Catal. B Environ.* **89,** 503–509 (2009).

32. Hintsho, N., Petrik, L., Nechaev, A., Titinchi, S. & Ndungu, P. Photo-catalytic activity of titanium dioxide carbon nanotube nano-composites modified with silver and palladium nanoparticles. *Appl. Catal. B Environ.* **156–157,** 273–283 (2014).

33. Zhang, Y., Tang, Z.R., Fu, X. and Xu, Y.J. Engineering the unique 2D mat of graphene to achieve graphene-TiO_2 nanocomposite for photocatalytic selective transformation: what advantage does graphene have over its forebear carbon nanotube. *ACS nano*, **5**, 7426-7435 (2011).

CONCLUSIONS AND FUTURE PERSPECTIVES

Conclusion

The two main purposes of this project were to show that: i) CFA could be used to synthesize useful materials which could be utilized to aid the photodegradation of organic contaminants in water (e.g. BPA) and ii) to synthesize nanomaterials/nanocomposites with tailor-made properties as well as to show the intrinsic connection between the physicochemical properties of these materials and their photocatalytic activity in the photodegradation of BPA in water.

CFA was shown to be an effective catalyst for the decomposition of melamine on its surface to grow NCNTs by 2-stage CVD setup as demonstrated in **Chapter 4**. Herewith, it was shown that upon the decomposition of melamine at different temperatures on the surface of CFA in a nitrogen atmosphere, this resulted in the formation of NCNTs. The morphological properties of the NCNTs which were obtained differed in several aspects: morphology, crystallinity and nitrogen content. These observations showed that CFA could be used for the synthesis of NCNTs, which are known to be useful materials in various existing applications.

The NCNTs discussed in **Chapter 4** were purified and composited with TiO_2 at various %m/m loadings and tested against TiO_2 for the photodegradation of BPA as was reported in **Chapter 5**. In order to do a comparison, CNFs were also synthesized, purified and composited with TiO_2 at the same loadings as those with NCNTs. Herewith, it was shown that the hydrothermally modified surfactant

assisted sol-gel technique was an effective method for the synthesis of homogeneously coated NCNTs/CNFs with TiO_2 nanoparticles. The UV-light driven photocatalytic efficiency of the materials was tested, where it was observed that there was a trade-off between the masses of CNFs/NCNTs used. Here the composites that consisted of 20 % CNFs/NCNTs showed the least activity whereas those with 5 % CNFs/NCNTs had a superior activity to the 1 % CNFs/NCNTs composites or even the unbound TiO_2. Furthermore, it was observed that the composites consisting of NCNTs and TiO_2 had higher photocatalytic activity than those of their CNFs counterparts. Indeed, in **Chapter 5** it was shown that materials grown from CFA could be used for photocatalysis.

CNFs and NCNTs are not the only materials that could be synthesized from CFA as it was demonstrated in **Chapter 6**. Here zeolites were derived from CFA using the 2-step alkali fusion hydrothermal method. These materials were found to be rod-like and were identified to be sodium aluminum silicate hydrate (CFA_Zeo). Composites consisting of CFA_Zeo and TiO_2 at various CFA_Zeo loadings were synthesized by a novel resin gel technique where it was observed that the CFA_Zeo rods were completely and homogeneously coated with TiO_2 nanoparticles. Compositing TiO_2 with these CFA derived zeolites was shown by UV-DRS to have left the absorption properties of TiO_2 unaltered. This meant that visible light driven photocatalysis was not feasible with these materials. In order to counteract this, Ag nanoparticles were deposited onto the surfaces of theseTiO_2 nanoparticles that were loaded on the CFA_Zeo. A wide SPR absorption band was observed in the UV-DRS spectra of the resulting composites which indicated that visible-light driven light photocatalysis with these composites was possible.

The photocatalytic efficiency of these composite materials was tested under both UV and visible-light ($\lambda > 400$ nm) irradiation. Herewith, it was observed that under UV light, the composite consisting of 30 % CFA_Zeo and TiO_2 (i.e. TiO_2/CFA_Zeo(30 %)) had a photocatalytic efficiency that was lower than that of TiO_2. However the TiO_2/CFA_Zeo(15 %) composite had higher photocatalytic efficiency than TiO_2. This also indicated that there was a trade-off between the mass of CFA_Zeo used and the increased photocatalytic efficiency. The materials that consisted of CFA_Zeo, TiO_2, and Ag nanoparticles had even superior photocatalytic efficiency, with Ag/TiO_2/CFA_Zeo showing the highest photocatalytic efficiency. Different trends were observed when the photocatalytic efficiencies of these materials were tested under visible-light irradiation. Herewith, TiO_2 and the materials without Ag nanoparticles were found to have the least photocatalytic efficiency as compared to those that contained Ag nanoparticles. Furthermore, it was observed that the material without CFA_Zeo, i.e. Ag/TiO_2 had the highest visible-light-driven photocatalytic efficiency. The results in **Chapter 6** showed that zeolites derived from CFA were effective at increasing the photocatalytic efficiency of TiO_2, especially under UV-light. Furthermore, it was shown that the deposition of Ag nanoparticles improved the photocatalytic efficiency of these materials under both UV and visible light.

Having demonstrated that composites consisting of CFA derived material (CFA_Zeo) could be modified to make it possible to harvest visible-light for photocatalysis in **Chapter 6**, in **Chapter 7** a different approach was investigated which aimed at achieving similar results. Herewith, W^{6+} and Zn^{2+} (up to 30 %m/m?) were incorporated into the crystal lattice of TiO_2 (anatase-phase) using the resin gel

technique to make QMMOs. The formation of QMMOs was confirmed by EDS, PXRD, TEM, and UV-DRS. It was observed from UV-DRS that the QMMOs had a broad absorption band in the visible region, indicating that it was possible that they could be used as visible-light photocatalysts. The QMMOs and TiO_2 nanoparticles were composited with CFA grown NCNTs (10 % m/m) using a hydrothermally modified resin gel technique. The NCNTs were observed to have been completely and homogeneously coated with TiO_2 nanoparticles. The visible-light photocatalytic efficiencies of these materials were tested, where it was found that QMMOs had a photocatalytic efficiency that increased with decreased concentration of W^{6+} that was incorporated into TiO_2. However, their efficiencies were higher than that of unbound TiO_2. Compositing QMMOs with NCNTs increased the observed photocatalytic efficiency. Compositing TiO_2 with NCNTs showed very little photocatalytic improvement.

Future perspective

This research has provided several strategies for the improvement of the photocatalytic efficiency of TiO_2. However, it has also thrown up several areas that will require further investigation.

Although it was shown that CFA could be used for the synthesis of beneficial materials, it was observed that in order to sufficiently use the CNFs and NCNTs synthesized from CFA it was necessary to dissolve CFA by acid. Further investigations should be done to see if the NCNTs and CNFs could be used without having to dissolute CFA.

In order to understand the type of nitrogen that dominated the various NCNTs that were synthesized, various additional spectroscopic techniques will need to be utilized.

The electron capacity of the NCNTs, CNFs and zeolitic material synthesized from CFA will need to be measured.

Further investigations on the structural properties of the zeolites formed, e.g. HRTEM to study the proposed porous structure of the materials and small angle XRD is required to further confirm the zeolization process.

Various spectroscopies will need to be applied to study the electronic structure of the QMMOs.

In order to study the mechanism by which W^{6+} and Zn^{2+} were incorporated into the crystal lattice of TiO_2 other techniques e.g. neutron powder diffraction, will need to be applied in more detail.

In order to elucidate the photodegradation pathways of BPA, using the composites that were synthesized in this research, several hyphenated-techniques such as: GC–MS or HPLC–MS will need to be applied.

The toxicity of the photodegradation by-products will need to be studied and their mineralization optimized.

In general, regardless of what method was used for the improvement of the photocatalytic efficiency of TiO_2, numerous spectroscopy studies will need to be

performed to investigate the very fast excitation and charge recombination processes. This would need to be performed in order to assist in recognizing the factors that inhibit the energy-conversion efficacy.

Another important factor in photocatalysis in general is that only a limited number of spectroscopic investigations have been done to establish the electron-hole transfer routes in semiconductors. A more detailed comprehension of the interfacial charge transfer kinetics would be imperative to the fabrication of more effective photocatalysts for the photodegradation of organic contaminants in water.

There are still key technical predicaments such as: the optimization of procedural setup and the recovery of catalyst nanoparticles. In the future, these will need to be studied in detail in order to establish the feasibility of using the types of photocatalysts that were synthesized in this research on a large scale.

APPENDIX

A.3

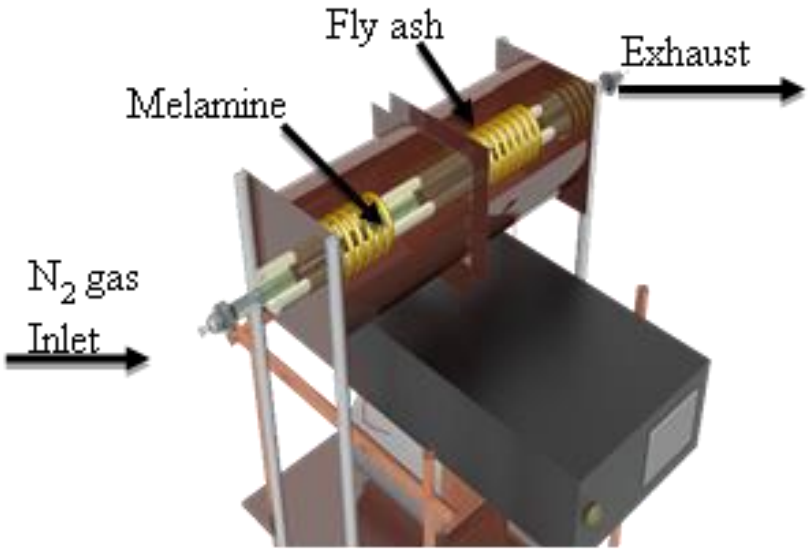

A.3.1. Two-stage chemical vapor deposition set-up.

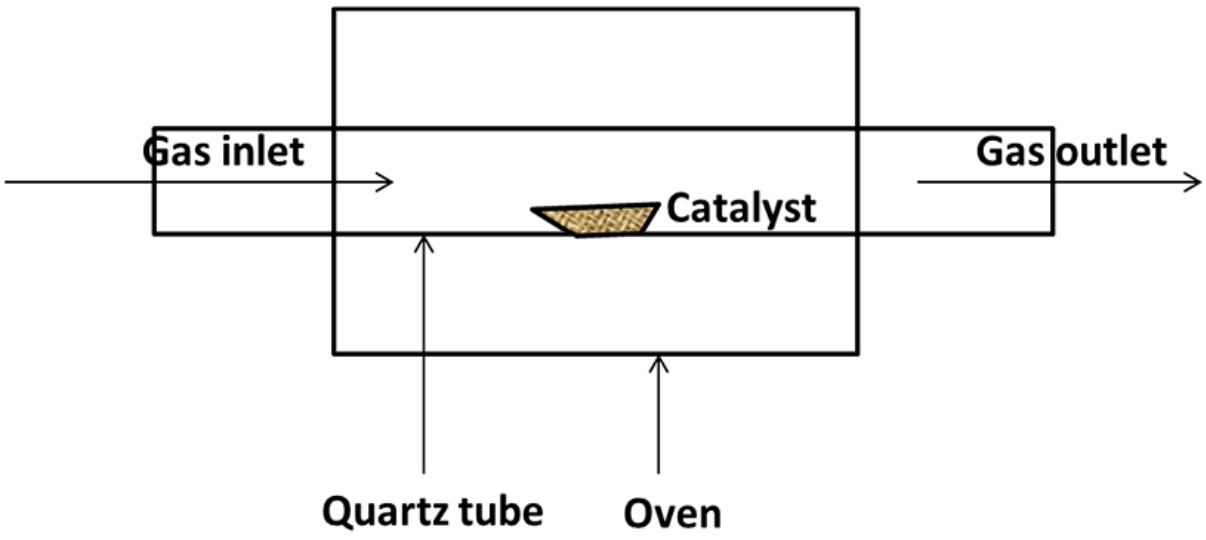

A.3.2. One-stage chemical vapor deposition setup

A. 5

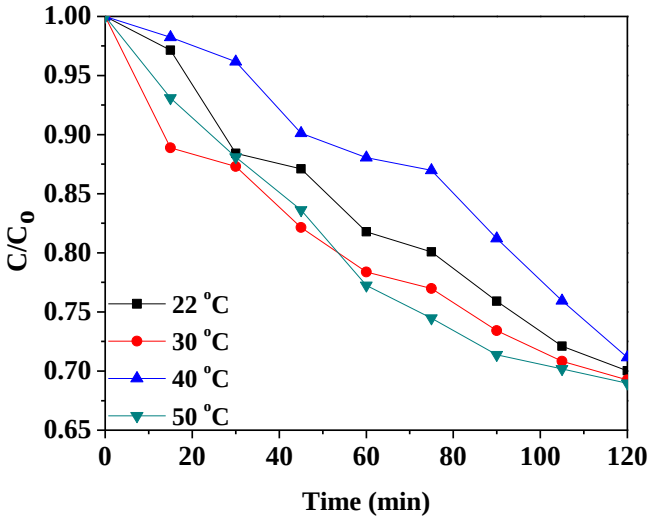

A5.1. Effect of temperature on the photodegradation of 50 ml of 120 ppm neutral solution of BPA in water at 22 °C.

A.7.

PXRD analysis was also done on the materials calcined at 800 °C where it was observed that the PXRD pattern of ZnO calcined at was similar to that of the un-calcined material (**A.7.1**), except for that the peaks were more sharper indicating improved crystallinity, which typically happens having subjected certain materials to high temperatures.

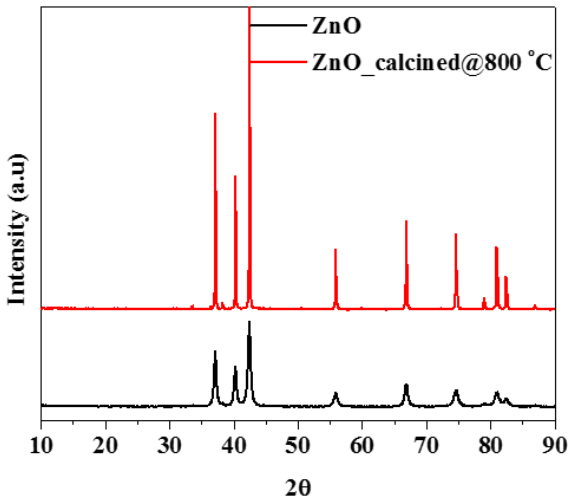

A.7.1. PXRD pattern of ZnO °C calcined at 400 and ZnO calcined at 800 °C.

In the case of WO_3, there was a slight difference observed in the two PXRD patterns (calcined at 800 °C and 400 °C). The disappearance of the (100) reflection at 16 ° was observed when the two patterns were compared **(A.7.2**). A similar PXRD pattern was reported by Leghari *et al*., who assigned the pattern as of monoclinic WO_3.[27] Furthermore, Szilagyi *et al*. observed that having calcined hexagonal WO_3 to temperatures beyond 550 °C, it changed into its hexagonal form.[1]

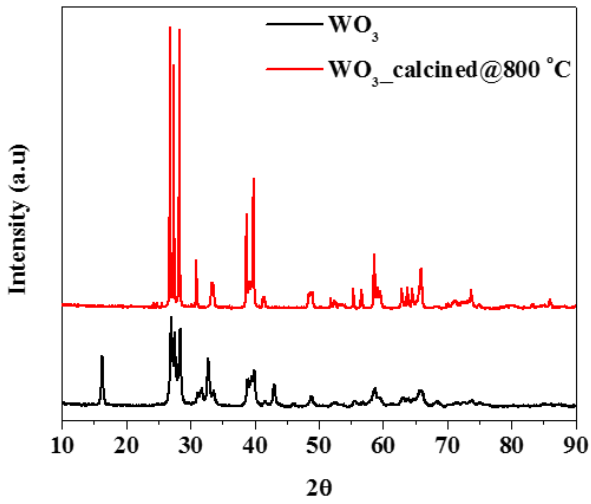

A.7.2. PXRD pattern of WO_3 calcined at 400 and 800 °C.

The PXRD pattern of TiO_2 after it had been calcined at 800 °C was totally different from that of TiO_2 before it was calcined (**A.7.3**). The reflections were observed at 2θ positions of: 32, 43, 46, 49, 52, 64, 67, 75 and 77 °, indexed as: (110), (101), (111), (211), (220), (002), (311), (301) and (112) (JC JCPDS, no. 21-1276) respectively. The peaks were consistent with those of tetragonal rutile phase.

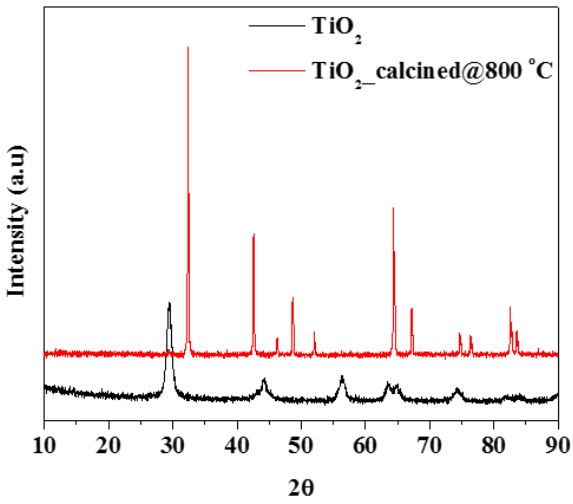

A.7.3. PXRD patterns of TiO_2 before (calcined at 400 °C) and after calcining at 800 °C.

The QMMOs consisting of 70 % TiO_2 were then calcined to 800 °C to induce phase transformation of TiO_2-anatase phase to the rutile phase. PXRD was used to study these materials. The PXRD patterns of the calcined QMMOs were different from those of the materials calcined at 400 °C (**refer to Chapter 7**). Furthermore, when compared to that of TiO_2 calcined at 800 °C, their patterns consisted of matching rutile peaks but also consisting of several other peaks which were suspected to have been those of WO_3 and ZnO (**A.7.(1-3)).**

The QMMOs consisting of 70 % TiO_2 were then calcined to 800 °C to induce phase transformation of TiO_2-anatase phase to the rutile phase. PXRD was used to study these materials (**A.7.4**). The PXRD patterns of the calcined QMMOs were different from those of the un-calcined materials. Furthermore, when compared to that of TiO_2 calcined at 800 °C, their patterns consisted of matching rutile peaks but also consisting of several other peaks which were those of WO_3 and ZnO.

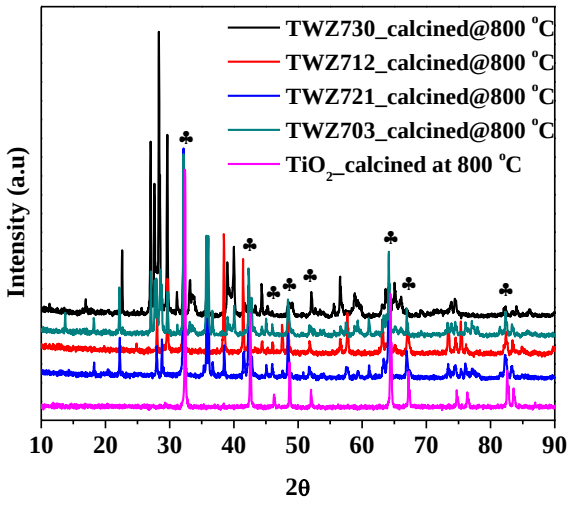

A.7.4. PXRD patterns of TiO_2 and the various QMMOs calcined at 800 °C.

Indeed, it was observed that some of the peaks that did not match those of the TiO_2-rutile phase matched those of ZnO for certain samples (**A.7.5**). Peaks that matched those of ZnO were not observed on the PXRD pattern of TWZ730 this was adjudged to be plausible as the material was only composed of Ti^{4+}, $W^{6+,}$ and O_2^{2-}. The observed ZnO peaks in the case of the other calcined QMMOs that consisted of Ti^{4+}, W^{6+}, Zn^{2+}, and O_2^{2-}, suggested that upon phase transformation of TiO_2-anatase phase to TiO_2-rutile phase the other metal ions or at least Zn^{2+} formed a corresponding oxide outside the lattice of TiO_2.

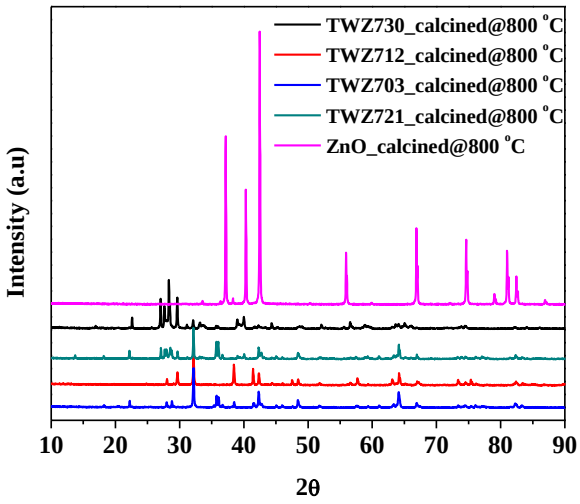

A.7.5. PXRD patterns of ZnO and the various QMMOs calcined at 800 °C.

References:

1. Leghari, S. A. K., Sajjad, S., Chen, F. and Zhang, J. WO_3/TiO_2 composite with morphology change via hydrothermal template-free route as an efficient visible light photocatalyst. *Chemi. Eng. Jour.* **166**, 906-915 (2011).
2. Szilagyi, I. M., Saukko, S., Mizsei, J., Toth, A. L., Madarazs, J and Pokol, G. Gas sensing selectivity of hexagonal and monoclinic WO_3 to H_2S. *Sol. Sta. Scie.*, 30, 1857-1860 (2010)

